UNIVERSITY OF LONDON

Imperial College of Science and Technology
Blackett Laboratory
Optics Section

OPTICAL PHASE CONJUGATION IN PHOTOREFRACTIVE MATERIALS AND ITS APPLICATION TO IMAGE PROCESSING.

Iain Lindsay

Thesis submitted for the degree of
Doctor of Philosophy of the University of London
and for the Diploma of Imperial College

September 1988

To my parents, brothers and
Venus.

ACKNOWLEDGEMENTS

First and foremost I would like to pay a special tribute to Professor J.C. Dainty, alias Chris, for his continual support, guidance and encouragement during the course of this research. His generosity and awareness provided me with excellent research facilities and the opportunity to travel and meet numerous people at many overseas conferences, and his patience at correcting my spelling and grammatical errors during the course of writing this thesis was admirable.

I would like to thank all the members of the Applied Optics Group, past and present, who through stimulating conversation and practical advice have helped me complete this work. Special mentions go to the computing intellects of 6M09, the motley crew of 612 and the happy friendly bunch of 629.

I am particularly grateful for the assistance of Nick J. Wooder in the laboratory, the company of Stella Cacoullis during the arduous task of writing a thesis and the special friendship, support and advice of Juanito Martinez, who taught me how to play Dominos while drinking *Cuba Libra*[†].

The support of the Science and Engineering Research Council is appreciated and I am grateful for the practical and financial assistance received from British Aerospace p.l.c. during my stay at Imperial College.

[†] Two fingers of *Barcardi*, one of *Coke*, served on the rocks with a slice of lime.

ABSTRACT

The photorefractive effect is discussed in detail and accompanied by a comprehensive analysis of coherent light amplification by two wave mixing and phase conjugation by degenerate four wave mixing optical configurations. A selection of photorefractive materials are studied and their photoconducting and electro–optic characteristics are compared. Experimental investigations are confined principally to barium titanate, $BaTiO_3$, and secondly cerium doped strontium barium niobate, SBN:60. The original contributions to the field consist of experimental demonstrations of a phase conjugate Fabry–Perot interferometer and an all optical autoassociative memory, and a theoretical investigation into the photorefractive response to spatially confined circularly symmetric intensity profiles in general and the Gaussian profile in particular.

CONTENTS

ACKNOWLEDGEMENTS 3

ABSTRACT 4

CONTENTS 5

NOTATION 8

LIST OF FIGURES 11

LIST OF TABLES 20

CHAPTER 1: INTRODUCTION 22
1.1 Historical review 22
1.2 Thesis synopsis 24
1.3 References 27

CHAPTER 2: THE PHOTOREFRACTIVE EFFECT AND MATERIALS 30
2.1 Introduction 30
2.2 Photoconductivity 30
2.2.1 Band Transport Model 31
2.2.2 Charge Hopping Model 39
2.3 The Electro-optic Effect 40
2.4 Photorefractive Materials and Properties 42
2.5 Geometric and polarisation considerations for $BaTiO_3$ and SBN 51
2.6 Conclusions 54
2.7 References 56

CHAPTER 3: TWO WAVE MIXING AND COHERENT LIGHT AMPLIFICATION 59
3.1 Introduction 59
3.2 Theory 59
3.2.1 Linear in generation and recombination regime 60
3.2.2 Saturation regime 65
3.2.3 Dynamic self-diffraction 68

3.3 Experimental Procedure and Results ____ 76
3.3.1 Steady state measurements ____ 77
3.3.2 Transient measurements ____ 84
3.4 Conclusions ____ 88
3.5 References ____ 89

CHAPTER 4: FOUR WAVE MIXING AND PHASE CONJUGATION ____ 90
4.1 Introduction ____ 90
4.2 Theory ____ 92
4.2.1 Phase conjugation by DFWM in PR materials ____ 93
4.3 Experimental procedure and results ____ 98
4.4 Self pumped phase conjugation by
$BaTiO_3$ and SBN ____ 103
4.5 Conclusions ____ 111
4.6 References ____ 112

CHAPTER 5: SPECULAR REFLECTION CANCELLATION AND
ENHANCEMENT BY A FABRY-PEROT INTERFEROMETER
WITH A PHASE CONJUGATE MIRROR ____ 115
5.1 Introduction ____ 115
5.2 Theory ____ 117
5.2.1 Specular reflection cancellation ____ 122
5.2.2 Specular reflection enhancement ____ 123
5.3 Experimental procedure and results ____ 124
5.4 Conclusions ____ 134
5.5 References ____ 135

CHAPTER 6: HOLOGRAPHIC ASSOCIATIVE MEMORIES USING
PHASE CONJUGATE FEEDBACK ____ 137
6.1 Introduction ____ 137
6.2 The Hopfield neural network model ____ 137
6.3 Computer simulation of Hopfield's
neural network model ____ 140
6.4 All optical autoassociative recall ____ 144
6.5 Conclusion ____ 150
6.6 References ____ 152

CHAPTER 7: THE ILLUMINATION OF PHOTOREFRACTIVE MATERIALS WITH A CIRCULARLY SYMMETRIC GAUSSIAN INTENSITY PROFILE ____ 154
7.1 Introduction ____ 154
7.2 Theory ____ 154
7.2.1 Initial transient regime ____ 156
7.2.2 Steady state regime ____ 161
7.3 Resultant refractive index profiles ____ 168
7.4 Experimental procedure and results ____ 173
7.5 Conclusions ____ 174
7.6 References ____ 176

CHAPTER 8: SUMMARY AND CONCLUSIONS ____ 177

APPENDIX A: THE ELECTRO-OPTIC NATURE OF BARIUM TITANATE AND STRONTIUM BARIUM NIOBATE ____ 182

APPENDIX B: SPECTROPHOTOMETRIC DATA ____ 186

APPENDIX C: ANALYTIC SOLUTION OF THE BAND TRANSPORT EQUATIONS FOR A ONE DIMENSIONAL COSINUSOIDAL INTENSITY PROFILE ____ 190

APPENDIX D: THE COUPLED WAVE THEORY FOR A DYNAMIC MEDIUM ____ 195

APPENDIX E: TABULATED TWO WAVE MIXING DATA FOR BARIUM TITANATE AND CERIUM DOPED STRONTIUM BARIUM NIOBATE ____ 203

APPENDIX F: PHASE CONJUGATION BY DEGENERATE FOUR WAVE MIXING ____ 208

APPENDIX G: PHOTOREFACTIVE DEGENERATE FOUR WAVE MIXING COUPLED WAVE THEORY ____ 213

APPENDIX H: STOKES'S RELATIONS FOR TIME REVERSED WAVES AT A LOSSLESS BEAM SPLITTER ____ 221

APPENDIX I: SPECULAR REFLECTION CANCELLATION AND ENHANCEMENT EXPERIMENTAL DATA ____ 224

REFERENCES ____ 226

PUBLICATIONS ____ 240

NOTATION

Roman characters:

c	Speed of light in vacuo
D	*Diffusion* coefficient
E	Electric field amplitude
E_q	Characteristic material electric field
E_A	Externally applied electric field
E_D	Characteristic *diffusion* field
E_ρ	Radial electric field amplitude
E	Electric field vector
G	*Generation* rate
h	Planck's constant
$\hbar$	Planck's constant/2π
i	$\sqrt{-1}$
I	Light intensity
I_o	Total light intensity
I_R	Reference wave intensity
I_S	Signal wave intensity
j	Current density amplitude
$\mathbf{j}'_D$	Rate of change of flux density
$\mathbf{j}_d$	*Drift* current density
$\mathbf{j}_D$	*Diffusion* current density
k	Grating wavenumber
k_o	Characteristic material grating wavenumber
k_B	Boltzmann constant
k	Grating wavevector
l	Material length
L_d	Characteristic *drift* length
L_D	Characteristic *Diffusion* length
m	Reduced modulation
M	Interference fringe contrast
M	*Migration* rate
n	Refractive index
n_o	Bulk ordinary refractive index

n_e	Bulk extra-ordinary refractive index
Δn	Refractive index change
n	Free electron number density
n_o	Peak free electron number density
N_A	Total acceptor number density
N_D	Total donor number density
N_D^+	Ionised donor number density
N_T	Total shallow trap number density
N_T^+	Ionised shallow trap number density
p	Free hole number density
q	Elementary unit of charge
r	Position vector
r_{eff}	Effective electro-optic coefficient
R	Reference wave amplitude
R′	Diffracted reference wave amplitude
R	Reference wave field vector
R	Recombination rate
s	Photoexcitation constant
s_e	Electron photoexcitation constant
s_h	Hole photoexcitation constant
S	Signal wave amplitude
S′	Diffracted signal wave amplitude
S	Signal wave field vector
t	Time
T	Absolute temperature
x	Cartesian co-ordinate
y	Cartesian co-ordinate
z	Cartesian co-ordinate

Greek characters:

α	Absorption coefficient
β	Thermal generation rate
β_e	Electron thermal generation rate
β_h	Hole thermal generation rate

β_o	Incident beam intensity ratio
β_{exit}	Exit beam intensity ratio
γ	Phase conversion factor
γ_R	Recombination constant
γ_e	Electron recombination constant
γ_h	Hole recombination constant
Γ	Intensity gain factor
ε	Relative permittivity
ε_o	Permittivity of free space
η	Diffraction efficiency
θ	Incident angle
λ	Wavelength of the incident light
Λ	Interference fringe spacing
μ	Relative permeability
μ_o	Permeability of free space
μ	Free carrier mobility
μ_e	Free electron mobility
μ_h	Free hole mobility
ν	Temporal frequency
π	3.14159265...
ρ	Radial co–ordinate
$\mathcal{R}$	Reference wave wavevector
$\mathcal{S}$	Signal wave wavevector
τ_D	Characteristic *diffusion* time
τ_R	Characteristic recombination time
τ_{rise}	Grating rise time
τ_{decay}	Grating decay time
τ_{dark}	Characteristic dark storage time
ϕ	Grating phase shift angle
ϕ_R	Reference wave phase angle
ϕ_S	Signal wave phase angle
Φ	Grating phase angle
Φ	Quantum efficiency
ω	Temporal angular frequency
ω	Characteristic beam width

LIST OF FIGURES

Chapter 2

Figure	Caption	Page No
2.1	Schematic illustration of the band transport model.	31
2.2	Schematic illustration of electron/hole competition in the band transport model.	36
2.3	Schematic illustration of deep donors/shallow traps in the band transport model.	37
2.4	Schematic illustration of charge hopping model.	39
2.5	Absorption spectra for $BaTiO_3$.	44
2.6	Photographs of the three crystals of $BaTiO_3$; from left to right, samples #1, #2 and #3.	44
2.7	Absorption spectra for cerium doped SBN:60.	45
2.8	Photograph of crystals #1 of cerium doped SBN:60.	46
2.9	Absorption spectrum for $Bi_{12}SiO_{20}$.	46
2.10	Photograph of sample #1 of $Bi_{20}SiO_{20}$.	47
2.11	Absorption spectra for chromium doped GaAs and iron doped InP.	48
2.12	Bulk indices of refraction for $BaTiO_3$.	49
2.13	Cartesian co-ordinate change to locate principal dielectric axes in $BaTiO_3$/SBN.	53

Chapter 3

Figure	Caption	Page No
3.1	Formation of a one dimensional cosinusoidal intensity profile.	60

3.2a) Induced electric field for *diffusion* dominant transport mechanism. 63

3.2b) Induced electric field for *drift* dominant transport mechanism. 64

3.3 Summarised PR effect for n–type photoconductivity, *diffusion* dominance and a one dimensional cosinusoidal intensity profile. 66

3.4 Schematic illustration of wavenumber dependence on induced electric field for both *drift* and *diffusion* dominant transport mechanisms. 67

3.5 Self–diffraction of signal and reference beams off a ϕ phase shifted induced holographic grating. 70

3.6 Fringe contrast variation and bending in a dynamic PR grating. 73

3.7a) Contrast variation of straight fringes for a *diffusion* dominated transport mechanism. 74

3.7b) Curved fringes of constant contrast for a *drift* dominated transport mechanism. 75

3.8 Schematic diagram of experimental apparatus used for TBC investigations in both steady state and transient regimes. 77

3.9 Beam coupling, $\Delta I/I$, versus normalised wavenumber, $k/(n\omega/c)$, for $BaTiO_3$. 78

3.10 Beam coupling, $\Delta I/I$, versus normalised wavenumber, $k/(n\omega/c)$, for cerium doped SBN:60. 79

3.11 Diffraction efficiency versus incident and exit beam ratios, β_o and β_{exit}, for $BaTiO_3$. 81

3.12 Diffraction efficiency versus incident and exit beam ratios, β_o and β_{exit}, for cerium doped SBN:60. 81

3.13 Schematic diagram of experimental apparatus used for coherent amplification of an image bearing signal beam. 82

3.14 Coherent image amplification by two beam coupling; a) original and b) amplified image. 83

3.15 Normalised diffracted probe beam intensity, I'_{Probe} versus the grating writing time, t, for $BaTiO_3^{\#1}$. 85

3.16 Characteristic grating rise time, τ_{rise}, versus the Log of I_o for $BaTiO_3^{\#1}$. 85

3.17 Normalised diffracted probe beam intensity, I'_{Probe}, versus grating erasure time, t, for $BaTiO_3^{\#1}$. 86

3.18 Characteristic grating decay time, τ_{decay}, versus the Log of I_{Probe} for $BaTiO_3^{\#1}$. 86

3.19 Characteristic grating decay time, τ_{decay}, versus the Log of I_{Probe} for cerium doped SBN:$60^{\#1}$. 87

Chapter 4

Figure	Caption	Page No
4.1	Comparison between a) conventional and b) phase conjugate mirror reflections.	91
4.2	Phase conjugation by DFWM in a PR material.	93
4.3	Phase conjugation by DFWM in a p–type photoconducting PR material for a *diffusion* dominated transport mechanism. a) Non–optimum and b) optimum orientation of the crystalline +c axis.	96

4.4 Schematic illustration of the optical systems used to demonstrate phase distortion correction of an image bearing beam using a PCM. 99

4.5 Experimental results of phase distortion correction using a PCM. a) Original test transparency (USAF resolution chart), b) double phase distorted image generated using a conventional plane mirror and c) recovered phase distortion free image generated using a PCM. 100

4.6 Schematic illustration of a phase conjugate Michelson interferometer used to perform EXOR digital logic. 101

4.7 Complex amplitudes at various locations and directions in a PC Michelson interferometer. 103

4.8 Experimental results of EXOR digital logic performed using PC Michelson interferometer and two binary transparencies. a) The PC of transparency$^{\#1}$, b) the PC of transparency$^{\#2}$ and c) their EXOR logical combination. 104

4.9 Schematic diagram of asymmetric beam fanning in $BaTiO_3$. 105

4.10 Induced steady state radial electric field profile, o, for an illuminating Gaussian intensity profile, —— . 106

4.11 RI modulation profiles along the z axis (+c axis) for *ordinary*, $\star$, and *extra–ordinary*, o, polarisations. 107

4.12 Asymmetric beam fanning observed for a) *ordinary* and b) *extra–ordinary* polarised light. 108

4.13 Schematic illustration of *self–pumped* phase conjugation by DFWM in $BaTiO_3$. 109

4.14 Top view of self–pumping $BaTiO_3^{\#2}$. 109

4.15 The temporal behaviour of *self*-pumped $BaTiO_3^{\#2}$. a) steady *cw*, b) regular oscillatory and c) chaotic modes of operation. 110

Chapter 5

Figure	Caption	Page No
5.1	The correction of extensive backscatter using a PCM.	116
5.2	Phase conjugate Fabry–Perot interferometer.	118
5.3	The relative intensities of I_r and I_c versus the phase conjugate reflectivity, R_{PC}, of the PCM for $(\phi_a - \phi_b) = 0$ and R=0.4.	122
5.4	The relative intensities of I_r and I_c versus the phase conjugate reflectivity, R_{PC}, of the PCM for $(\phi_a - \phi_b) = 0$ and R=0.9.	123
5.5	The relative intensities of I_r and I_c versus the phase conjugate reflectivity, R_{PC}, of the PCM for $(\phi_a - \phi_b) = \pi$ and R=0.4.	124
5.6	The relative intensities of I_r and I_c versus the phase conjugate reflectivity, R_{PC}, of the PCM for $(\phi_a - \phi_b) = \pi$ and R=0.9.	124
5.7	Schematic representation of the experimental apparatus used in the first experiment.	126
5.8	The normalised intensity of the specular reflection versus time.	127
5.9	The relative intensity of the specular reflection, I_r versus the phase conjugate reflectivity, R_{PC}; theoretical curve,—— , and experimental points, o.	128
5.10	Normalised intensity of the cancelled specularly reflection versus time.	129

5.11 Schematic representation of the experimental apparatus used in the second experiment. 130

5.12 The normalised specularly reflected intensity, I_r, versus time for a slow scan of the relative intrinsic phase, $(\phi_a - \phi_b)$. 130

5.13 Graphical representation of the maximum and minimum of the relative specularly reflected intensity, I_r, versus the phase conjugate reflectivity, R_{PC}, for R=0.37. The theoretical curves correspond to cancellation and enhancement for an infinite number of iterations, —— , and a single iteration, ..., established in the resonant cavity. The experimental points, o and $\star$, correspond to the measured lower and upper intensity limits respectively. 132

5.14 The conservation of energy and momentum in FWM optical geometries. 133

Chapter 6

Figure	Caption	Page No
6.1	The sharp step thresholding function.	139
6.2	The three original 64×64 square array data sets with eight gray levels.	141
6.3	The three bipolar binary 64×64 object vectors; a) $\mathbf{s}^{(1)}$, b) $\mathbf{s}^{(2)}$ and c) $\mathbf{s}^{(3)}$.	142
6.4	The initial and three subsequent bipolar binary 64×64 object vectors generated after three iterations.	143
6.5	Schematic representation of the experimental apparatus.	145
6.6	The two stored memory elements M_1 and M_2, a) and b) respectively and c) the input test transparency.	147

6.7 Schematic illustration of autoassociative recall of a) memory element M_1 and b) memory element M_2 using a Maltese and diagonal cross respectively. 148

6.8 Autoassociative recall for differing partial inputs; a) Maltese cross, b) Diagonal cross, c) circle and d) hexagon. 149

6.9 Autoassociative recall for selected pairs of geometric figures; a) the circle and Maltese cross and b) the circle and diagonal cross. 151

Chapter 7

Figure	Caption	Page No

7.1 The circularly symmetric *Gaussian* intensity profile. 155

7.2 The temporal numerical data, o, of the induced electric field at $\rho = 0.71\omega$ for a *Gaussian* illuminating intensity profile. The solid curve, —— , corresponds to a t^2 data fit. 160

7.3 The spatial numerical data, o, of the normalised induced electric field at $t = 1.0 \times 10^{-9}\tau_D$ for a *Gaussian* illuminating intensity profile. The solid curve, —— , corresponds to the normalised and inverted first derivative of the *Gaussian* illuminating intensity. 161

7.4 The two dimensional perspective projection of a *soft tophat*intensity profile. 162

7.5 The spatial numerical data, o, of the normalised induced electric field at $t = 1.0 \times 10^{-9}\tau_D$ for a *soft tophat* intensity profile. 162

7.6 The two dimensional perspective projection of a *difference of Gaussians* intensity profile. 163

7.7 The spatial numerical data, o, of the normalised induced electric field at t = $1.0\times10^{-9}\tau_D$ for a *difference of Gaussians* intensity profile. 163

7.8 The normalised non–saturated steady state electric field profile induced by *Gaussian* illumination. 165

7.9 The temporal numerical data, o, of the induced electric field at $\rho = 2.55\omega$. The solid curve, —— , corresponds to a $E_\rho = E_{\rho o}[1 - \exp(-t/\tau_{rise})]$ data fit with $\tau_{rise} = 0.45\tau_D$. 167

7.10 The spatial numerical data of the induced electric field for 20%, +, 60%, ⋆, and 100%, o, of the total time period. The solid curve, —— , is the non–saturated electric field profile, Eq. (7.38). 167

7.11 Cartesian co–ordinate system used to define the ray direction of the incident light and the induced electric field plane. 169

7.12 The one dimensional profile of $\Delta n_{y'}$ along the z′ axis for $\alpha = -5°(\times)$, $0°(+)$, $10°(\star)$ and $25°(o)$ for $BaTiO_3$. 170

7.13 The one dimensional profile of $\Delta n_{z'}$ along the z′ axis for $\alpha = -5°(\times)$, $0°(+)$, $10°(\star)$ and $25°(o)$ for $BaTiO_3$. 171

7.14 The two dimensional perspective projection of $\Delta n_{z'}$ at $\alpha = 0°$ for $BaTiO_3$. 172

7.15 The intensity cross section of the argon ion laser beam (λ = 514.5nm), o, accompanied by the *Gaussian* profile data fit, —— . 173

7.16 Schematic diagram of asymmetric beam fanning in $BaTiO_3$. 174

Appendices

Figure	Caption	Page No
A.1	Cartesian co-ordinate change to locate principle dielectric axis in $BaTiO_3$ and SBN.	183
C.1	The linear in modulation approximation.	194
F.1	Degenerate four wave mixing geometry.	208
G.1	Phase conjugation by DFWM in a PR material.	213
H.1	Complex amplitudes at various locations and both directions in a PC Michelson interferometer.	221
H.2	The principle of time reversal invariance of light.	222

LIST OF TABLES

Chapters

Table	Caption	Page No
2.I	Bulk indices of refraction for $BaTiO_3$.	49
2.II	Material parameters of selected PR materials.	51
2.III	Electro-optic parameters of selected PR materials.	52
4.I	EXOR digital logic.	102
5.I	Doppler frequency shifts for the succesive components of the intercavity fields.	133
6.I	The mutual orthogonalities between the three bipolar binary object vectors, $\mathbf{s}^{(1)}$, $\mathbf{s}^{(2)}$ and $\mathbf{s}^{(3)}$.	140
6.II	The correlation between the three bipolar binary object vectors, $\mathbf{s}^{(1)}$, $\mathbf{s}^{(2)}$ and $\mathbf{s}^{(3)}$ and the current object vector of the Hopfield algorithm.	144
7.I	Parameter values used in transient numerical analysis.	159
7.II	Parameter values used in the steady state numerical analysis.	166
7.III	Peak values of $\Delta n_{y'}$ and $\Delta n_{z'}$ for chosen ray directions in $BaTiO_3$.	172

Appendices

Table	Caption	Page No
B.I	Bismuth silicon oxide spectrophotometric data.	186
B.II	Barium titanate spectrophotometric data.	187
B.III	Cerium doped strontium barium niobate spectrophotometric data.	188

B.IV Gallium arsenide and indium phosphide spectrophotometric data. 189

E.I Two beam coupling of $BaTiO_3^{\#2}$ and $^{\#3}$ versus the normalised grating wavenumber. 203

E.II Two beam coupling of cerium doped SBN:$60^{\#1}$ versus the normalised grating wavenumber. 204

E.III Diffraction efficiency, η versus the incident, β_o, and exit, β_{exit}, writing beam ratios for $BaTiO_3^{\#1}$. 205

E.IV Diffraction efficiency, η, versus the incident, β_o, and exit, β_{exit}, writing beam ratios for SBN : $60^{\#1}$. 206

E.V Characteristic grating rise time, τ_{rise}, versus the total incident writing intensity, I_o, for $BaTiO_3^{\#1}$. 206

E.VI Characteristic grating decay time, τ_{decay}, versus the probe beam intensity, I_{probe}, for $BaTiO_3^{\#1}$. 207

E.VII Characteristic grating decay time, τ_{decay}, versus the probe beam intensity, I_{probe}, for SBN:$60^{\#1}$. 207

I.I Phase conjugate reflectivity, R_{PC}, versus the relative intensity of the specularly reflected intensity, I_r, for R=0.37. 225

I.II Phase conjugate reflectivity, R_{PC}, versus the relative intensity of the cancelled and enhanced specularly reflected intensities, I_r, for R=0.37. 225

CHAPTER 1

INTRODUCTION

1.1 Historical review.

The photorefractive effect was first observed by researchers at Bell Laboratories in 1966 [1.1]. They noticed an induced change in refractive index at the focus of an intense green laser beam in lithium niobate, $LiNbO_3$, and lithium tantalate, $LiTaO_3$, [1.1]. The refractive index inhomogeneity served to hinder the subject of their research and they initially referred to it as *laser damage*. However it was found later that the crystals could be returned to their initial homogeneous states after heat treatment and hence the *damage* was quite different in origin from the irreversible catastrophic damage incurred at much higher optical power densities. The term *photorefractive effect* has since been adopted to describe the light induced change in refractive index.

Chen published the first charge migration model of the photorefractive effect in 1969 specific to ferroelectric crystals [1.2]. He proposed that the migration of free charge was due to the *drift* transport mechanism under the influence of the internal electric field of the material. Thaxter supported these predictions by demonstrating the influence of an externally applied electric field on a crystal of strontium barium niobate [1.3]. Amodei amended the original theoretical model by including the contribution of *diffusion* to the migration of the free charged species [1.4,1.5] and finally a third transport mechanism, the photovoltaic effect, was added in 1974 by Glass *et al* [1.6] to accommodate for anomalous behaviour exhibited by certain materials. The inclusion of feedback between the migrating free charged carriers and the induced electric field was introduced by Kim *et al* [1.7] in 1974. This allowed the theoretical prediction of the temporal evolution, in addition to the spatial profile, of the induced electric field. In 1979 Kukhtarev *et al* [1.8,1.9] published the most complete and rigorous model of the effect to date which has since been verified extensively by experiment and modified only recently to accommodate for electron/hole competition [1.10] and deep donors/shallow traps [1.11]. The following year, 1980, J. Feinberg *et al* [1.12] published a statistical model of the photorefractive effect which replaced the three stage mechanism of the band transport model, *generation*, *migration* and *recombination*, by a *hop* from one fixed impurity site to its nearest neighbour. The model, in comparison to the

band transport model of Kukhtarev *et al* [1.8,1.9], is less flexible to modification and eludes the science of the effect.

Concurrent with the progress in the theoretical understanding of the photorefractive effect, much effort has been devoted to experimental investigations. The models have been verified, new materials have been explored and potential applications of the effect have been assessed. The photorefractive effect has been observed in a large number of materials which include $BaTiO_3$ [1.13], $KNbO_3$ [1.14], $Ba_{1-x}Sr_xNb_2O_6$, $Bi_{12}TiO_{20}$ [1.15] and $Bi_{12}(Si,Ge)O_{20}$ [1.16,1.17] to name a few. Reduction and oxidation treatments have been employed and varieties of dopents introduced to optimise the photorefractive properties of each material. The demonstration by Huignard *et al* [1.17] in 1979 of optical phase conjugation by degenerate four wave mixing at mW *cw* optical powers in BSO brought the photorefractive effect into prominence. Continuous wave phase conjugate optics at low power levels had become avaliable with relatively inexpensive materials.

Many applications have been demonstrated and exotic optical nonlinearities observed. Real time image processing and adaptive optics constitute the main thrust of the proposed applications of the effect which, in general, employ coherent light amplification by two wave mixing and phase conjugation by degenerate four wave mixing optical configurations. Applications demonstrated include edge enhancement [1.18], real–time optical correlation [1.19], parallel image subtraction [1.20], optical tracking novelty filter [1.21], photolithography [1.22], dynamic beam deflection [1.23], incoherent–to–coherent light convertor [1.24] and optical associative memories [1.25] to name a few. Exotic optical nonlinearities have been exhibited principally by the ferroelectric oxide photorefractive material barium titanate, $BaTiO_3$. This material was the first to demonstrate self–pumped phase conjugation by internal reflection in 1982 [1.26] and has since displayed many other strange and fascinating optical phenomena. They include the self–location of a specularly reflecting object [1.27], the mutual self–location of two self–pumped $BaTiO_3$ crystals [1.28], double phase conjugate mirrors [1.29→1.31] and image colour conversion [1.32].

Recently a few laboratories, worldwide, have begun to investigate the response of photorefractive materials to both very short pulse illumination and high repetition rates [1.11,1.33→1.36]. The laser sources were pulsed with typically nano/picosecond pulse durations and $\sim$ 1mJ energies per pulse. Photorefractive grating rise times of $<$ 100ps and $\sim$ 4ns have been observed in $BaTiO_3$ [1.33] and BSO [1.36] respectively. The very fast response of these materials offers the potential of very

high speed digital optical logic, switching and adaptive image processing and is currently an area of active research.

The photorefractive effect, the materials and their applications will continue to progress as theoretical interpretations develop, material growth/preparation techniques improve and more potential applications are perceived.

1.2 Thesis synopsis.

This chapter has so far provided a brief historical introduction into the fields of the photorefractive effect, materials and their potential applications. The scope of the thesis will now be outlined by brief introductions of the major topics covered on a chapter by chapter basis.

In chapter 2 the photorefractive effect is formally introduced and the photoconducting and electro–optic characteristics discussed separately. The band transport model is analysed in detail and the coupled equations are rigorously derived. The amendments to the model to accommodate for both electron/hole competition and deep donor/shallow traps are discussed. The charge hopping model is briefly described and its differences, similarities and limitations are highlighted. The linear electro–optic effect is analysed using the conventional contracted electro–optic tensor notation. The three main families of photorefractive materials, *ferroelectric oxides*, *paraelectric oxides* and III–V *semiconductors*, are introduced and discussed. Absorption spectra, photographs and typical material and electro–optic properties of each family are presented and compared. Finally the electro–optic nature of the two ferroelectric oxides barium titanate, $BaTiO_3$, and cerium doped strontium barium niobate, SBN:60, are investigated in detail.

Chapter 3 introduces and discusses in detail the first of the two most common optical configurations, namely two wave mixing. The photorefractive response to a one dimensional cosinusoidal intensity profile is analysed in the linear in generation/recombination and saturation regimes and the effects of dynamic feedback are considered. Experimental procedures and results are presented which serve to highlight the main material characteristics of $BaTiO_3$ and cerium doped SBN:60 in both steady state and transient regimes. Coherent light amplification of an image by two beam coupling is demonstrated.

Next, in chapter 4, the second most common optical configuration, four wave mixing, is introduced. Phase conjugation by degenerate four wave mixing is of particular interest and is analysed in detail. Two experiments were performed

and the pictorial results are presented to provide qualitative evidence of the phase conjugate fidelity achieved by wave mixing in $BaTiO_3$. Asymmetric beam fanning and self pumped phase conjugation in $BaTiO_3$ and SBN are briefly discussed and the different temporal modes are highlighted.

Chapter 5 briefly introduces a generalised model of phase conjugation based on scattering theory which predicts the complete correction of extensive backscatter, introduced by an arbitrary lossless phase distorter, by a perfect phase conjugate mirror. A phase conjugate Fabry–Perot interferometer is discussed in detail and both specular reflection cancellation and enhancement are predicted. Experimental results are presented which verify the theoretical predictions of the interferometer and lend support to the generalised theory.

In chapter 6 holographic associative memories using phase conjugate feedback are investigated as a potential application of the photorefractive effect. The simple neural network model of Hopfield is discussed and computer simulated results are presented. An all optical autoassociative memory is described and the experimental results are presented. With the simple information stored the optical configuration was successful at recalling the correct complete stored image when provided with only partial information.

Chapter 7 presents a theoretical investigation into the photorefractive response to circularly symmetric and spatially confined intensity profiles in general and the Gaussian intensity profile in particular. The response was numerically analysed in both the initial transient and steady state regimes and resultant refractive index modulations within barium titanate are proposed.

Finally, in chapter 8, there is a brief summary of the thesis, concluding remarks and suggestions for future research in the field.

The thesis presents a number of original theoretical and experimental contributions to the field, most of which have both been presented at conference and published in the scientific literature by the author. Much of the theoretical and experimental results of Chapter 5 have been presented at the International school of material sciences and technology–11th Course: "Electro-optic and Photorefractive Materials: Applications in Optical Signal Processing and Phase Conjugation", Erice, Sicily, Italy 1986, presented as paper MM2 at the 1986 annual meeting of the Optical Society of America, Seattle, Washington and as paper 136 at the Eighth National Quantum Electronics Conference of the Institute of Physics, St Andrews, Scotland 1987. The results have, in addition, been published by Lindsay and Dainty (1986)

and Lindsay (1987). The experimental results of Chapter 6 have been presented as paper PD9–1 at the 1987 Optical Society of America topical meeting on "Photorefractive materials, effects and devices", Los Angeles, California and as paper 137 at the Eighth National Quantum Electronics Conference of the Institute of Physics, St Andrews, Scotland 1987, and published by White, Aldridge and Lindsay (1988). The theoretical results of Chapter 7 are the most recent contributions by the author and a manuscript will be prepared for publication in due course.

1.3 References.

[1.1] A. Ashkin, G.D. Boyd, J.M. Dziedzic, R.G. Smith, A.A. Ballman, J.J. Levinstein and K. Nassau, "Optically–induced refractive index homogenities in $LiNbO_3$ and $LiTaO_3$," Appl.Phys.Lett. **9**, 72–74 (1966).

[1.2] F.S. Chen, "Optically induced change in refractive indices in $LiNbO_3$ and $LiTaO_3$," J.Appl.Phys. **40**, 3389–3396 (1969).

[1.3] J.B. Thaxter, "Electrical control of holographic storage in strontium barium niobate," Appl.Phys.Lett. **15**, 210–212 (1969).

[1.4] J.J. Amodei, "Analysis of transport processes during holographic recording in insulators," RCA Review **32**, 185–198 (1971).

[1.5] J.J. Amodei, "Electron diffusion effects during hologram recording in crystals," Appl.Phys.Lett. **18**, 22–24 (1971).

[1.6] A.M. Glass, D. von der Linde and T.J. Negran, "High–voltage bulk photovoltaic effect and the photorefractive process in $LiNbO_3$," Appl.Phys.Lett. **25**, 233–235 (1974).

[1.7] D.M. Kim, R.R. Shah, T.A. Rabson and F.K. Tittel, "Nonlinear dynamic theory for photorefractive phase hologram formation," Appl.Phys.Lett. **28**, 338–340 (1974).

[1.8] N.V. Kukhtarev, V.B. Markov, S.G. Odulov, M.S. Soskin and V.L. Vinetskii, "Holographic storage in electro–optic crystals. I Steady state," Ferroelectrics **22**, 949–960 (1979).

[1.9] N.V. Kukhtarev, V.B. Markov, S.G. Odulov, M.S. Soskin and V.L. Vinetskii, "Holographic storage in electro–optic crystals. II Beam coupling – light amplification," Ferroelectrics **22**, 961–964 (1979).

[1.10] F.P Strohkendl, J.M.C. Jonathan and R.W. Hellwarth, "Hole–electron competition in photorefractive gratings," Optics Lett **11**, 312–314 (1986).

[1.11] G. Le Saux and A. Brun, "Photorefractive material response to short pulse illuminations," IEEE J.Quantum Electron **QE–23**, 1680–1688 (1979).

[1.12] J. Feinberg, D. Heiman, A.R. Tanguay Jr. and R.W. Hellwarth, "Photorefractive effects and light–induced charge migration in barium titanate," J.Appl.Phys. **51**, 1297–1305 (1980).

[1.13] R.L. Townsend and J.T. La Macchia, "Optically induced refractive index changes in $BaTiO_3$," J.Appl.Phys. **41**, 5188–5192 (1970).

[1.14] P. Günter, U. Flückiger, J.P. Huignard and F. Micheron, "Optically induced refractive index changes in $KNbO_3$: Fe," Ferroelectrics **13**, 297–299 (1976).

[1.15] L.H. Lin, "Holographic measurements of optically induced refractive index inhomogeneties in bismuith titanate," Proc. IEEE **57**, 252–253 (1969).

[1.16] M. Peltier and F. Micheron, "Volume hologram recording and charge transfer process in $Bi_{12}SiO_{20}$ and $Bi_{12}GeO_{20}$," J.Appl.Phys. **48**, 3683–3690 (1977).

[1.17] J.P. Huignard, J.P. Herriau, P. Aubourg and E. Spitz, "Phase conjugate wavefront generation via real time holography in $Bi_{12}SiO_{20}$ crystals," Opt.-Lett. **4**, 21–23 (1979).

[1.18] J. Feinberg, "Real-time edge enhancement using the photorefractive effect," Opt.Lett. **5**, 330–332 (1980).

[1.19] M.G. Nicholson, I.R. Cooper, G.G. Gibbons and C.R. Petts, "Optimization of an updatable optical image correlator," Opt.Eng. **26**, 445–452 (1987).

[1.20] A.E. Chiou and P. Yeh, "Parallel image subtraction using a phase conjugate Michelson interferometer," Opt.Lett. **11**, 306–308 (1986).

[1.21] D.Z. Anderson, D.M. Lininger and J. Feinberg, "Optical tracking novelty filter," Opt.Lett. **12**, 123–125 (1987).

[1.22] M.C. Gower, "Phase conjugate mirrors," Phys.Bull. **38**, 220–222 (1987).

[1.23] G. Pauliat, J.P. Herrriau, A. Delboulbé, G. Roosen and J.P. Huignard, "Dynamic beam deflection using photorefractive gratings in $Bi_{12}SiO_{20}$ crystals," J.Opt.Soc.Am.B **3**, 306–314 (1986).

[1.24] Y. Shi, D. Psaltis, A. Marrakchi and A.R. Tanguay, Jr., "Photorefactive incoherent-to-coherent optical converter," Appl.Opt **22**, 3665–3667 (1983).

[1.25] Y. Owechko, G.J. Dunning, E. Marom and B.H. Soffer, "Holographic associative memory with nonlinearities in the correlation domain," Appl.Opt. **26**, 1900–1910 (1987).

[1.26] J. Feinberg, "Self-pumped, continuous-wave phase conjugator using internal reflection," Opt.Lett. **7**, 486–488 (1982).

[1.27] Fisher R.A., "Optical Phase Conjugation," (Academic Press, New York, 1983).

[1.28] M.D. Ewbank, P. Yeh, M. Khoshnevisan and J. Feinberg, "Time reversal by an interferometer with a coupled phase–conjugate reflectors," Opt.Lett. **10**, 282–284 (1985).

[1.29] S. Weiss, S. Sternklar and B. Fischer, "Double phase conjugate mirror: analysis, demonstration and applications," Opt.Lett. **12**, 114–116 (1987).

[1.30] R.W. Eason and A.M.C. Smout, "Bistability and noncommutative behaviour of multiple–beam self–pulsing and self–pumping in $BaTiO_3$," Opt.-Lett. **12**, 51–53 (1987).

[1.31] M.B. Ewbank, "Mechanism for photorefractive phase conjugation using incoherent beams," Opt.Lett. **13**, 47–49 (1988).

[1.32] S. Sternklar and B. Fischer, "Double–colour–pumped photorefractive oscillator and image colour conversion," Opt.Lett. **12**, 711–713 (1987).

[1.33] A.L. Smirl, G.C. Valley, R.A. Mullen, K. Bohnert, C.D. Mire and T.F. Boggess, "Picosecond photorefractive effect in $BaTiO_3$," Opt.Lett. **12**, 501–503 (1987).

[1.34] G.C. Valley, A.L. Smirl, M.B. Klein, K. Bohnert and T.F. Boggess, "Picosecond photorefractive beam coupling in GaAs," Opt.Lett. **11**, 647–649 (1986).

[1.35] G. Le Saux, G. Roosen and A. Brun, "Nanosecond light energy transfer in $Bi_{12}SiO_{20}$ at 532nm," Opt.Commun. **58**, 238–240 (1986).

[1.36] J.M.C. Jonathan, G. Roosen and Ph. Roussignol, "Time resolved build-up of the photorefractive effect produced in $Bi_{12}SiO_{20}$ by picosecond light pulses," OSA Top.Meet. Technical Digest **17**, 97–100 (1987).

CHAPTER 2

THE PHOTOREFRACTIVE EFFECT AND MATERIALS.

2.1 Introduction.

The *Photorefractive effect* has become the generic term used to describe the light induced change of refractive index exhibited by materials which are both photoconductive and electro–optic in nature and is directly analogous in name to the *photochromic effect*, which describes light induced changes in absorption.

When a photorefractive (PR) material is illuminated by a spatially varying intensity pattern, preferential photogeneration of free carriers, from fixed impurity sites, is experienced at regions of high irradiance. The mobile charged species migrate towards regions of lower irradiance where they become retrapped. The resultant separation of charged species from their original parent impurities creates a static electric field which modulates the refractive index via the electro–optic effect. The induced refractive index profile or phase volume hologram can remain semi–permanently within the bulk of the material for many seconds, minutes and even hours if left in darkness. The dark relaxation of the hologram is due to thermal regeneration and can be assisted greatly by illuminating the material with a uniform intensity profile (optical erasure). Both mechanisms serve to destroy the induced electric field and return the material back to its original homogeneous state.

There are two sets of material qualities to be considered when analysising photorefractives, namely a) the source and nature of the photogenerated charged species and b) the magnitudes and configuration of the non–zero electro–optic coefficients.

2.2 Photoconductivity.

Thus far two theoretical models have been derived to describe the PR effect. The more complete was by N. V. Kukhtarev *et al* [2.1,2.2], and published in 1979. The model consists of rigorous material equations coupled with Gauss's law of electro–statics, the electro–static condition and are collectively referred to as the *Band Transport Model.* Only recently have minor modifications been made to accomodate for electron/hole competition [2.3,2.4] and deep donor/shallow traps [2.5].

The second model was by Feinberg *et al* [2.6] and published in 1980. This model does not consider the physical mechanisms responsible for the redistributed of charge under illumination. Rather, using a statistical approach, the model considers the charged species to *hop* from one fixed impurity site to another. The direction and rate of *hopping* is dictated by both the source and termination environments for each hop with only nearest neighbour interactions considered. Referred to as the *Charge Hopping Model*, the model does serve to predict much of PR behaviour but eludes the science of the effect.

2.2.1 Band Transport Model.

The band transport model considers a combination of three operational mechanisms to describe the redistribution of charge under non–uniform illumination, namely *Generation*, *Migration* and *Recombination*. It is assumed that electrons (*or holes*) are photogenerated from fixed occupied donor (*acceptor*) sites, in the forbidden energy gap, to the conduction (*valence*) band. The electrons (*holes*) migrate with characteristic mobilities to regions of lower irradiance where they recombine with empty donor (*acceptor*) sites. The resultant spatial separation of electrons (*holes*) from their original parent impurities creates a static electric field within the bulk of the material. This field modulates the refractive index via the linear (Pockels) electro–optic effect. The three stage mechanism is schematically illustrated in Fig. 2.1. for electrons as the charged carriers.

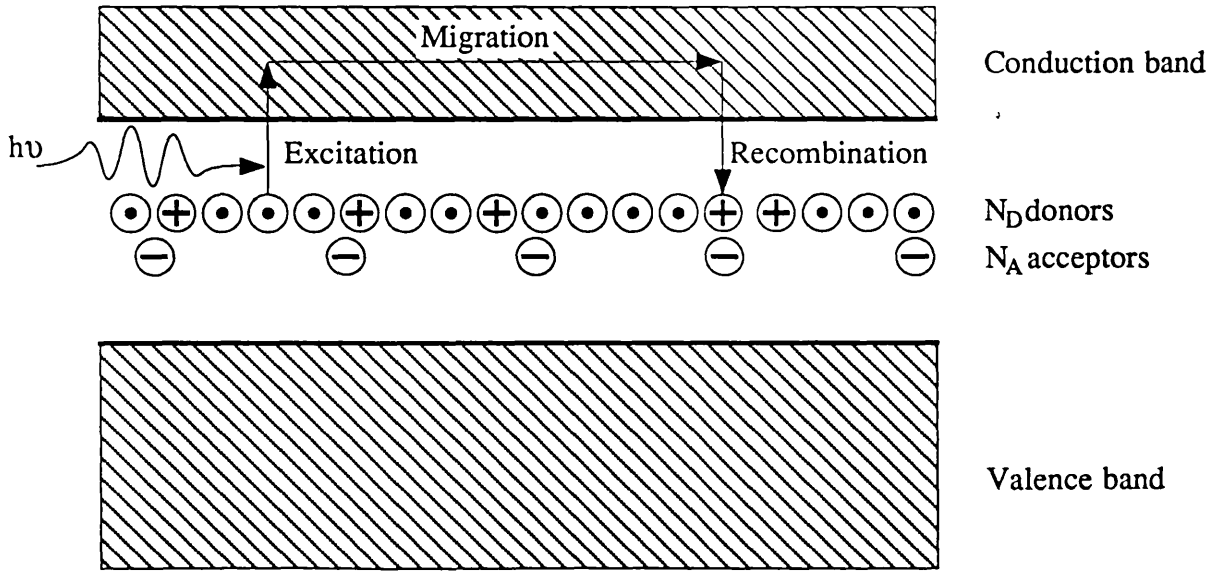


Figure 2.1 Schematic illustration of the band transport model.

The source of PR donor/acceptors are either prescribed dopants introduced during the crystal growing stage or trace impurities located in the nominally pure as grown material. The schematic representation of the band structure, Fig. 2.1, is realistic within the constraints of its simplicity. Having assumed n–type photoconduction, the large number density of donors, N_D, act as the PR agents. The smaller number density (and at a reduced potential) of acceptors, N_A, are equally significant. They provide the material with a uniform background of ionised donors, N_D^+, while in darkness which act as trapping centres for subsequent photogenerated free electrons. An unrealistic feature of the Fig. 2.1 is the arrangement of all the donor sites at one potential energy . In reality this cannot exist otherwise the absorption spectra would reveal a well defined secondary absorption edge located in the region $\lambda > \lambda_{\mathbf{Bandgap}}$. The typically smooth profiles of absorption spectra suggest that the impurities exist in a continuous band like structure throughout the forbidden energy gap.

The three stage mechanism of excitation, migration and recombination can be represented analytically in the continuity equation for the mobile conduction band electrons as follows,

$$\frac{\partial n}{\partial \mathrm{t}} = G + M - R, \tag{2.1}$$

where n and t are the free electron number density and time. G, M and R are the rates of *generation*, *migration* and *recombination* respectively for the free electrons. Equation (2.1) is accompanyed by the continuity equation for the fixed ionised donors,

$$\frac{\partial \mathrm{N_D^+}}{\partial \mathrm{t}} = G - R, \tag{2.2}$$

where N_D^+ is the number density of ionised donors. Note the absence of the *migration* term due to the immobility of this species. The two continuity equations are obviously coupled as the *generation* or *recombination* of any free electron results in the creation or removal of an ionised donor site.

The rate of *generation* of mobile conduction band electrons must be proportional to the probability of an unionised donor site being present, the probability of a conduction band state being empty and a photoexcitation cross section. Assuming the density of occupied conduction band states to be very much less than the total, the probability of a conduction band state being unoccupied can be taken to be unity. Including the thermal contribution, the *generation* rate can therefore be

expressed as

$$\begin{aligned} G &= G_{\text{Photon}} + G_{\text{Thermal}} \\ &= \left(N_D - N_D^+\right)(sI + \beta), \end{aligned} \tag{2.3}$$

where N_D is the total number density of donors. s, I and β are the photoexcitation constant, light intensity and thermal generation rate respectively.

Consider incident radiation of angular frequency ω and an intensity change of δI about I on propagating from x to $x + \delta x$ through the PR material. The number of photons absorbed per unit volume per unit time is,

$$\frac{1}{\hbar\omega}\frac{\delta I}{\delta x}. \tag{2.4}$$

Introducing a quantum efficiency, Φ, to accomodate for non–PR absorption mechanisms, the number of free electrons generated per unit volume per unit time, the *photogeneration* rate, is given by,

$$G_{\text{Photon}} = \frac{\Phi}{\hbar\omega}\frac{\delta I}{\delta x}, \tag{2.5a}$$

and using the Beer–Lambert law for absorption,

$$= \frac{\Phi}{\hbar\omega}\alpha I, \tag{2.5b}$$

where α is the optical absorption. This expression is comparable to Eq. (2.3),

$$G_{\text{Photon}} = \left(N_D - N_D^+\right) sI,$$

and hence the photoexcitation constant, s, and bulk absorption coefficients, α, are linearly related as follows

$$s = \frac{\Phi}{\hbar\omega}\frac{\alpha}{(N_D - N_A)}. \tag{2.6}$$

The rate of *migration* of the mobile conduction band electrons is dictated by the environment in which the free electrons exist. There are two main transport mechanisms to be considered, namely *diffusion* and *drift*. Whenever a spatial variation of the number density of a mobile species exists the phenomenon of *diffusion* will take place, causing the species to redistribute themselves in an attempt to remove the nonuniformity.

The rate of change of flux density is proportional to the density gradient.

This is Fick's first law of *diffusion* and can be analytically expressed as

$$j_D' = -D\nabla n. \tag{2.7}$$

Where $\mathbf{j}'_D$ is the rate of change of flux density, D the *diffusion* coefficient and n the number density of the mobile species. In the present context the migrating specie is the electron which bears a −ve electric charge. Fick's law can be re–expressed as a diffusion current density, $\mathbf{j}_D$, as follows,

$$\mathbf{j}_D = qD\nabla n, \tag{2.8}$$

where q is the elementary unit of charge. In the presence of an electric field the electron will *drift* counter–directional to the field direction, yielding a drift current density, $\mathbf{j}_d$, given by

$$\mathbf{j}_d = qn\mu\mathbf{E}, \tag{2.9}$$

where μ and $\mathbf{E}$ are the characteristic electron mobility and electric field vector. The resultant current density is the superposition of $\mathbf{j}_D$ and $\mathbf{j}_d$ to yield

$$\mathbf{j} = q\left(D\nabla n + \mu n\mathbf{E}\right). \tag{2.10}$$

The *diffusion* coefficient and mobility are linked via the Einstein relationship,

$$D = \frac{k_B T}{q}\mu. \tag{2.11}$$

The photovoltaic effect is a third contributer to current density and is exhibited by materials in which trapped PR species are held in asymmetric potential wells. On photoexcitation the species is encouraged to migrate along one prefered direction and is analogous to *drift* under the influence of an externally applied d.c. electric field. The contribution is very small in $BaTiO_3$ and unobserved in BSO and the III–V semiconductor GaAs and hence can be neglected. The *migration* rate or *flow* is given by the divergence of the rate of change of flux density,

$$M = -\nabla.\mathbf{j}', \tag{2.12}$$

which is related simply to the current density,

$$= \frac{1}{q}\nabla.\mathbf{j}, \tag{2.13}$$

for electrons. Hence the *migration* rate is given by,

$$M = \nabla.\left(D\nabla n + \mu n\mathbf{E}\right). \tag{2.14}$$

Finally, the *recombination* rate, similar to the *generation rate*, is proportional to the number density of free electrons and ionised donor sites,

$$R = \gamma_R n N_D^+, \tag{2.15}$$

where γ_R is the recombination constant.

The coupled material equations, Eqs. (2.1) and (2.2), become,

$$\frac{\partial n}{\partial t} = \frac{\partial N_D^+}{\partial t} + \nabla.(D\nabla n + \mu n\mathbf{E}), \tag{2.16}$$

$$\frac{\partial N_D^+}{\partial t} = (N_D - N_D^+)(sI + \beta) - \gamma_R n N_D^+. \tag{2.17}$$

Accompanyed by Gauss's law of electro-statics in differential form,

$$\nabla.(\varepsilon\varepsilon_o\mathbf{E}) = q(N_D^+ - N_A - n), \tag{2.18}$$

and the electro-static condition,

$$\nabla \times \mathbf{E} = 0. \tag{2.19}$$

The system of Eqs. (2.16)→(2.19) serve to predict both the spatial and temporal evolution of the induced static electric field, **E**, for a given intensity profile, I, and initial conditions. However the nonlinearity in their coupling prevents an analytic solution being attained for all but the simplest of intensity profiles.

The mathematical modeling is further complicated when the dynamic interaction of light and matter is considered. The induced electric field modulates the refractive index (RI) by the linear (Pockels) electro-optic effect. In a scalar context this is expressed as

$$\Delta n = -\frac{1}{2} r_{eff} n^3 E, \tag{2.20}$$

where Δn, n, r_{eff} and E are the induced change in RI, the bulk RI, the effective electro-optic coefficient (accomodating for geometric and polarisation considerations) and the electric field amplitude. The incident light, having changed its own RI environment, is itself modified. This re-adjusts further the RI and dynamic feedback ensues. Equilbrium is finally attained when the, in general complicated, intensity and RI profiles become established in the steady state.

Kukhtarev's band transport equations have proved successful in predicting much of the observed PR behaviour. However their main idealisations are to assume a solitary migrating charged species and a single type of donor–acceptor combination. The demonstration by Ducharme and Feinberg [2.7] that barium titanate can be conditioned to be either n or p-type photoconducting illustrated that electrons and holes can simultaneously contribute to the PR effect. Preferential photogeneration of both species will occur at regions of high irradiance. They will both migrate, in a coupled fashion, to regions of lower irradiance where they will become retrapped, Fig. 2.2. The nett redistribution of charge is the difference rather than

the sum of their contributions, due to the opposite charge signs they bear. The resultant induced electric field is governed by which of the two competing carriers dominates.

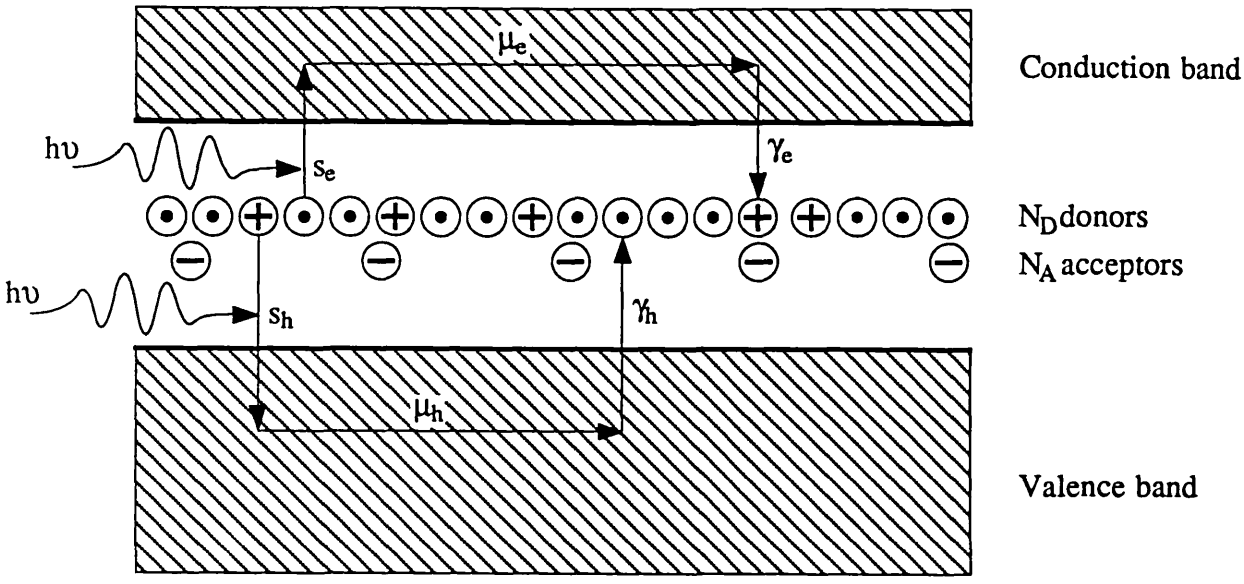


Figure 2.2 Schematic illustration of electron/hole competition in the band transport model.

The band transport equations were first extended by Strohkendl *et al* [2.3] in 1986. A single species of donor, number density N_D, was assumed. The ionised donors, N_D^+, acted as centers for electron recombination and hole photogeneration. The remaining unionised donors acted as the converse. The electrons and holes are considered to have differing photoexcitation constants, thermal generation rates, mobilities and recombination constants, denoted by s_e, β_e, μ_e, γ_e and s_h, β_h, μ_h, γ_h. The continuity equations and Gauss's law in differential form become,

$$\frac{\partial n}{\partial t} = (N_D - N_D^+)(s_e I + \beta_e) + \nabla.(\mu_e k_B T \nabla n + \mu_e n \mathbf{E}) - \gamma_e n N_D^+, \tag{2.21}$$

$$\frac{\partial p}{\partial t} = N_D^+ (s_h I + \beta_h) + \nabla.(-\mu_h k_B T \nabla p + \mu_h p \mathbf{E}) - \gamma_h p (N_D - N_D^+), \tag{2.22}$$

$$\frac{\partial N_D^+}{\partial t} = (N_D - N_D^+)(s_e I + \beta_e) - N_D^+ (s_h I + \beta_h) - \gamma_e n N_D^+ + \gamma_h p (N_D - N_D^+), \tag{2.23}$$

and

$$\nabla.(\varepsilon \varepsilon_o \mathbf{E}) = q (N_D^+ - N_A + p - n). \tag{2.24}$$

The number densities of free electrons and holes are given by n and p respectively and the diffusion coefficient has been re–expressed using Einstein's relationship, Eq. (2.11). This model has accurately accounted for anomalous PR barium titanate behaviour reported by Klein and Valley [2.8], lending further support to the concept of electron–hole competition.

Using short pulse illumination of nanosecond pulse duration, anomalous photocurrent behaviour in bismuth silicon oxide has been reported by G. Le Saux and A. Brun [2.5]. The photocurrent response consisted of two characteristic decay times, one fast (50ns) and one slow (10μs), suggesting the presence of a long lived intermediate state in addition to the normal PR species. The model proposed by the authors consists of a combination of deep donors, shallow traps and a single charge carrying species (electrons in the case of BSO). Photoexcited electrons from the deep donors migrate through the conduction band until they become trapped by either deep ionised donors in the conventional manner or by the shallow acceptors. From the shallow acceptors (traps) the electrons can escape by either thermal excitation back up into the conduction band or by relaxation down into ionised donors. The model is illustrated in Fig. 2.3.

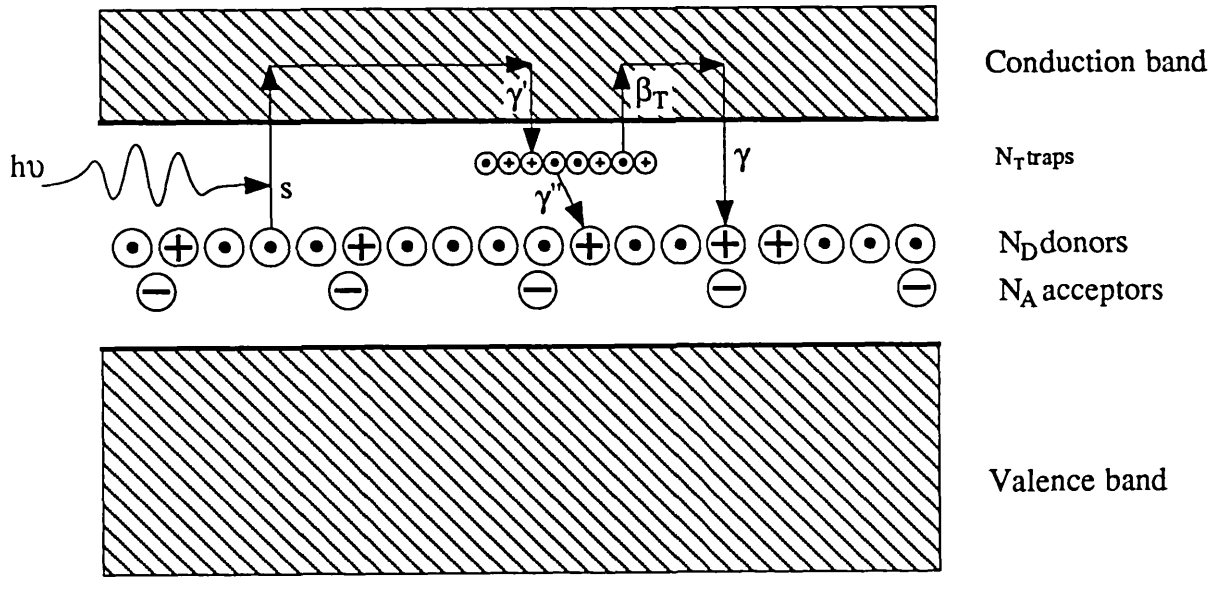


Figure 2.3 Schematic illustration of deep donors/shallow traps in the band transport model.

The shallow traps, once filled, act as long lived temporary stores for the electrons, released slowly, long after the illuminating pulse has passed. The continuity equations for the immobile ionised deep donors, N_D^+, and ionised shallow traps, N_T^+,

are,

$$\frac{\partial N_D^+}{\partial t} = (N_D - N_D^+)\, sI - \gamma_R n N_D^+ - \gamma_R''\,(N_T - N_T^+)\, N_D^+, \tag{2.25}$$

$$\frac{\partial N_T^+}{\partial t} = (N_T - N_T^+)\, \beta_T - \gamma_R' n N_T^+ + \gamma_R''\,(N_T - N_T^+)\, N_D^+, \tag{2.26}$$

where N_T is the total number density of shallow traps and n is the number density of free electrons. The recombination constants γ_R, γ_R' and γ_R'' are from the conduction band to the deep donors, conduction band to the shallow traps and from the shallow traps to the deep donors. The thermal generation rate from the shallow traps and photoexcitation constant for the deep donors are given by β_T and s respectively. For uniform illumination and no externally applied electric field the nett migration of free electrons is zero and their continuity equation becomes,

$$\frac{\partial n}{\partial t} = (N_D - N_D^+)\, sI + (N_T - N_T^+)\, \beta_T - \gamma_R n N_D^+ - \gamma_R' n N_T^+. \tag{2.27}$$

Constant recombination rates are assumed and hence can let $\gamma_R' N_T^+ = 1/\tau_1$, $\gamma_R'' N_D^+ = 1/\tau_2$, $\beta_T = 1/\tau_3$ and $\gamma_R N_D^+ = 1/\tau_4$. The second derivative of n with respect to time can be shown to be given by,

$$\begin{aligned} &\frac{\partial^2 n}{\partial t^2} + \left(\frac{1}{\tau_1} + \frac{1}{\tau_2} + \frac{1}{\tau_3} + \frac{1}{\tau_4}\right) \frac{\partial n}{\partial t} \\ &\qquad + \left(\frac{1}{\tau_1 \tau_2} + \frac{1}{\tau_2 \tau_4} + \frac{1}{\tau_3 \tau_4}\right) n \\ &\qquad = sIN_D \left(\frac{1}{\tau_2} + \frac{1}{\tau_3}\right) \end{aligned} \tag{2.28}$$

which indicates that $n(t)$ varies with two time constants given by

$$\begin{aligned} r_\pm = \frac{1}{2}\Bigg[&- \left(\frac{1}{\tau_1} + \frac{1}{\tau_2} + \frac{1}{\tau_3} + \frac{1}{\tau_4}\right) \\ &\pm \Bigg\{ \left(\frac{1}{\tau_1} + \frac{1}{\tau_2} + \frac{1}{\tau_3} + \frac{1}{\tau_4}\right)^2 \\ &- 4\left(\frac{1}{\tau_1 \tau_2} + \frac{1}{\tau_2 \tau_4} + \frac{1}{\tau_3 \tau_4}\right) \Bigg\}^{1/2} \Bigg]. \end{aligned} \tag{2.29}$$

The time constants T_1 and T_2, describing the photocurrent response, are given by,

$$T_1 = -\frac{1}{r_-}, \tag{2.30a}$$

$$T_2 = -\frac{1}{r_+}. \tag{2.30b}$$

Shallow intermediate traps are also thought to exist in PR barium titanate. Using a variety of pulse durations, energies and repetition rates, D. Mahgerefteh and J. Feinberg [2.9] have observed the erasure efficiency of a PR grating in $BaTiO_3$ to be repetition rate dependent and that the grating erasure continued after the erasing pulse had passed. This *coasting* of the grating erasure suggests again the presence of longer lived intermediate shallow traps.

2.2.2 Charge Hopping Model.

The charge hopping model describes the re–distribution of charge under non–uniform illumination as a series of *hops* between adjacent PR impurity sites [2.6]. The probability and direction of any given hop is dependent on the intensities and occupancy of sites in the local environment with only nearest neighbour transitions considered. The hopping rate is considered to be directly proportional to the intensity and the model is schematically illustrated in Fig. 2.4.

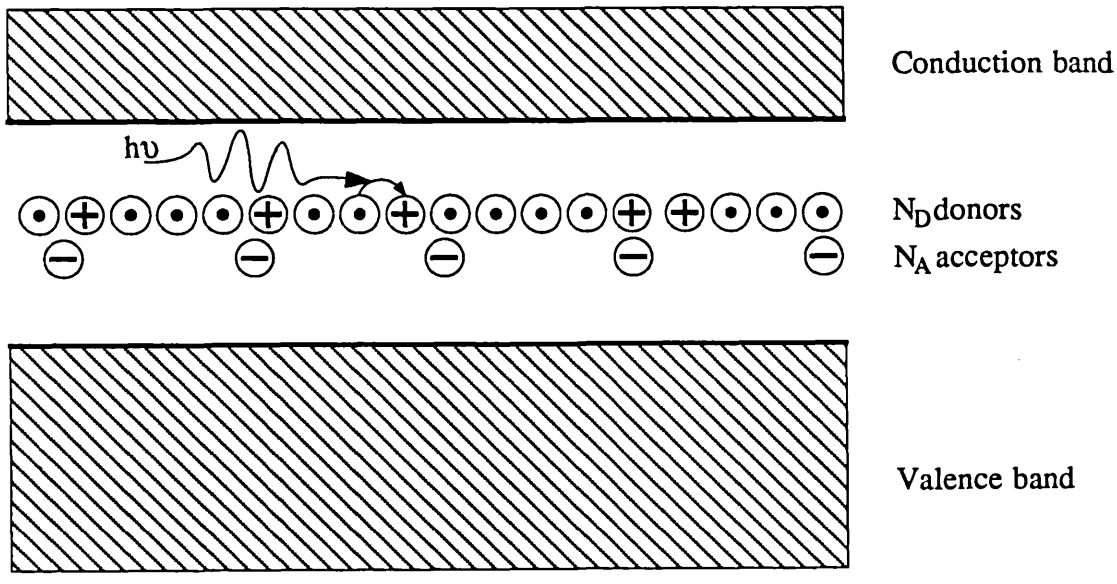


Figure 2.4 Schematic illustration of charge hopping model.

The mathematical description of the model is statistical in its approach with little account taken of the physical mechanisms involved. Consider W_n to be the probability that a migrant charge occupies the n_{th} site at position x_n. Accompanied by an optical intensity I_n the model can be expressed as

$$\frac{\partial W_n}{\partial t} = -\sum_m D_{mn}\left[W_n I_n \exp\left(\frac{1}{2}\beta\phi_{nm}\right) - W_m I_m \exp\left(\frac{1}{2}\beta\phi_{mn}\right)\right], \quad (2.31)$$

where the summation is over all adjacent neighbouring sites. The rate constant $D_{mn} \exp\left(\frac{1}{2}\beta\phi_{mn}\right)$ is a measure of the tendency for light induced hopping from site m to n, expressed in terms of D_{mn} ($\equiv D_{nm}$) and the static potential difference $\phi_{nm} = \phi_n - \phi_m$ ($\phi_{nm} \equiv -\phi_{mn}$) between the sites. The parameter β equals q/k_BT where q is the elementary unit of charge, k_B is Boltzmann's constant and T is the absolute temperature. Under weak uniform illumination the re–distribution of charge is zero and from Eq. (2.31), $W_m/W_n = \exp(\beta\phi_{nm})$ ans hence statistical mechanics is obeyed. The model, in its simplicity, serves to predict energy exchange between two and among four optical beams for one dimensional cosinusoidal intensity profiles. The energy exchange, in both transient and steady state regimes, is shown to be dependent on the relative beam intensities, polarisations, beam geometries and externally applied static electric field for a given crystal orientation. However it would appear that the model, as a whole, is less flexible than the *Band Transport Model.* It would have difficulty accomodating for more complicated intensity profiles, the hopping of both electrons and holes between PR impurity sites and for longer lived intermediate states (shallow traps), making it the less attractive of the two photorefractive models.

2.3 The Electro–optic Effect.

The variation of refractive index, n, with propagation direction, s, can be characterised by a three dimensional surface known as the index ellipsoid or optical indicatrix [2.10]. In general the surface is elliptical within each axis plane and mathematically expressed as

$$\frac{x^2}{n_x^2} + \frac{y^2}{n_y^2} + \frac{z^2}{n_z^2} = 1, \tag{2.32}$$

in normalised form. The directions x, y and z are chosen to eliminate cross terms and are referred to as the principle dielectric axes. The values $1/n_x^2$, $1/n_y^2$ and $1/n_z^2$, equaling η_{xx}, η_{yy} and η_{zz} respectively, are the principle values of the second rank impermeability tensor, where $\eta_{ij} = \varepsilon_o/\varepsilon_{ij}$. The relative values of n_x, n_y and n_z define the precise shape of the surface, a reflection on the crystalline symmetries exhibited in the material. For $n_x = n_y = n_z$ the material is isotropic, having a cubic crystalline structure and a spherical index surface. For $n_x = n_y \neq n_z$ the material is uniaxial with either hexagonal, tetragonal or trigonal structures and an ellipsoid of revolution index surface. Finally for $n_x \neq n_y \neq n_z$ the material is biaxial with either orthorhombic, monoclinic or triclinic structures and an index elliptical surface within each axis.

The first electro–optic effect was observed by the Scottish physicist John Kerr (1824–1907) in 1875 [2.11]. He found that an isotropic transparent material became birefringent when placed in a static electric field. The medium took on the characteristics of a uniaxial crystal with the induced optics axis corresponding to the electric field direction. The difference in the two resultant refractive indices, n_e and n_o, $\Delta n = n_e - n_o$, known as the birefringence, was found to be proportional to the square of the electric field,

$$\Delta n \propto \mathbf{E}^2, \tag{2.33}$$

and has since been referred to as the quadratic (Kerr) electro–optic effect. The German physicist Fredrich Carl Alwin Pockels (1865–1913) in 1893 observed that certain crystalline materials, having no central point symmetry, exhibited a linear relation between the induced birefringence and the applied electric field. Hence has been denoted as the linear (Pockels) electro–optic effect,

$$\Delta n \propto \mathbf{E}. \tag{2.34}$$

The optical indicatrix, Eq. (2.32), can be re–expressed as

$$x^2\eta_{xx} + y^2\eta_{yy} + z^2\eta_{zz} = 1, \tag{2.35a}$$

$$\sum_i i^2\eta_{ii} = 1, \tag{2.35b}$$

where i=x, y and z. In general, for x, y and z not the principle dielectric axis, all six impermeability matrix elements must be considered to accomodate the resultant cross terms. Analogus to Eq. (2.35b), the generalised expression becomes

$$\sum_{ij} ij\eta_{ij} = 1, \tag{2.36}$$

where i,j=x, y and z and $\eta_{ij} = \eta_{ji}$. By convention the linear electro–optic coefficient, r, is defined as the constant of proportionality between the change in impermeability and the electric field,

$$\Delta\eta = r\mathbf{E}, \tag{2.37}$$

which when re–expressed in tensor notation becomes

$$\Delta\eta_{ij} = r_{ijk}E_k. \tag{2.38}$$

The linear electro–optic tensor, r_{ijk}, is of third rank and can be represented as a $3 \times 3 \times 3$ matrix. However due to the inherent symmetry of the impermeability,

$\eta_{ij} = \eta_{ji}$, it is more convenient to adopt a standard contacted notation. The index combinations of ij are defined as; xx=1, yy=2, zz=3, yz=zy=4, xz=zx=5 and xy=yx=6, and for k; x=1, y=2 and z=3. The full matrix representation of Eq. (2.38) then becomes

$$\begin{pmatrix} \Delta\eta_1 \\ \Delta\eta_2 \\ \Delta\eta_3 \\ \Delta\eta_4 \\ \Delta\eta_5 \\ \Delta\eta_6 \end{pmatrix} = \begin{pmatrix} r_{11} & r_{12} & r_{13} \\ r_{21} & r_{22} & r_{23} \\ r_{31} & r_{32} & r_{33} \\ r_{41} & r_{42} & r_{43} \\ r_{51} & r_{52} & r_{53} \\ r_{61} & r_{62} & r_{63} \end{pmatrix} \begin{pmatrix} E_1 \\ E_2 \\ E_3 \end{pmatrix} \tag{2.39}$$

The number and orientation of the non–zero r_{ijk} coefficients are determined by the crystalline symmetries of the material. Equations (2.36) and (2.37) combine in the presence of an electric field to yield a general description of the induced optical indicatrix,

$$\left(\sum_{ij} ij\eta_{ij}\right)_{E=0} + \left(\sum_{ij} ij\Delta\eta_{ij}\right)_{E\neq 0} = 1. \tag{2.40}$$

Using $\eta = 1/\varepsilon_r$ and $\varepsilon_r = n^2$ in a lossless medium, the change in impermeability can be re–defined as a change in refractive index,

$$\begin{aligned} \Delta\eta &= \Delta\left(\frac{1}{n^2}\right), \\ &= -2\frac{\Delta n}{n^3}, \end{aligned}$$

and hence Eq. (2.37) can be re–expressed as

$$\Delta n = -\frac{1}{2}n^3 rE. \tag{2.40}$$

This is the simplest and most common expression used to describe the linear electro–optic effect where the tensor nature, previously described, has obviously been neglected.

2.4 Photorefractive Materials and Properties.

The photorefractive (PR) effect has been studied in many materials and much effort has been devoted to the optimisation of their PR performances. The two key attributes to be considered are the materials photoconductive and electro–optic properties. The photoconductive properties of the material are dictated by the number densities of impurity donors and acceptors and the photogeneration constant, mobility and recombination constant of the migrating species. All of which

determine the temporal response and amplitude of the induced electric field for a given optical intensity and spatial frequency. The magnitudes and configuration of the non–zero electro–optic coefficients determines the optimal crystal orientation and light polarisation to best employ the induced electric field in modulating the refractive index.

The source and nature of the active PR species is fundamental to the material's ultimate PR performance. The species are either prescribed dopants introduced during the crystal growing stage or trace impurities located in the nominally pure grown material. For potassium niobate, $KNbO_3$, as in many other oxygen octahedra ferroelectrics, the PR species is iron with the bi–tri intervalence exchange acting as a donor–acceptor trap [2.12,2.13]. In reduced samples of iron doped $KNbO_3$ there is an abundance of Fe^{2+} ions and the photogeneration process for electrons can be summarised as,

$$Fe^{2+} + h\nu \rightarrow Fe^{3+} + e^{-}. \tag{2.41}$$

For oxidised iron doped lithium niobate, $LiNbO_3$, iron is again the acting PR agent but the photoconductivity is p–type and thus holes are ejected from Fe^{3+} and retrapped by Fe^{2+} ions [2.14]. Further, barium titanate, $BaTiO_3$, also has iron as the dominant PR species [2.15] and it has been demonstrated that the material can be tailored to be either n or p–type photoconducting [2.7] by employing suitable reduction and oxidation techniques. The transition metal cerium, Ce, has been succesfully used to dope strontium barium niobate, $Sr_xBa_{1-x}Nb_2O_6$, [2.16,2.17,2.18]. The photogeneration process now due to the tri–quad valence exchange of the cerium ion,

$$Ce^{3+} + h\nu \rightarrow Ce^{4+} + e^{-}, \tag{2.42}$$

and hence is n–type photoconducting.

The optical absorption profiles of these materials, across the visible region of the spectrum, serve to act as identification signatures from which the presence of active PR species can be qualitatively observed. Such measurments were performed using a Varian 2300 spectrophotometer, scanning from 800 $\rightarrow$ 400 nm with a spectral bandwidth of 1nm. The results are graphically shown in Figs. 2.5, 2.7 and 2.9 and tabulated in Appendix B. For all the absorption spectra, the intrinsic absorption edge located at $\sim$ 400nm is due to interband transitions from the valence to the conduction bands, generating electron–hole pairs. In the absence of impurities the absorption would drop off rapidly at longer wavelengths to reveal a featureless profile. Any deviation from this response serves to indicate the presence of active PR species located in the forbidden energy gap.

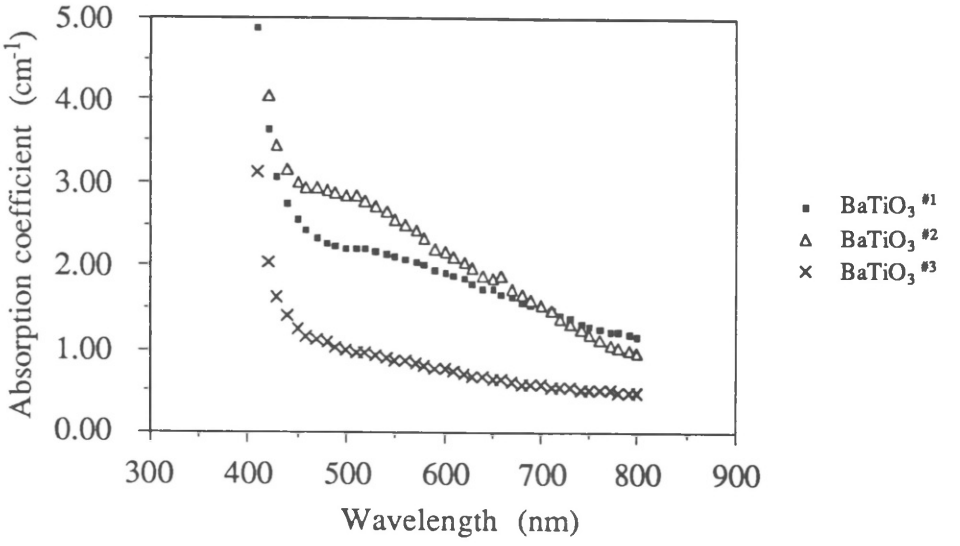


Figure 2.5 Absorption spectra for $BaTiO_3$.

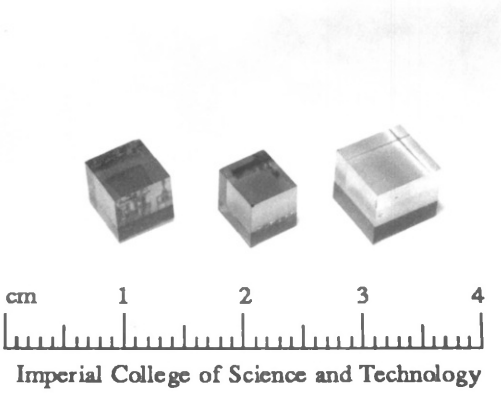


Figure 2.6 Photograph of the three crystals of $BaTiO_3$; from left to right, samples #1, #2 and #3.

The absorption spectra of three samples of barium titanate are shown in Fig. 2.5. and tabulated in Appendix B. Pictured in Fig. 2.6, all three samples were grown and mechanically/electrically poled by Saunders Associates, Nashua, N.H. Crystals #1 and #2, denoted by ■ and △ Fig. 2.5, appear to have similar profiles. Obvious absorption structure is apparent for $\lambda > \lambda_{\text{Bandgap}}$ and indeed these two samples

demonstrated the PR effect very efficiently. However crystal #3, denoted by ×, exhibited no such structure with only a slow monotonic fall in absorption with wavelength which is more characteristic of an impurity free material. The sample, visibly the most transparent of the three Fig. 2.6, performed very inefficiently to the extent of rendering it useless for many *wavemixing* applications. These two observations are obviously consistent with the preceding discussion.

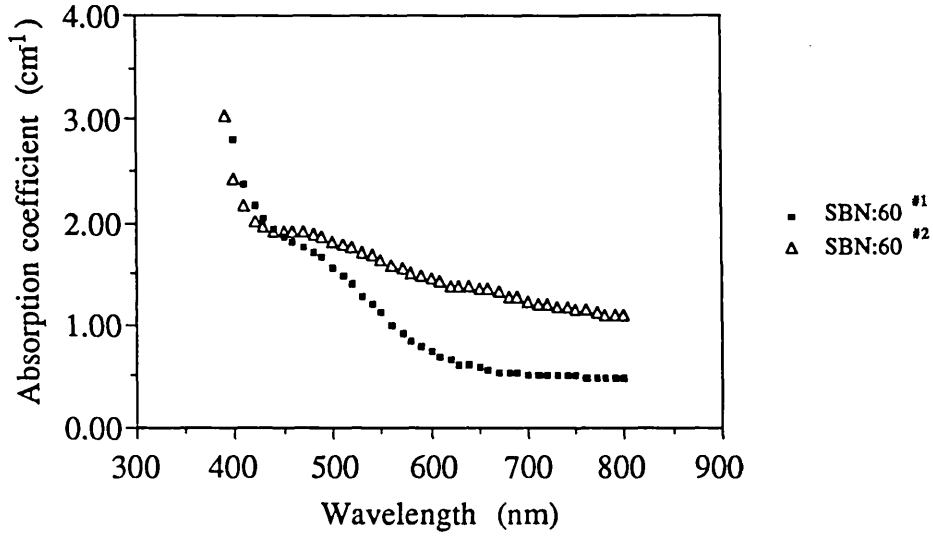


Figure 2.7 Absorption spectra for cerium doped SBN:60.

The absorption spectra for two separate samples of cerium doped $Sr_{0.6}Ba_{0.4}Nb_2O_6$, SBN:60 are shown in Fig. 2.7. and tabulated in Appendix ß. Both were grown and poled by Rockwell International, Science Centre, Thousand Oaks, C.A. and sample #1 is pictured in Fig. 2.8. The absorption spectrum of crystal #2, △, was extracted from reference [2.17], that of crystal #1, ▪ , was measured using the instrumentation previously described. They have the same bandgap absorption edge however their absorption signatures for $\lambda > \lambda_{Bandgap}$ differ markedly. Both confirm the presence of impurity sites located in the forbidden energy gap, while their differences may be due to differing concentrations of the cocktail of many trace impurities in addition to the prescribed cerium.

The undoped paraelectric materials sillenite $Bi_{12}SiO_{20}$ (BSO) and bismuth germanium oxide $Bi_{12}GeO_{20}$ (BGO) are very efficient photoconductors with low dark photoconductivities [2.19,2.20]. Photogenerated electrons are generated from an extrinsic centre and trapping occurs at an empty photoluminescence centre. However electron–hole competition has been reported in BSO [2.21] and the third

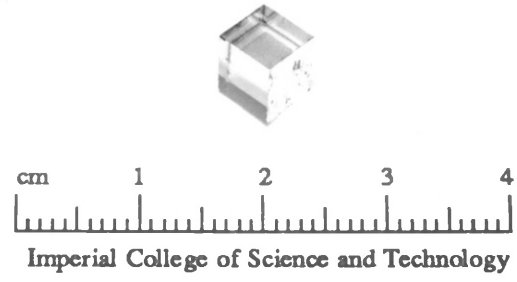


Figure 2.8 Photograph of crystal #1 of cerium doped SBN:60.

family member bismuth titanate $Bi_{12}TiO_{20}$ (BTO) [2.22]. The absorption spectrum of a crystal of BSO, ■ , grown by Sumitomo Electric Industries Ltd, Osaka, Japan, is shown in Fig. 2.9, tabulated in Appendix B and the sample is pictured in Fig. 2.10. The absorption edge is nearer 500nm and a featureless signature is observed for $\lambda > \lambda_{\text{Bandgap}}$.

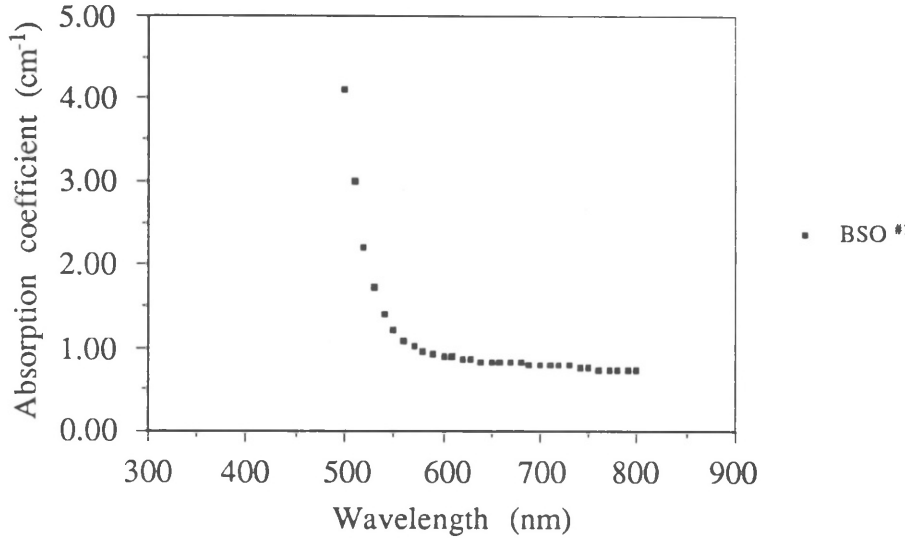


Figure 2.9 Absorption spectrum for $Bi_{12}SiO_{20}$.

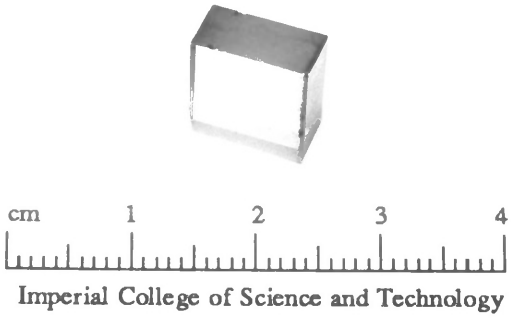


Figure 2.10 Photograph of sample #1 of $Bi_{20}SiO_{20}$.

The III–V semiconductors represent a third catagory of PR materials. Their useful operating wavelength range is in the near infrared, typically $0.8 \rightarrow 1.8\mu$m, and exhibit very fast characteristic reponse times, $\sim \mu$s. Gallium arsenide, GaAs, and indium phosphide, InP, are the two member semiconductors most commonly studied. The absorption spectra for chromium doped GaAs and iron doped InP, extracted from reference [2.23], are shown in Fig. 2.11 and tabulated in Appendix B. Both the GaAs, ■ , and InP, △, exhibit long tails to their strong absorption edges corresponding to photoexcitations from deep lying impurity sites to the conduction band [2.24]. The absorption edges are located at 0.86μm and 0.95μm respectively with the chromium doped GaAs displaying more absorption features for $\lambda > \lambda_{\text{Bandgap}}$.

Of the three catagories of PR materials, *ferroelectric oxides*, *paraelectric oxides* and III–V *semiconductors*, the *ferroelectrics* display the largest electro–optic coefficients which has made them the most popular PR materials investigated and optimised. Barium titanate is currently the most popular ferroelectric PR material being studied. Prepared as a single domain crystal by mechanical and electrical poling techniques [2.25], it has two of the largest electro–optic coefficients, r_{42} and

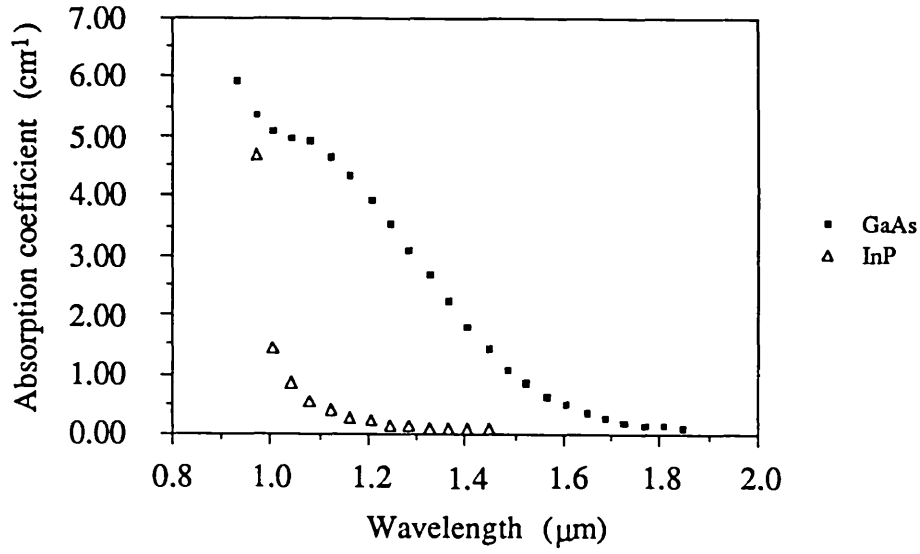


Figure 2.11 Absorption spectra for chromium doped GaAs and iron doped InP.

r_{51}, displayed by PR materials. The electro-optic tensor has the form [2.10]

$$\begin{pmatrix} 0 & 0 & r_{13} \\ 0 & 0 & r_{23} \\ 0 & 0 & r_{33} \\ 0 & r_{42} & 0 \\ r_{51} & 0 & 0 \\ 0 & 0 & 0 \end{pmatrix}, \tag{2.43}$$

where $r_{13} = r_{23}$ and $r_{42} = r_{51}$. It has a perovskite structure and exists in the tetragonal phase (4mm point group symmetry) at room temperature. As a consequence the material is (negative) uniaxial birefringent in the absence of electric fields. The dispersive nature of the bulk ordinary, n_o, and extra-ordinary, n_e, RI indices are shown in Fig. 2.12 and Table 2.I, [2.26], for the wavelength range $420 \rightarrow 670$nm.

The Curie, T_c, and a phase transition temperature exist at 133°C and 6°C [2.27] respectively. The phase is cubic above the upper and orthorhombic below the lower temperatures. Predominately p-type photoconducting with a low mobility and short recombination time, the material has a very slow response time of typically $10^0 - 10^1$seconds for nominal optical intensities of $\sim 1\text{Wcm}^{-2}$ in the *cw* regime. The material's main attraction being its ability to induce very large changes in refractive index, RI, ($\Delta n \sim 10^{-3}$) by employing the r_{42} and r_{51} coefficients which are also responsible for its exotic *self-pumping* PR behaviour.

The second ferroelectric oxide of particular interest is strontium barium niobate. A

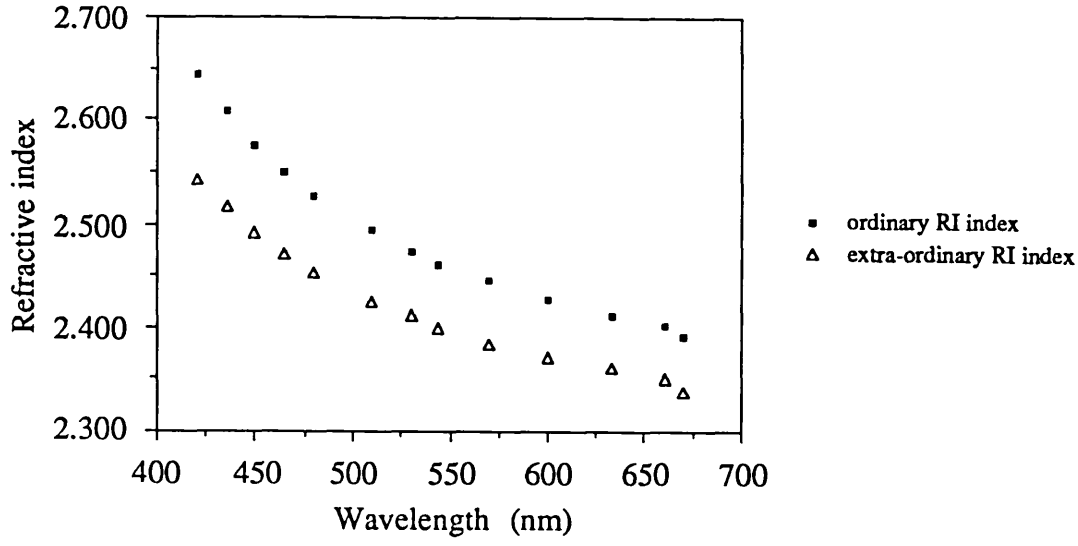


Figure 2.12 Bulk indices of refraction for $BaTiO_3$.

λ nm	n_e	n_o
420	2.543	2.644
435	2.517	2.608
450	2.490	2.574
465	2.470	2.549
480	2.453	2.526
510	2.425	2.493
514.5	2.424	2.488
530	2.411	2.474
544	2.400	2.461
570	2.385	2.444
600	2.372	2.427
632.8	2.361	2.413
660	2.351	2.401
670	2.339	2.392

Table 2.I Bulk indices of refraction for $BaTiO_3$.

member of the tungsten bronze family, it also has a 4mm point group symmetry. Similar to $BaTiO_3$, the material is (negative) uniaxial birefringent and has an electro-optic tensor identical in form, Eq. (2.43). However, it's Curie temperature, T_c, is 78°C for the SBN:60 stoichiometry and the r_{33} is the dominant electro-optic coefficient. The cerium doped material is n-type photoconducting and is observed to have a shorter characteristic grating rise time and a longer dark decay time than $BaTiO_3$. The material displays *self-pumping* due to the strength of the r_{33}

coefficient, an optical phenomenon demonstrated only by itself and $BaTiO_3$.

There are three main PR members to the paraelectric oxide family, namely sillenite ($Bi_{12}SiO_{20}$, BSO), bismuth germanium oxide ($Bi_{12}GeO_{20}$, BGO) and bismuth titanate ($Bi_{12}TiO_{20}$, BTO). Each material exists in a cubic phase (23 point group symmetry) at room temperature and are consequently optically isotropic in the absence of electric fields. Their corresponding electro-optic tensor consists of only three non-zero elements,

$$\begin{pmatrix} 0 & 0 & 0 \\ 0 & 0 & 0 \\ 0 & 0 & 0 \\ r_{41} & 0 & 0 \\ 0 & r_{52} & 0 \\ 0 & 0 & r_{63} \end{pmatrix}, \tag{2.44}$$

with $r_{41} = r_{52} = r_{63}$. They are all strongly optically active although BTO has a lower activity compared to BSO and BGO ($\rho_o = 45°mm^{-1}$ for BSO at $\lambda =$ 514.5nm). Hence the polarisation states of the incident and diffracted light in general differ which can be exploited to improve the signal to noise ratio in many optical systems. Their PR performances can be optimised using moving fringe techniques and dc and ac [2.28] externally applied electric fields. Predominately n-type photoconducting, their mobilities are larger and recombination times longer than the ferroelectric oxides and hence have faster response times of typically 10^{-2} seconds for nominal intensities in the *cw* regime.

Thirdly there is the III-V semiconductor family of PR materials with gallium arsenide, GaAs, and indium phosphide, InP, as the two main members. They exist in the cubic phase ($\bar{4}3m$ point group symmetry) at room temperature, optically isotropic in the absence of electric fields and have an electro-optic tensor identical in form to the paraelectric oxides, Eq. (2.44). Their shallow forbidden energy gaps have optimum PR quantum efficiencies in the near infrared spectral region however their dark conductivities are much larger due to their fast thermal generation rates. Predominately n-type photoconducting, they have high mobilities and moderate recombination times to give them very fast characteristic response times of 10^{-4} seconds in the *cw* regime.

The key material and electro-optic parameters of a selection of PR materials from all three familes are given in Tables 2.II and 2.III respectively.

Material	Useful wavelength range (μm)	L_d [E= 2kVcm^{-1}] (μm)	Mobility ($cm^2V^{-1}s^{-1}$)	τ_R (ns)	τ_{dark} (s)
$BaTiO_3$	0.4–0.9	0.1	~ 1	≤ 1	10^2
SBN	0.4–0.6				10^2
$LiNbO_3$: Fe	0.4–0.7	$\leq 10^{-4}$			300
$KNbO_3$	0.4–0.7	0.3			10^{-3}
BSO	0.4–0.7	3	50	100	10^5
GaAs:Cr	0.8–1.8	3	6000	≥ 1	10^{-4}
InP:Fe	0.85–1.3	3			10^{-4}

Table 2.II Material parameters of selected PR materials.

2.5 Geometric and polarisation considerations for $BaTiO_3$ and SBN.

The space charge electric field within the bulk of a PR material is induced by the light intensity, a scalar quantity. However the polarisation of the light, a vector quantity, determines the modulated RI environment experienced. Considering Eqs. (2.38), (2.40) and (2.43), the most general form of the optical indicatrix for both barium titanate and strontium barium niobate is

$$\begin{aligned} &\frac{x^2}{n_o^2} + \frac{y^2}{n_o^2} + \frac{z^2}{n_e^2} \\ &+ r_{13}x^2E_z + r_{23}y^2E_z + r_{33}z^2E_z \\ &+ 2r_{43}yzE_y + 2r_{51}xzE_x \\ &= 1, \end{aligned} \tag{2.45}$$

where the principle optic axis of the crystal, +c, is coincident with the z co-ordinate axis. It is apparent from Eq. (2.45) that there exists a symmetry between the x and y axis and a mutual asymmetry with the z axis. To employ the dominant electro-optic coefficients of $BaTiO_3$, r_{42} and r_{51}, an electric field component along the y or x axis is required. For SBN the dominant coefficient, r_{33}, requires a field component along the z axis. For simplicity, consider an induced electric field which is confined to the xz plane i.e. $E_x \neq 0$, $E_y = 0$ and $E_z \neq 0$. Using the co-ordinate change illustrated in Fig. 2.13, the new principal dielectric axis x′, y′ and z′ are located and accompanied by the optical indicatrix

$$\frac{x'^2}{n_{x'}^2} + \frac{y'^2}{n_{y'}^2} + \frac{z'^2}{n_{z'}^2} = 1. \tag{2.46}$$

Material	Dielectric Constant	λ (μm)	EO coeffs (pmV^{-1})	Index of Refraction
Ferroelectric oxides:				
$BaTiO_3$ ($T_c = 395K$)	$\varepsilon_x = 3600$ $\varepsilon_y = \varepsilon_x$ $\varepsilon_z = 135$	0.546	$r_{13} = 8$ $r_{23} = r_{13}$ $r_{33} = 28$ $r_{42} = 1640$ $r_{51} = r_{42}$	$n_o = 2.437$ $n_e = 2.365$
$Sr_{0.75}Ba_{0.25}Nb_2O_6$ ($T_c = 395K$)	$\varepsilon_x = 500$ $\varepsilon_y = \varepsilon_x$ $\varepsilon_z = 3000$	0.633	$r_{13} = 67$ $r_{23} = r_{13}$ $r_{33} = 1400$ $r_{42} = 42$ $r_{51} = r_{42}$	$n_o = 2.3117$ $n_e = 2.2987$
$Sr_{0.60}Ba_{0.40}Nb_2O_6$ ($T_c = 351K$)	$\varepsilon_x = 450$ $\varepsilon_y = \varepsilon_x$ $\varepsilon_z = 820$		$r_{33} = 420$ $r_{42} = 42$ $r_{51} = r_{42}$	
$LiNbO_3$ ($T_c = 1503K$)	$\varepsilon_x = 78$ $\varepsilon_y = \varepsilon_x$ $\varepsilon_z = 32$	0.633	$r_{13} = 9.6$ $r_{22} = 6.8$ $r_{33} = 30.9$ $r_{51} = 32.6$	$n_o = 2.286$ $n_e = 2.200$
$KNbO_3$		0.633	$r_{13} = 28$ $r_{23} = 1.3$ $r_{33} = 64$ $r_{42} = 380$ $r_{51} = 105$	$n_1 = 2.280$ $n_2 = 2.329$ $n_3 = 2.169$
Paraelectric oxides:				
$Bi_{12}SiO_{20}$		0.633	$r_{41} = 5.0$	2.54
$Bi_{12}GeO_{20}$		0.666	$r_{41} = 3.22$	2.54
$Bi_{12}TiO_{20}$		0.633	$r_{41} = 5.17$	
III–V Semiconductors:				
GaAs	$\varepsilon = 13.2$	0.9	$r_{41} = 1.1$	3.60
InP			$r_{41} = 1.45$	

Table 2.III Electro-optic parameters of selected PR materials.

The principal refractive indices are given by

$$n_{x'} = \left[1/n_o^2 + r_{13}E_z + r_{51}E_x \tan\theta\right]^{-1/2}$$

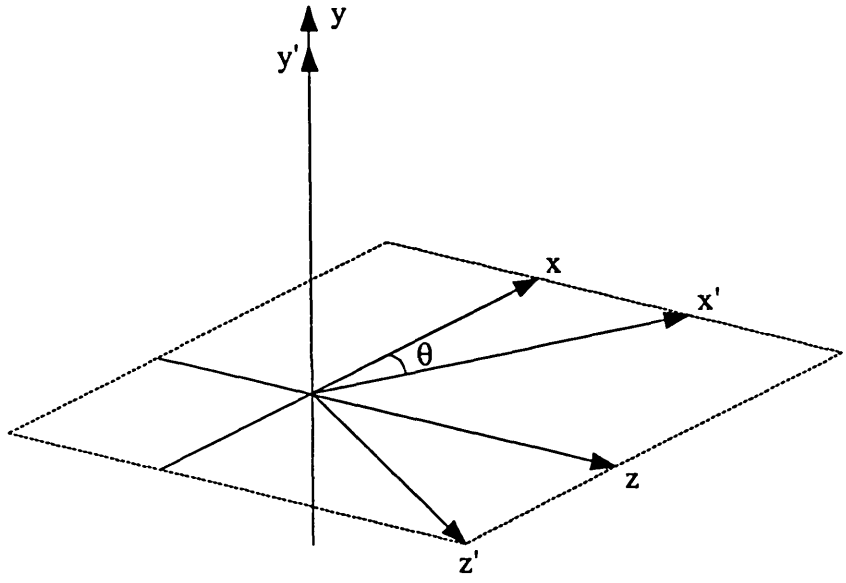


Figure 2.13 Cartesian co–ordinate change to locate principal dielectric axes in $BaTiO_3$/SBN.

$$\approx n_o\left(1-\frac{1}{2}n_o^2\left(r_{13}E_z+r_{51}E_x\tan\theta\right)\right), \tag{2.47a}$$

$$n_{y'}=\left[1/n_o^2+r_{23}E_z\right]^{-1/2}$$

$$\approx n_o\left(1-\frac{1}{2}n_o^2 r_{23}E_z\right) \tag{2.47b}$$

and

$$n_{z'}=\left[1/n_e^2+r_{33}E_z-r_{51}E_x\tan\theta\right]^{-1/2}$$

$$\approx n_e\left(1-\frac{1}{2}n_e^2\left(r_{33}E_z-r_{51}E_x\tan\theta\right)\right). \tag{2.47c}$$

The angle of axis rotation, θ, is given by

$$\tan 2\theta=\frac{2r_{51}E_x}{\left(1/n_o^2+r_{13}E_z\right)-\left(1/n_e^2+r_{33}E_z\right)} \tag{2.48}$$

The full derivation of Eqs. (2.47a), (2.47b), (2.47c) and (2.48) are given in Appendix A.

It is evident from Eqs. (2.47a), (2.47b) and (2.47c) that $n_{x'}\neq n_{y'}\neq n_{z'}$ and hence the material has been transformed from its original uniaxial birefringent form to biaxial birefringent. To create an induced static electric field confined to the xz plane the spatial variation in *writing* intensity and hence the mutually coherent *writing* laser beams must also be confined to the xz plane. The two orthogonal polarisations, s (*ordinary*) and p (*extra–ordinary*), correspond to the electric field

vector of the light parallel and orthogonal to the y axis respectively. For s or *ordinary* polarisation the RI environment experienced is given by Eq. (2.47b). Only the relatively small valued r_{23} coefficent for both $BaTiO_3$ and SBN is employed and hence a weakly modulated RI is experienced. However for p or *extra–ordinary* polarisation a combination of Eqs. (2.47a) and (2.47c) determine the RI environment. Both equations employ the dominant r_{51} and r_{33} coefficients of $BaTiO_3$ and SBN respectively and hence both materials exhibit much larger RI modulations and display more exotic optical nonlinearities (e. g. self pumping) for this polarisation state. The two materials however differ in their preferred crystal orientations and optical configurations. The r_{51} coefficient is associated with an electric field component in the x direction, E_x. Thus for $BaTiO_3$ an asymmetric optical configuration w. r. t. the normal to the crystalline +c axis is adopted. The combination of principal dielectric axis rotation and electric field saturation effects make it difficult to deduce the most optimum geometric orientations of crystal and laser beams. The r_{33} coefficient is employed by the z component of the induced electric field E_z. The optimum orientation for SBN corresponds to a symmetric optical configuration w. r. t. the normal to the +c axis which reduces E_x and θ to zero.

2.6 Conclusions.

The photorefractive effect is exhibited by materials which are both photoconducting and electro–optic in nature. Illuminating a photorefractive material with a spatially varying intensity profile, free charged carriers are preferentially photogenerated in the bright regions. The mobile species migrate by *diffusion* into the dark regions or *drift* under the influence of an externally applied electric field and subsequently become retrapped. The resultant displacement of charge creates a static electric field within the bulk of the material which modulates the refractive index by the electro–optic effect. In summary, the illuminating intensity profile induces a phase volume hologram within the bulk of the material.

There are three principal families of photorefractive materials, namely the *ferroelectric oxides*, *paraelectric oxides* and III–V *semiconductors*. The *ferroelectric oxides* exhibit the largest linear electro–optic coefficients, $r_{42} = 1640 pmV^{-1}$ for $BaTiO_3$, making them attractive to investigate. However they appear to be inherently slow with typical response times of 10^0–10^1 seconds for nominal optical intensities, $\sim 1 Wcm^{-2}$. The *paraelectric oxides* have much smaller linear electro–optic coefficients, $r_{41} = 5.0 pmV^{-1}$ for BSO, but have faster response times, 10^{-3}–10^{-2} seconds. They, like the *ferroelectric oxides*, have an optimum operating range in the mid–visible spectral region and have very long dark storage times. The third

family of photorefractives, III–V semiconductors, operating in the near–IR spectral region, also have small linear electro–optic coefficients, $r_{41} = 1.1 \text{pmV}^{-1}$ for GaAs. Their response times are very fast, $\sim 10^{-6}$ seconds, but have very short dark storage times, $\sim 10^{-4}$ seconds, due to their fast thermal generation rate.

2.7 References.

[2.1] N.V. Kukhtarev, V.B. Markov, S.G. Odulov, M.S. Soskin and V.L. Vinetskii, "Holographic storage in electro–optic crystals. I Steady state," Ferroelectrics **22**, 949–960 (1979).

[2.2] N.V. Kukhtarev, V.B. Markov, S.G. Odulov, M.S. Soskin and V.L. Vinetskii, "Holographic storage in electro–optic crystals. II Beam coupling – light amplification," Ferroelectrics **22**, 961–964 (1979).

[2.3] F.P Strohkendl, J.M.C. Jonathan and R.W. Hellwarth, "Hole–electron competition in photorefractive gratings," Optics Lett **11**, 312–314 (1986).

[2.4] G.C. Valley, "Simultaneous electron/hole transport in photorefractive materials," J.Appl.Phys **59**, 3363–3366 (1986).

[2.5] G. Le Saux and A. Brun, "Photorefractive material response to short pulse illuminations," IEEE J.Quantum Electron **QE–23**, 1680–1688 (1979).

[2.6] J. Feinberg, D. Heiman, A.R. Tanguay jr and R.W. Hellwarth, "Photorefractive effects and light induced charge migration in barium titanate," J.Appl.Phys. **51**, 1297–1305 (1980).

[2.7] S. Ducharme and J. Feinberg, "Altering the photorefractive properties of $BaTiO_3$ by reduction and oxidation at 650 °C," J.Opt.Soc.Am. B **3**, 283–292 (1986).

[2.8] M.B. Klein and G.C. Valley, "Beam coupling in $BaTiO_3$ at 442nm," J.-Appl.Phys. **57**, 4901–4905 (1985).

[2.9] D. Mahgerefteh and J. Feinberg, "Nanosecond reponse and "coasting" in photorefractive barium titanate," OSA Topical meeting on *Photorefractive materials, effects and devices* (Los Angeles, C.A.), Technical Digest **17**, 92 (August 1987).

[2.10] Yariv A. and Yeh P., "Optical Waves in Crystals," (Wiley series in pure and applied optics, New York, 1984).

[2.11] Hecht E. and Zajac A., "Optics," (Addison–Wesley publishing company, Massachusetts 5th Ed, 1980).

[2.12] M.G. Clarke, F.J. DiSalvo, A.M. Glass and G.E. Peterson, "Electronic structure and optical index damage of iron doped lithium niobate," J.-Chem.Phys. **59**, 6209–6219 (1973).

[2.13] D.L. Staebler and W. Philips, "Fe–doped $LiNbO_3$ for read–write applications," Appl.Opt. **13**, 788–794 (1974).

[2.14] E. Krätzig, "Photorefractive effect and photoconductivity in $LiNbO_3$: Fe," Ferroelectrics **21**, 635–636 (1978).

[2.15] M.B. Klein and R.N. Schwartz, "Photorefractive effect in $BaTiO_3$: microscoptic origins," J.Opt.Soc.Am. B **3**, 293–305 (1986).

[2.16] K. Megumi, H. Kozuka, M. Kobayashi and Y. Furuhata, "High–sensitive holographic storage in Ce–doped SBN," Appl.Phys.Lett. **30**, 631–633 (1977).

[2.17] G.A. Rakuljic, A. Yariv and R.R. Neurgaonkar, "Photorefractive properties of undoped, cerium doped and iron doped single crystal $Sr_{0.6}Ba_{0.4}Nb_2O_6$," Opt.Eng. **25**, 1212–1216 (1986).

[2.18] R.R. Neurgaonkar, W.K. Cory, J.R. Oliver, M.D. Ewbank, W.F. Hall, "Development and modification of photorefractive properties in the tungsten bronze family crystals," Opt.Eng. **26**, 392–405 (1987).

[2.19] R.A. Sprague, "Effect of bulk carriers on PROM sensitivity," J.Appl.Phys. **46**, 1673–1678 (1975).

[2.20] S.L. Hou, R.B. Lauer and R.E. Aldrich, "Transport processes of photoinduced carriers in $Bi_{12}SiO_{20}$," J.Appl.Phys. **44**, 2652–2658 (1973).

[2.21] F.P. Strohkendl, P. Tayebati and R.W. Hellwarth, "A comparative study of the photorefractive effect in $Bi_{12}SiO_{20}$ crystals," OSA Topical meeting on *Photorefractive materials, effects and devices* (los Angeles, C.A.), Technical Digest **17**, 32–34 (August 1987).

[2.22] D. Rutz, M.B. Klein, B.A. Wechsler, R.N. Schwartz and K.W. Kirby, "Growth and Characterization of photorefractive $Bi_{12}TiO_{20}$ (BTO)," OSA Topical meeting on *Photorefractive materials, effects and devices* (los Angeles, C.A.), Technical Digest **17**, 41–43 (August 1987).

[2.23] A.M. Glass, A.M. Johnson, D.H. Olson, W. Simpson and A.A. Ballman, "Fourwave mixing in semi–insulating InP and GaAs using photorefractive effect," Appl.Phys.Lett. **44**, 948–950 (1979).

[2.24] D.C. Look, "Model for Fe^{2+} intracenter–induced photoconductivity in InP:Fe," Phys.Rev. B **20**, 4160–4166 (1979).

[2.25] Sanders Associates, Inc., "Guidelines for the preparation of single domain $BaTiO_3$ crystals," Sanders Associates, Inc., Defense Systems Division, 15 Canal St, Nashua, New Hampshire, U.S.A.

[2.26] Bechmann R., Hearmon R.F.S. and Kurtz S.K., "Elastic, Piezoelectric, Piezooptic, Electrooptic Constants, and Nonlinear Dielectric Susceptibilities of Crystals," (Springer–Verlag, Heidelberg, 1969).

[2.27] S.H. Wemple, M. DiDomenico Jr. and I. Camlibel, "Dielectric and optical properties of melt–grown $BaTiO_3$," J.Phys.Chem.Solids **29**, 1797–1803 (1968).

[2.28] S.I. Stepanov and M.P. Petrov, "Efficient unstationary holographic recording in photorefractive crystals under an external alternating electric field," Optics Comm. **53**, 292–295 (1985).

CHAPTER 3

TWO WAVE MIXING AND COHERENT LIGHT AMPLIFICATION.

3.1 Introduction.

The generalised band transport equations of the photorefractive (PR) effect were derived in Chapter 2 and are re–stated here as follows [3.1]

$$\frac{\partial n}{\partial t} = \frac{\partial N_D^+}{\partial t} + \nabla.(D\nabla n + \mu n\mathbf{E}), \tag{3.1}$$

$$\frac{\partial N_D^+}{\partial t} = (N_D - N_D^+)(sI + \beta) - \gamma_R n N_D^+, \tag{3.2}$$

$$\nabla.(\varepsilon\varepsilon_o\mathbf{E}) = q(N_D^+ - N_A - n) \tag{3.3}$$

and

$$\nabla \times \mathbf{E} = 0. \tag{3.4}$$

The modifications to accomodate for electron/hole competition and deep donor/-shallow traps have been neglected. The non–linearity in coupling between the equations prevents an analytic solution of **E** being derived for all but the very simplest of intensity profiles, I. The one dimensional cosinusoidal is one such simple profile and is discussed in more detail in this chapter.

3.2 Theory.

A cosinusoidal intensity pattern can be generated from the interaction or *mixing* of two mutually coherent plane wavefronts, reference R and signal S, angularly separated and of intensities I_R and I_S. The profile is depicted in Fig. 3.1 and analytically expressed as

$$I = I_o[1 + M\cos(\mathbf{k}.\mathbf{r})] \tag{3.5}$$

where I_o, M and **k** are the total intensity, fringe contrast and fringe pattern wavevector and are equal to $I_R + I_S$, $2\sqrt{I_R I_S}/I_o$ and $\mathcal{Q} - \mathcal{Q}$ respectively. The axis system was chosen to be consistent with the linear electro–optic tensor notation and common crystallographic orientation of the PR materials of interest, namely $BaTiO_3$ and SBN:60. The fringe separation, Λ, and wavelength, λ, are related as follows

$$\lambda = 2\Lambda\sin\theta. \tag{3.6}$$

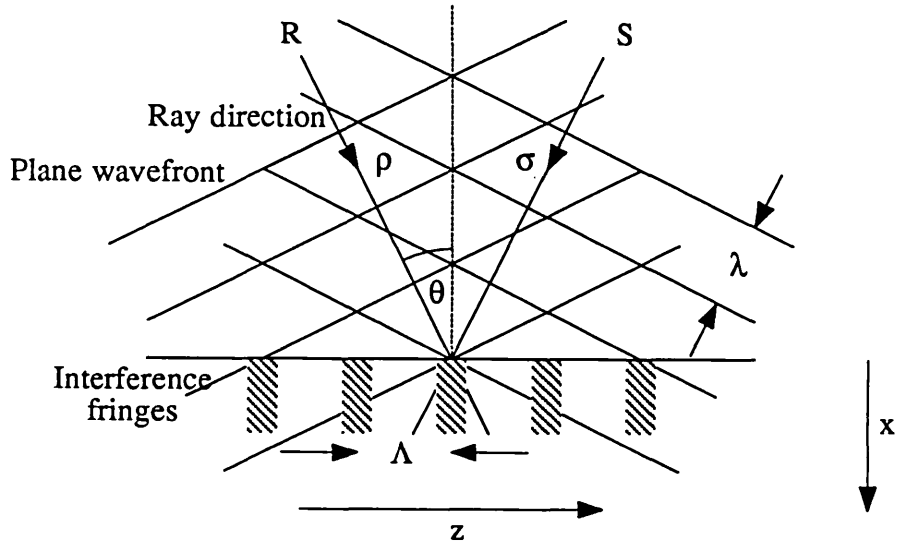


Figure 3.1 Formation of a one dimensional cosinusoidal intensity profile.

For a one dimensional intensity profile, I(z), the spatial variations in n, N_D^+ and **E** must also be confined to that dimension, z, and hence the generalised band transport equations, Eqs. (3.1), (3.2) and (3.3), are reduced to the following simpler forms

$$\frac{\partial n}{\partial t} = \frac{\partial N_D^+}{\partial t} + \frac{\partial}{\partial z}\left(D\frac{\partial n}{\partial z} + \mu n E_z\right), \tag{3.7}$$

$$\frac{\partial N_D^+}{\partial t} = \left(N_D - N_D^+\right)(sI(z) + \beta) - \gamma_R n N_D^+, \tag{3.8}$$

$$\frac{\partial E_z}{\partial z} = \frac{q}{\varepsilon_z \varepsilon_o}\left(N_D^+ - N_A - n\right) \tag{3.9}$$

where ε_z is the relative permittivity of the material in the z direction.

3.2.1 Linear in generation and recombination regime.

We wish to solve the coupled Eqs (3.7), (3.8) and (3.9), in the steady state and linear in generation/recombination regimes. Consequently the time derivatives are reduced to zero and an abundance of both ionised and unionised donors are assumed to exist through the forbidden energy gap. Hence $n \ll N_A$, $N_D - N_A$ and $N_D^+ \approx N_A$ i.e. the number density of ionised donors under the spatially varying illumination is assumed to differ little from its original homogeneous dark value of N_A.

Incorporating the above conditions, the equations can be re–expressed as follows

$$0 = 0 + \frac{d}{dz}\left[D\frac{dn}{dz} + \mu n E_z\right], \tag{3.10}$$

$$0 = (N_D - N_A)(sI_o[1 + M\cos kz] + \beta) - n/\tau_R, \tag{3.11}$$

$$\frac{dE_z}{dz} = \frac{q}{\varepsilon_z \varepsilon_o} N^+_{D_{Migration}}, \tag{3.12}$$

where the characteristic recombination time, τ_R, is given by

$$\tau_R = \frac{1}{\gamma_R N_A}. \tag{3.13}$$

The Eqs. (3.10) and (3.11) state that in the steady state regime the free electron and ionised donor number densities, n and N_D^+, and the induced electric field, E_z, all co–exist in mutual equilibrium. The *generation* and *recombination* rates are equal while the *migration* rate is reduced to zero. The *diffusion* of the free electrons due to their concentration gradient is balanced exactly by an equal but opposite *drift* under the influence of the induced electric field i. e. the spatially varying profile of free electrons in the conduction band is held fixed in both time and space by the induced electric field. Finally, Eq. (3.12) states that the induced electric field, E_z, is due to the migration of charge during the initial transient stage.

The coupled Eqs. (3.10), (3.11) and (3.12) can be solved analytically [3.2,3.3], Appendix C, to yield a solution for the induced electric field as follows

$$E_z = E_A \frac{\sqrt{1 - m^2}}{(1 + m\cos kz)} - E_D \frac{m\sin kz}{(1 + m\cos kz)}. \tag{3.14}$$

The characteristic electric fields E_A and E_D are associated with *drift* and *diffusion* transport mechanisms respectively. E_A is the externally applied d. c. electric field while E_D is given by

$$E_D = \frac{Dk}{\mu} = \frac{k_B T}{q}k, \tag{3.15}$$

where the Einstein relationship, Eq. (2.11), has been employed, T is the absolute temperature and k_B the Boltzmann constant. The reduced modulation, m , is related to the fringe contast, M, as follows

$$m = \frac{M}{(1 + \beta/sI_o)}. \tag{3.16}$$

The *drift* of the free electrons in the non–uniform illumination is accommodated by the $\sqrt{1 - m^2}$ term in Eq. (3.14). Due to the photoconductive character of

PR materials the dark regions are less conductive than the bright and hence serve to restrict the transverse flow or *drift* of the electrons. In the limit as $m \rightarrow 1$ i.e. in the limit as $M \rightarrow 1$ in the absence of thermal generation, Eq. (3.16), the dark regions become perfectly insulating and all *drift* is quenched (electronically equivalent to a parallel plate capacitor), leaving *diffusion* as the only transport mechanism contributing to the induced electric field.

The electric field induced by cosinusoidal illumination for reduced modulations of 0.1, 0.5 and 0.9 are graphically represented in Figs. 3.2a) and b), ■ , for *diffusion* dominant, $E_A \ll E_D$, and *drift* dominant, $E_A \gg E_D$, transport mechanisms respectively. It is observed that for small modulations the induced electric fields are of negative sinusoidal and cosinusoidal forms respectively. However for large values of m the induced electric field responses, remaining periodic, becomes very non–sinusoidal with small electric field amplitudes in the bright regions (large conductivity), $kz = 0$, and large amplitude fluctations in the dark regions (large resistivity), $kz = \pm\pi$.

In the small reduced modulation limit, $m \ll 1$, the induced electric field can be approximated accurately by the fundamental Fourier components of Eq. (3.14) which were derived in Appendix C and given as follows

$$\begin{aligned} E_z &\simeq E_A - \frac{2}{m}\left[1 - \sqrt{1-m^2}\right](E_A \cos kz + E_D \sin kz), \\ &\simeq E_A - \frac{2}{m}\left[1 - \sqrt{1-m^2}\right]\sqrt{E_A^2 + E_D^2}\cos(kz + \phi), \\ &\approx E_A - m\sqrt{E_A^2 + E_D^2}\cos(kz + \phi) \end{aligned} \tag{3.17}$$

where

$$\tan\phi = E_D/E_A. \tag{3.18}$$

It is observed from Eq. (3.17) that the amplitude of the induced electric field is approximately linear in reduced modulation, m, and hence in fringe contrast, M, but weakly dependent on the total intensity, I_o Eq. (3.16). From Eq. (3.18) the corresponding phase shift between the induced electric field and the intensity profile, ϕ, is very dependent on which transport mechanism dominates. For *diffusion* dominance, $E_A \ll E_D$, and $\phi \sim \pi/2$ while for *drift* dominance, $E_A \gg E_D$, and $\phi \sim 0$. The significance of the phase shift, especially when equal to $\pi/2$ is highlighted later in this chapter. The resultant refractive index (RI) modulation, Δn, induced by the static electric field in linear (Pockels) electro-optic materials was discussed in Chapter 2. Mathematically expressed as follows

$$\Delta n = -\frac{1}{2}n^3 rE, \tag{2.40}$$

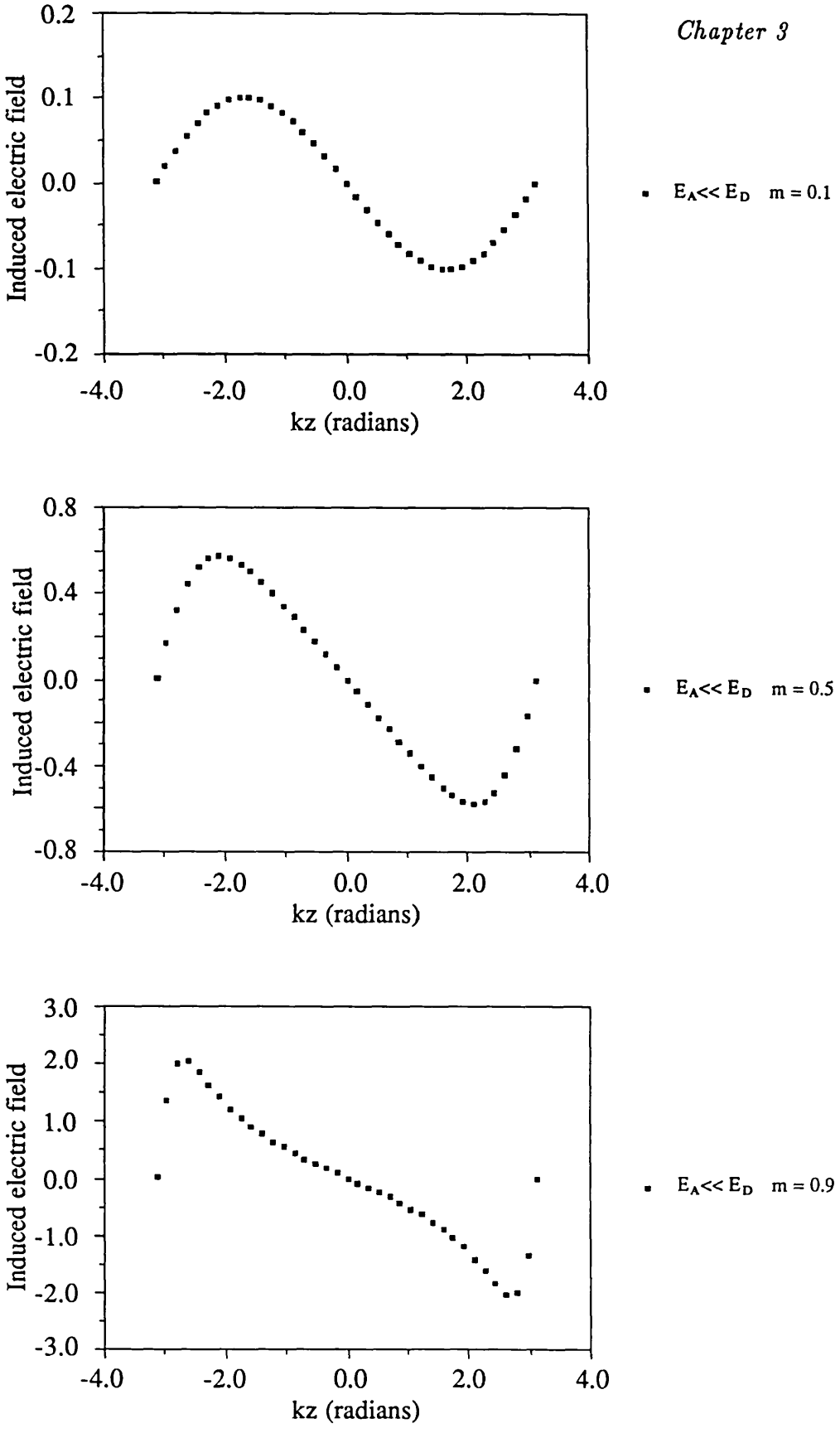


Figure 3.2a) Induced electric field for *diffusion* dominant transport mechanism.

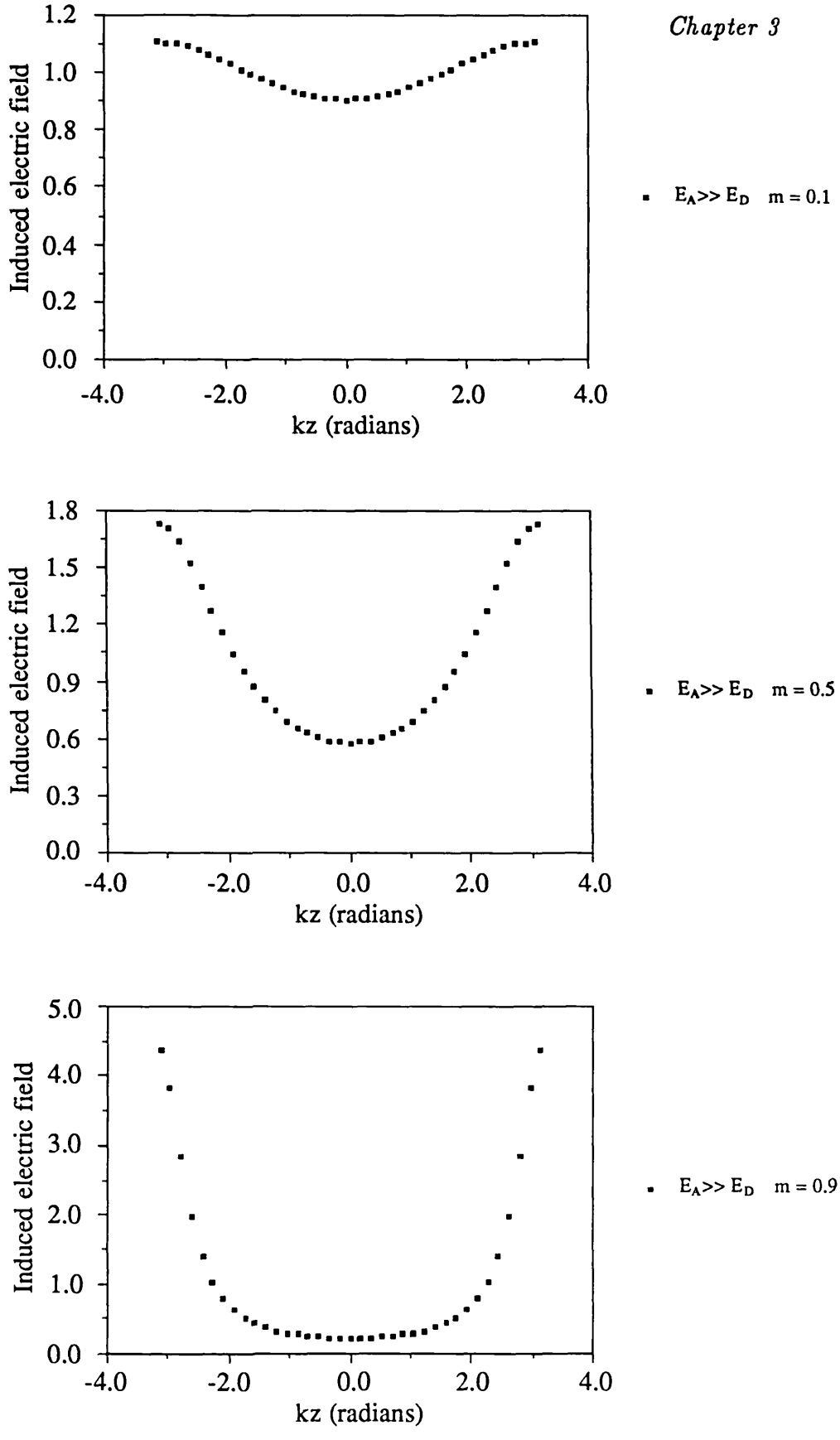


Figure 3.2b) Induced electric field for *drift* dominant transport mechanism.

the PR effect for n–type photoconductivity, diffusion dominance and a one dimensional cosinusoidal intensity profile is summarised in Fig. 3.3.

3.2.2 Saturation regime.

It would appear from Eq. (3.17) that the amplitude of the induced electric field can be increased to arbitary large values as both E_A and E_D are relatively unconstrained. This observation is however unrealistic as only a finite supply of donors, N_D, are able to contribute to the PR effect and hence support the induced field.

It has been established that the band transport model of the PR effect consists of three operational mechanisms, *generation*, *migration* and *recombination*. For n–type photoconductivity, electrons generated in the bright regions from unionised donor sites preferentially migrate towards the darker regions where they eventually recombine with ionised donor sites. Assuming a uniform background of compensating ionised acceptors, N_A, we can thus predict that $N_D^+ > N_A$ and $N_D^+ < N_A$ in the bright and dark regions respectively. The number density of ionised donors is however rigorously confined to within the following limits

$$0 \leq N_D^+ \leq N_D. \tag{3.19}$$

The maximum value of $|N_D^+ - N_A|$ corresponds to which of the two limits is encountered first, namely

$$|N_D^+ - N_A| = \begin{cases} N_A, & \text{if } N_D^+ = 0 \\ N_D - N_A, & \text{if } N_D^+ = N_D \end{cases}$$

and hence

$$|N_D^+ - N_A|_{Max} = \text{ the smaller of } N_A \text{ or } (N_D - N_A). \tag{3.20}$$

The limit N_A or $(N_D - N_A)$ is encountered if there are insufficient ionised or unionised donors respectively. The optimal condition being the simultaneous encounter of both limits which corresponds to the unique material condition of $N_A = N_D/2$.

The maximum value of $|N_D^+ - N_A|$ determines the maximum field amplitude capable of being supported by the material. Referring back to Gauss's law in one dimension, Eqs. (3.9) and (3.12), and substituting the earlier derived expression for the induced field, Eq. (3.17), we obtain

$$\frac{dE_z}{dz} = \frac{q}{\varepsilon_z \varepsilon_o}\left(N_D^+ - N_A - n\right), \tag{3.21}$$

$$mk\sqrt{E_A^2 + E_D^2}\sin(kz + \phi) = \frac{q}{\varepsilon_z \varepsilon_o}\left(N_D^+ - N_A\right), \tag{3.22}$$

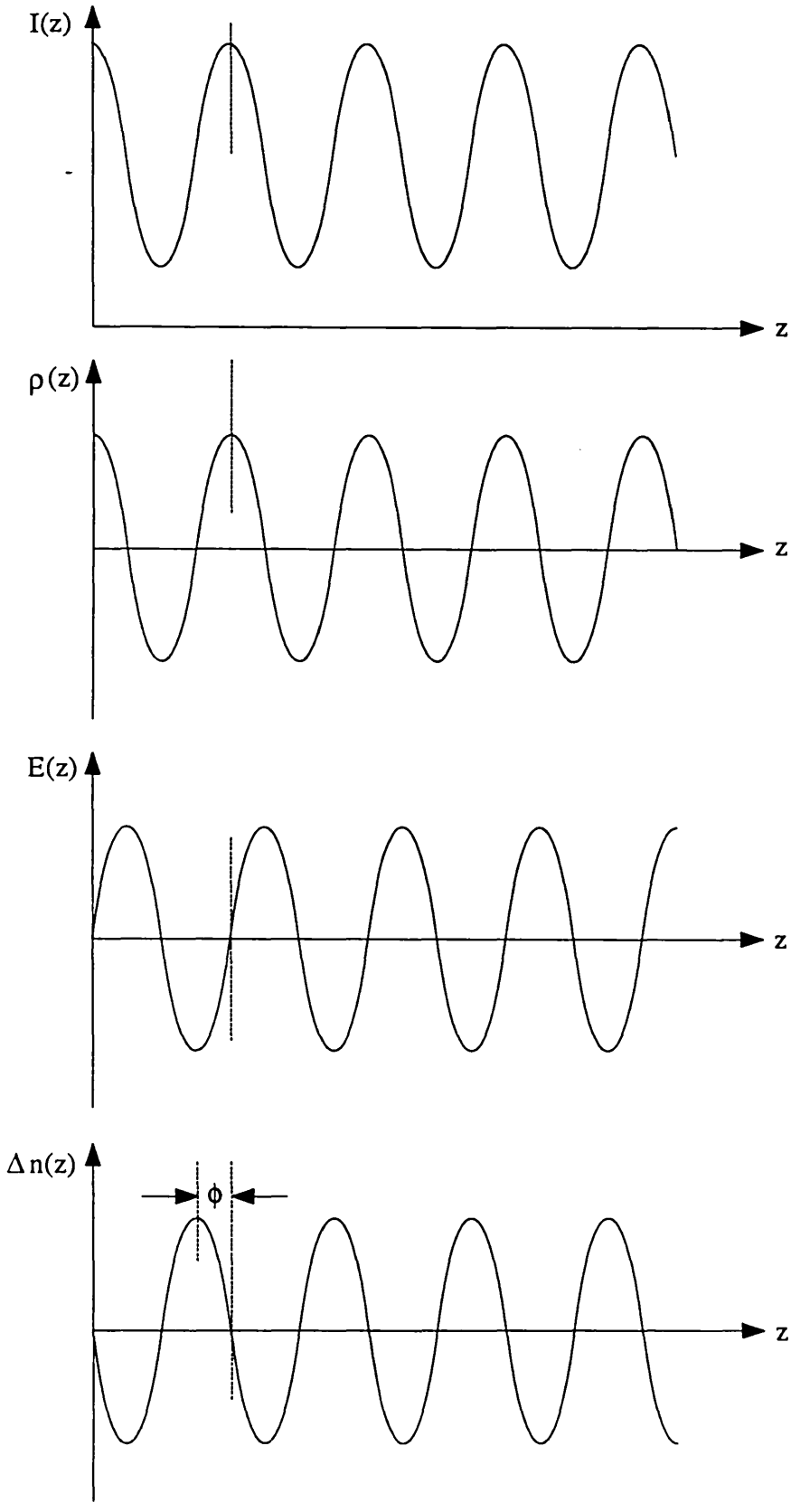


Figure 3.3 Summarised PR effect for n–type photoconductivity, *diffusion* dominance and a one dimensional cosinusoidal intensity profile.

where the original assumption of $n \ll N_A$, $N_D - N_A$ has been maintained but now $N_D^+ \approx N_A$ has been relaxed. The maximum field amplitude, $m\sqrt{E_A^2 + E_D^2}$ Eq. (3.17), is clearly given by

$$(E_{Amp})_{Max} = \frac{q}{\varepsilon_z \varepsilon_o} \frac{1}{k} |N_D^+ - N_A|_{Max}. \tag{3.23}$$

Employing Eq. (3.20)

$$= \text{ the smaller of } E_q \left(\frac{N_A}{N_D} \right) \text{ or } E_q \left(\frac{N_D - N_A}{N_D} \right), \tag{3.24}$$

where the characteristic electric field E_q is given by

$$E_q = \frac{q}{\varepsilon_z \varepsilon_o} \frac{N_D}{k}. \tag{3.25}$$

The two characteristic fields, E_D and E_q, differ markedly. The former has no material dependence, linearly proportional to the fringe wavenumber and derived from the linear in generation/recombination regime. The latter has a strong material dependence through N_D and ε_z, inversely proportional to the wavenumber and is a consequence of material saturation.

The wavenumber, k, dependence on the induced electric field, E_z, for both *drift* and *diffusion* dominance and for both linear in generation/recombination and saturation regimes are schematically illustrated in Fig. 3.4.

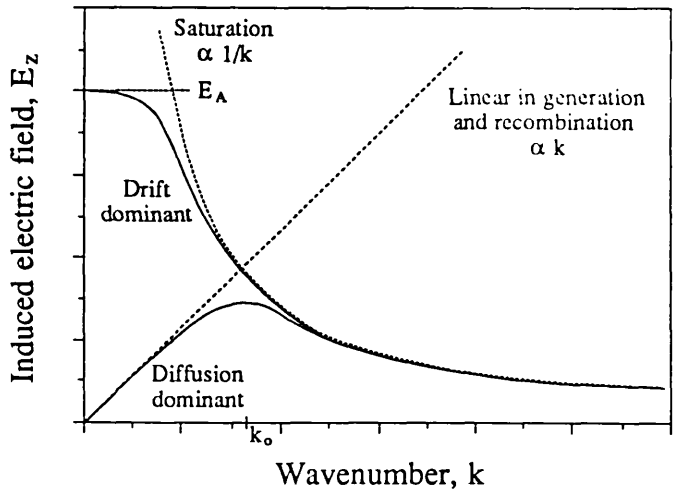


Figure 3.4 Schematic illustration of wavenumber dependence on induced electric field for both *drift* and *diffusion* dominant transport mechanisms.

At low spatial frequencies, linear in generation and recombination, the phase shift ϕ is 0 for *drift* and $\pi/2$ for *diffusion* dominance repectively. At high spatial frequencies, saturation, it can be shown that $\phi = \pi/2$ for both transport mechanisms [3.3]. The peak induced electric field for *diffusion* dominance, $E_A = 0$, is accompanied by the approximation

$$E_D \simeq \text{ the smaller of } E_q\left(\frac{N_A}{N_D}\right) \text{ or } E_q\left(\frac{N_D - N_A}{N_D}\right). \tag{3.26}$$

i. e. the equality of the limiting electric fields in linear in generation/recombination and saturation regimes. Using their definitions, Eqs. (3.15) and (3.25), the location of the peak field, k_o, can be deduced as follows

$$\frac{k_B T}{q} k_o \simeq \frac{q}{\varepsilon_z \varepsilon_o} \frac{N}{k_o},$$

$$k_o \simeq \left[\frac{N q^2}{\varepsilon_z \varepsilon_o k_B T}\right]^{1/2}, \tag{3.27}$$

where N is the number density of charge carriers avaliable for migration, [3.4], equal to the smaller of (N_A/N_D) or $[(N_D - N_A)/N_D]$. Note that N is a characteristic constant of any given material sample but k_o may differ with direction due to possible anisotropy of the relative permittivity, ε.

3.2.3 Dynamic self–diffraction.

The previous discussions on linear in generation/recombination and saturation regimes neglected to consider any possible *dynamic feedback* incurred during the initial transient stage, prior to reaching the steady state. As the induced electric field and hence the phase volume hologram develop, the incident writing beams may self–diffract off their own grating. This will modify the illuminating intensity and phase profiles accordingly, causing a re–adjustment of the developing hologram. Consequently the material and incident light interact in a dynamic manner via this feedback mechanism, ultimately creating both complicated phase volume holographic and intensity profiles throughout the volume of the material in the steady state.

The phenomenon of self–diffraction invokes energy exchange between the two writing beams, reference R and signal S, Fig. 3.1. The PR writing mechanism pseudo satisfies the Bragg matching condition for self–diffraction off the induced phase volume hologram. Consequently the signal beam, S, is diffracted, S′, along the direction of the reference beam R and similarly the reference is diffracted, R′, along

the direction of the signal. These two observations are schematically illustrated in Figs. 3.5a) and b) for diffraction of the reference and signal beams respectively. The figures are generalised to accomodate the phase shift, ϕ, between the writing intensity profile and induced hologram, where ϕ is relative to the fringe separation Λ.

It is observed in Fig. 3.5a) that the wavefront of the diffracted reference beam, R', is in advance of its corresponding signal wavefront, S. The associated relative phase shift can be shown to be $-\phi$, now relative to the wavelength λ. R' also acquires an additional intrinsic phase shift of $\pi/2$ on Bragg diffraction which is a consequence of energy conservation between the two coupled waves. The resulting nett phase shift is $(\pi/2 - \phi)$. The diffracted signal, S' Fig. 3.5b), lags behind its corresponding reference by $+\phi$ to yield a nett phase shift of $(\pi/2 + \phi)$.

The earlier discussions on linear generation/recombination and saturation regimes illustrated that ϕ can take any value between $-\frac{\pi}{2}$ and $\frac{\pi}{2}$. For low spatial frequencies and *diffusion* dominance and for high spatial frequencies the phase $\phi = \pi/2$. Hence S and R' are in phase and constructively interfere while S' and R are out of phase by π and destructively interfere, the nett result being that energy is transferred from the reference beam into the signal. This phenomenon of energy exchange is more commonly referred to as two beam coupling, TBC, or coherent light amplification. The direction of energy exchange is always in the direction of the original ϕ phase shift which is dictated by the crystallographic nature and photoconductive type of the material.

The energy exchange or TBC between signal and reference beams can be extensive, resulting in one of the beams being greatly attenuated at the expense of the other. A complete and rigorous description of PR beam coupling would have to accommodate the dynamic feedback between light and matter and require the simultaneous solution of the coupled transport equations with Maxwell's wave equation in both transient and steady state regimes. This analysis would be clearly nontrivial and highlights the considerable difference between dynamic and static (fixed) holographic gratings.

The coupled–wave theory of Kogelnik [3.5] for static holographic gratings was adapted to analyse TBC in PR materials. Consider two mutually coherent light

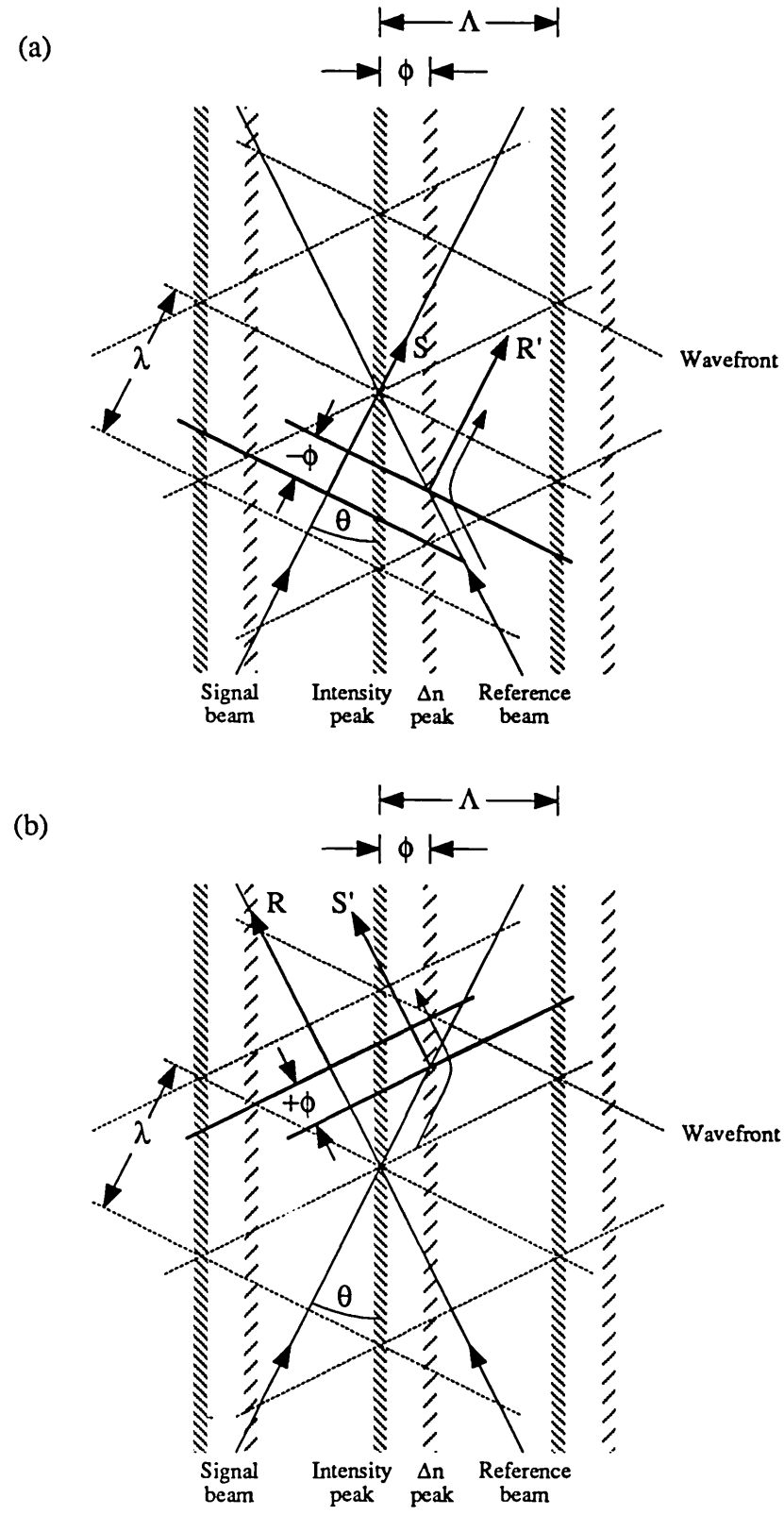


Figure 3.5 Self-diffraction of signal and reference beams off a ϕ phase shifted induced holographic grating.

beams, reference R and signal S, entering the PR material symmetrically as shown in Fig. 3.1. Assuming for simplicity that both beams are *s* polarised, polarised perpendicular to the plane of incidence, their two fields can be expressed as

$$\mathbf{R} = \mathrm{R(x)}\exp[i(\omega t - \varrho.\mathbf{r} + \phi_{\mathrm{R}}(\mathrm{x}))\hat{\mathbf{e}}_{\mathrm{y}} \tag{3.28a}$$

and

$$\mathbf{S} = \mathrm{S(x)}\exp[i(\omega t - \varsigma.\mathbf{r} + \phi_{\mathrm{S}}(\mathrm{x}))]\hat{\mathbf{e}}_{\mathrm{y}}, \tag{3.28b}$$

where the electric field vectors, **R** and **S**, are parallel to the unit vector in the y direction, $\hat{\mathbf{e}}_{\mathrm{y}}$. The resultant electric field, **E**, and intensity, I, are given by

$$\begin{aligned}\mathbf{E} = {} & \mathrm{R(x)}\exp[i(\omega t - \varrho.\mathbf{r} + \phi_{\mathrm{R}}(\mathrm{x}))]\hat{\mathbf{e}}_{\mathrm{y}} \\ & + \mathrm{S(x)}\exp[i(\omega t - \varsigma.\mathbf{r} + \phi_{\mathrm{S}}(\mathrm{x}))]\hat{\mathbf{e}}_{\mathrm{y}},\end{aligned} \tag{3.29}$$

and

$$\mathrm{I} = \mathrm{I_o}\left[1 + \mathrm{M}\cos[\mathbf{k}.\mathbf{r} + (\phi_{\mathrm{R}}(\mathrm{x}) - \phi_{\mathrm{S}}(\mathrm{x}))]\right]. \tag{3.30}$$

We wish to solve Maxwell's wave equation for a lossless medium,

$$\nabla^2\mathbf{E} - \frac{1}{\mathrm{c}^2}\frac{\partial^2(\mathrm{n}^2\mathbf{E})}{\partial t^2} = 0, \tag{3.31}$$

in the slowly varying amplitude and phase approximations, for the steady state refractive index (RI) profile

$$\mathrm{n} = \mathrm{n_o} + \mathrm{n_{dc}(x)} + \mathrm{n_c(x)}\cos\mathbf{k}.\mathbf{r} + \mathrm{n_s(x)}\sin\mathbf{k}.\mathbf{r}, \tag{3.32}$$

where only the d. c. and fundamental Fourier components of Δn have been considered as extracted from Eqs. (3.17) and (2.40). The analysis generates the following coupled differential equations, reference [3.1] and Appendix D, as follows

$$\frac{\mathrm{dI_R}}{\mathrm{dx}} + \frac{\alpha}{\cos\theta}\mathrm{I_R} = -\frac{\Gamma}{\cos\theta}\frac{\mathrm{I_R I_S}}{\mathrm{I_o}}, \tag{3.33a}$$

$$\frac{\mathrm{dI_S}}{\mathrm{dx}} + \frac{\alpha}{\cos\theta}\mathrm{I_S} = \frac{\Gamma}{\cos\theta}\frac{\mathrm{I_R I_S}}{\mathrm{I_o}} \tag{3.33b}$$

and

$$\frac{\mathrm{d}\Phi}{\mathrm{dx}} = \frac{\gamma}{\cos\theta}\frac{\mathrm{I_R} - \mathrm{I_S}}{\mathrm{I_o}}. \tag{3.33c}$$

The intensity gain and phase conversion factors, Γ and γ respectively, are given by

$$\Gamma = 2\delta\frac{\mathrm{E'_{sc}}}{\mathrm{M}}\sin\Phi, \tag{3.34a}$$

$$\gamma = \delta\frac{\mathrm{E'_{sc}}}{\mathrm{M}}\cos\Phi, \tag{3.34b}$$

where δ and the RI modulation, Δn, are

$$\delta = -\frac{\pi}{\lambda} n_o^3 r_{eff},$$

$$\Delta n = -\frac{1}{2} n_o^3 r_{eff} E'_{sc},$$

The angle $\Phi = \phi_R - \phi_S + \phi$ is the phase of the induced grating. The coupled nature of Eqs. (3.33a) and (3.33b) reflects that the energy exchange between the beams is due to the $\pi/2$ shifted component of the PR grating. The intensity gain factor, Γ, is associated with $\sin\Phi$, Eq. (3.34a), which confirms the earlier discussion on TBC by self-diffraction, Fig. 3.5. Equation (3.33c) illustrates that in addition to the beams exchanging energy they can also exchange phase. The phase exchange arises from the unshifted grating component, γ associated with $\cos\Phi$ Eq. (3.34b), and results in the planes of equal intensity and RI being curved through the materials depth.

Equations (3.33a), (3.33b) and (3.33c) can be readily solved in the absence of absorption, [3.1] and Appendix D, to yield,

$$I_R = \frac{I_o}{[1 + \beta_o \exp(\Gamma x)]}, \tag{3.35a}$$

$$I_S = \frac{I_o \beta_o \exp(\Gamma x)}{[1 + \beta_o \exp(\Gamma x)]}, \tag{3.35b}$$

$$\Phi(x) = \Phi_o + \frac{\gamma}{\Gamma} \ln \frac{[1 + \beta_o]^2 \exp(\Gamma x)}{[1 + \beta_o \exp(\Gamma x)]^2}, \tag{3.35c}$$

where β_o and Φ_o are the incident signal to reference beam intensity ratio, I_{So}/I_{Ro}, and grating phase angle, $\phi_R(0) - \phi_S(0) + \phi$, respectively. The summation of I_R and I_S, Eqs. (3.35a) and (3.35b), yields the constant total intensity I_o which is consistent with transmission through an absorption free medium.

The intensity and RI profiles extending through the volume of the PR material can be deduced from Eqs. (3.30) and (3.32) using Eqs. (2.40), (3.17) and (3.35a), (3.35b) and (3.35c). The resultant expressions are given by

$$I(x,z) = I_o + 2\sqrt{I_R(x) I_S(x)} \cos[kz + \Phi(x) - \phi] \tag{3.36}$$

and

$$n(x,z) = n_o(1 + \delta) + n_o^3 r_{eff} \frac{\sqrt{I_R(x) I_S(x)}}{I_o(1 + \beta/sI_o)} \sqrt{E_A^2 + E_D^2} \cos[kz + \Phi(x)], \tag{3.37}$$

where $\delta = n_{dc}/n_o$. The two dimensional intensity profile of Eq. (3.36) was calculated, using Eqs. (3.35a), (3.35b) and (3.35c), and is shown in Fig. 3.6. The fringe contrast variation and bending have been exaggerated to illustrate the effects of energy and phase exchanges respectively.

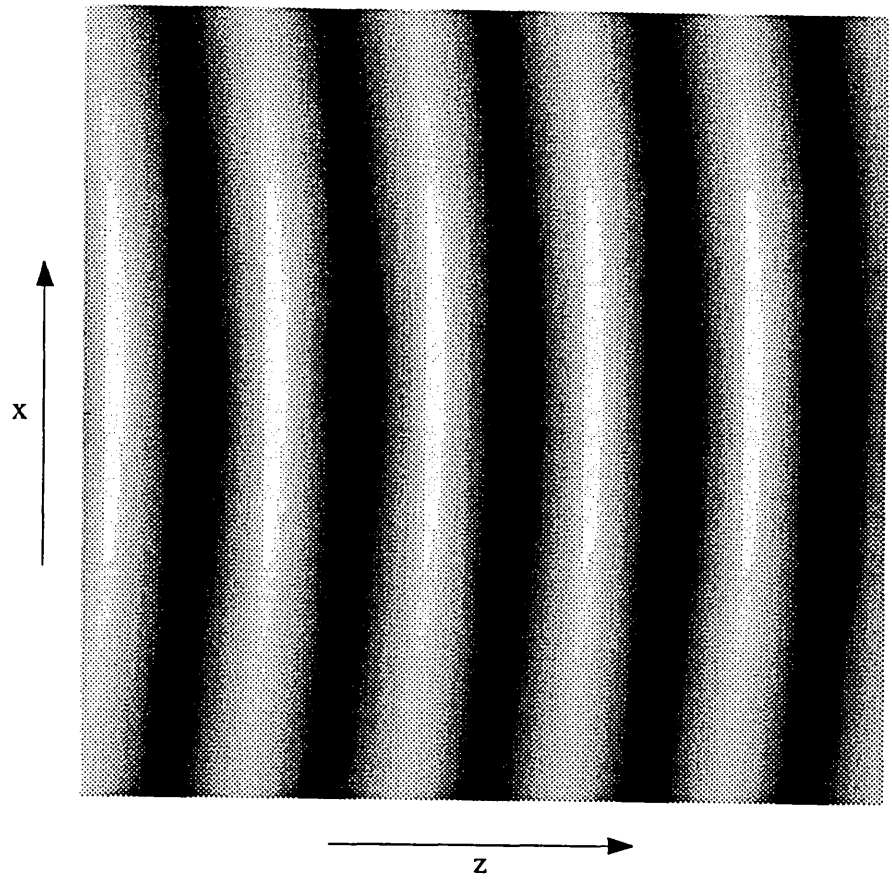


Figure 3.6 Fringe contrast variation and bending in a dynamic PR grating.

From the earlier discussion on the linear in generation/recombination regime, section 3.1, the dominant transport mechanism will greatly influence the form of dynamic feedback incurred. For *diffusion* dominance the phase $\phi \sim \pi/2$, $\Gamma \gg \gamma$ and hence energy is but phase is not exchanged between the beams. For *drift* dominance the phase $\phi \sim 0$, $\Gamma \ll \gamma$ and the converse is true, energy is not but phase is exchanged. The associated intensity profiles are shown in Figs. 3.7a) and b) for *diffusion* and *drift* dominance and illustrate straight fringes with varying contrast and slanted fringes with constant contrast respectively.

It is important to note that a PR material without absorption loss is inconceivable. The generation of a free charged carrier by photoexcitation, Fig. 2.1, obviously involves the absorption of light, Figs.2.5,2.7,2.9,2.11 Equations (3.35a) and (3.35b) are amended as follows

$$I_R = \exp(-\alpha x/\cos\theta)\frac{I_o}{[1+\beta_o \exp(\Gamma x)]}, \qquad (3.38a)$$

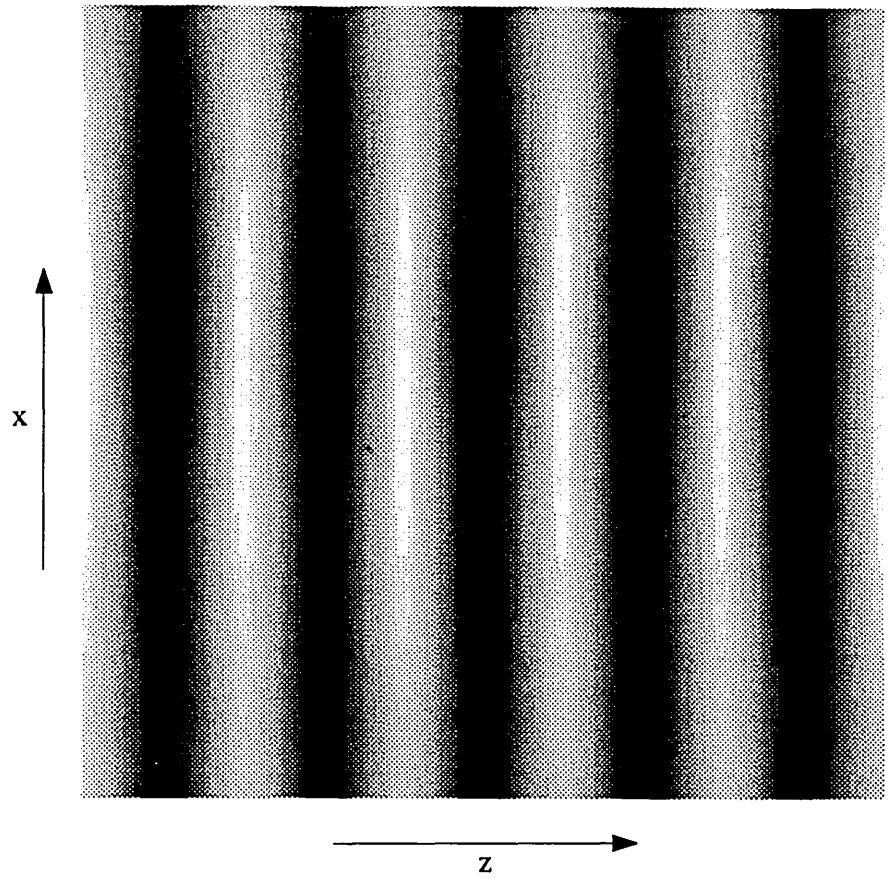


Figure 3.7a) Contrast variation of straight fringes for a *diffusion* dominated transport mechanism.

$$I_S = \exp(-\alpha x/\cos\theta)\frac{I_o\beta_o\exp(\Gamma x)}{[1+\beta_o\exp(\Gamma x)]}, \tag{3.38b}$$

where α is the characteristic absorption coefficient.

The optimal thickness of PR material, d_{opt}, for signal beam amplification is evaluated using $dI_S(x)/dx|_{d_{opt}} = 0$ and given by [3.6]

$$d_{opt} = \frac{1}{\Gamma}\ln\left[\frac{(\Gamma/\alpha - 1)}{\beta_o}\right]. \tag{3.39}$$

The diffraction efficiency, η, defined as the ratio of diffracted and incident beam intensities, was derived by Kogelnik [3.5] for plane phase volume holographic gratings to be

$$\eta = \exp(-\alpha d/\cos\theta)\sin^2\left(\frac{\pi\Delta n d}{\lambda\cos\theta}\right), \tag{3.40}$$

where d is the hologram thickness and θ the Bragg angle corresponding to the incident wavelength λ. The factor $\exp(-\alpha d/\cos\theta)$ accomodates for uniform background absorption.

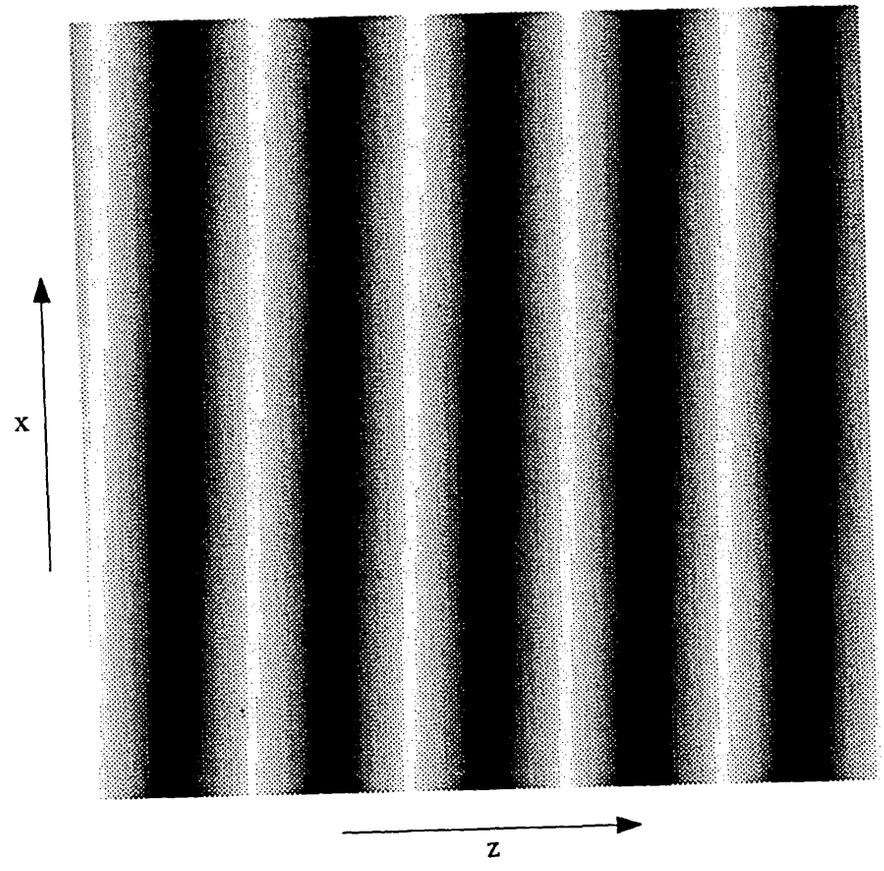


Figure 3.7b) Curved fringes of constant contrast for a *drift* dominated transport mechanism.

The diffraction efficiency for a dynamic hologram was derived by Kukhtarev *et al* [3.1] to be

$$\eta = \exp(-\alpha d/\cos\theta)\frac{2\beta_o \exp(\Gamma d/2)\,[\cosh(\Gamma d/2) - \cos(\gamma d)]}{(1+\beta_o)[1+\beta_o \exp(\Gamma d)]}, \qquad (3.41)$$

where the probe beam is assumed only to read the dynamic hologram and not to affect the induced RI profile by virtue of its small intensity.

In the limit of an unshifted grating, $\Gamma = 0$, Eq. (3.41) reduces to the much simpler Eq. (3.40). For a $\pi/2$ shifted grating the diffraction efficiency becomes

$$\eta = \exp(-\alpha d/\cos\theta)\frac{\beta_o[\exp(\Gamma d/2) - 1]^2}{(1+\beta_o)[1+\beta_o \exp(\Gamma d)]}. \qquad (3.42)$$

3.3 Experimental Procedure and Results.

Experimental investigations were performed using both the three barium titanate samples, $BaTiO_3^{\#1}$, $^{\#2}$ and $^{\#3}$ and the cerium doped strontium barium niobate sample, $SBN{:}60^{\#1}$. Their corresponding absorption spectra are shown in Figs. 2.5 and 2.7 respectively.

The laser sources were a Spectra Physics 2020 (3W *cw* all lines) argon ion, operating on $\lambda = 514.5$nm, for writing the PR gratings and a Hughes 3222H–PC (5mW *cw* @ $\lambda = 632.8$nm) helium neon to probe the gratings with minimal optical disturbance. All the experiments were conducted on an Ealing Electro–optics plc steel honeycomb optical table mounted on vibration isolation support. A combination of conventional optical components and United Detector Technology model–350 and Newport Corporation model–815 photometers, were used. The experiments conducted were designed to evaluate the principle PR material characteristics of both $BaTiO_3$ and SBN:60. Measurements were made in both steady state and transient regimes using the experimental arrangement schematically illustrated in Fig. 3.8.

Both materials display negative uniaxial birefringence with the characteristic optical axis, positive z direction, denoted by +c. For all the experiments conducted the +c axis lay in the plane of incidence and hence the *s* and *p* polarisations were more conveniently expressed as *ordinary* and *extra–ordinary* polarisation states respectively. The combination of polarising cube beamsplitter and two $\lambda/2$ waveplates served to act as a variable beamsplitter, preserving the *ordinary* polarisation of the two writing beams, $\lambda = 514.5$nm, and maintaining a constant total intensity, $I_S + I_R = constant$. *Ordinary* polarisation was chosen to quench the extensive beam fanning incurred by *extra–ordinary* polarised light which would have served only to complicate the optical situation and distort the measurements made. The probe beam, $\lambda = 632.8$nm, was *extra–ordinary* polarised to exploit the much stronger r_{42} and r_{33} linear electro–optic coefficients of $BaTiO_3$ and SBN:60 respectively. The beam was angularly offset to locate the Bragg matching condition which satisfied both wavelength and polarisation criteria.

By convention the signal beam always gained energy at the expense of the reference beam. The p–type photoconductivity of $BaTiO_3$ insured that energy exchange was along the same direction as the +c axis and hence consistent with Fig. 3.8. However cerium doped SBN:60 is n–type photoconducting, Eq. (2.42), and hence the +c axis was reversed in sense to that in Fig. 3.8.

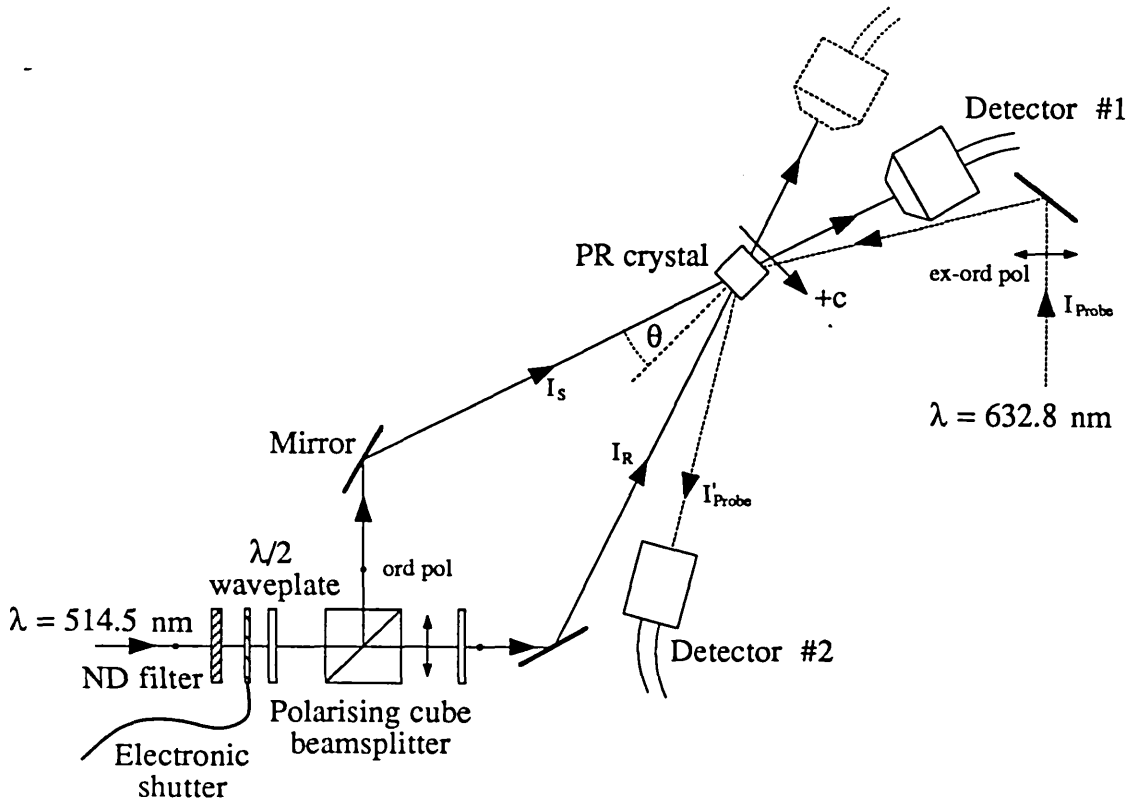


Figure 3.8 Schematic diagram of experimental apparatus used for TBC investigations in both steady state and transient regimes.

3.3.1 Steady state measurements.

The steady state measurements were subdivided into three. Energy exchange or TBC was measured as a function of the induced grating wavenumber, k, the induced grating diffraction efficiency, η, was measured as a function of the incident and exit beam intensity ratios, β_o and β_{exit} respectively and finally, coherent light amplification of a two dimensional image was demonstrated using barium titanate, *extra-ordinary* polarised light and a modified optical arrangment.

Beam coupling, defined as the intensity change of the signal beam, ΔI_S, divided by the initial intensity of the signal, I_S, $\Delta I_S/I_S$, was measured in the absence of the probe beam, $I_{probe} = 0$, and for a fixed incident beam ratio, $\beta_o = 1$ i.e. equal writing intensities. The grating wavenumber, k, is related to the external writing beam crossing angle, 2θ, by

$$k = 2\frac{\omega}{c}\sin\theta, \tag{3.43}$$

and normalised by the wavenumber of the light in the medium, $n\omega/c$, to yield

$$\frac{k}{(n\omega/c)} = \frac{2}{n}\sin\theta. \tag{3.44}$$

Using detector$^{\#1}$, alternating between the two locations indicated, Fig. 3.8, the intensity changes of signal and the reference beams were measured for reference and signal respectively, turned on and off. The total incident optical power and intensity were 6mW and 1.2Wcm^{-2} respectively for a writing beam diameter of 0.8mm. The beam crossing angle, 2θ, was varied from 5.5° to 77.5°.

The experimental results for samples $^{\#2}$ and $^{\#3}$ of $BaTiO_3$ and $^{\#1}$ of cerium doped SBN:60 are shown in Figs. 3.9 and 3.10 respectively and tabulated in Appendix E.

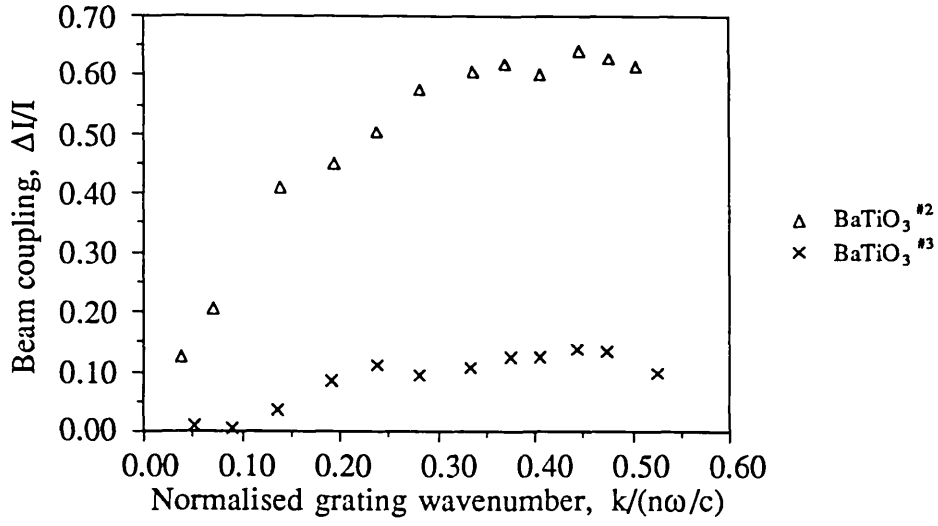


Figure 3.9 Beam coupling, $\Delta I/I$, versus normalised wavenumber, $k/(n\omega/c)$, for $BaTiO_3$.

The principle observation made from the results is that for all three data sets the beam coupling initially rises, rolls over and finally falls at large k values. The peak values of $\Delta I/I$ for $BaTiO_3^{\#2}$, Δ, and SBN:60$^{\#1}$, ▪ , are comparable; however their locations differ considerably. The locations are estimated to be 0.44 and 0.12 $(n\omega/c)$ for $BaTiO_3^{\#2}$ and SBN:60$^{\#1}$ respectively. The corresponding number densities of charge avaliable for migration are calculated using Eq. (3.27). The *ordinary* RI, n_o, @ λ = 514.5nm and static dielectric constant along the z direction, ε_z, are 2.488 and 135 respectively for $BaTiO_3$. Assuming an ambient

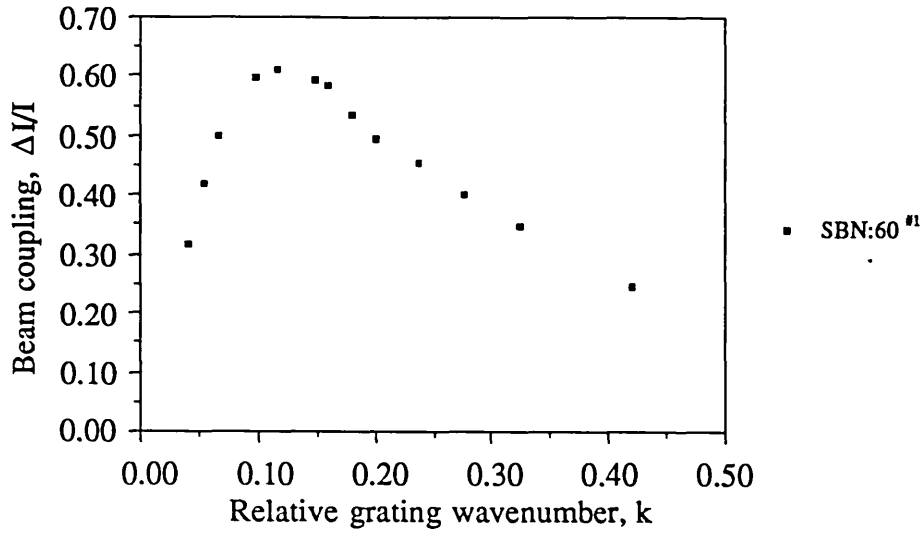


Figure 3.10 Beam coupling, ΔI/I, versus normalised wavenumber, k/(nω/c), for cerium doped SBN:60.

temperature of 293K (20°C), Eq. (3.27) predicts an available number density of $\sim 3.4 \times 10^{16}\text{cm}^{-3}$ which is similar to the number density of $1.9 \times 10^{16}\text{cm}^{-3}$ quoted in reference [3.4]. Similarly for cerium doped SBN:60, using $n_o \sim 2.384$ @ $\lambda = 514.5\text{nm}$ and $\varepsilon_z = 820$, a number density of $\sim 1.4 \times 10^{16}\text{cm}^{-3}$ is deduced. The maximum induced electric field amplitudes supported by the number density limits can be approximated by Eq. (3.24). Substituting the corresponding k_o values, peak electric fields of $\sim 3.37\text{kVcm}^{-1}$ and $\sim 0.88\text{kVcm}^{-1}$ are calculated for $BaTiO_3^{\#1}$ and SBN:60$^{\#1}$ respectively.

The symmetric optical configuration and *ordinary* polarisation of the writing light beams exploit their relatively small r_{23} linear electro-optic coefficients and yields an induced RI modulation, Δn, given by Eq. (2.47b),

$$\Delta n_y \simeq -\frac{1}{2} n_o^3 r_{23} E_z. \tag{3.45}$$

For $BaTiO_3$ the r_{23} linear electro-optic coefficient has a value of 8pmV^{-1}, Table 2.II, and hence Δn is calculated to be 2.08×10^{-5}. The similarity in peak ΔI/I for both materials indicates that the cerium doped SBN:60 supports a RI modulation of comparable size, suggesting that their difference in peak induced electric field amplitudes is compensated by SBN:60 having a larger r_{23} coefficient.

The transition from the linear in generation/recombination regime to saturation is most evident in Fig. 3.10 for the SBN:60. The beam coupling response appears

initially linear in k followed by a 1/k dependence, the same response predicted for the induced electric field for *diffusion* dominance, Fig. 3.4.

The second crystal of $BaTiO_3$, sample $^{\#3}$, displayed a greatly reduced coupling strength, × Fig. 3.9. The precise cause for the anomalous behaviour is not known but the corresponding absorption spectra, × Fig. 2.5, suggests that the number density of participating PR species was small in comparison to the other samples, $^{\#1}$ and $^{\#2}$. This would result in early saturation, restricting greatly the magnitude of the induced electric field and hence Δn of the phase grating.

The diffraction efficiency, η, of the induced grating was measured as a function of the incident beam ratio, β_o, for a fixed grating wavenumber, k. The induced grating was constantly monitored by the low intensity Bragg matched probe beam, I_{Probe}. The diffracted intensity, I'_{Probe}, was measured with detector$^{\#2}$ and used to calculate η. In addition, detector$^{\#1}$, alternating between the two indicated locations, measured the writing beam intensity ratio on exit from the sample, β_{exit}. The total intensity, I_o, of writing beams was held fixed at $1.2 Wcm^{-2}$ while their incident ratio, β_o, was varied from 0.012 to 454. The writing beam external crossing angle, 2θ, was 40° corresponding to normalised grating wavenumbers of ~ 0.275 and $\sim 0.287(n\omega/c)$ for $BaTiO_3$ and SBN:60 respectively. The incident probe beam optical power and intensity were fixed at 0.9mW and $0.3 Wcm^{-2}$ respectively for a probe diameter of 0.6mm. The experiments were conducted using $^{\#1}$ samples of both materials and their results are shown in Figs. 3.11 and 3.12 respectively and tabulated in Appendix E.

Both data sets display very similar behaviour with comparable peak diffraction efficiencies accompanyed by $\beta_o < 1$ and $\beta_{exit} > 1$. The corresponding incident and exit interference fringe contrasts, M_o and M_{exit}, at the peak η were found to be similar, $M_o = 0.96$ (0.96) and $M_{exit} = 0.97$ (0.99) for $BaTiO_3^{\#1}$ (SBN:60$^{\#1}$). This observation suggests that the peak in η is accompanied by a symmetric variation in fringe contrast across the samples with unit modulation near the centre and illustrates the significance of energy exchange on diffraction efficiency.

The symmetric optical configuration of the writing beams and *extra-ordinary* polarisation of the probe beam exploit the larger r_{33} of both materials. The corresponding RI environment experienced by the probe beam was deduced in Appendix A and given by

$$n_{Probe} = [(1/n_o^2 + r_{13}E_z)\sin^2\theta_o + (1/n_e^2 + r_{33}E_z)\cos^2\theta_o]^{-1/2} \qquad (3.46)$$

where θ_o is the Bragg matching angle of the probe beam. For $BaTiO_3$ the linear

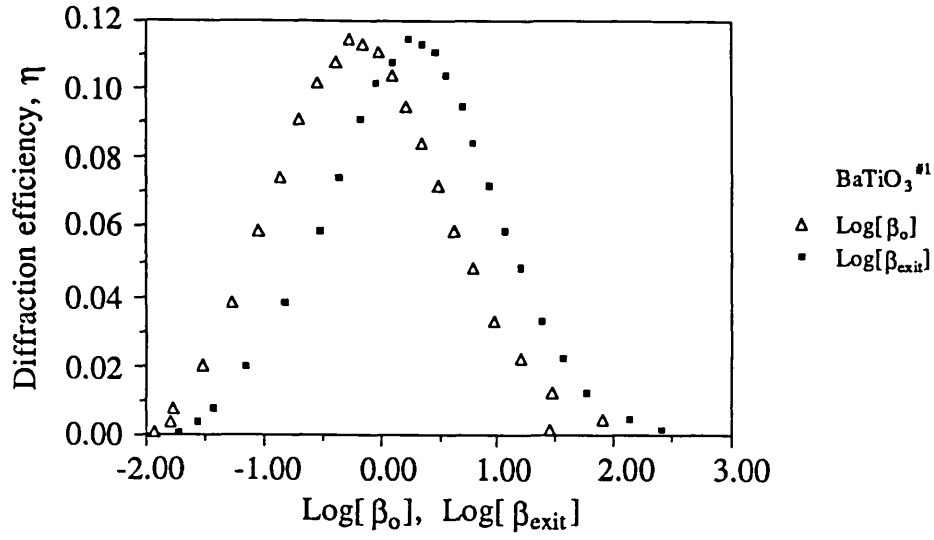


Figure 3.11 Diffraction efficiency versus incident and exit beam ratios, β_o and β_{exit}, for $BaTiO_3$.

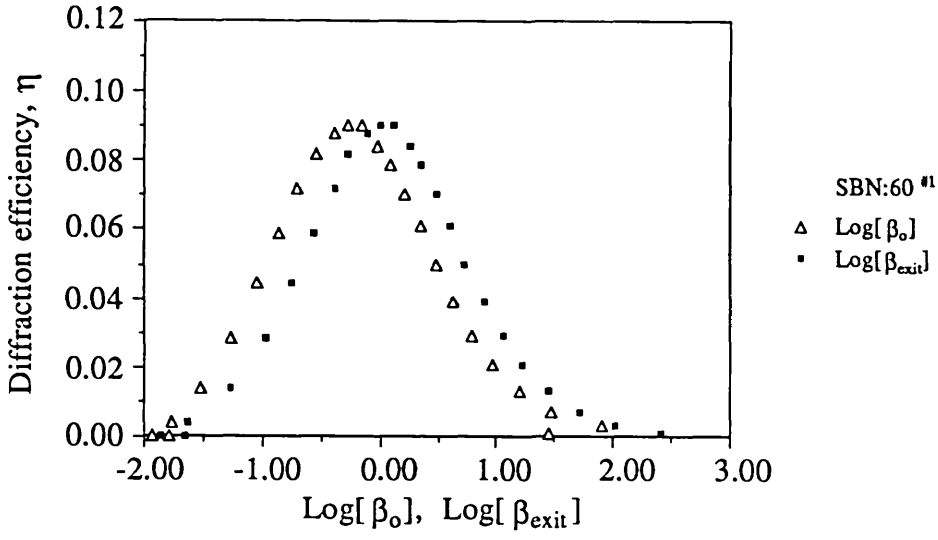


Figure 3.12 Diffraction efficiency versus incident and exit beam ratios, β_o and β_{exit}, for cerium doped SBN:60.

electro-optic coefficients r_{13}, r_{33} and the principal refractive indices n_o, n_e @ $\lambda = 632.8$nm are 8pmV^{-1}, 28pmV^{-1} and 2.413, 2.361 respectively, Table 2.II and 2.III. The external Bragg matching angle was measured as 26°, corresponding to $\theta_o = 10.7°$, and assuming an induced electric field amplitude of 3.0kVcm^{-1} a RI modulation, Δn, of 5.53×10^{-5} was calculated. This value is not large for $BaTiO_3$ as the optical configuration shown in Fig. 3.8 is non-optimal because the induced

electric field is confined to the z axis which does not exploit the dominant r_{42} (r_{51}) electro-optic coefficient of the material. For SBN:60 the $r_{33} = 420 pmV^{-1}$, Table 2.II, is the dominant coefficient and hence the optical configuration/probe beam polarisation combination is optimal. However the induced RI modulation, Δn and hence η are restricted by the lower induced electric field amplitude supported by the material as deduced by the previous TBC experiment.

Two beam coupling can be employed to coherently amplify an image bearing signal beam and has been proposed as one potential application of this phenomenon. Image amplification was demonstrated using $BaTiO_3^{\#1}$, *extra-ordinary* polarised writing beams, a spiral resolution chart and the modified optical arrangement shown in Fig. 3.13.

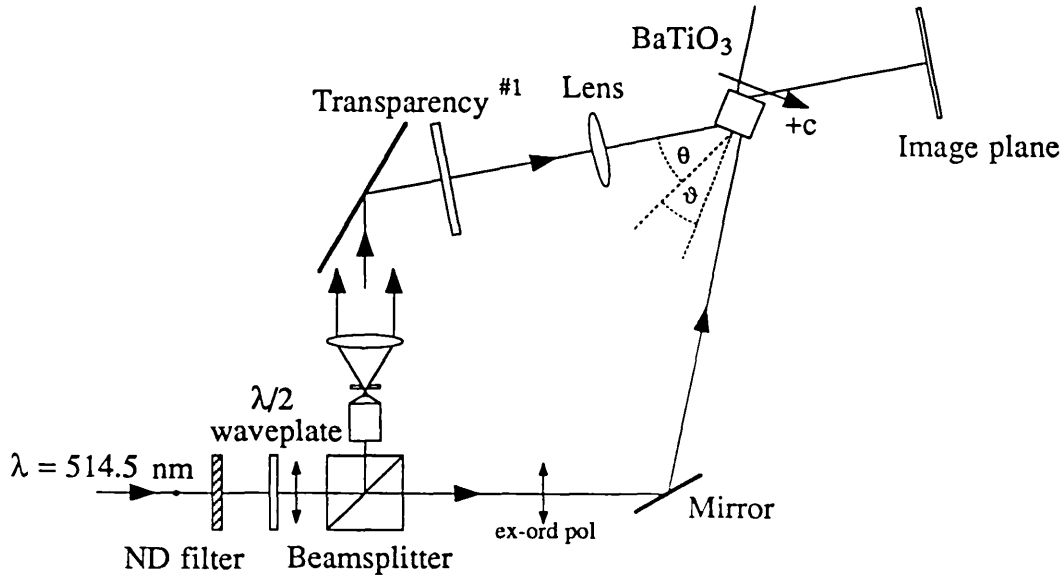


Figure 3.13 Schematic diagram of experimental apparatus used for coherent amplification of an image bearing signal beam.

The external crossing angle, 2θ, of the writing beams and angle between front face normal of crystal and bisecting axis of the beams, ϑ, were 55° and 17° respectively.

An asymmetric optical configuration was adopted to exploit the much larger r_{42} electro-optic coefficient of $BaTiO_3$. The signal beam was first spatially filtered and then collimated before passing through transparency#1, a spiral resolution chart. The lens imaged the chart through the $BaTiO_3$ crystal on to the image plane. The incident intensity ratio of the signal to reference beams was estimated to be 1:100 at the crystal with a total optical power of $\sim$ 15mW. The transmitted image before and after amplification is shown in Fig. 3.14 and an intensity gain of 11.7 was measured!

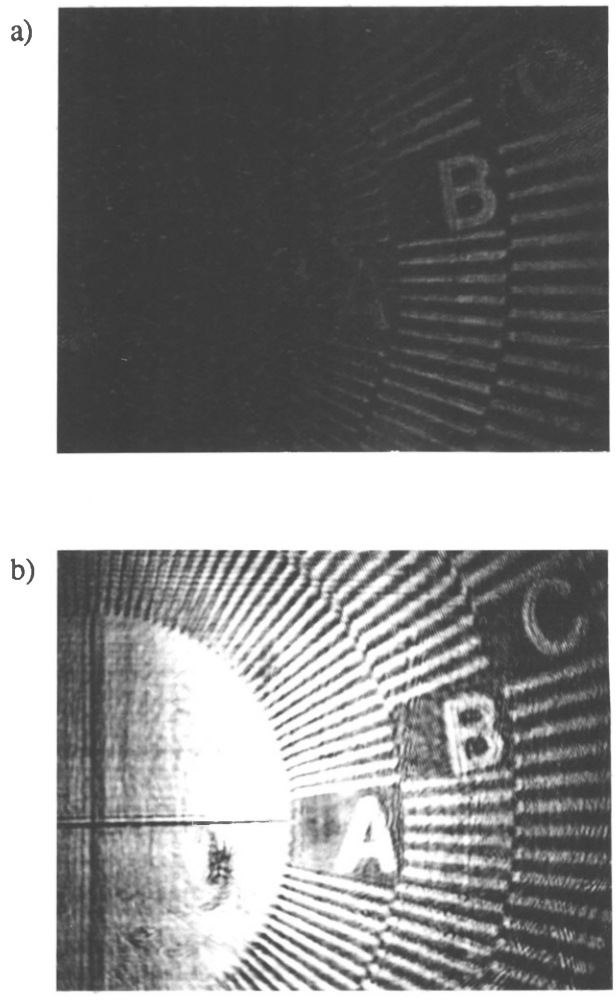


Figure 3.14 Coherent image amplification by two beam coupling; a) original and b) amplified image..

3.3.2 Transient measurements.

The transient measurements were conducted using the apparatus illustrated in Fig. 3.8 and were subdivided into two. The characteristic rise time, τ_{rise}, of the induced grating was measured as a function of the total incident writing intensity, I_o, and the characteristic decay time, τ_{decay}, of the grating was measured as a function of the probe beam intensity, I_{Probe}. The external crossing angle of the writing beams, 2θ, was fixed at 40° and the intensity of the diffracted probe beam, I'_{Probe}, measured using detector$^{\#2}$, monitored the current diffraction efficiency, η, of the grating with time. The progammable electronic shutter controlled the switching on and off of the writing beams.

The characteristic rise time, τ_{rise}, was measured as a function of the total writing intensity, I_o, for a fixed incident writing beam ratio, β_o, of unity. The low powered, *extra–ordinary* polarised, probe beam had an incident intensity, I_{Probe}, of $0.04 Wcm^{-2}$ and sample $BaTiO_3^{\#1}$ was investigated. Before each measurement the sample was uniformly illuminated with light to optically erase any *old* gratings and return the bulk material back to its homogeneous state. At t=0 the writing beams were turned on using the electronic shutter and the diffracted probe beam intensity was recorded as a function of time using detector$^{\#2}$ and a BBC micro computer. A typical data set, o, is presented in Fig. 3.15 for $I_o = 4.81 Wcm^{-2}$. The solid curve, ——, is the best fit by the analytic function

$$I = I_o [1 - \exp(-t/\tau_{rise})] \tag{3.47}$$

and yielded $\tau_{rise} = 0.67$seconds. The same experimental procedure was repeated for different total incident writing beam intensities, I_o, ranging from 0.15 to $4.81 Wcm^{-2}$. In each case the corresponding rise time, τ_{rise}, was deduced and the combined results are presented in Fig. 3.16 and tabulated in Appendix E.

The data points appear to be co–linear with the best fit line given by

$$\tau_{rise} = 1.52 - 1.40 \log(I_o) \tag{3.48}$$

from which the material can be assigned a characteristic grating writing time of 1.52 seconds, corresponding to a total writing intensity of $1 Wcm^{-2}$.

The characteristic decay time, τ_{decay}, of the grating was measured as a function of the incident probe beam intensity, I_{Probe}, at an ambient temperature of 293K (20°C). Prior to each measurement a steady state grating was created with a total writing intensity, I_o, and incident beam ratio, β_o, of $1.2 Wcm^{-2}$ and unity

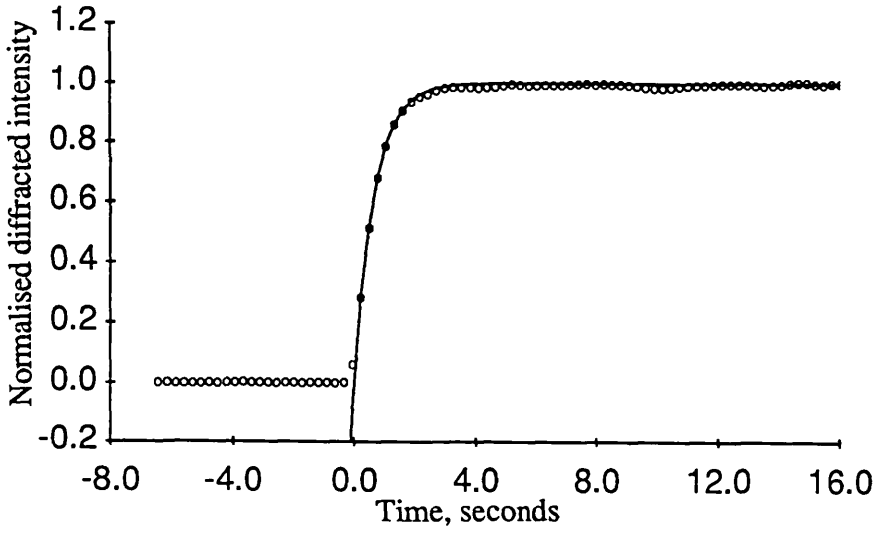


Figure 3.15 Normalised diffracted probe beam intensity, I'_{Probe} versus the grating writing time, t, for $BaTiO_3^{\#1}$.

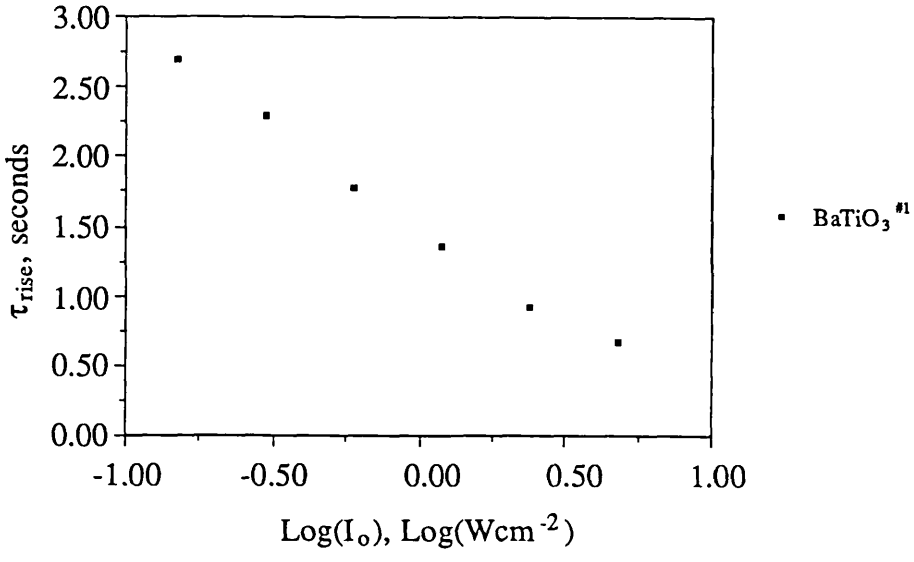


Figure 3.16 Characteristic grating rise time, τ_{rise}, versus the Log of I_o for $BaTiO_3^{\#1}$.

respectively. At t=0 the writing beams were switched off using the shutter and again the diffracted probe beam intensity was recorded in time. A typical data set, o, is presented in Fig. 3.17 for $I_{Probe} = 0.060 Wcm^{-2}$. The solid curve, ——, is the best data fit by the analytic function

$$I = I_o \exp(-t/\tau_{decay}) \tag{3.49}$$

and provided τ_{decay} = 4.38seconds. The same experimental procedure was repeated for different incident probe beam intensities, I_{Probe}, ranging from 4.92×10^{-4} to 1.12Wcm^{-2}. The decay time, τ_{decay}, was deduced in each case and the combined results are presented in Fig. 3.18 and tabulated in Appendix E.

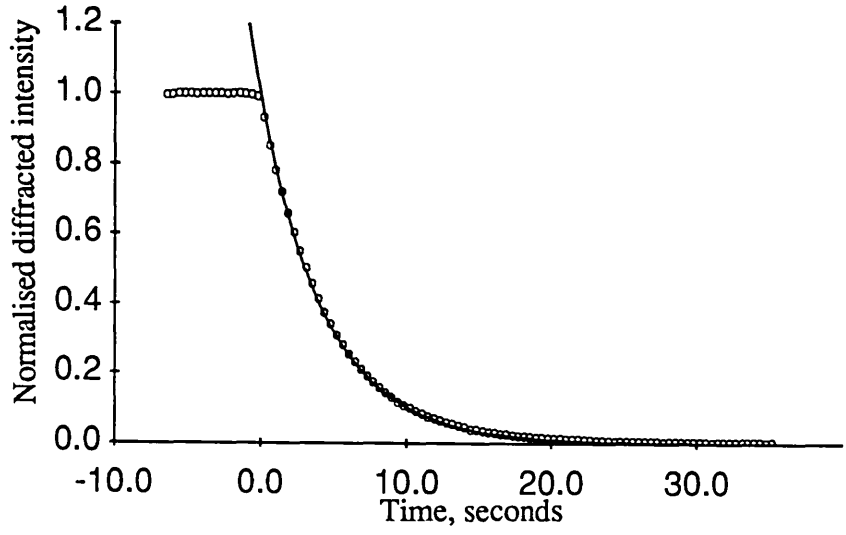


Figure 3.17 Normalised diffracted probe beam intensity, I'_{Probe}, versus grating erasure time, t, for $BaTiO_3^{\#1}$.

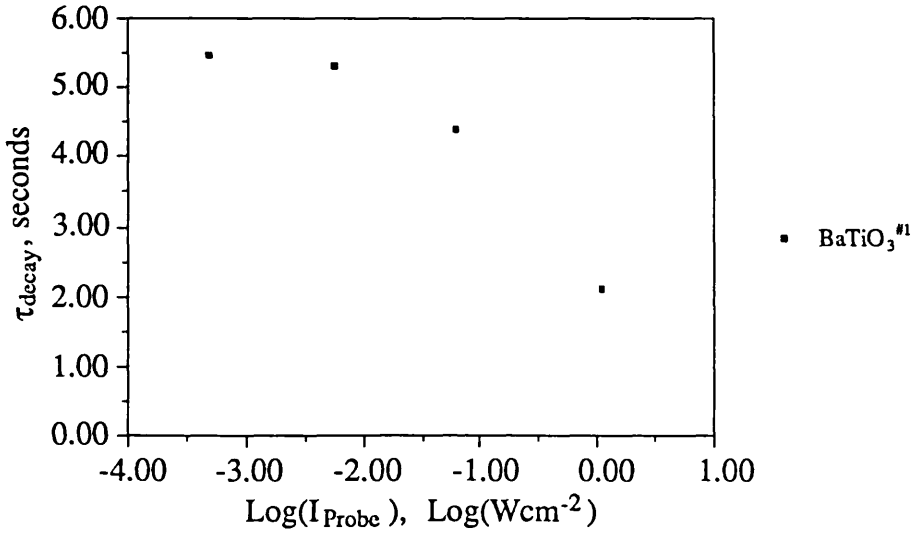


Figure 3.18 Characteristic grating decay time, τ_{decay}, versus the Log of I_{Probe} for $BaTiO_3^{\#1}$.

The data points display a variation in τ_{decay} with I_{Probe}, indicating that the probe beam was disrupting the induced grating by optical erasure, contrary to the earlier assumption. The decay time appears to tend asymptotically to a constant value of ~ 5.75 seconds in the limit as $I_{Probe} \rightarrow 0$. This time can be considered to be the characteristic dark storage time, τ_{dark}, of the material, dependent on the thermal relaxation of the induced grating. The above result is not consistent with previous reported dark storage times of many hours [3.4], this anomaly can not be explained from the limited measurements made and consequently remains a mystery.

Similar transient measurements were made with the cerium doped SBN:60$^{\#1}$ sample. The characteristic rise times, τ_{rise}, were similar to those of the $BaTiO_3^{\#1}$ sample but the dark storage time was very much longer. The SBN:60$^{\#1}$ decay time, τ_{decay}, was again measured as a function of the probe beam intensity, I_{Probe}, and the results are graphically shown in Fig. 3.19 and tabulated in Appendix E.

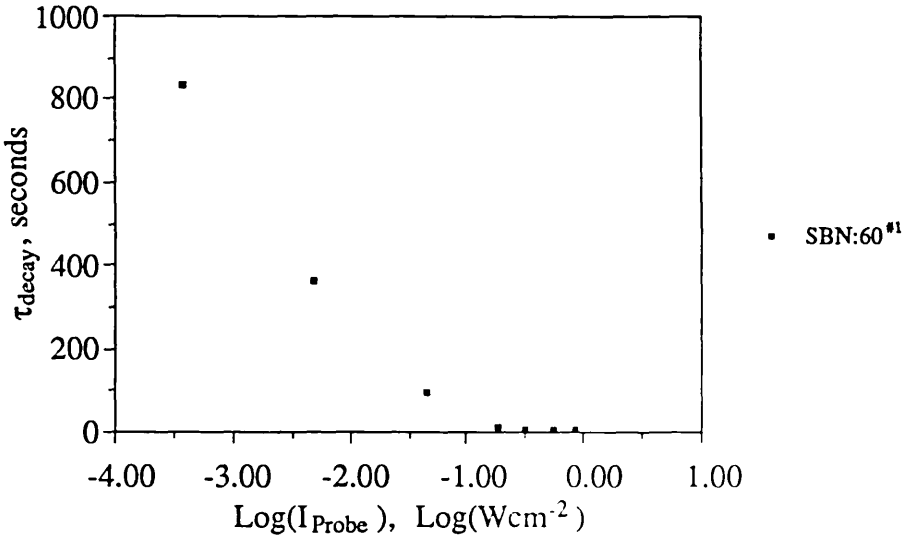


Figure 3.19 Characteristic grating decay time, τ_{decay}, versus the Log of I_{Probe} for cerium doped SBN:60$^{\#1}$.

It is evident from Fig. 3.19 that optical erasure of the grating by the probe beam was still significant even at $I_{Probe} = 3.7 \times 10^{-4}$Wcm^{-2}. The upward trend in the data points, ■ Fig. 3.19, shows no sign of relenting and additional experiments suggested the sample had a characteristic dark storage time, τ_{dark}, of approximately 19 hours!

3.4 Conclusions.

The photorefractive response to a simple one dimensional cosinusoidal intensity profile was rigorously examined for both linear in generation/recombination and saturation regimes. It was deduced that, in general, the illuminating intensity profile and induced refractive index modulation, Δn, were shifted in phase, ϕ. The phase shift, ϕ, was responsible for the exchange of both energy and phase between the two *mixing* waves. The sign and value of ϕ was determined by the sign of the charge carrier and the dominant operational transport mechanism.

Using samples $^{\#1}$ of $BaTiO_3$ and cerium doped SBN:60, steady state and transient measurements were made. With no externally applied d.c. electric field, the transport mechanisms were dominated by *diffusion* and extensive two beam coupling, TBC, was recorded. The available number densities of PR species were estimated to be $3.4\times10^{16}cm^{-3}$ and $1.4\times10^{16}cm^{-3}$ respectively which corresponded to peak electic fields of $3.37kVcm^{-1}$ and $0.88kVcm^{-1}$ capable of being supported by $BaTiO_3^{\#1}$ and cerium doped SBN:$60^{\#1}$ respectively. The characteristic grating rise and decay times, τ_{rise} and τ_{decay}, of the two samples were measured. They both had similar grating rise times with $BaTiO_3^{\#1}$ having $\tau_{rise} = 1.52$seconds for $I_o = 1Wcm^{-1}$. Their dark storage times, τ_{dark}, however differed considerably; the $BaTiO_3^{\#1}$ sample was found to have $\tau_{dark} = 5.75$seconds while the cerium doped SBN:$60^{\#1}$ exhibited $\tau_{dark} = 19$hours!

3.5 References.

[3.1] N.V. Kukhtarev, V.B. Markov, S.G. Odulov, M.S. Soskin and V.L. Vinetskii, "Holographic storage in electro-optic crystals. I Steady state," Ferroelectrics **22**, 949–960 (1979).

[3.2] P. Günter and F. Micheron, "Photorefractive effects and photocurrents in $KNbO_3$: Fe," Ferroelectrics **18**, 27–38 (1978).

[3.3] T.J. Hall, R. Jaura, L.M. Connors and P.D. Foote, "The photorefractive effect–a review," Prog.Quant.Electr. **10**, 77–146 (1985).

[3.4] J. Feinberg, D. Heiman, A.R. Tanguay,Jr. and R.W. Hellwarth, "Photorefractive effects and light-induced charge migration in barium titanate," J.Appl.Phys. **51**, 1297–1305 (1980).

[3.5] H. Kogelnik, "Coupled Wave Theory for Thick Hologram Gratings," Bell.-Syst.Tech.J. **48**, 2909–2947 (1969).

[3.6] P. Günter, "Holography, coherent light amplification and optical phase conjugation with photorefractive materials," Physics Reports **93**, 199–299 (1982).

CHAPTER 4

FOUR WAVE MIXING AND PHASE CONJUGATION.

4.1 Introduction.

Four wave mixing (FWM) is a category of nonlinear optics which describes the interaction of a nonlinear material with three incident electromagnetic fields to generate a fourth field or wave. The fourth wave can differ in both temporal and spatial angular frequencies, ω and $\mathbf{k}$ respectively, from the incident waves but the energy and momentum of the system must be conserved.

Degenerate four wave mixing (DFWM) is the term used to describe the particular FWM nonlinearity where all four fields have the same energy, equivalent to all having the same temporal angular frequency, ω. DFWM is of particular interest in the current discussion as it is one mechanism to generate a *phase conjugate* (PC) field. Optical phase conjugation is a technique that exploits the nonlinear optical response of a material to precisely reverse both the direction of propagation and spatial phase of the wavefront of any arbitrary incident field. The mechanism can be expressed explicitly using the following complex mathematical notation

$$\mathrm{E} = \mathrm{A(r)} \exp[i(\omega t - \mathbf{k}.\mathbf{r})], \tag{4.1a}$$

$$\mathrm{E_{PC}} = \mathrm{A^*(r)} \exp[i(\omega t + \mathbf{k}.\mathbf{r})], \tag{4.1b}$$

where E and $\mathrm{E_{PC}}$ are the incident field and its corresponding PC respectively and their polarisation states have been neglected for simplicity. The conjugating operation acts only on the spatial part of the incident field, reversing both propagating direction and wavefront. The immediate consequence of this is that the PC wave retraces, in a backward direction, the exact path of the incident field, preserving the conjugate nature between the wavefronts at all points between the phase conjugator and source. The phase conjugator is more commonly referred to as a phase conjugate mirror (PCM) due to its unique reflecting characteristic. The remarkable difference between a PCM reflection and a conventional mirror reflection are illustrated in Fig. 4.1. A conventional plane mirror reflection reverses the sign of only the $\mathbf{k}$ vector component normal to the mirror surface, leaving the tangential components unchanged. Hence an incident ray can be redirected arbitrary by suitably tilting the mirror. However a PCM reflection reverses the sign of all the components of $\mathbf{k}$ and hence the ray is redirected back along itself, independent of the angle of incidence. Figure 4.1 illustrates the reflection of

a spherically converging wave at non–normal incidence off a conventional plane mirror, Fig. 4.1a) , and a PCM, b). The conventional mirror reflection obeys conventional mirror geometry and the reflected wavefront continues to converge to a focus at an oblique angle. The PCM reflects the wavefront as a spherically diverging wave travelling back on itself, passing back through the lens and finally focused back down to the original point source. An observer positioned to the left of the lens would observe the conjugate nature between the outward travelling and returned spherical wavefronts, implying the presence of a PCM down beam from his location. However the observer would be unaware of the presence of the lens as the optical transformation it performs is exactly compensated by the returned wave. Replacing the lens by any other lossless optical element or configuration, including severe phase distortion, would not change the observation he makes. Hence a PCM is not only self–aligning but also corrects for any phase distortion introduced by poor quality optical components or a turbulent atmosphere through which the wave propagates.

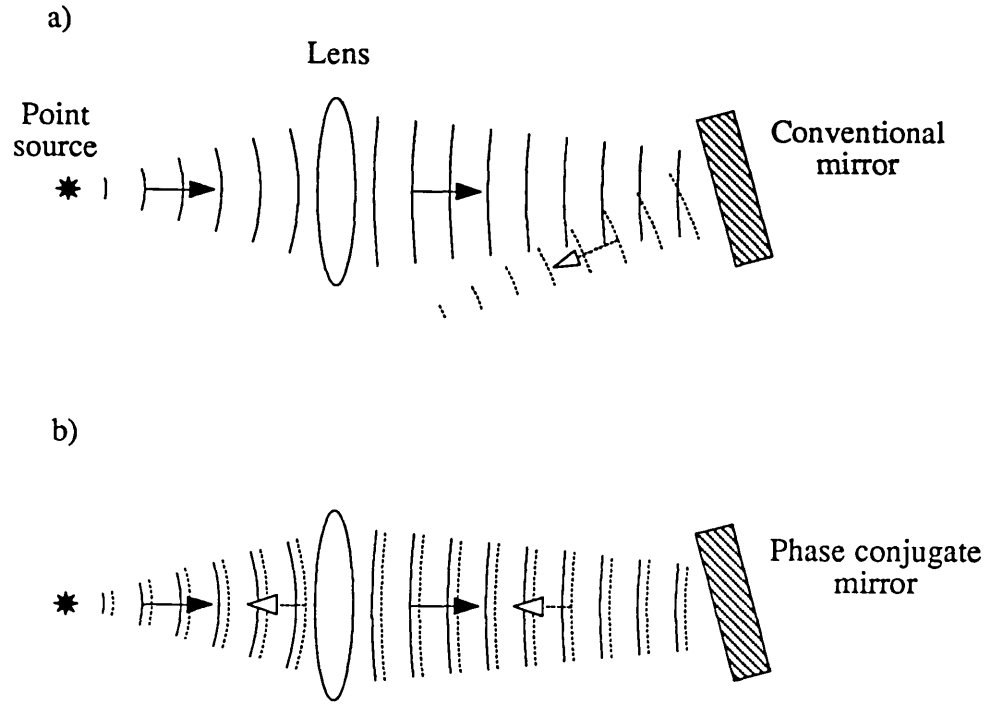


Figure 4.1 Comparison between a) conventional and b) phase conjugate mirror reflections.

The first demonstration of phase distortion correction by phase conjugation was by B.Ya. Zel'dovich *et al* in 1972 [4.1,4.2]. They observed that the back–scattered light from a stimulated Mandel'shtam–Brillouin scattering (SMBS) cell reproduced

the wavefront of the exciting incident radiation even when a phase distorter was deliberately placed in the path of the laser beam. This pioneering work has since generated much interest and activity within the science community with many new techniques and applications to generate and employ phase conjugation demonstrated [4.3]. Phase conjugation has now been demonstrated using other stimulated inelastic scattering mechanisms like Raman [4.4,4.5] and Rayleigh [4.6], and photon echoes [4.7], three wave mixing [4.8,4.9] and DFWM [4.10→4.14]. Applications include image transmission in fibers, self-targeting, novel laser resonator design and image processing to name a few.

4.2 Theory.

Nonlinear optics in general can be analysed using the paraxial wave equation and a Taylor series expansion of the induced polarisation in the medium [4.15]. Assuming a lossless medium the polarisation is given by

$$P_i = \varepsilon_o \chi_{ij} E_j + 2 d_{ijk} E_j E_k + 4 \chi_{ijkl} E_j E_k E_l + \dots \ , \tag{4.2}$$

where P_i is the ith component of the instantaneous polarisation, E_j is the jth component of the instantaneous electric field and summations over repeated indices is assumed. The χ_{ij} term is the linear susceptibility and is characteristic of the linear optical properties displayed by the medium, including index of refraction, absorption and birefringence. The second and third-order nonlinear susceptibilities of the medium are denoted by d_{ijk} and χ_{ijkl} respectively. The second-order nonlinear susceptibility is responsible for second-order or three wave mixing optical nonlinearities, including second harmonic generation, optical rectification, parametric mixing and the linear (Pockels) electro-optic effect, and is exhibited only by materials which lack inversion symmetry. The χ_{ijkl} nonlinearity occurs independent of the material symmetry and is responsible for third-order/FWM optical nonlinearities. These include third harmonic generation, degenerate and non-degenerate FWM, Raman and Brillouin scattering, two photon absorption, dc-induced harmonic generation and the quadratic (Kerr) electro-optic effect.

The third-order nonlinear susceptibility, χ_{ijkl}, is responsible for many demonstrations of PC optics. In particular, exploiting this nonlinearity for phase conjugation by DFWM was first proposed by Yariv *et al* [4.16]. The analysis consisted of solving the nonlinear paraxial wave equation for third-order nonlinearities, a lossless medium and in the nondepleted pumping waves and slowly varying envelope approximations, [4.16] and Appendix F.

The induced nonlinear electric polarisation, P, as defined by Eq. (4.2), is considered to respond both instantaneously and locally to the *driving* electric field, E. The linear and nonlinear components can be interpreted as forced harmonic and anharmonic oscillations respectively of electronic charge within the medium. The nonlinear optical response of photorefractive (PR) materials is neither local nor instantaneous, the phase shift, ϕ, between induced phase volume hologram and incident writing intensity is in general non zero and a transient stage always precedes the steady state. However, phase conjugation by DFWM in PR materials can be characterised by an *effective* third–order nonlinear susceptibility, χ_{ijkl}. This interpretation should be observed with caution as all three families of PR materials employ the linear (Pockels) electro–optic effect to exhibit their optical nonlinearities. However, the linear electro–optic effect is due to the second–order nonlinear susceptibility, $\chi^{(2)}$, and not $\chi^{(3)}$. The linear electro–optic and $\chi^{(2)}$ tensors, r_{ijk}, Chapter 2, and d_{ijk}, Eq. (4.2), respectively, are related as follows [4.15]

$$d_{ijk} = -\frac{\varepsilon_{ii}\varepsilon_{jj}}{4\varepsilon_o} r_{ijk}. \tag{4.3}$$

4.2.1 Phase conjugation by DFWM in PR materials.

The first observation of phase conjugation by DFWM in a PR material was by Huignard *et al* [4.13] using PR bismuth silicon oxide, $Bi_{12}SiO_{20}$. The phase conjugation mechanism can be best interpreted as the simultaneous reconstructing and recording of the induced holographic grating. This holographic approach was first proposed by Yariv [4.17,4.18] and considered the fourth wave generated, E_4, to be the diffracted component of one of the two pumping waves, E_2 in transmission or E_1 in reflection geometries, off the induced phase grating recorded by the interference of the incident signal wave, E_3, and the other pump wave, E_1 or E_2 respectively.

The DFWM geometry is generalised in Fig. 4.2 and all the fields are considered to be plane wave as follows

$$E_j = A_j(r) \exp[i(\omega t - \mathbf{k}_j.\mathbf{r}], \tag{4.4}$$

where j=1, 2, 3 and 4. Assuming the four interacting waves are mutually coherent, each wave will interfere with each of the other three to generate three spatially distinct intensity profiles. Collectively all four waves create six intensity profiles of which there are four spatially distinct. Hence in general four phase gratings are simultaneously induced in the PR material.

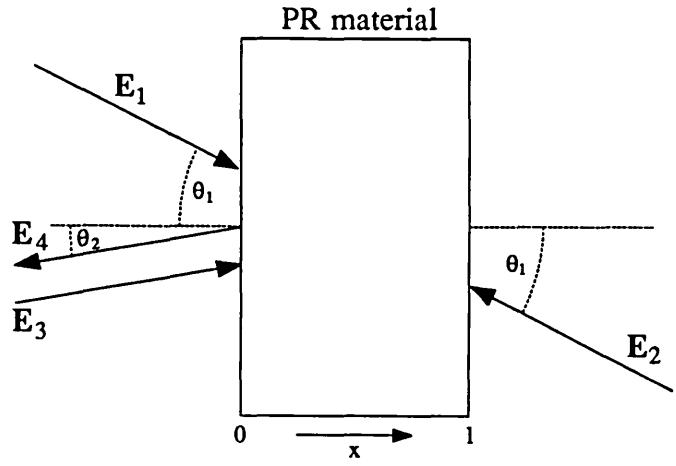


Figure 4.2 Phase conjugation by DFWM in a PR material.

Consider the transmission grating to dominate as dictated by the choice of geometry, polarisation and relative coherence of the four interacting waves. The principal grating is recorded by the intensity profile, I_{13}, of the reference pump and incident signal waves, E_1 and E_3 respectively, and will be $\pi/2$ phase shifted for a *diffusion* dominated transport mechanism. The direction of the phase shift, as discussed in Chapter 3, is dependent on the crystallographic orientation and sign of the dominant charge carrier in the material. Assume the readout pump wave, E_2, to have a coherence length in excess of the interaction length of the medium, l, and to be incoherent with both writing waves, E_1 and E_3. The Bragg diffracted component of E_2, E_4 is coherent with E_2 and they will interfere to generate an intensity profile, I_{24}, which shares the same wavevector, $\mathbf{k}$, as I_{13}. This fourth wave, E_4, acquires an intrinsic $\pi/2$ phase shift on Bragg diffraction and a further $\pm\pi/2$ shift due to the shift in phase of the principal grating. If E_4 is diffracted in the opposite direction to the grating shift then these two phase shifts add and E_4 and E_2 are out of phase by π. The immediate consequence of this is that I_{13} and I_{24} are also out of phase by π and the intensity maxima of one lies along the intensity minima of the other, Fig. 4.3a). The two intensity profiles, given as follows

$$I_{13} = (I_1 + I_3) + 2\sqrt{I_1 I_3}\cos(\mathbf{k}.\mathbf{r}), \qquad (4.5a)$$

$$I_{24} = (I_2 + I_4) + 2\sqrt{I_2 I_4}\cos(\mathbf{k}.\mathbf{r} + \pi),$$

$$I_{24} = (I_2 + I_4) - 2\sqrt{I_2 I_4}\cos(\mathbf{k}.\mathbf{r}), \qquad (4.5b)$$

add in a scalar fashion to spatially smooth the nett intensity profile, I, by reducing

the resultant fringe contrast M

$$I = I_o[1 + M\cos(\mathbf{k}.\mathbf{r})], \tag{4.6}$$

$$M = \frac{2\left[\sqrt{I_1 I_3} - \sqrt{I_2 I_4}\right]}{I_o}, \tag{4.7a}$$

where $I_o = I_1 + I_2 + I_3 + I_4$, and hence deplete the induced refractive index (RI) modulation, Δn. If E_4 is diffracted in the same direction as the grating shift the two phase shifts subtract to yield both E_4, E_2 and I_{13}, I_{24} in phase, Fig. 4.3b). Hence the intensity maxima of both profiles coincide and the resultant fringe contrast is now increased

$$M = \frac{2\left[\sqrt{I_1 I_3} + \sqrt{I_2 I_4}\right]}{I_o}, \tag{4.7b}$$

and the induced RI modulation is enhanced. Obviously the second optical configuration, Fig. 4.3b), is the more optimum. Considering all three incident waves to be mutually coherent, the reflection grating, induced principally by the intensity profile of E_2 and E_3, may also become significant. The generation of the fourth wave, E_4, is now the superposition of the Bragg diffractions of E_2 off the transmission and E_1 off the reflection gratings. The two components add coherently where their relative phase is dictated by the relative phase of the two pump waves, E_1 and E_2. Further, including the dynamic feedback effects of phase and energy exchange on the induced gratings, the optical system becomes very complicated.

The beam coupling between the four waves by DFWM in a PR medium has been extensively studied [4.19→4.24]. Neglecting light absorption and dynamic feedback Fischer *et al* [4.20] solved Maxwell's wave equation for the transmission grating in the slowly varying envelope approximation. The following coupled wave equations in both amplitude and intensity were derived, Appendix E,

$$\frac{dA_1}{dx} = -\frac{\gamma}{I_o}(A_1 A_3^* + A_2^* A_4)A_3, \tag{4.8a}$$

$$\frac{dA_2^*}{dx} = -\frac{\gamma}{I_o}(A_1 A_3^* + A_2^* A_4)A_4^*, \tag{4.8b}$$

$$\frac{dA_3^*}{dx} = \frac{\gamma}{I_o}(A_1 A_3^* + A_2^* A_4)A_1^*, \tag{4.8c}$$

$$\frac{dA_4}{dx} = \frac{\gamma}{I_o}(A_1 A_3^* + A_2^* A_4)A_2 \tag{4.8d}$$

and

$$\frac{dI_1}{dx} = \frac{\Gamma}{I_o}\left[I_1 I_3 + \sqrt{I_1 I_2 I_3 I_4}\cos(\varphi)\right], \tag{4.9a}$$

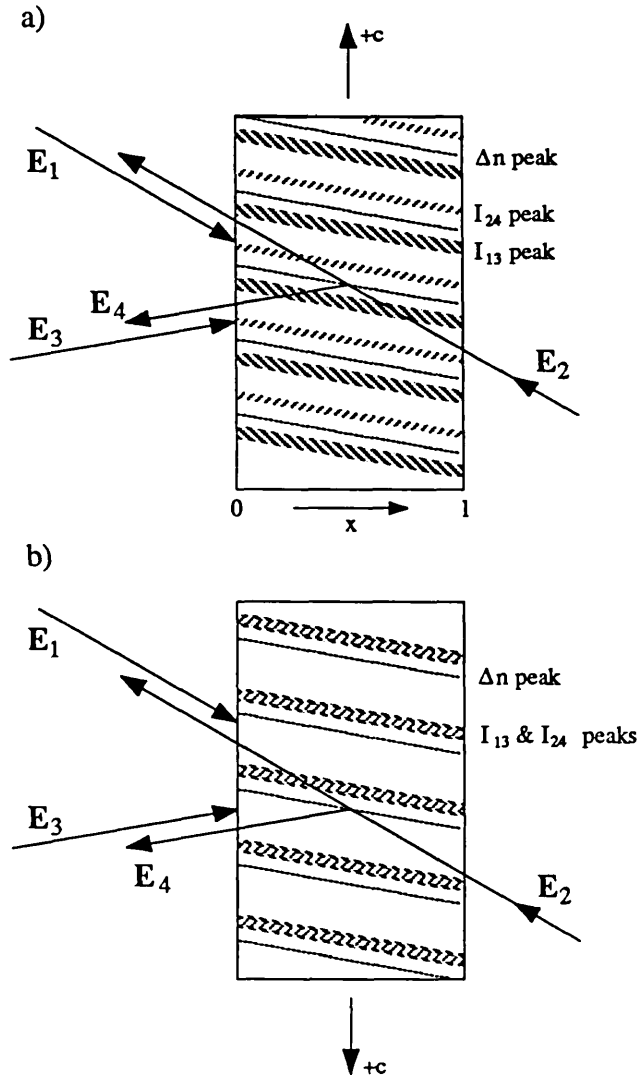


Figure 4.3 Phase conjugation by DFWM in a p–type photoconducting PR material for a *diffusion* dominated transport mechanism. a) Non–optimum and b) optimum orientation of the crystalline +c axis.

$$\frac{dI_2}{dx} = \frac{\Gamma}{I_o}\left[I_2 I_4 + \sqrt{I_1 I_2 I_3 I_4}\cos(\varphi)\right], \tag{4.9b}$$

$$\frac{dI_3}{dx} = -\frac{dI_1}{dx}, \tag{4.9c}$$

$$\frac{dI_4}{dx} = -\frac{dI_2}{dx}. \tag{4.9d}$$

The total intensity, I_o, amplitude and intensity coupling constants, γ and Γ re-

spectively, and the relative phase of the four interacting waves, φ, are given by

$$I_o = I_1 + I_2 + I_3 + I_4, \tag{4.10}$$

$$\gamma = \frac{i\omega\Delta n \exp(i\phi)}{2c\cos\theta_1}, \tag{4.11a}$$

$$\Gamma = \frac{\omega\Delta n \sin\phi}{c\cos\theta_1}, \tag{4.11b}$$

$$\varphi = \varphi_3 + \varphi_4 - \varphi_1 - \varphi_2, \tag{4.12}$$

where ϕ is the phase shift of the induced transmission grating.

Assuming the nondepleted pump approximation, $I_1, I_2 \gg I_3, I_4$, the coupled equations, Eqs. (4.8a), (4.8b), (4.8c) and (4.8d), become

$$\frac{dA_1}{dx} = 0, \tag{4.13a}$$

$$\frac{dA_2^*}{dx} = 0, \tag{4.13b}$$

$$\frac{dA_3^*}{dx} = \frac{\gamma}{I_o}[|A_1|^2 A_3^* + (A_1^* A_2^*)A_4], \tag{4.13c}$$

$$\frac{dA_4}{dx} = \frac{\gamma}{I_o}[(A_1 A_2)A_3^* + |A_2|^2 A_4], \tag{4.13d}$$

which are solved using the boundary conditions $A_3^*(0) = constant$ and $A_4(l) = 0$, [4.20] and Appendix G, to yield the following solutions

$$A_3^*(x) = A_3^*(0)\frac{1}{[\exp(-\gamma l)/\beta + 1]}[\exp[\gamma(x-l)]/\beta + 1], \tag{4.14a}$$

$$A_4(x) = A_3^*(0)\frac{A_1/A_2^*}{[\exp(-\gamma l)/\beta + 1]}[\exp[\gamma(x-l)] - 1], \tag{4.14b}$$

where $\beta = I_2/I_1$ is the ratio of the pumping beam intensities. It is observed that the complex amplitude of E_4 leaving the medium is proportional to the phase conjugate of the incident wave amplitude,

$$A_4(0) \propto A_3^*(0). \tag{4.15}$$

The phase conjugate reflectivity, R_{PC}, defined by

$$R_{PC} = \left|\frac{A_4(0)}{A_3^*(0)}\right|^2, \tag{4.16}$$

becomes

$$= \left|\frac{\sinh(\gamma l/2)}{\cosh[(\gamma l + \ln\beta)/2]}\right|^2. \tag{4.17}$$

For a suitable combination of pumping beam intensity ratio, β, and amplitude coupling constant, γ, the phase conjugate reflectivity, R_{PC} Eq. (4.17), can exceed unity. This constitutes a phase conjugate mirror with gain and in practice it is readily demonstrated using PR barium titanate.

4.3 Experimental procedure and results.

Two experimental investigations were performed to determine the fidelity of the phase conjugate wavefront generated by DFWM in PR barium titanate. The barium titanate crystal used was sample $^{\#1}$, with the laser sources, optical table/support and conventional optical components outlined in Chapter 3. Both experiments were conducted using the argon ion laser operating on single transverse and longtitudinal modes at $\lambda = 514.5$nm and the light was *extra–ordinary* polarised with respect to the +c axis of the crystal.

The first experiment illustrated the ability of a PCM to correct for phase distortion imparted on an image bearing beam on passing through poor quality optics. The optical system, schematically illustrated in Fig. 4.4, consisted of a spatially filtered and collimated light beam passing through an input test transparency, a USAF resolution chart Fig. 4.5a). The then image bearing beam passed through the lossless phase distorter, a piece of very poor quality cellophane, before being reflected back through the same phase distorter and finally sampled using the beam splitter. The output plane and input test transparency were both orthogonal to the light beam and equidistant from the beamsplitter. For comparison, the reflection was first performed using a conventional plane mirror, Fig 4.4a). The mirror was aligned with its normal parallel to the ray direction of the incident beam. The image recorded at the output plane, Fig. 4.5b), was observed to be double phase distorted and bore little resemblance to the original transparency, Fig. 4.5a). The conventional mirror was then replaced by the PR crystal of $BaTiO_3$ and a set of counterpropagating pumping beams, Fig. 4.4b). A lens was used to contract the cross section of the phase distorted image bearing beam in order to fit the small entrance aperture of the crystal. All three interacting light beams were mutually coherent and by DFWM the PC was generated with ease. The PC wavefront was self–aligned and passed back through both lens and phase distorter. The recovered image, observed at the output plane Fig. 4.5c), was free of the severe distortion obtained with the conventional plane mirror, Fig. 4.5b), and was easily recognisable as the input test transparency. The output plane was noted to be coincident with a natural image plane of the system, illustrating the lensless imaging property of PC optics when input transparency and output plane are equidistant from the sampling beam splitter.

The second experiment again illustrated qualitatively the fidelity of the PC generated by DFWM in PR $BaTiO_3$. The optical system, schematically illustrated in Fig. 4.6, consisted of a Michelson interferometer with the conventional plane

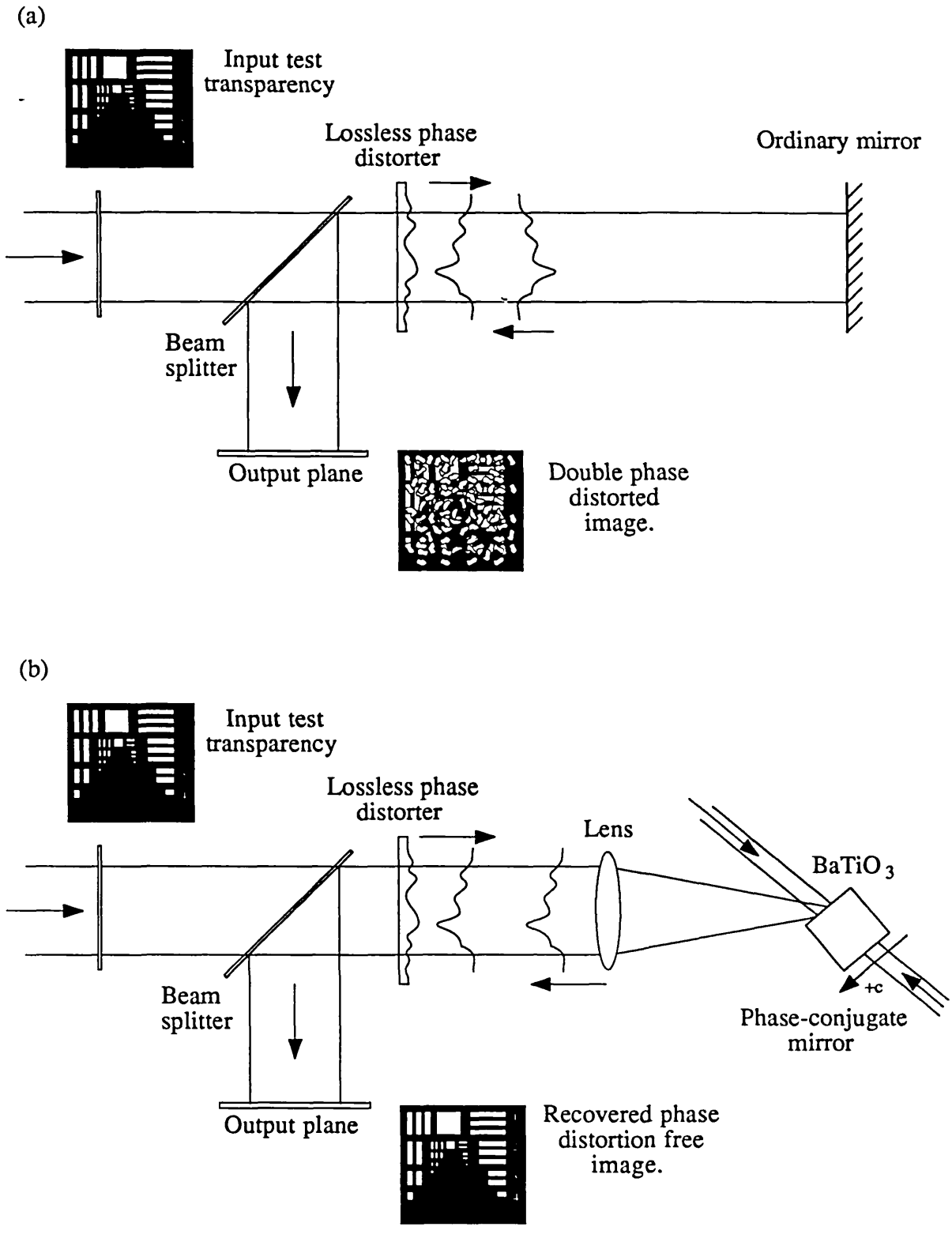


Figure 4.4 Schematic illustration of the optical systems used to demonstrate phase distortion correction of an image bearing beam using a PCM.

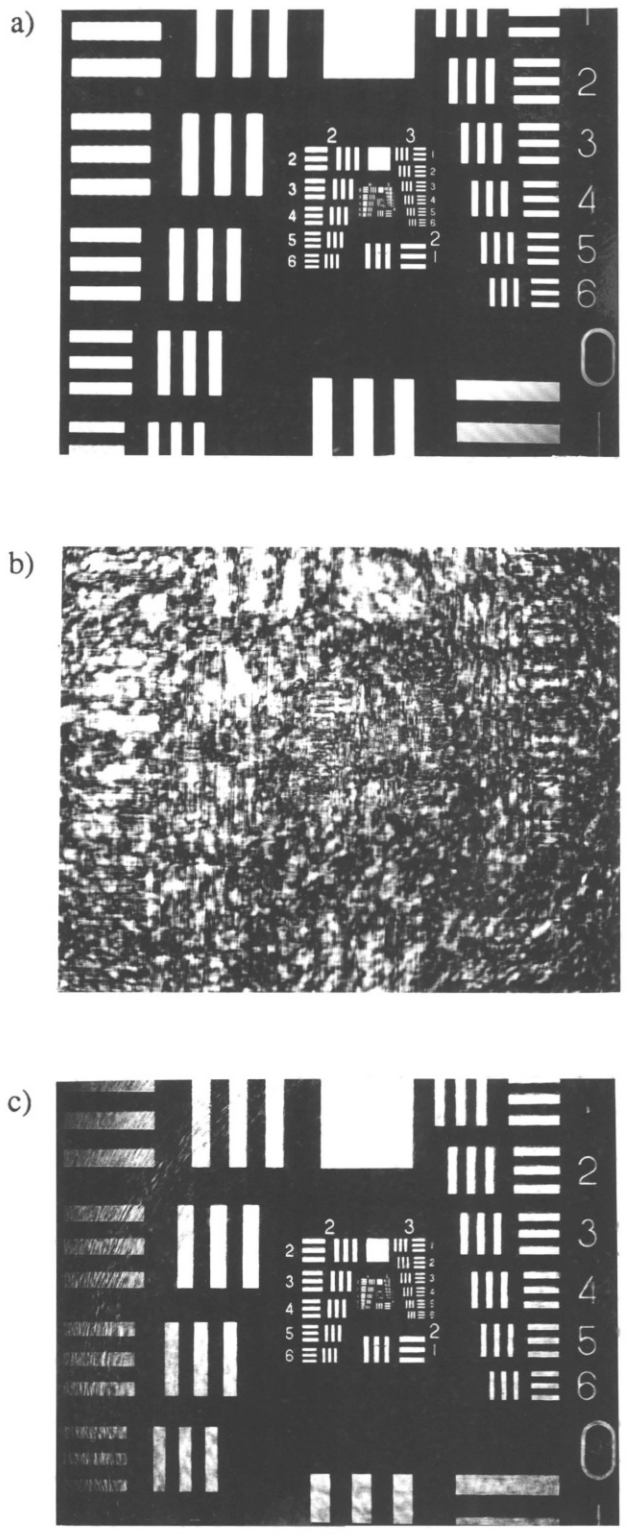


Figure 4.5 Experimental results of phase distortion correction using a PCM. a) Original test transparency (USAF resolution chart), b) double phase distorted image generated using a conventional plane mirror and c) recovered phase distortion free image generated using a PCM.

mirrors replaced by two PCMs, [4.25→4.27]. The spatially filtered and collimated plane wave was first divided into two by the lossless beam splitter. The two beams, travelling along the two arms of the interferometer, pass through two separate transparencies, $^{\#1}$ and $^{\#2}$, schematically illustrated as fine horizontal and coarse vertical bars respectively. Both beams were phase conjugated by DFWM at the same PR crystal of $BaTiO_3$ and the lens, L_1 and L_2, were used only to contract the beam size to fit the small entrance aperture of the crystal. The returned PC wavefronts passed back through their respective lenses/transparencies and were imaged together at the output plane using lens L_3.

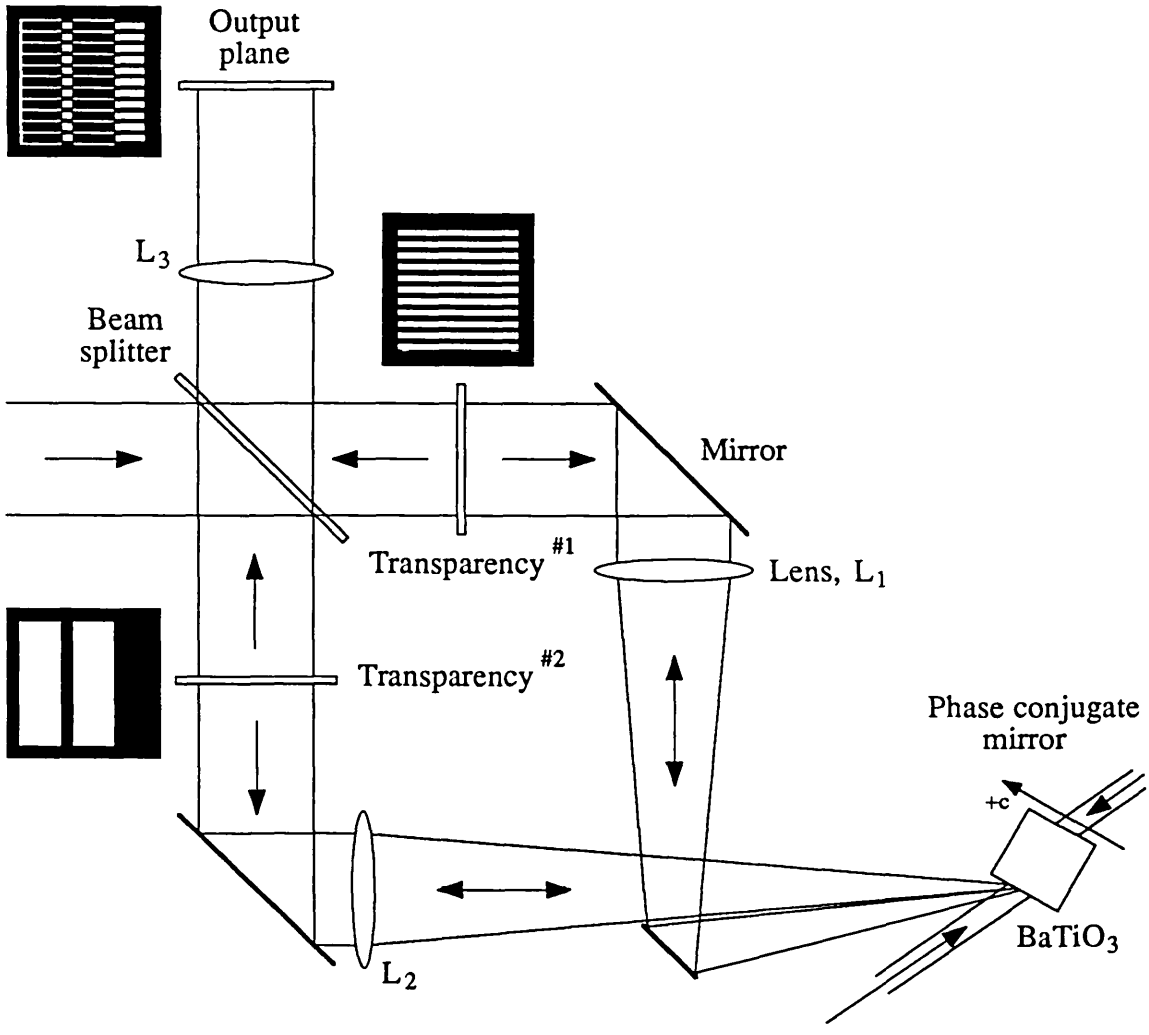


Figure 4.6 Schematic illustration of a phase conjugate Michelson interferometer used to perform EXOR digital logic.

T_1	T_2	$[T_1 - T_2]^2$
0	0	0
0	1	1
1	0	1
1	1	0

Table 4.I EXOR digital logic.

Consider the complex amplitude coefficients of transmittance and reflectance for the lossless beam splitter, transmittance for the two transparencies and reflectance for the two PCMs to be r and t, τ_1 and τ_2 and μ_1 and μ_2 respectively. The complex amplitudes, at various locations and directions, are illustrated in the schematic diagram Fig. 4.7. The resultant complex amplitude at the output plane, $A_{o/p}$, is found to be

$$A_{o/p} = A^* [\mu_1 \tau_1 \tau_1^* r' t^* + \mu_2 \tau_2 \tau_2^* r^* t], \tag{4.18}$$

where A is the complex amplitude of the incident plane wavefront. Assuming the two PC reflectivities to be identical i. e. their intrinsic phase shifts and amplitude reflectivities are the same, then $\mu_1 = \mu_2 = \mu$, and using Stokes's relation for a lossless beam splitter, [4.28] and Appendix H,

$$r' t^* + r^* t = 0, \tag{4.19}$$

the complex amplitude, $A_{o/p}$, becomes

$$A_{o/p} = A^* \mu r' t^* [T_1 - T_2], \tag{4.20}$$

where $T_1 = |\tau_1|^2$ and $T_2 = |\tau_2|^2$ are the intensity transmittance functions of transparencies $^{\#1}$ and $^{\#2}$ respectively. The intensity at the output plane is given by

$$I_{o/p} = |A_{o/p}|^2, \tag{4.21a}$$

$$= I R_{PC} R (1 - R) [T_1 - T_2]^2, \tag{4.21b}$$

$$\propto [T_1 - T_2]^2, \tag{4.21c}$$

where I, R and $R_{PC} = |\mu|^2$ are the incident intensity and reflectivities of the lossless beam splitter and PCM respectively. Note the intensity at the output plane, $I_{o/p}$, is proportional to the square of the difference of the intensity transmittance functions of the two transparencies, Eq. (4.21c). This functional dependence is equivalent to exclusive–OR, EXOR, digital logic for binary transparencies and the corresponding logic truth table is shown by Table 4.I.

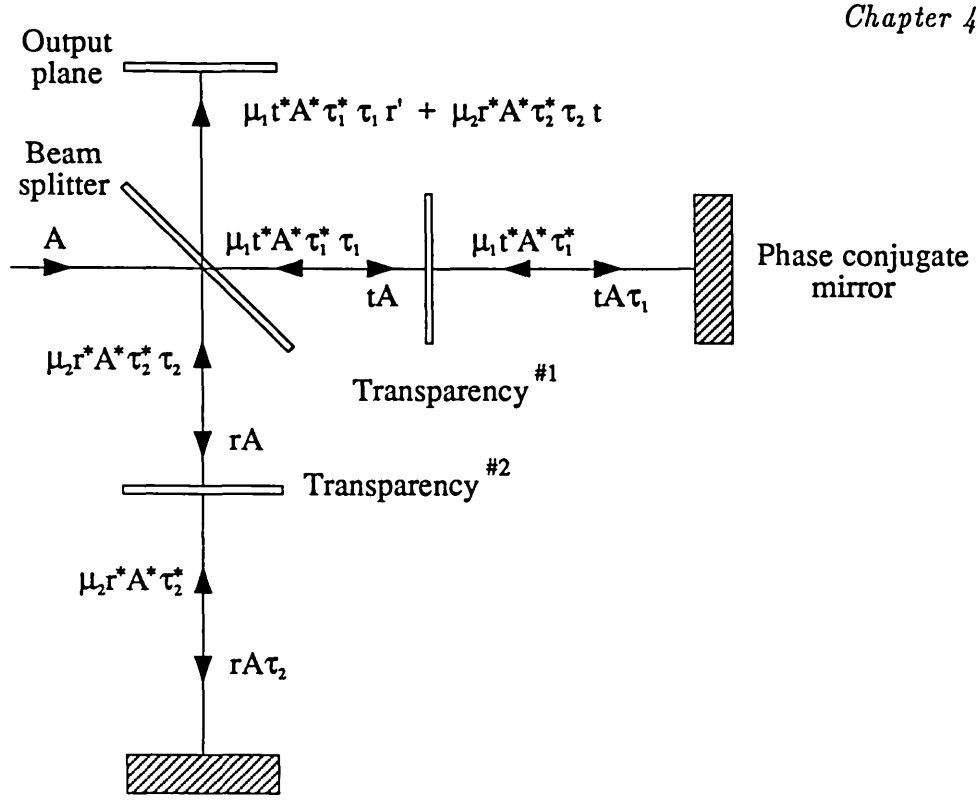


Figure 4.7 Complex amplitudes at various locations and directions in a PC Michelson interferometer.

The EXOR logic is interpreted as the destructive interference between the two PC wavefronts coincident at the output plane. The relative π phase shift is introduced at the lossless beam splitter as dictated by Stokes's relation, Eq. (4.19), and is a direct consequence of the time reversibility of light by phase conjugation. The schematic diagram of the optical system, Fig. 4.6, illustrates the EXOR relation between the two transparencies $^{\#1}$ and $^{\#2}$ at the output plane. The experimental results obtained are shown in Fig. 4.8. The two binary transparencies used were a radial resolution chart and two coarse vertical bars. Their individual PCs, imaged at the output plane, are shown in Fig. 4.8a) and b) respectively and indeed their combination, Fig. 4.8c), is observed to display EXOR digital logic. The quality of the result is considered to be very good which again emphasises the high fidelity of PC generated by DFWM in PR $BaTiO_3$. The self-alignment of the PC wavefronts ensured the absence of tilt fringes commonly observed with a Michelson interferometer using conventional plane mirrors.

4.4 Self pumped phase conjugation by $BaTiO_3$ and SBN.

The two PR ferroelectric oxides barium titanate, $BaTiO_3$, and strontium barium niobate, $Sr_xBa_{1-x}Nd_2O_6$, exhibit particularly large linear (Pockels) electro-

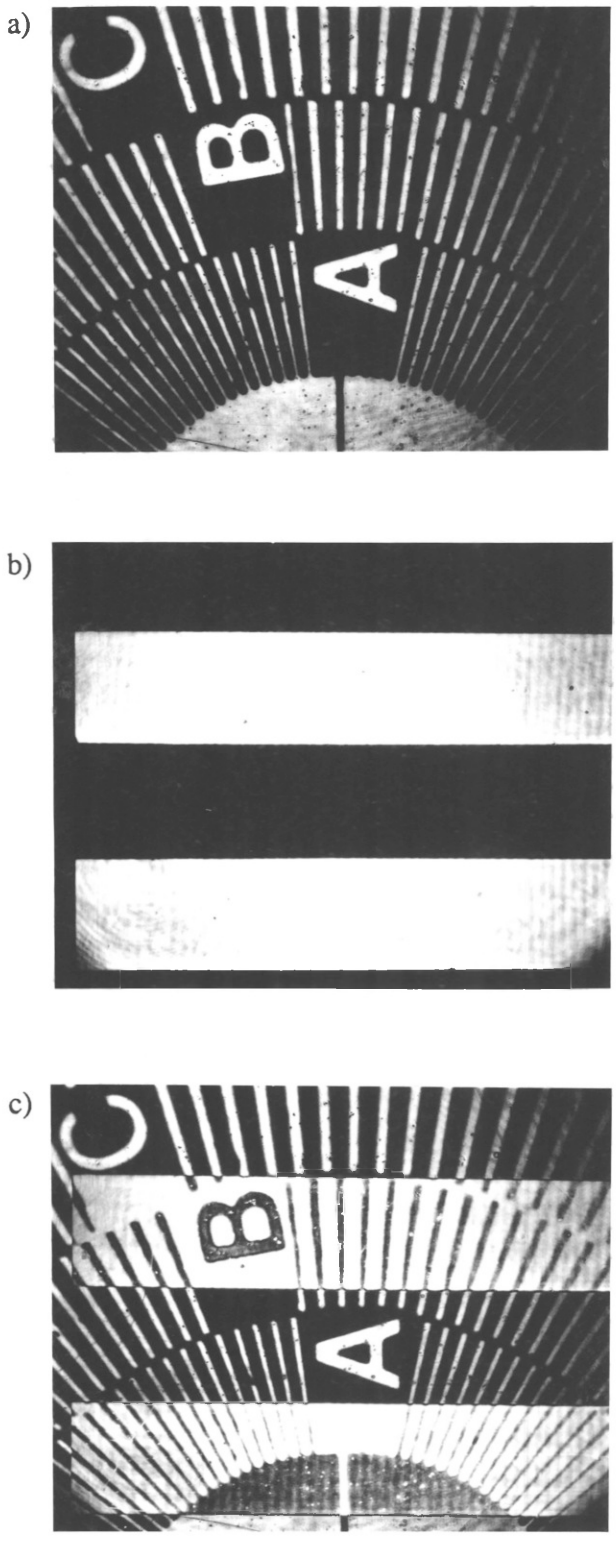


Figure 4.8 Experimental results of EXOR digital logic performed using PC Michelson interferometer and two binary transparencies. a) The PC of transparency$^{\#1}$, b) the PC of transparency$^{\#2}$ and c) their EXOR logical combination.

optic coefficients. At room temperature they both have a 4mm point group symmetry and hence share the same configuration of electro-optic tensor. The $r_{42} = 1640 pmV^{-1}$ and $r_{33} = 1340 pmV^{-1}$ and $420 pmV^{-1}$ are the dominant coefficients for $BaTiO_3$ and SBN:75 and SBN:60 respectively, Table 2.III. Exploiting these coefficients, using an intelligent choice of both optical configuration and polarisation, Chapter 2, very large RI modulations can be induced, $\Delta n \sim 10^{-3}$. As a consequence, both $BaTiO_3$ and SBN exhibit strong PR optical nonlinearities and display particularly exotic effects.

Asymmetric fanning or self-defocusing of a laser beam transmitted through these materials is a simple demonstration of the extent of their PR optical nonlinearities [4.29,4.30]. Consider the PR material to be illuminated by a single Gaussian laser beam, passing through the front and back faces and spatially confined within the transverse plane of the medium, Fig. 4.9. The spatial variation in intensity induces the radial migration of the mobile PR species away from the central beam axis. Equilibrium and hence the steady state is achieved when the radial outward *diffusion* of charge is exactly balanced by the radial inward *drift*. The modulus of the normalised steady state radial electric field profile, numerically calculated as decribed in Chapter 7, is shown in Fig. 4.10, o, accompanied by the illuminating Gaussian intensity, ——. For p-type $BaTiO_3$ the radial electric field will point inwards while for n-type cerium doped SBN:60 the electric field will point radially outwards.

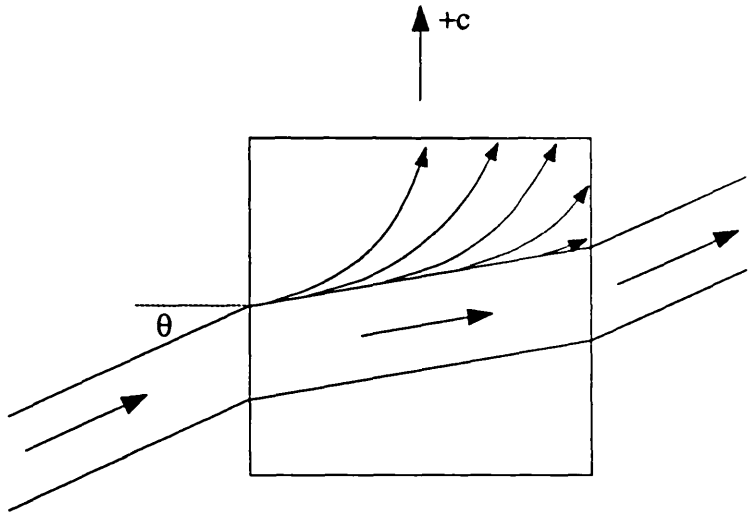


Figure 4.9 Schematic diagram of asymmetric beam fanning in $BaTiO_3$.

The corresponding refractive index (RI) modulation profiles for *ordinary*, ⋆, and

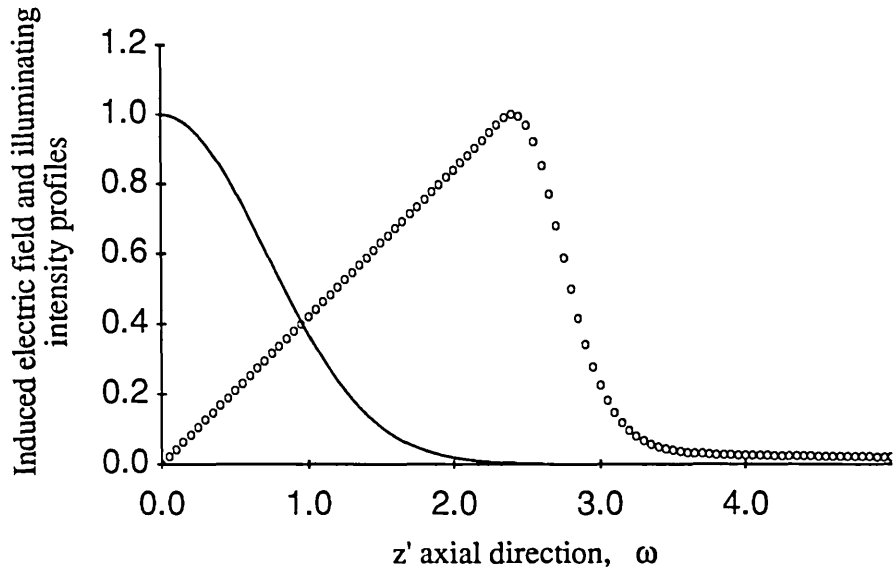


Figure 4.10 Induced steady state radial electric field profile, o, for an illuminating Gaussian intensity profile, ——.

extra–ordinary, o, polarisation states along the z axis (+c axis) for $BaTiO_3$ at $\theta = 0$ are shown in Fig. 4.11. The RI amplitudes for the two polarisation states differ markedly due to the difference in magnitude of the r_{13} and r_{33} electro–optic coefficients respectively employed, $\Delta n_o = 2.08 \times 10^{-6}$ and $\Delta n_e = 2.35 \times 10^{-4}$, Chapter 7. Consequently much stronger optical nonlinearities are forecast for the *extra–ordinary* polarised state. The steep positive gradient in Δn_e extending across the cental axis, is predicted to refract the central and most intense part of the laser beam asymmetrically in the direction of the +c axis. The shallow negative gradient in Δn_o is predicted to have minimal effect on the transmitted beam with perhaps slight refraction in the –c direction.

The barium titanate sample #2 was illuminated using a single Gaussian argon ion laser beam ($\lambda = 514.5$nm) taken direct from the source. The incident angle and intensity were $\theta = 20°$ and $\sim 1 Wcm^{-2}$ respectively. The beam was initially *ordinary* polarised and the recorded intensity profile of the transmitted beam is shown in Fig. 4.12a). The minimal optical disturbance predicted was observed. The incident light polarisation was changed to *extra–ordinary* and after an initial transient stage the transmitted intensity profile displayed a pronounced asymmetric fan in the steady state, Fig. 4.12b), directed along the +c axis as earlier forecast.

The geometry of the $BaTiO_3$ sample and laser beam were such that the fanned light inside the bulk of the material illuminated one of the back corner edges of the crystal. The light was then retroreflected by total internal reflection and

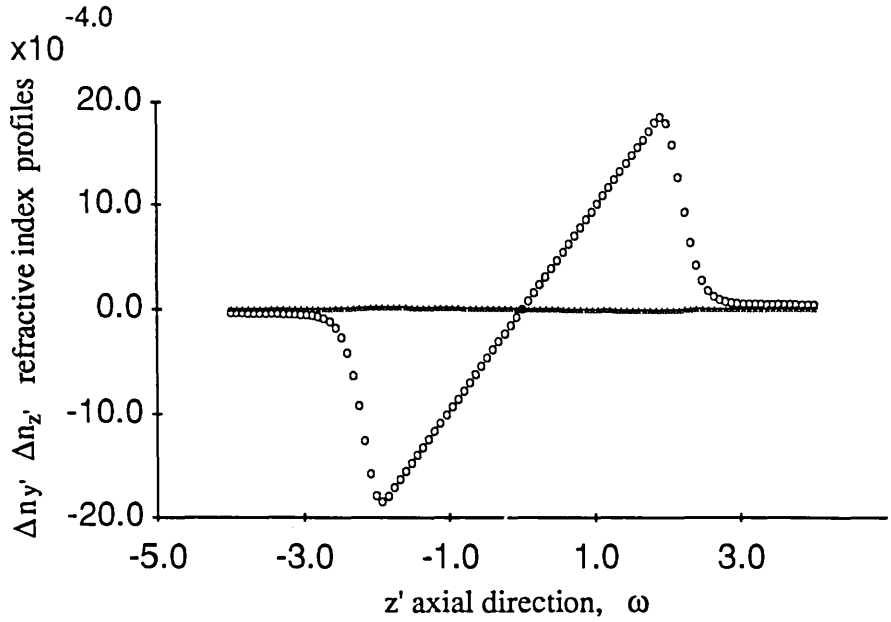


Figure 4.11 RI modulation profiles along the z axis (+c axis) for *ordinary*, ⋆, and *extra-ordinary*, ∘, polarisations.

directed back towards the front face. Given time, the flood of fanned light collapsed into a well defined loop which was accompanyed by the appearence of a phase conjugate wave, travelling in the opposite direction to the incident beam. This fascinating phenomenon was first observed by Feinberg [4.31] using $BaTiO_3$ and has since been demonstrated using SBN:60 [4.30], SBN:75 [4.32] and BSKNN-III [4.33]. The phase conjugation mechanism is considered to be DFWM with the counterpropagating pump beams self-generated by the formed loop of light and has since been denoted as *self-pumped* DFWM. The wave mixing scheme is illustrated in Fig. 4.13 and a top view photograph of self-pumping $BaTiO_3^{\#2}$ is shown in Fig. 4.14. The fidelity of the PC wave, generated by the *self-pumping* mechanism, was observed to be very high but accompanied by slight spectral instabilities. Typically the PC wave had a 0.1 → 1Hz Doppler frequency shift which wandered between both the red and blue.

The PC was found to display interesting and unusual temporal characteristics. Dependent on both the optical geometry and incident intensity, the self-pumped PCM could operate in steady *cw*, regular oscillatory or chaotic modes [4.34→4.37]. Experimental observations of the three operational modes are shown in Fig. 4.15a), b) and c). The *cw* phase conjugate reflectivity was measured upto 30.5%, Fig. 4.15a), and the regular oscillations, Fig. 4.15b), self-sustained for many hours.

Once *cw* self-pumped phase conjugation had become established it was found [4.38] that the self-generated counterpropagating pump beams could be employed

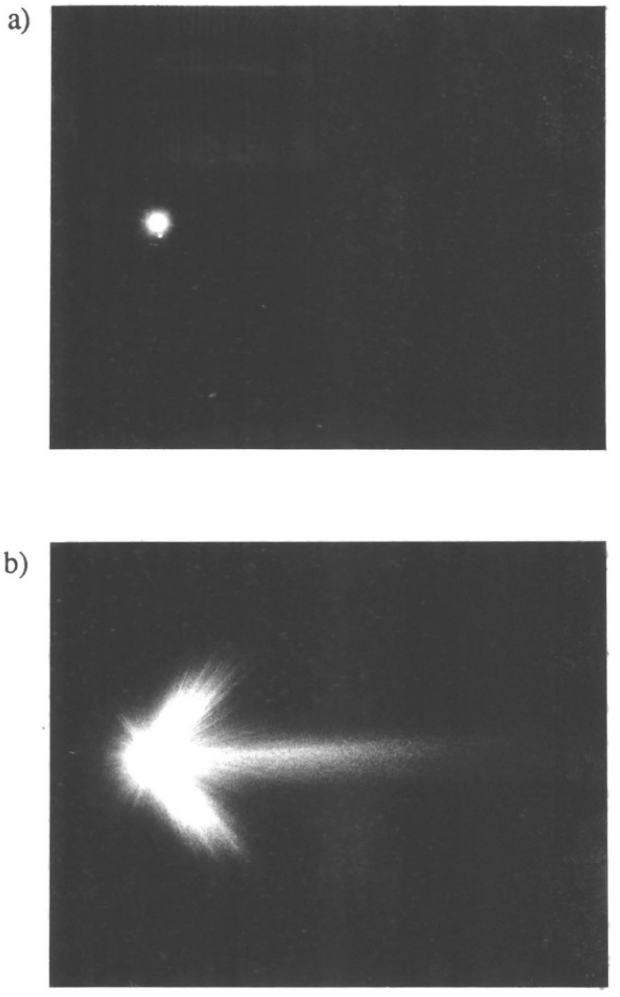


Figure 4.12 Asymmetric beam fanning observed for a)*ordinary* and b)*extra–ordinary* polarised light.

to phase conjugate a second low intensity and angularly offset probe beam. The two PCs did not cross talk when the incident waves were image bearing and R_{PC} for the second weak probe beam could exceed unity. The phase conjugation of a weak probe beam using this technique has proved an attractive alternative to the more conventional externally pumped DFWM geometry. The pumping beams are self–aligned and amplified high fidelity PC wavefronts were easily attained. The gain exhibited by the *self–pumped* phase conjugator is sufficiently large to induce self–oscillation between the crystal and any nearby specularly reflecting object [4.3]. The oscillation is seeded by only the background scattered light and is self–sustaining once established. The optical quality of the reflecting object is not important as the phase conjugate nature of the oscillation insures that a stable

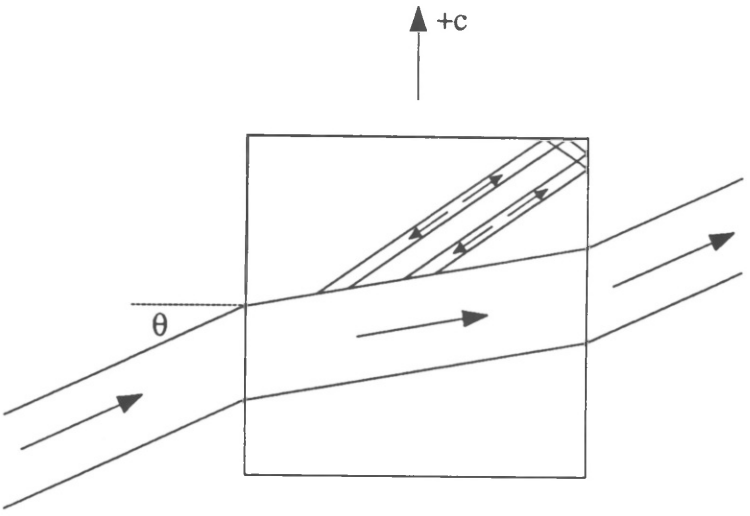


Figure 4.13 Schematic illustration of *self–pumped* phase conjugation by DFWM in $BaTiO_3$.

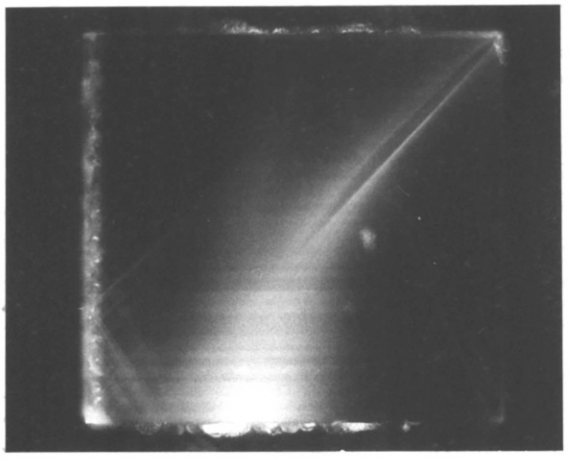


Figure 4.14 Top view of self–pumping $BaTiO_3^{\#2}$.

resonant mode will always exist. On slowly tilting the reflecting object, the light path adjusts to locate the new normal component of the object to the crystal and steady state oscillation is re-established.

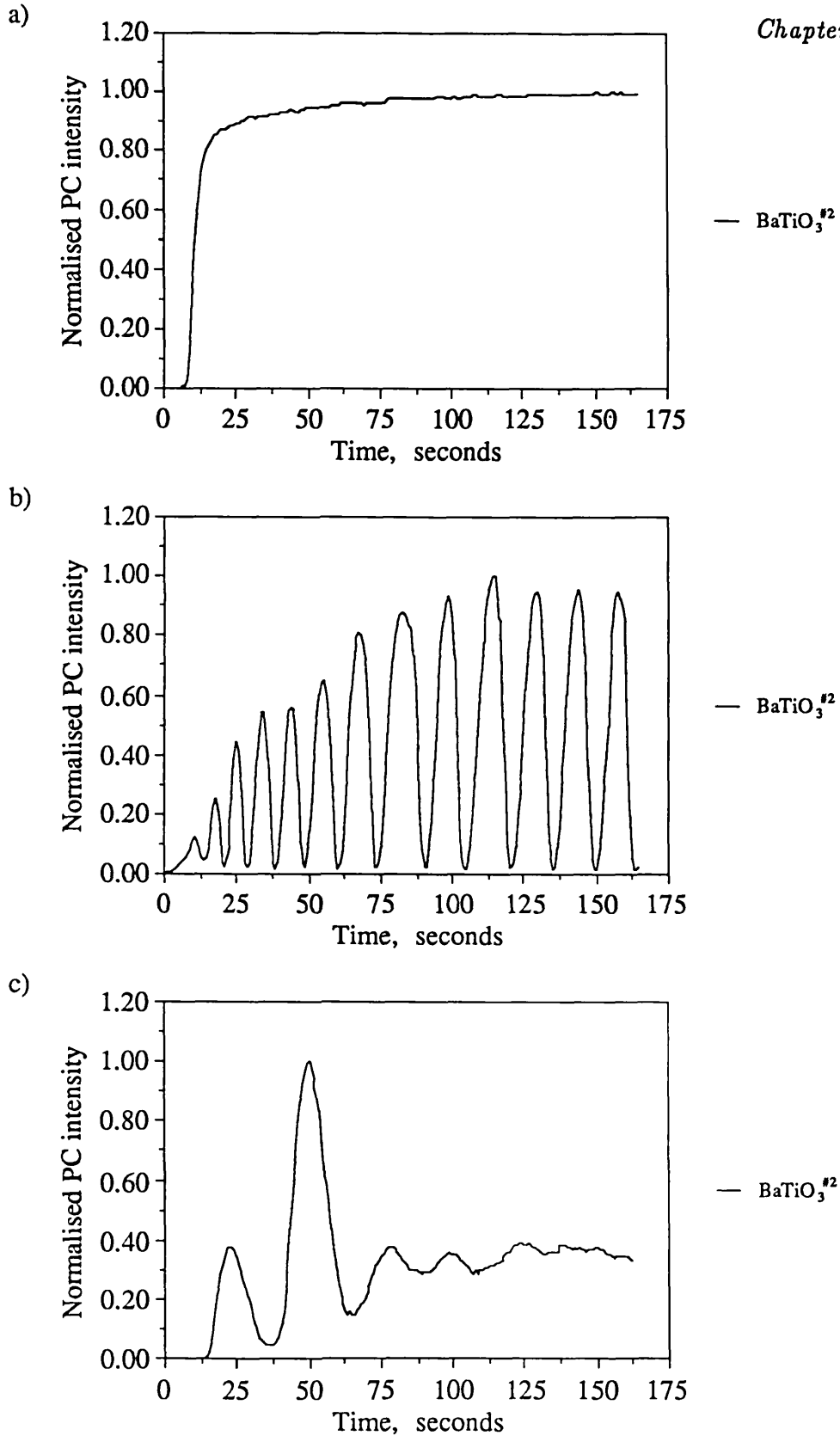


Figure 4.15 The temporal behaviour of *self-pumped* $BaTiO_3^{\#2}$. a) steady *cw*, b) regular oscillatory and c) chaotic modes of operation.

4.5 Conclusions.

High fidelity phase conjugation by degenerate four wave mixing (DFWM) in photorefractive (PR) barium titanate was demonstrated. Employing an intelligent choice of geometry and *extra–ordinary* polarisation state, externally pumped $BaTiO_3$ could achieve phase conjugate reflectivities, R_{PC}, in excess of unity. The phase conjugate fidelity was qualitatively judged from the aesthetic quality of the images generated by phase conjugation. Phase distortion correction and EXOR digital logic were experimentally demonstrated using binary transparencies and the results were of a high standard.

The exotic optical nonlinearity *self–pumping* was demonstrated by PR barium titanate. Phase conjugation by this mechanism exhibited steady *cw*, regular oscillatory and randomly chaotic temporal modes and a maximum *cw* R_{PC} of 0.30 was recorded. The phase conjugate fidelity was judged to be excellent and within a certain angular window the gain was sufficient to stimulate oscillation with any nearby specularly reflecting object.

4.6 References.

[4.1] B.Ya. Zel'dovich, V.I. Popovichev, V.V. Ragul'skii and F.S. Faizullov, "Connection between the wave fronts of the reflected and exciting light in stimulated Mandel'shtam–Brillouin scattering," Sov.Phys. JETP **15**, 109–113 (1972).

[4.2] O.Yu. Nosach, V.I. Popovichev, V.V. Ragul'skii and F.S. Faizullov, "Cancellation of phase distortion in an amplifying medium with a "Brillouin Mirror"," Sov.Phys. JETP **16**, 435–438 (1972).

[4.3] Fisher R.A. Ed., "Optical Phase Conjugation," (Academic Press, Inc., New York 1983).

[4.4] B.Ya. Zel'dovich and V.V. Shkunov, "Wavefront reproduction in stimulated Raman scattering," Sov.J.Quantum.Electron. **7**, 610 (1977).

[4.5] A.I. Sokolovskaya, G.L. Brekhovskikh and A.D. Kudryavtseva, "Restoration of wavefront of light beams during stimulated Raman scattering," Sov.Phys.Dokl. **22**, 156 (1977).

[4.6] A.D. Kudryavtseva, A.I. Sokolovskaya, J. Gazengel, N.P. Xuan and G. Rivoire, "Reconstruction of the laser wavefront by stimulated scattering in the picosecond range," Opt.Commun **26**, 446 (1978).

[4.7] E.I. Shtyrkov and V.V. Samartsev, "Imaging properties of dynamic echo holograms in resonant media," Opt.Spectrosc. **40**, 224 (1976).

[4.8] A. Yariv, "On transmission and recovery of three–dimensional image information in optical waveguides," J.Opt.Soc.Am. **66**, 301 (1976).

[4.9] A. Yariv, "Compensation for atmospheric degradation of optical beam transmission by nonlinear optical mixing," Opt.Commun. **21**, 49 (1977).

[4.10] D.M. Bloom, P.F. Liao and M.P. Economoo, "Observation of amplified reflection by degenerate four wave mixing in a sodium vapour," Opt.Lett. **2**, 58 (1978).

[4.11] S.M. Jenson and R.W. Hellwarth, "Observation of the time reversed replica of a monochromatic optical wave," Appl.Phys.Lett. **32**, 166 (1978).

[4.12] E.E. Bergmann, I.J. Bigio, B.J. Feldman and R.A. Fisher, "High–efficiency pulsed 10.6μm phase–conjugate reflection via degenerate four–wave mixing," Opt.Lett. **3**, 82 (1978).

[4.13] J.P. Huignard, J.P. Herriau, P. Auborg and E. Spitz, "Phase–conjugate wavefront generation via real–time holography in $Bi_{12}SiO_{20}$," Opt.Lett. **4**, 21–23 (1979).

[4.14] J. Feinberg and R.W. Hellwarth, "Phase conjugating mirror with continuous wave gain," Opt.Lett. **5**, 519 (1980).

[4.15] Yariv A. and Yeh P., "Optical Waves in Crystals," (John Wiley & Sons, Inc., New York, 1984).

[4.16] A. Yariv and D.M. Pepper, "Amplified reflection, phase conjugation and oscillation in degenerate four wave mixing," Opt.Lett **1**, 16–18 (1977).

[4.17] A. Yariv, "Phase conjugate optics and real–time holography," IEEE J.-Quant.Electron. **QE–14**, 650 (1978).

[4.18] A. Yariv, "Four wave nonlinear optical mixing as real time holography," Opt.Commun **25**, 23–25 (1978).

[4.19] N. Kukhtarev and S. Odoulov, "Degenerate four–wave mixing in $LiNbO_3$ and $LiTaO_3$," Opt.Commun. **32**, 183–186 (1980).

[4.20] B. Fischer, M. Cronin–Golomb, J.O. White and A. Yariv, "Amplified reflection, transmission and self oscillation in real time holography," Opt.Lett. **6**, 519–521 (1981).

[4.21] M. Cronin–Golomb, J.O. White, B. Fischer and A. Yariv, "Exact solution of a nonlinear model of four–wave mixing and phase conjugation," Opt.Lett **7**, 313–315 (1982).

[4.22] A. Bledowski, W. Krolikowski and A. Kujawski, "Multistability in reflection grating real–time holography," IEEE J.Quant.Electron. **QE–22**, 1547–1550 (1986).

[4.23] W. Krolikowski, "Multi–grating phase conjugation in photorefractive media," Opt.Commun. **60**, 319–322 (1986).

[4.24] J. Goltz, F. Laeri and T. Tschudi, "Nearly degenerate four–wave mixing in photorefractive crystals, an analytical treatment," Opt.Commun. **64**, 63–66 (1987).

[4.25] J. Feinberg, "Interferometer with a self–pumped phase–conjugating mirror," Opt.Lett **8**, 569–571 (1983).

[4.26] Sze–Keuung Kwong, G.A. Rakuljic and A. Yariv, "Real time image subtraction and "exclusive or" operation using a self–pumped phase conjugate mirror," Appl.Phys.Lett **48**, 201–203 (1986).

[4.27] A.E. Chiou and P. Yeh, "Parallel image subtraction using a phase conjugate Michelson interferometer," Opt.Lett. **11**, 306–308 (1986).

[4.28] Hecht E. and Zajac A., "Optics," (Addison–Wesley, Reading 1976).

[4.29] J. Feinberg, "Asymmetric self–defocusing of an optical beam from the photorefractive effect," J.Opt.Soc.Am. **72**, 46–51 (1982).

[4.30] G. Salamo, M.J. Miller, W.W. Clark III, G.L. Wood and E.J. Sharp, "Strontium barium niobate as a self–pumped phase conjugator," Opt.Commun. **59**, 417–422 (1986).

[4.31] J. Feinberg, "Self–pumped, contiuous–wave phase conjugator using internal reflection," Opt.Lett. **7**, 486–488 (1982).

[4.32] M.J. Miller, E.J. Sharp, G.L. Wood, W.W. Clark III, G. J. Salamo and R.R. Neurgaonkar, "Time response of a cerium–doped $Sr_{0.75}Ba_{0.25}Nb_2O_6$ self–pumped phase–conjugate mirror," Opt.Lett. **12**, 340–342 (1987).

[4.33] S.R. Montgomery, J. Yarrison–Rice, D.O. Pederson, M.J. Miller, W.W. Clark III, G.L. Wood, E.J. Sharp and R.R. Neurgaonkar, "Self–pumped phase conjugation in the red in photorefractive $Ba_{2-x}Sr_xK_{1-y}Na_yNb_5O_{15}$ and $Sr_xBa_{1-x}Nb_2O_6$ with cerium 9–fold coordinated sites," OSA Topical Meeting on *Photorefactive Materials, Effects and Devices* Technical Digest Series **17**, 171–174 (1987).

[4.34] P. Günter, E. Voit, M.Z. Zha and J. Albers, "Self–pulsation and optical chaos in self–pumped photorefractive $BaTiO_3$," Opt.Commun. **55**, 210–214 (1985).

[4.35] Sze–Keung Kwong and A. Yariv, "Bistable oscillations with a self–pumped phase–conjugate mirror," Opt.Lett. **11**, 377–379 (1986).

[4.36] A.M.C. Smout, R.W. Eason and M.C. Gower, "Regular oscillations and self–pulsating in self–pumped $BaTiO_3$," Opt.Commun. **59**, 77–82 (1986).

[4.37] R.W. Eason and A.M.C. Smout, "Bistability and noncommutative behaviour of multiple beam self pulsing and self pumping in $BaTiO_3$," Opt.Lett. **12**, 51–53 (1987).

[4.38] J. Feinberg, "Continuous–wave self–pumped phase conjugator with wide field of view," Opt.Lett. **8**, 480–482 (1983).

CHAPTER 5

SPECULAR REFLECTION CANCELLATION AND ENHANCEMENT BY A FABRY–PEROT INTERFEROMETER WITH A PHASE CONJUGATE MIRROR.

5.1 Introduction.

The self alignment and phase distortion correction characteristics of a phase conjugate wavefront have made phase conjugate (PC) optics a particularly fascinating topic to study [5.1,5.2,5.3]. Many new and ingenious applications have been proposed and demonstrated which exploit these unique properties, they include nonlinear image processing [5.4,5.5], novel resonator cavities [5.6], self–targeting [5.7], photolithography [5.8] and optical computing [5.9,5.10]. By various techniques, PC reflectivities up to and in excess of unity have been achieved [5.11,5.12,5.13] which offers the additional flexibility of a combined phase conjugate mirror (PCM) and amplifier.

The unique reflection properties of a PCM can be explained qualitatively by a naive *time–reversal* argument. The PC wavefront is considered to be the *time–reversed* replica of the incident wavefront. Travelling backwards in time, retracing exactly the return path and ultimately arriving back at the original source. The initial quantitative description was based on the paraxial wave equation, [5.14,5.15] and Appendices F and G, and is restricted to the paraxial approximation. The model is valid only for weak phase distorting media where the plane wave components of the wavefront propagate at small angles w. r. t. the incident wavefront direction and backscatter can be neglected. Both the qualitative *time–reversed* and quantitative paraxial arguments are limited in that they both predict that only that portion of the distorted wavefront incident on the PCM can be succesfully corrected for and the remaining scattered field is irretrievable.

More recently, a new model based on general scattering theory has been developed [5.16,5.17,5.18] which is not restricted to either the paraxial or first Born approximations. It is able to accomodate wavefront components which differ substantially from the incident wavefront direction, including extensive backscatter, and multiple reflections between the perturbing medium and PCM. The conclusion of the new model is that distortions imparted on a wavefront by *any* linear, isotropic, nonmagnetic, nonabsorbing and spatially nondispersive scatterer will be completely eliminated when in the presence of a PCM, provided the PCM is of

unit reflectivity and the same polarisation state is preserved on reflection. The implications of this statement are schematically illustrated in Fig. 5.1.

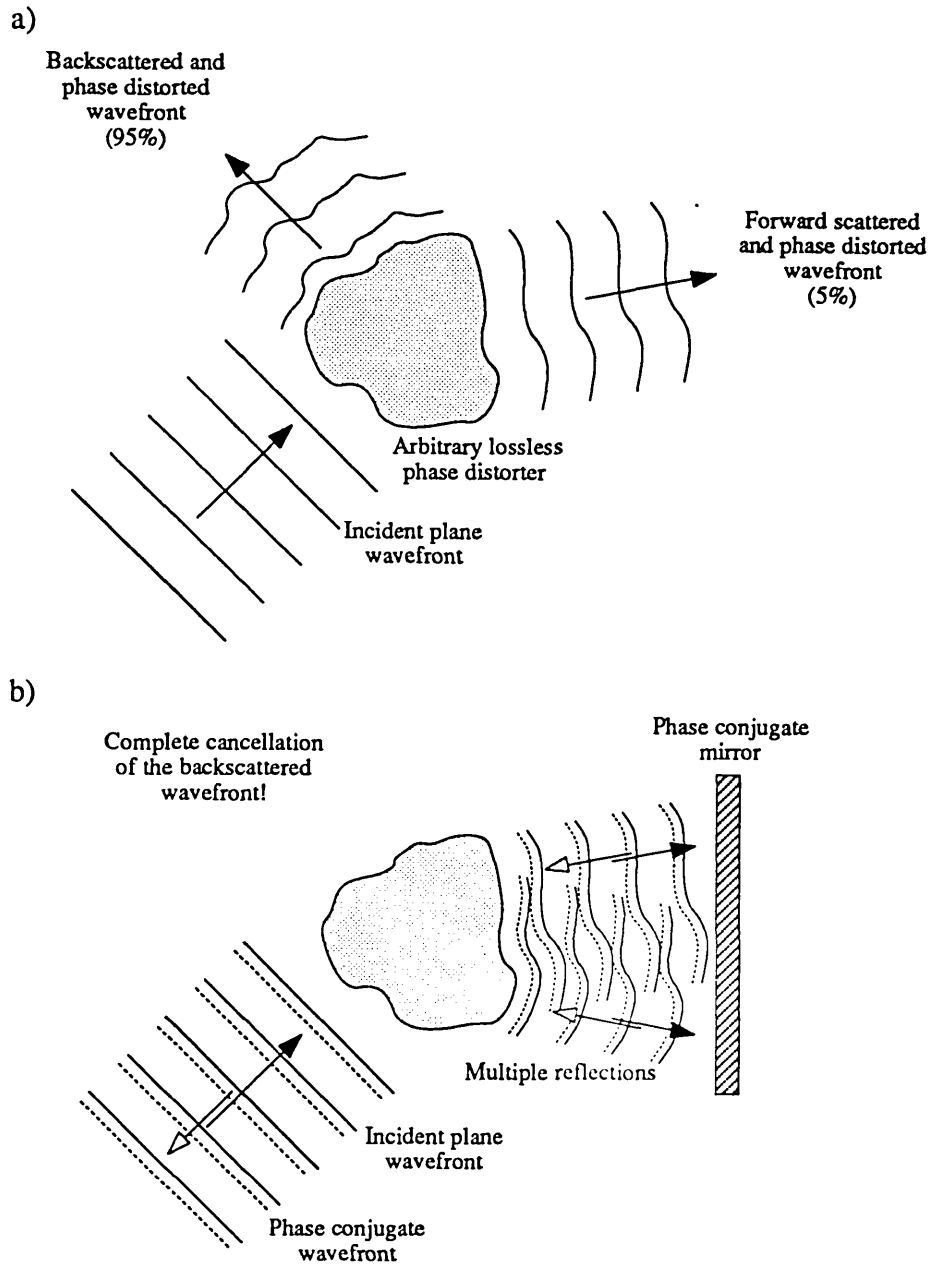


Figure 5.1 The correction of extensive backscatter using a PCM.

Consider any arbitrary lossless phase distorter illuminated by a plane wave, Fig. 5.1a). In general the distorter will scatter the light into the full 4π solid angle with complicated amplitude and phase profiles. Consider for the present discussion that only 5% of the incident radiation is scattered into the forward direction, with

the remaining 95% scattered into the backward direction, Fig. 5.1a). Consider the forward scattered light to be phase conjugated by a unit reflecting (R_{PC} = 1) PCM as illustrated in Fig. 5.1b). The naive *time–reversal* argument would predict that at best only 5% of the scattered light intensity would be successfully corrected to generate at best a phase conjugate plane wavefront of only 5% of the incident intensity. Employing the generalised scattering theory by Agarwal *et al* [5.18] multiple reflections between the arbitrary lossless phase distorter and the PCM are accomodated and a complex resonant cavity is revealed. The coupling between the intercavity fields and the exterior serve to cancel all the backscattered phase distorted light and generate a perfect PC reconstruction of the incident plane wavefront with 100% of the incident intensity i. e. all the phase distortions introduced by the arbitrary distorter are corrected.

5.2 Theory.

The simplest example of a nonparaxial lossless scatterer is a partially transparent lossless conventional plane mirror (e. g. dielectric beamsplitter). When illuminated by an incident plane wave, $\mathbf{E}_i$, the transmitted and reflected components, $\mathbf{E}_1$ and $\mathbf{E}_r$, constitute the forward scattered and backscattered waves respectively. The complex amplitudes of the three waves are related via the complex amplitude coefficients of transmittance and reflectance, t and r respectively, of the conventional reflecting surface as follows

$$A_1 = tA_i, \tag{5.1a}$$

$$A_r = rA_i. \tag{5.1b}$$

Replacing the arbitrary lossless phase distorter in Fig. 5.1b) with a partially transparent lossless conventional plane mirror the optical system immediately resembles a Fabry–Perot interferometer with a PCM in place of one of the conventional reflecting surfaces, Fig. 5.2. The self aligning characteristic of the PCM insures that a simple two arm resonant mode is established between the PCM and the conventional plane reflecting surface. The intercavity fields are denoted by $\mathbf{E}_1$, $\mathbf{E}_2$, $\mathbf{E}_3$ and $\mathbf{E}_4$ as depicted in Fig. 5.2 and are accompanied by the incident, reflected and phase conjugate fields, $\mathbf{E}_i$, $\mathbf{E}_r$ and $\mathbf{E}_c$ respectively. The intercavity complex amplitudes, A_1, A_2, A_3 and A_4, are inter–linked due to the multiple reflections of the resonant mode and are coupled to the external field amplitudes A_i, A_r and A_c.

The intercavity complex amplitudes are related as follows

$$A_1 = tA_i + r'A_4, \tag{5.2a}$$

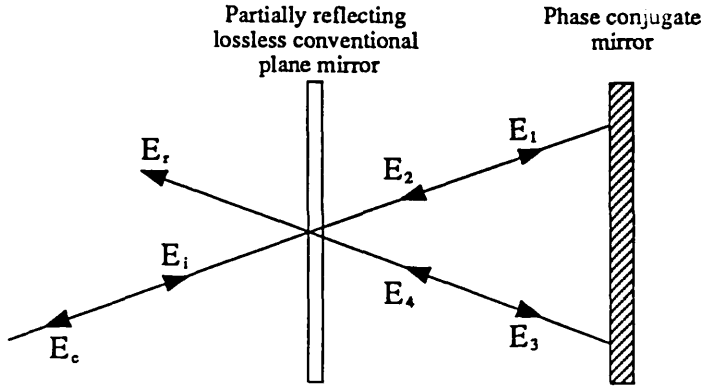


Figure 5.2 Phase conjugate Fabry–Perot interferometer.

$$A_2 = \mu_a A_1^*, \tag{5.2b}$$

$$A_3 = r' A_2, \tag{5.2c}$$

$$A_4 = \mu_b A_3^*, \tag{5.2d}$$

where the complex amplitude coefficients of transmittance and reflectance of the partially reflecting lossless conventional plane mirror are t, r and t′, r′ for illumination from the left and right hand sides respectively. The complex amplitude coefficients of reflectance of the PCM, μ_a and μ_b, defined by Eqs. (5.2b) and (5.2d), will in general differ in both magnitude and intrinsic phase and are expressed explicitly as follows

$$\mu_a = u_a \exp[i\phi_a], \tag{5.3a}$$

$$\mu_b = u_b \exp[i\phi_b]. \tag{5.3b}$$

The intercavity complex amplitudes can also be expressed by the infinite series

$$A_1 = \left[t + t\mu_a^*\mu_b|r'|^2 + t(\mu_a^2)^*\mu_b^2|r'|^4 + \dots\right] A_i, \tag{5.4a}$$

$$A_2 = \left[\mu_a t^* + \mu_a^2 t^*\mu_b^*|r'|^2 + \mu_a^3 t^*(\mu_b^2)^*|r'|^4 + \dots\right] A_i^*, \tag{5.4b}$$

$$A_3 = \left[\mu_a t^* r' + \mu_a^2 t^*\mu_b^*|r'|^2 r' + \mu_a^3 t^*(\mu_b^2)^*|r'|^4 r' + \dots\right] A_i^*, \tag{5.4c}$$

$$A_4 = \left[\mu_b\mu_a^* t(r')^* + \mu_b^2(\mu_a^2)^* t|r'|^2(r')^* + \mu_b^3(\mu_a^3)^* t|r'|^4(r')^* + \dots\right] A_i. \tag{5.4d}$$

which are simplified to

$$A_1 = t\sum_{n=0}^{\infty}(\mu_a^n)^*\mu_b^n|r'|^{2n} A_i, \tag{5.5a}$$

$$A_2 = \mu_a t^* \sum_{n=0}^{\infty} \mu_a^n (\mu_b^n)^* |r'|^{2n} A_i^*, \tag{5.5b}$$

$$A_3 = \mu_a t^* r' \sum_{n=0}^{\infty} \mu_a^n (\mu_b^n)^* |r'|^{2n} A_i^*, \tag{5.5c}$$

$$A_4 = \mu_b \mu_a^* t (r')^* \sum_{n=0}^{\infty} (\mu_a^n)^* \mu_b^n |r'|^{2n} A_i. \tag{5.5d}$$

The n^{th} component of each infinite series constitutes the contribution to that field from the n^{th} cavity round trip. The external complex field amplitudes, A_r and A_c, are coupled to the intercavity fields as follows

$$A_r = rA_i + t'A_4, \tag{5.6a}$$

$$= \left[r + \mu_b \mu_a^* t' t (r')^* \sum_{n=0}^{\infty} (\mu_a^n)^* \mu_b^n |r'|^{2n} \right] A_i \tag{5.6b}$$

and

$$A_c = t'A_2, \tag{5.6c}$$

$$= \mu_a t' t^* \sum_{n=0}^{\infty} \mu_a^n (\mu_b^n)^* |r'|^{2n} A_i^* \tag{5.6d}$$

where Eqs. (5.5b) and (5.5d) have been employed.

Using Eqs. (5.2) the complex amplitude A_1 can be re–expressed in terms of A_i only, consider

$$A_4 = \mu_b A_3^*, \tag{5.2d}$$

$$= \mu_b (r')^* A_2^* = \mu_b (r')^* \mu_a^* A_1, \tag{5.7}$$

and substituting into (5.2a) yields

$$A_1 = tA_i + r'A_4, \tag{5.2a}$$

$$= \frac{t}{[1 - \mu_a^* \mu_b |r'|^2]} A_i \tag{5.8a}$$

and similarly

$$A_2 = \frac{\mu_a t^*}{[1 - \mu_a \mu_b^* |r'|^2]} A_i^* \tag{5.8b}$$

$$A_3 = \frac{\mu_a t^* r'}{[1 - \mu_a \mu_b^* |r'|^2]} A_i^* \tag{5.8c}$$

$$A_4 = \frac{\mu_b \mu_a^* t (r')^*}{[1 - \mu_a^* \mu_b |r'|^2]} A_i \tag{5.8d}$$

Equations (5.5) and (5.8) are equivalent expressions. Employing Eqs. (5.8b) and (5.8d), the external complex field amplitudes are simplifies as follows

$$A_r = rA_i + t'A_4, \tag{5.6a}$$

$$= \left\{ r + \frac{\mu_b \mu_a^* t' t(r')^*}{[1 - \mu_a^* \mu_b |r'|^2]} \right\} A_i, \tag{5.9a}$$

$$= \frac{r[1 - \mu_a^* \mu_b \xi]}{[1 - \mu_a^* \mu_b |r'|^2]} A_i \tag{5.9b}$$

where

$$\xi = |r'|^2 - \frac{t' t(r')^*}{r}, \tag{5.10}$$

which is dependent only on the complex amplitude coefficients of the partially reflecting conventional plane mirror. Recall the generalised Stokes relations for *time reversed* waves at a lossless plane beamsplitter, Appendix H,

$$t^* r' + r^* t = 0, \tag{5.11a}$$

$$t^* t' + r^* r = 1 \tag{5.11b}$$

and substituting into the equation for ξ, Eq. (5.10),

$$\xi = |r'|^2 - \frac{t' t(r')^*}{r}, \tag{5.10}$$

$$= |r'|^2 + \frac{r t^* t'}{r},$$

$$= |r'|^2 + 1 - |r|^2,$$

$$= 1 \tag{5.12}$$

for any lossless plane reflecting surface. The complex amplitude of the specularly reflected wave, A_r Eq. (5.9b), becomes

$$A_r = \frac{r[1 - \mu_a^* \mu_b]}{[1 - \mu_a^* \mu_b |r'|^2]} A_i. \tag{5.13}$$

The complex amplitude of the phase conjugate wave, A_c, is similarly re-expressed using Eqs. (5.6c), (5.8b) and (5.11b) to reveal

$$A_c = \frac{\mu_a t' t^*}{[1 - \mu_a \mu_b^* |r'|^2]} A_i^*,$$

$$= \frac{\mu_a [1 - |r|^2]}{[1 - \mu_a \mu_b^* |r'|^2]} A_i^*. \tag{5.14}$$

The intensities of the specularly reflected and phase conjugate waves, I_r and I_c respectively, can be deduced from their complex amplitudes, A_r, A_c and Eqs. (5.13), (5.14), as follows

$$\begin{aligned} I_r &= |A_r|^2, \\ &= A_r A_r^*, \\ &= \frac{r[1-\mu_a^*\mu_b]}{[1-\mu_a^*\mu_b|r'|^2]}\frac{r^*[1-\mu_a\mu_b^*]}{[1-\mu_a\mu_b^*|r'|^2]}A_i A_i^*, \\ &= \frac{|r|^2\left[1+|\mu_a|^2|\mu_b|^2-2\Re(\mu_a^*\mu_b)\right]}{\left[1+|\mu_a|^2|\mu_b|^2|r'|^4-2\Re(\mu_a^*\mu_b|r'|^2)\right]}I_i \end{aligned}$$

and employing Eqs. (5.3a) and (5.3b)

$$I_r = \frac{R\left[1+R_{c_a}R_{c_b}-2\sqrt{R_{c_a}R_{c_b}}\cos(\phi_a-\phi_b)\right]}{\left[1+R^2R_{c_a}R_{c_b}-2R\sqrt{R_{c_a}R_{c_b}}\cos(\phi_a-\phi_b)\right]}I_i, \tag{5.15}$$

where the intensity coefficients of reflectance of the conventional and phase conjugate mirrors, R, R_{c_a} and R_{c_b}, are given by

$$R = |r|^2, \tag{5.16a}$$

$$= |r'|^2, \tag{5.16b}$$

$$R_{c_a} = |\mu_a|^2, \tag{5.16c}$$

$$R_{c_b} = |\mu_b|^2. \tag{5.16d}$$

Similarly for I_c

$$\begin{aligned} I_c &= |A_c|^2, \\ &= \frac{\mu_a[1-|r|^2]}{[1-\mu_a\mu_b^*|r'|^2]}\frac{\mu_a^*[1-|r|^2]}{[1-\mu_a^*\mu_b|r'|^2]}A_i^*A_i, \\ &= \frac{|\mu_a|^2[1-|r|^2]^2}{\left[1+|\mu_a|^2|\mu_b|^2|r'|^4-2\Re(\mu_a^*\mu_b|r'|^2)\right]}I_i, \end{aligned}$$

$$I_c = \frac{R_{c_a}[1-R]^2}{\left[1+R^2R_{c_a}R_{c_b}-2R\sqrt{R_{c_a}R_{c_b}}\cos(\phi_a-\phi_b)\right]}I_i. \tag{5.17}$$

The expressions for both the complex amplitudes and relative intensities of the specularly reflected and phase conjugate waves, A_r, A_c, I_r, I_c and Eqs. (5.13), (5.14), (5.15) and (5.17), are cited in references [5.19,5.20] and are a generalisation of the expressions originally derived by Drummond and Friberg [5.21,5.22], Nazarathy [5.23] and Nieto-Vesperinas [5.24].

5.2.1 Specular reflection cancellation.

Consider the relative intrinsic phase of the two phase conjugate reflections, $(\phi_a - \phi_b)$, to equal zero, the specularly reflected and phase conjugate field intensities, Eqs. (5.15) and (5.17) respectively, become

$$I_r = \frac{R\left[1 - \sqrt{R_{c_a} R_{c_b}}\right]^2}{\left[1 - R\sqrt{R_{c_a} R_{c_b}}\right]^2} I_i, \tag{5.18a}$$

$$I_c = \frac{R_{c_a}[1 - R]^2}{\left[1 - R\sqrt{R_{c_a} R_{c_b}}\right]^2} I_i \tag{5.18b}$$

and are graphically represented in Figs. 5.3 and 5.4 for $R_{PC} = R_{c_a} = R_{c_b}$ and R=0.4 and 0.9 respectively.

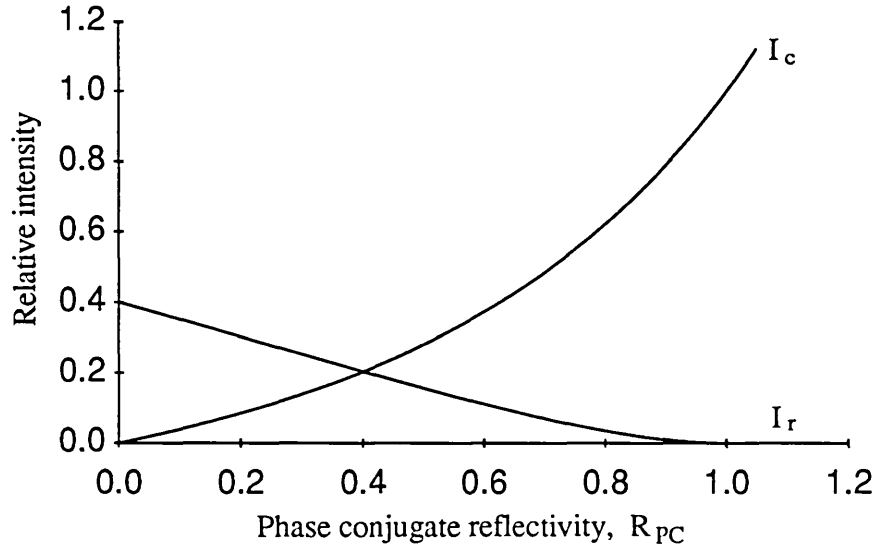


Figure 5.3 The relative intensities of I_r and I_c versus the phase conjugate reflectivity, R_{PC}, of the PCM for $(\phi_a - \phi_b) = 0$ and R=0.4.

For both values of R the relative intensities of the specular reflection, I_r, and the phase conjugate, I_c, are seen to drop off monotonically to zero and rise monotonically to unity respectively as functions of R_{PC} and at $R_{PC} = 1$ the two relative intensities become $I_r = 0$ and $I_c = 1$. These two observations are consistent with the conservation of energy and serve to support the generalised scattering theory of PC optics by Agarwal *et al* [5.18], Fig. 5.1. The extensive backscatter, the specular reflection off the partially reflecting lossless conventional mirror Fig. 5.2, is

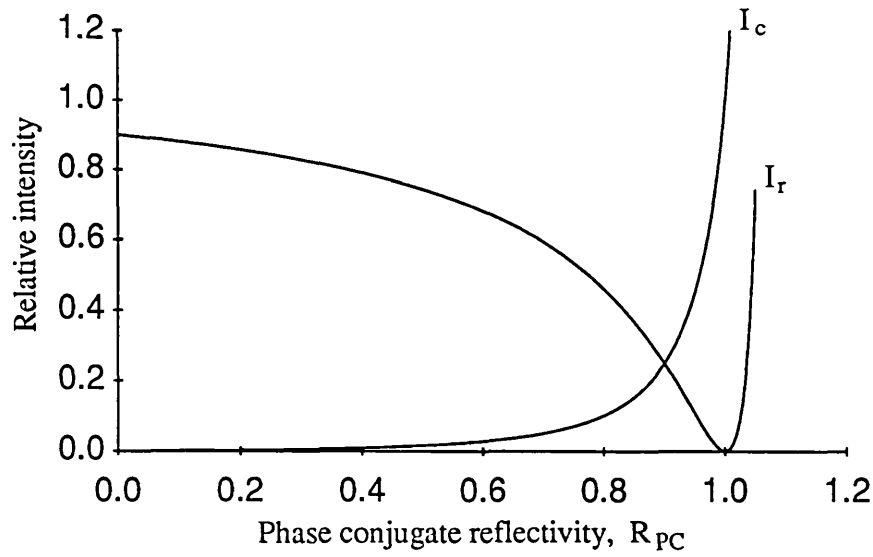


Figure 5.4 The relative intensities of I_r and I_c versus the phase conjugate reflectivity, R_{PC}, of the PCM for $(\phi_a - \phi_b) = 0$ and R=0.9.

completely extinguished at $R_{PC} = 1$, independent of the value of R for $0 < R < 1$. Concurrently, the relative PC intensity is unity and also is independent of R. For $R_{PC} > 1$ the PCM exhibits gain which amplifies the intercavity fields and causes both I_r and I_c to rise monotonically from zero and unity respectively w. r. t. R_{PC}.

5.2.2 Specular reflection enhancement.

Consider the relative intrinsic phase, $(\phi_a - \phi_b)$, to equal π, the specularly reflected and phase conjugate intensities, Eqs. (5.15) and (5.17) respectively, become

$$I_r = \frac{R\left[1 + \sqrt{R_{c_a} R_{c_b}}\right]^2}{\left[1 + R\sqrt{R_{c_a} R_{c_b}}\right]^2} I_i, \qquad (5.19a)$$

$$I_c = \frac{R_{c_a}[1 - R]^2}{\left[1 + R\sqrt{R_{c_a} R_{c_b}}\right]^2} I_i \qquad (5.19b)$$

and are graphically represented in Figs. 5.5 and 5.6 for again R=0.4 and 0.9 respectively.

For both values of R the relative intensity of the specular reflection rises monotonically from R w. r. t. R_{PC} i. e. the specular reflection intensity is enhanced as R_{PC} is increased. Similtaneously I_c also rises monotonically, from zero, but much slower than for $(\phi_a - \phi_b) = 0$. The values of I_r and I_c at $R_{PC} = 1$ sum to unity and are functionally dependent on R.

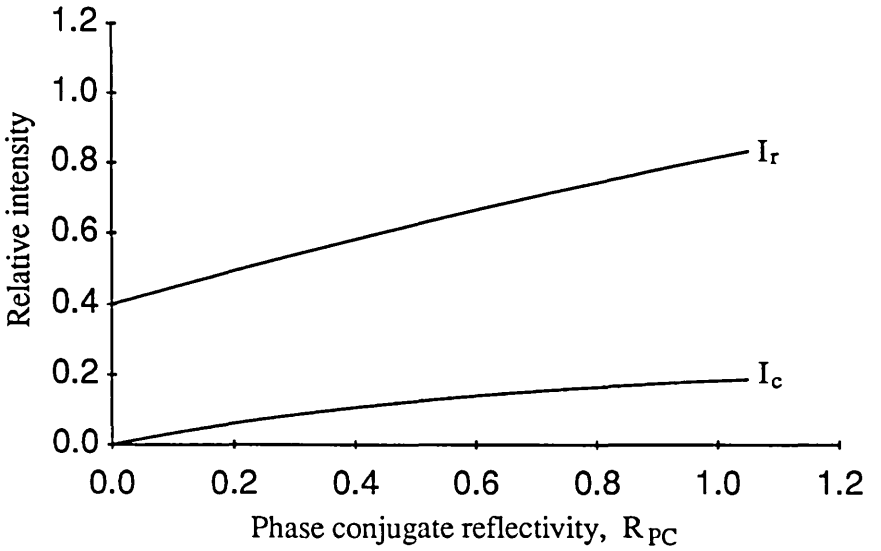


Figure 5.5 The relative intensities of I_r and I_c versus the phase conjugate reflectivity, R_{PC}, of the PCM for $(\phi_a - \phi_b) = \pi$ and R=0.4.

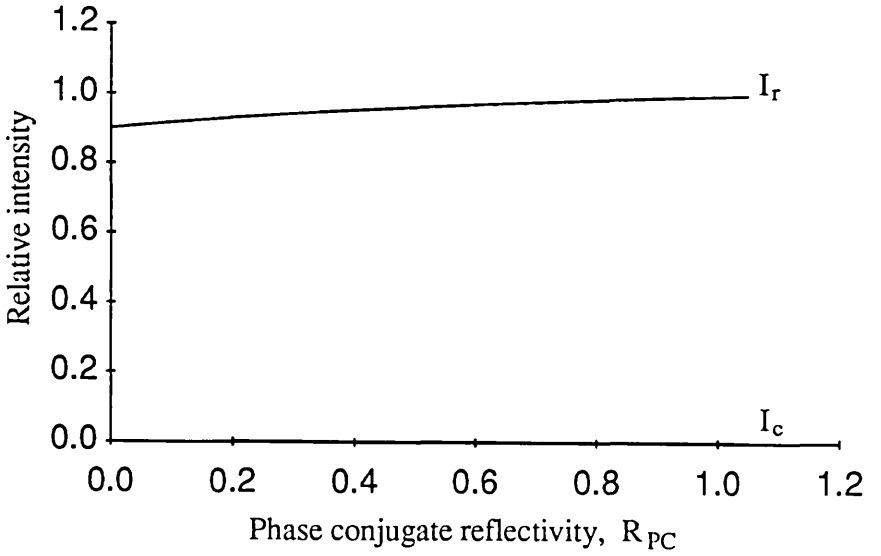


Figure 5.6 The relative intensities of I_r and I_c versus the phase conjugate reflectivity, R_{PC}, of the PCM for $(\phi_a - \phi_b) = \pi$ and R=0.9.

5.3 Experimental procedure and results.

Two experimental investigations were devised and performed to verify the functional dependence of the phase conjugate reflectivity, R_{PC}, and relative intrinsic

phase, $(\phi_a - \phi_b)$, on the specularly reflected intensity, I_r. The experiments were conducted using an argon ion laser operating at $\lambda = 514.5$nm in single transverse and long-itudinal modes. The light was phase conjugated by degenerate four wave mixing, DFWM, in photorefractive barium titanate and a dielectric plane beam splitter acted as the partially reflecting lossless conventional plane mirror.

The first of the two complementary experiments employed only one PR crystal of barium titanate, $BaTiO_3^{\#1}$, and a single self-pumping pump beam to act as the phase conjugate mirror, PCM, Fig. 5.7. The intensity and geometry of the pump beam were chosen to generate a steady *cw* self-pumped phase conjugate, PC, beam, Fig. 4.16a). The incident low intensity *p* polarised light, spatially filtered and collimated, I_i, was reflected off the dielectric beam splitter, I_r, with a characteristic intensity reflectance of R=0.37. The transmitted light, I_1, was steered towards the self-pumping crystal of $BaTiO_3$ using a mirror. The existing high fidelity counterpropagating conjugate pair of wavefronts in the PR material served to act as the pumping beams for the phase conjugation of the angularly offset weak probe beam by DFWM, [5.25]. The phase conjugate beam, I_2, retraced the return path to arrive back at the dielectric beam splitter. The transmitted component, I_c, constitutes the phase conjugate of the incident beam, I_i, and the reflected component, I_3, was steered back towards the same self-pumping $BaTiO_3$ crystal. This second low intensity probe beam was also phase conjugated by DFWM in the self-pumped crystal of $BaTiO_3$. The PC wavefront generated, I_4, travelled back to the dielectric beam splitter where its transmitted component contributed to the intensity of the specular reflection, I_r. The reflected component, contributing to I_1, constituted the beginning of the second cavity round trip. The round trip length of the resonant cavity was $\sim$ 1m and the intercavity field intensities I_3 and I_4 were sampled using the beam splitter and measured with detector$^{\#2}$, Fig. 5.7. The variable neutral density, ND, filter served to control the intensity reflectance of the second PC reflection, R_{c_b}. The additional phase introduced onto the transmitted beam, I_3, by the beam splitter and ND filter, was of no importance as it was accomodated by the phase conjugate nature of the return beam, I_4.

Both PC reflections were performed using the same set of counterpropagating conjugate pump beams and consequently the two PCs, I_2 and I_4, were linked in phase. In the absence of the amplitude and spectral instabilities inherent with the self-pumped phase conjugator [5.26], the intrinsic phases, ϕ_a and ϕ_b Eqs. (5.3a) and (5.3b), are equal and the relative intrinsic phase, $(\phi_a - \phi_b)$, is reduced to zero; the phase condition for specular reflection cancellation. The PC reflectivity, R_{PC},

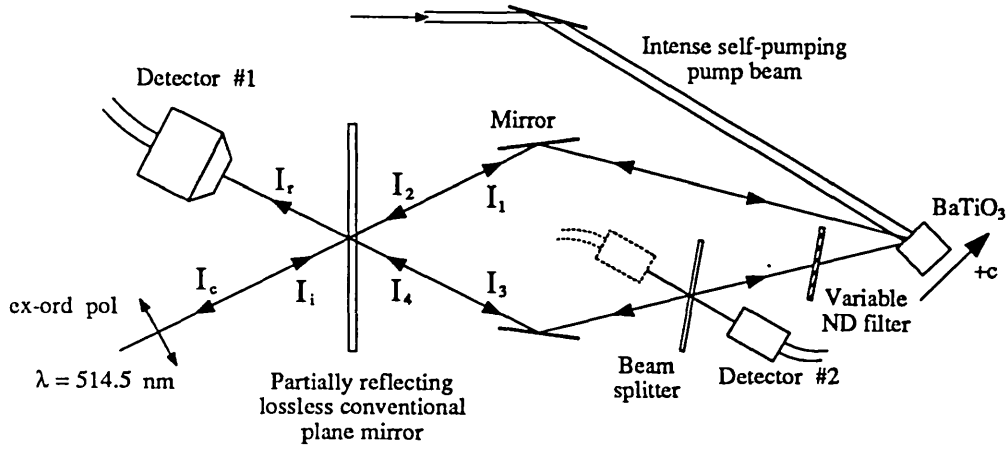


Figure 5.7 Schematic representation of the experimental apparatus used in the first experiment.

was measured independent of the intensity of the specular reflection, I_r. Blocking the intercavity beam after the sampling beam splitter broke the resonant loop and reduced I_4 to zero. The sampled intensity of I_3, measured using detector$^{\#2}$, revealed the PC reflectivity of the first PC reflection, R_{c_a}. Unblocking the intercavity beam allowed the resonant loop to establish and the ratio of the sampled intensities of I_3 and I_4, both having changed, revealed the PC reflectivity of the second PC reflection, R_{c_b}. Combining the two results the resultant PC reflectivity was deduced using the relation

$$R_{PC} = \sqrt{R_{c_a} R_{c_b}}. \tag{5.20}$$

Concurrently, the intensity of the specular reflection, I_r, was monitored using detector$^{\#1}$. A typical temporal response of the specularly reflected intensity, highlighting the extent of the cancellation mechanism, is shown in Fig. 5.8. Initially, $t < 0$, the incident beam and hence the specular reflection were zero. At t=0 the incident beam was applied while the resonant cavity was incomplete, $I_4 = 0$, and the specularly reflected intensity rose to a constant value corresponding to R=0.37. After $\sim$ 7seconds the cavity was completed and a resonant loop of light became established, $I_4 > 0$. Immediately the intensity of the specular reflection began to fall, continuing to drop as the intercavity intensities grew. From $\sim 12 < t <\sim$ 16seconds the greatly reduced specular reflection held steady, except for the odd spurious spike. At $t \sim$ 16seconds the intercavity beam was re–blocked and the specularly reflected intensity switched immediately back up to its original

steady state value.

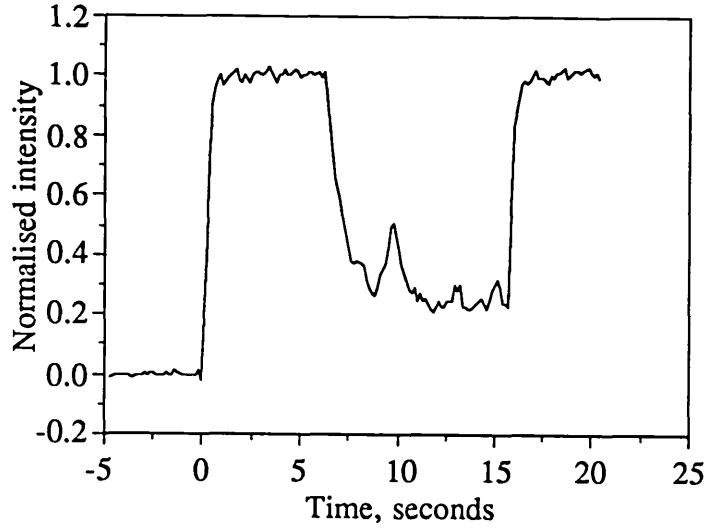


Figure 5.8 The normalised intensity of the specular reflection versus time.

A systematic series of experiments were performed, measuring the change in specularly reflected intensity, I_r, as a function of R_{PC} by controlling the variable ND filter and hence R_{c_b}. The experimental results, o, are shown in Fig. 5.9 and tabulated in Appendix I. The data points are accompanied by the theoretical curve, ——, for R=0.37, Eq. (5.18a). The two data sets are in good agreement, especially for $R_{PC} < 0.6$, and both display a minimum value for I_r at $R_{PC} = 1$. These two observations lend support to the earlier theoretical interpretation of a Fabry–Perot interferometer with a PCM, Section 5.2, and the generalised scattering theory of phase conjugation by Agarwal *et al* [5.18].

However, the manner in which the raw experimental data was interpreted should be appreciated. A typical temporal response of the steady state cancelled specular reflection is shown in Fig. 5.10. As can be observed the temporal profile is not a well behaved time invariant trace but consists of a random series of spikes, rising from what appears to be a baseline. This particular data set, Fig. 5.10, was analysed and found to have the following statistics; a maximum of 3.11, a minimum of 0.91 and an average of 1.26. The average value of this typical data set was as much a function of the fluctuations as it was of the cancellation process. Consequently the minimum value of the data set was considered to be a more realistic measure of the extent of cancellation of the specularly reflected beam and

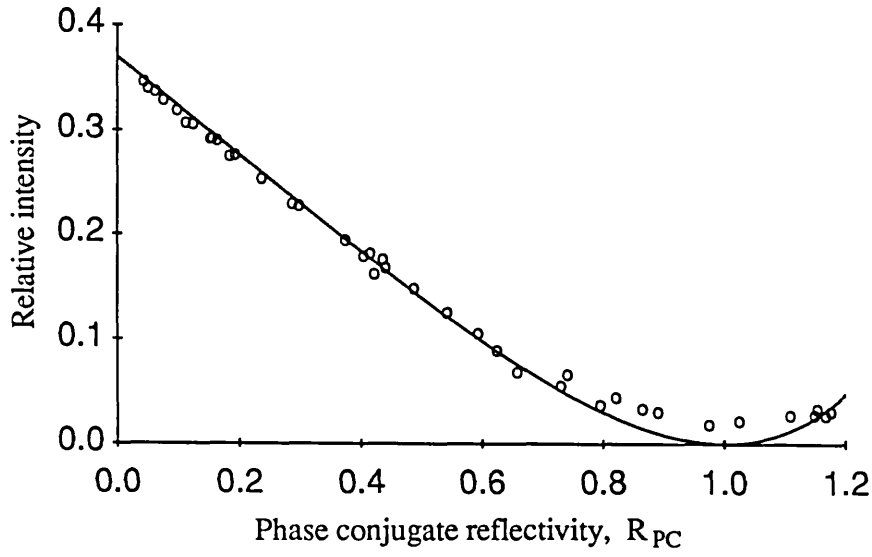


Figure 5.9 The relative intensity of the specular reflection, I_r, versus the phase conjugate reflectivity, R_{PC}; theoretical curve, ——, and experimental points, o.

was used to deduce the experimental points shown in Fig. 5.9, o. The cause of the fluctuations was not identified, however air turbulance in the laboratory and instabilities in the self pumped phase conjugator [5.26] were considered the most likely candidates. In particular the spectral instabilities of the phase conjugator [5.26], observed as a Doppler frequency shift of 0.1–1 Hz randomly wandering between both red and blue, would serve to disrupt the spectral and amplitude stabilities of the intercavity fields and cause a fluctuating specularly reflected intensity.

Complete cancellation of the specular reflection was not observed, a minimum of $I_r = 0.018$ (5%) @ $R_{PC} = 0.975$ was recorded, Fig. 5.9 and Appendix I. The effect of absorption in the partially reflecting conventional plane mirror was theoretically investigated by Drummond and Friberg [5.22] and was shown to cause both incomplete cancellation and a shift in the cancellation minimum to $R_{PC} > 1$. However the absorption of the dielectric beam splitter used in the experiment discussed above and shown in Fig. 5.7, was negligibly small ($< 1\%$) and its contribution to the results can be neglected. The cancellation of the specularly reflected beam was observed to be spatially non uniform which was particularly noticable for $R_{PC} \sim 1$. This observation suggests the fidelity of the phase conjugates generated by the self pumped PCM, although high, were less than unity and responsible for the incomplete cancellation of the specularly reflected beam at $R_{PC} = 1$.

The second of the two experiments employed two PR crystals of barium titanate,

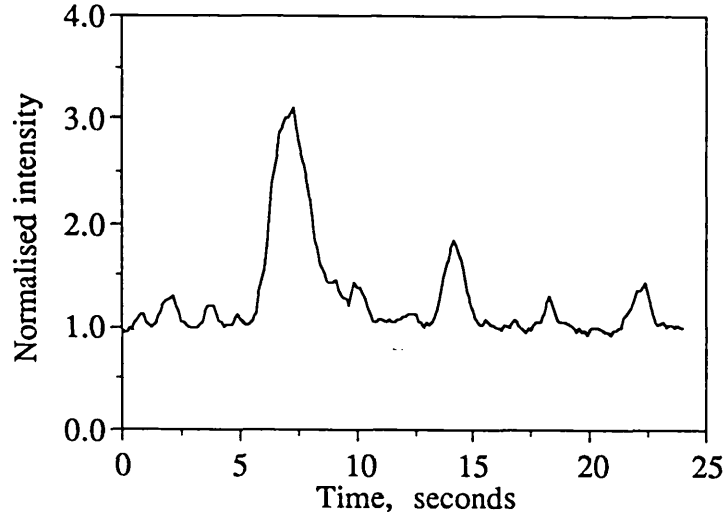


Figure 5.10 Normalised intensity of the cancelled specularly reflection versus time.

$BaTiO_3^{\#1}$ and $BaTiO_3^{\#2}$, which were independently externally pumped using intense counterpropagating pump beams. The phase conjugate reflectivities, R_{c_a} and R_{c_b}, of the two PCMs were independently controlled using the variable ND filters placed in the two readout pump beams. The phases introduced by the ND filters were significant as they were directly related to the values of the intrinsic phase shifts of the PC reflections, ϕ_a and ϕ_b and Eqs. (5.3a) and (5.3b). The relative intrinsic phase, $(\phi_a - \phi_b)$, now also a free parameter, was controlled using the variable phase shifter placed in the second of the two readout pump beams. The experimental arrangment is schematically illustrated in Fig. 5.11.

The incident *p* polarised beam, I_i, was unchanged from the previous experiment, the characteristic reflectivity of the conventional plane mirror, the dielectric beam splitter, remained unchanged @ R=0.37 and the transmitted component, I_1, was steered towards the first externally pumped $BaTiO_3$ crystal using a mirror. The phase conjugate reflection, generated by DFWM, I_2, returned back to the dielectric beam splitter and was partially reflected, I_3, and steered towards the second externally pumped $BaTiO_3$ crystal. The second PC reflection, I_4, returned to the dielectric beam splitter to complete the resonant cavity round trip. Once again the sampling beam splitter and detector$^{\#2}$ were used to monitor the intercavity field intensities I_3 and I_4 which were used to deduce the phase conjugate reflectivity, R_{PC} Eq. (5.20).

There was no means to directly measure the relative intrinsic phase shift, $(\phi_a - \phi_b)$,

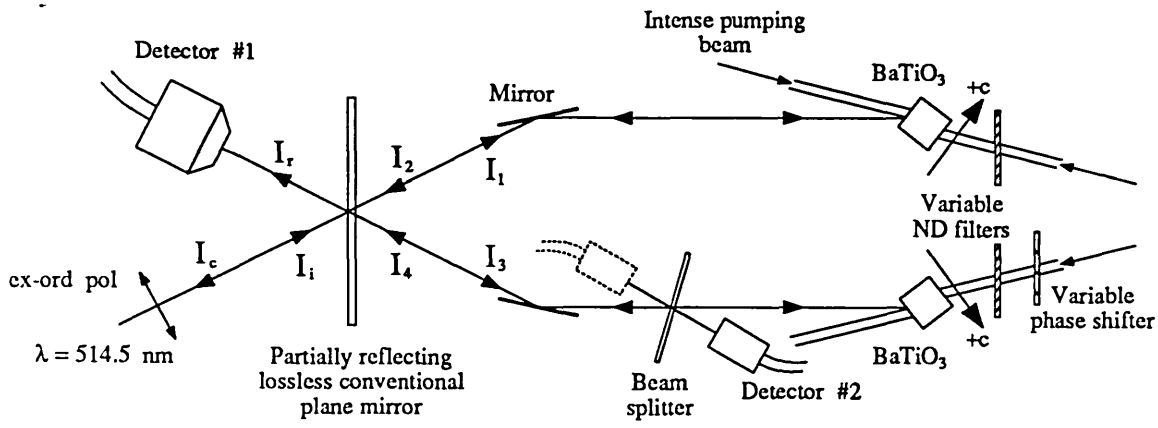


Figure 5.11 Schematic representation of the experimental apparatus used in the second experiment.

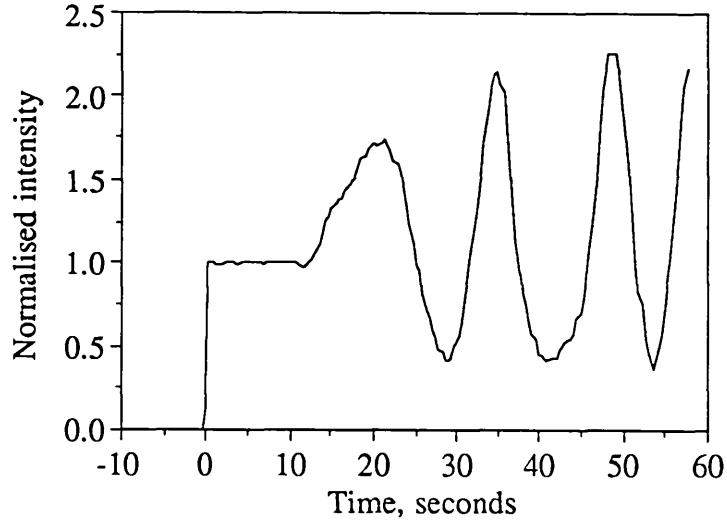


Figure 5.12 The normalised specularly reflected intensity, I_r, versus time for a slow scan of the relative intrinsic phase, $(\phi_a - \phi_b)$.

due to the interplay of both variable ND filters and phase shifter. To acquire meaningful experimental data the variable phase shifter was made to scan slowly through all 2π angles and more. The relative intrinsic phase shift was then compelled to pass through zero; the phase condition for specular reflection cancellation,

and π; specular reflection enhancement, during any 2π phase cycle. A typical temporal response of the specularly reflected intensity, I_r, is shown in Fig. 5.12. Initially, $t < 0$, the incident beam and hence the specular reflection were zero, $I_i = 0$ and $I_r = 0$. At t=0 the incident beam was applied, $I_i > 0$, while the resonant cavity was incomplete, $I_4 = 0$. Consequently the specularly reflected intensity rose immediately to a constant value corresponding to R=0.37. After $t \sim$ 10seconds the resonant cavity was completed while the variable phase shifter was slowly scanning. The intercavity field intensities, I_3 and I_4, grew and the specularly reflected intensity begain to oscillate between well defined upper and lower intensity limits. The limits, 2.259 and 0.370 respectively, were asymmetricaly located w. r. t. the originally constant specularly reflected intensity, $0 < t <$ 10seconds, of unity. When the scan rate or induced Doppler frequency shift was reduced, the period of oscillation grew accordingly but the two limits became less well defined. In the limit of the Doppler shift reduced to zero, the specularly reflected intensity was observed to wander slowly in an uncontrolled manner between cancellation and enhancement states.

Operating at a sufficiently fast phase scan rate to give well defined limits, as shown in Fig. 5.12, a systematic series of experiments were conducted. The upper and lower limits to the specularly reflected intensity, I_r, were measured as a function of the phase conjugate reflectivity, R_{PC}, and the results are shown in Fig. 5.13.

The experimental data points, for both cancellation, o, and enhancement, $\star$, appear to follow the dotted theoretical curves, ..., rather than the solid curves, ——, with the minimum specularly reflected intensity, I_r recorded at $R_{PC} > 1$. The solid curves, ——, correspond to specular reflection cancellation, $(\phi_a - \phi_b) = 0$, and enhancement, $(\phi_a - \phi_b) = \pi$, for an infinite number of iterations established in the resonant cavity, Eqs. (5.18a) and (5.19a) respectively. The dotted curves, ..., correspond to only one iteration established in the cavity. The trends in the experimental data suggests that the latter was true in the experimental situation.

The variable phase shifter was placed in the readout pump beam of the second PCM and consequently the intrinsic phase ϕ_b adopted a time dependence of

$$\phi_b = \varrho t, \tag{5.21}$$

where ϱ is the Doppler frequency shift introduced by the scanning phase shifter which was typically 0.1Hz in practise. The complex amplitude coefficient of reflectance of the second PCM, μ_b Eq. (5.3b), becomes

$$\mu_b = u_b \exp[i\varrho t]. \tag{5.22}$$

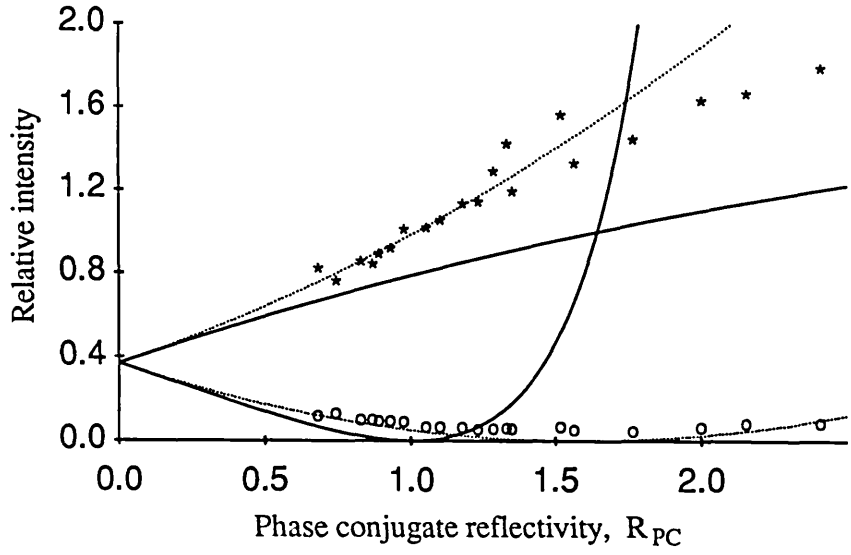
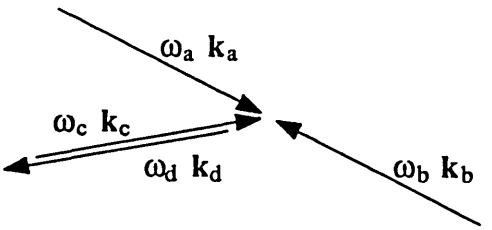


Figure 5.13 Graphical representation of the maximum and minimum of the relative specularly reflected intensity, I_r, versus the phase conjugate reflectivity, R_{PC}, for R=0.37. The theoretical curves correspond to cancellation and enhancement for an infinite number of iterations, ——, and a single iteration, ..., established in the resonant cavity. The experimental points, o and ⋆, correspond to the measured lower and upper intensity limits respectively.

The implications of the Doppler frequency shift, ϱ, on the intercavity fields, $\mathbf{E}_1$, $\mathbf{E}_2$, $\mathbf{E}_3$ and $\mathbf{E}_4$, are best explained by considering individually each successive iteration around the resonant cavity. Enforcing the conservation of energy condition for FWM optical geometries, schematically illustrated in Fig. 5.14, and employing the intercavity complex amplitudes, A_1, A_2, A_3 and A_4, expressed by their infinite series, Eqs. (5.5a), (5.5b), (5.5c) and (5.5d) respectively, the angular temporal frequencies of the succesive field components are summarised in the Table 5.I.

It is observed from Table 5.I that the Doppler frequency shift, ϱ, accumulates as the light re–iterates around the resonant cavity. The $\mathbf{E}_1$ and $\mathbf{E}_4$ field components acquire blue Doppler shifts while the $\mathbf{E}_2$ and $\mathbf{E}_3$ field components gain red. For such a complex system of fields to become established in the resonant cavity the PCMs are required to phase conjugate all the incident field components, $\mathbf{E}_1$ and $\mathbf{E}_3$, independent of what frequency they bear.

Wave mixing in photorefractive materials with a Doppler frequency shifted sig-



Conservation of momemtum: $\mathbf{k}_d = \mathbf{k}_a + \mathbf{k}_b - \mathbf{k}_c$

Conservation of energy: $\omega_d = \omega_a + \omega_b - \omega_c$

Figure 5.14 The conservation of energy and momentum in FWM optical geometries.

Iteration component number n	Angular temporal frequencies E_1	E_2	E_3	E_4
0	ω	ω	ω	$\omega+\varrho$
1	$\omega+\varrho$	$\omega-\varrho$	$\omega-\varrho$	$\omega+2\varrho$
2	$\omega+2\varrho$	$\omega-2\varrho$	$\omega-2\varrho$	$\omega+3\varrho$
3	$\omega+3\varrho$	$\omega-3\varrho$	$\omega-3\varrho$	$\omega+4\varrho$
⋮	⋮	⋮	⋮	⋮

Table 5.I Doppler frequency shifts for the succesive components of the intercavity fields.

nal wave generates an interference pattern which scans through the volume of the medium along the direction of the grating wavevector, **k**. A phase volume hologram will only be succefully induced in the medium, scanning with the interference pattern, if the characteristic response time of the PR material is less than the period of the Doppler frequency shift. The characteristic response time of $BaTiO_3$ is typically 1–10 seconds at nominal wave mixing intensities. Hence it is proposed that in the second experiment, Fig. 5.11, the first iteration around the cavity, iteration number 0 Table 5.I, was established but the second iteration and consequently all further iterations were quenched due to the slow speed of response of the $BaTiO_3$ crystals employed. Employing the equation for the complex

amplitude of the specularly reflected field, A_r, Eq. (5.6b), for n=0 only,

$$A_r = \left[r + \mu_a^* \mu_b t' t (r')^*\right] A_i, \tag{5.23a}$$

$$= r\left[1 - \mu_a^* \mu_b (1 - |r|^2)\right] A_i, \tag{5.23b}$$

the specularly reflected intensities for the relative intrinsic phase conditions $(\phi_a - \phi_b) = 0$ and $(\phi_a - \phi_b) = \pi$ were calculated and are shown as follows

$$I_r = R\left[1 - (1 - R)\sqrt{R_{c_a} R_{c_b}}\right]^2 I_i \tag{5.24a}$$

and

$$I_r = R\left[1 + (1 - R)\sqrt{R_{c_a} R_{c_b}}\right]^2 I_i \tag{5.24b}$$

for $(\phi_a - \phi_b) = 0$ and π respectively. Equations (5.24a) and (5.24b) are graphically represented in Fig. 5.13 by the dotted, ..., curves. Increasing the size of the Doppler frequency shift had no effect on the observed results which supports the above proposal. Decreasing ϱ, as stated earlier, led to the upper and lower limits of the oscillating specularly reflected intensity, I_r, to become less well defined. The apparent instability of I_r was considered to be a combination of air turbulance in the laboratory and additional iterations, e. g. n=1, becoming established in the cavity.

Again incomplete extinction of the specularly reflected intensity was observed with a minimum of $I_r = 0.045$ (12%) @ $R_{PC} = 1.767$recorded, Fig. 5.13 and Appendix I. The cancellation of the specularly reflected beam was again observed to be spatially non uniform, visibly poorer than for the first experiment, and was considered responsible for the incomplete cancellation.

5.4 Conclusions.

Extensive specular reflection cancellation was observed in the presence of a phase conjugate mirror. The maximum extinction was an intensity drop to 5% of the original, measured for with a phase conjugate reflectivity, R_{PC} of unity. Incomplete cancellation was observed as the fidelity of the phase conjugate reflections, although high, were less than unity. The two sets of experimental results were in good agreement with the theoretical predictions originally derived by Friberg and Drummond [5.21,5.22] and generalised by Lindsay and Dainty [5.19,5.20]. The results support ultimately the general scattering theory of wave front phase distortion correction by phase conjugation by Agarwal *et al* [5.18].

5.5 References.

[5.1] A. Yariv, "Phase conjugate optics and real time holography," IEEE J.Quant Electron. **QE–14**, 650–660 (1978).

[5.2] D.M. Pepper, "Non–linear optical phase–conjugation," Opt.Eng. **21**, 156–183 (1983).

[5.3] R.A. Fisher, ed., "Optical Phase Conjugation," (Academic, New York, 1983).

[5.4] A.E. Chiou and P. Yeh, "Parallel image subtraction using a phase–conjugate Michelson interferometer," Opt.Lett. **11**, 306–308 (1986).

[5.5] D.Z. Anderson, D.M. Lininger and J. Feinberg, "Optical tracking novelty filter," Opt. Lett. **12**, 123–125 (1987).

[5.6] M.B. Klein, G.J. Dunning, G.C. Valley, R.C. Lind and T.R. O'Meara, "Imaging threshold detector using a phase–conjugate resonator in $BaTiO_3$," Opt.Lett. **11**, 575–577 (1986).

[5.7] C.R. Giuliano, "Applications of optical phase conjugation," Phys.Today **34**, 27–35 (April 1981).

[5.8] M.C. Gower, "Phase conjugate mirrors," Phys.Bull. **38**, 220–222 (June 1987).

[5.9] G.J. Dunning, E. Marom, Y. Owechko and B.H. Soffer, "All–optical associative memory with shift invariance and multiple–image recall," Opt.Lett. **12**, 346–348 (1987).

[5.10] H.J. White, N.B. Aldridge and I. Lindsay, "Digital and analogue holographic associative memories," Opt.Eng. **27**, 30–37 (1988).

[5.11] D.M. Bloom, P.F. Liao and N.P. Economov, "Observation of amplified reflection by degenerate four wave mixing in atomic sodium vapour," Opt. Lett. **2**, 58–60 (1978).

[5.12] J. Feinberg and R.W. Hellwarth, "Phase–conjugating mirror with continuous wave gain," Opt.Lett. **5**, 519–521 (1980).

[5.13] A. Yariv and D.M. Pepper, "Amplified reflection, phase conjugation and oscillation in degenerate four wave mixing," Opt.Lett. **1**, 16–18 (1977).

[5.14] A. Yariv, "Compensation for atmospheric degradation of optical beam transmission by nonlinear optical mixing," Opt.Commun. **21**, 49 (1977).

[5.15] B. Ya Zel'dovich, V.I. Popovichev, V.V. Ragul'skii and F.S. Faizullov, "Connection between the wavefronts of the reflected and exciting light in stimulated Mandel'Shtam–Brillouin scattering," JETP Lett. **15**, 109–113 (1972).

[5.16] G.S. Agarwal and E. Wolf, "Theory of phase conjugation with weak scatters," J.Opt.Soc.Am. **72**, 321–326 (1982).

[5.17] G.S. Agarwal, A.T. Friberg and E. Wolf, "Effect of backscattering in phase conjugation with weak scatterers," J.Opt.Soc.Am. **72**, 861–863 (1982).

[5.18] G.S. Agarwal, A.T. Friberg and E. Wolf, "Scattering theory of distortion correction by phase conjugation," J.Opt.Soc.Am. **73**, 529–538 (1983).

[5.19] I. Lindsay and J.C. Dainty, "Partial cancellation of specular reflection in the presence of a phase–conjugate mirror," Opt.Commun. **59**, 405–410 (1986).

[5.20] I. Lindsay, "Specular reflection cancellation/enhancement in the presence of a phase–conjugate mirror," J.Opt.Soc.Am. B **4**, 1810–1815 (1987).

[5.21] A. T. Friberg and P.D. Drummond, "Reflection of a linearly polarized plane wave from a lossless stratified mirror in the presence of a phase–conjugate mirror," J.Opt.Soc.Am. **73**, 1216–1219 (1983).

[5.22] P.D. Drummond and A. T. Friberg, "Specular reflection cancellation in an interferometer with a phase–conjugate mirror," J.Appl.Phys. **54**, 5618–5625 (1983).

[5.23] M. Nazarathy, "A Fabry–Perot etalon with one phase–conjugate mirror," Opt.Commun. **45**, 5618–5625 (1983).

[5.24] M. Nieto–Vesperinas, "Fields generated by a Fabry–Perot interferometer with a phase–conjugate mirror," J.Opt.Soc.Am. A **2**, 427–436 (1985).

[5.25] J. Feinberg, "Continuous–wave self–pumped phase conjugator with wide field of view," Opt.Lett. **8**, 480–482 (1983).

[5.26] P. Günter, E. Voit, M.Z. Zha and J. Albers, "Self–pulsation and optical chaos in self–pumped photorefractive $BaTiO_3$," Opt.Commun. **55**, 210–214 (1985).

CHAPTER 6

HOLOGRAPHIC ASSOCIATIVE MEMORIES USING PHASE CONJUGATE FEEDBACK.

6.1 Introduction.

The principle of information retrieval by association has been suggested as the foundation architecture for the future generations of parallel optical computers. Associative recall is the ability to generate at the output, retrieved from the global memory, the associate or near associate of the input and is suggested as the process by which the human memory functions [6.1]. There are two classes of associative recall, namely by *autoassociation* and *heteroassociation* [6.1]. Autoassociative (homoassociative) recall is the ability to retrieve a complete memory element at the output when presented with only a small arbitrary fragment at the input; this is analogous to someone being able to recognise another persons face from seeing the eyes only. Heteroassociative recall is the ability to retrieve again a single memory element at the output but now bearing no structural resemblance to its associate input; this is analogous to someone being able to recognise another person by the car they are driving.

The implementation of associative recall by an optical scheme has received considerable attention during the recent past [6.2→6.15]. The main stimulus for such interest has come from the potential of high processing power due to the huge parallelism and global interconnectivity inherent in optical systems. These are two of the main characteristics specified in a recent *neural network* model of associative memory proposed by Hopfield [6.16]. Holography offers the further potential of a global memory with high information storage capacity, retaining both amplitude and phase information, and relatively insensitive to damage as the stored information is distributed across the majority of the holographic plate. By exploiting these qualities with the inclusion of multiple iterations, feedback, thresholding and amplification, the basic requirements for an associative memory are fulfilled [6.16].

6.2 The Hopfield neural network model.

The Hopfield neural network model is a nonlinear outer–product associative memory which has a particularly simple form and is amenable to optical implementation. The data sets or objects of the model constitute clusters of N neurons where

each neuron can assume only one of two values, ON (+1) or OFF (-1). Hence the m^{th} data set or object can be conveniently represented as a bipolar binary vector of length N, $\mathbf{s}^{(m)}$. The storage of M such objects, $\mathbf{s}$, generates N^2 interconnection weights, T_{ij}, and are represented by an N × N association matrix, $\mathbf{T}$. The neuron interconnection weights are calculated from a sum of outer-product matrices in accordance with the following algorithm

$$T_{ii} = 0, \tag{6.1a}$$

$$T_{ij} = \sum_{m}^{M} s_i^{(m)} s_j^{(m)} \tag{6.1b}$$

and the association matrix, $\mathbf{T}$, constitutes the global memory of the system. The T_{ij} matrix element, Eq. (6.1b), is the sum of ij matrix components of the outer-product of each stored object, $\mathbf{s}^{(m)}$, with itself. This results in an autoassociative memory where distorted or incomplete objects can recall undistorted versions of themselves. The process of each neuron of a distorted object adjusting its state based on the weighted sum of inputs from the other neurons is represented mathematically, in the synchronous case, by the nonlinear matrix vector equation as follows

$$\tilde{s}_i^{(m_o)} = 1 \quad \text{if} \quad \sum_{j}^{N} T_{ij} \hat{s}_j^{(m_o)} \geq 0 \tag{6.2a}$$

and

$$\tilde{s}_i^{(m_o)} = -1 \quad \text{if} \quad \sum_{j}^{N} T_{ij} \hat{s}_j^{(m_o)} < 0 \tag{6.2b}$$

where $\hat{\mathbf{s}}^{(m_o)}$ is a distorted input object vector resembling the stored object vector $\mathbf{s}^{(m_o)}$ and $\tilde{\mathbf{s}}^{(m_o)}$ is the current output state of the neural net. A sharp step function threshold has been employed which is illustrated in Fig. 6.1.

Substituting the associative matrix algorithm, Eqs. (6.1a) and (6.1b), into Eqs. (6.2a) and (6.2b) yields

$$\tilde{s}_i^{(m_o)} = \pm 1 \quad \text{if} \quad \sum_{j}^{N} \sum_{m}^{M} s_i^{(m)} s_j^{(m)} \hat{s}_j^{(m_o)} \gtrless 0, \tag{6.3a}$$

$$= \pm 1 \quad \text{if} \quad \left[s_i^{(m_o)} \sum_{j}^{N} s_j^{(m_o)} \hat{s}_j^{(m_o)} + \sum_{m \neq m_o}^{M} s_i^{(m)} \sum_{j}^{N} s_j^{(m)} \hat{s}_j^{(m_o)} \right] \gtrless 0. \tag{6.3b}$$

The object vectors, $\mathbf{s}^{(m)}$, are bipolar binary by definition and hence if N_{m_o} of the total N neurons of $\hat{\mathbf{s}}^{(m_o)}$ match its stored associate object vector, $\mathbf{s}^{(m_o)}$, then Eq.

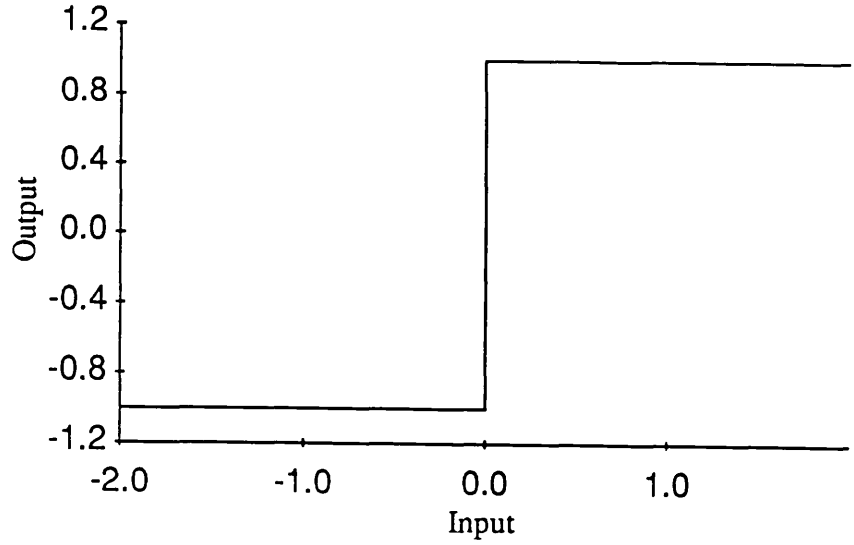


Figure 6.1 The sharp step thresholding function.

(6.3b) becomes

$$\tilde{s}_i^{(m_o)} = \pm 1 \quad \text{if} \quad \left[s_i^{(m_o)} (N_{m_o} - (N - N_{m_o})) + \sum_{m \neq m_o}^{M} s_i^{(m)} \sum_{j}^{N} s_j^{(m)} \hat{s}_j^{(m_o)} \right] \gtrless 0, \tag{6.3c}$$

$$= \pm 1 \quad \text{if} \quad \left[s_i^{(m_o)} (2N_{m_o} - N) + \sum_{m \neq m_o}^{M} s_i^{(m)} \sum_{j}^{N} s_j^{(m)} \hat{s}_j^{(m_o)} \right] \gtrless 0. \tag{6.3d}$$

The quantity $(2N_{m_o} - N)$ is the value of the inner product between the input object vector $\hat{\mathbf{s}}^{(m_o)}$ and its stored associate $\mathbf{s}^{(m_o)}$. Preceeded by $s_i^{(m_o)}$, the term constitutes the *signal* of the association. The second term, $\sum_{m \neq m_o}^{M} s_i^{(m)} \sum_{j}^{N} s_j^{(m)} \hat{s}_j^{(m_o)}$, represents the summation of inner products between the input object vector and all the other stored vectors and constitutes the *noise* accompanying the association.

The dynamics of the model are such that the current output object vector, $\tilde{\mathbf{s}}^{(m_o)}$, is re–entered into the system as an input vector. The matrix vector multiplication $\rightarrow$ thresholding $\rightarrow$ feed forward cycle is repeated and after a finite number of iterations the system ultimately converges to a stable state. This occurs when the cycling vector is unaltered by the operation of Eq. (6.3d) which is achieved when the vector has been previously stored in the association memory matrix, **T** Eqs. (6.1a) and (6.1b); the original input vector $\hat{\mathbf{s}}^{(m_o)}$ stimulates the system to converge to its own associate at the output, $\mathbf{s}^{(m_o)}$.

6.3 Computer simulation of Hopfield's neural network model.

The Hopfield neural network model was computer simulated to illustrate clearly the algorithm's capabilities and limitations at performing autoassociative recall when using practical data. The data sets or object vectors, **s**, employed were a series of three portraits of differing individuals, obtained using a video camera/ digitiser and computer. They were initially prepared as 64 × 64 square arrays with eight gray levels and are shown in Fig. 6.2. They constitute a total of 4096 neurons per object vector and the datasets were binarised to two bipolar levels, □ (+1) and ■ (−1), in accordance with Hopfield's model; they are shown in Fig. 6.3.

The object vectors were analysed and their mutual orthogonalities or correlations are given in Table 6.I. The orthogonality or correlation between any two vectors was defined as the number of neuron states which match divided by the total number of neurons, 4096. Values of unity and zero correspond to correlations taken between two identical vectors and between a vector and its complement respectively. The object vectors $\mathbf{s}^{(1)}$ and $\mathbf{s}^{(2)}$ are the most orthogonal with a correlation value of 0.611 while vectors $\mathbf{s}^{(1)}$ and $\mathbf{s}^{(3)}$ are the most similar with a correlation of 0.729. The optimum data set conditions are a mutual orthogonality of 0.500 between all the data sets and an equal number of □ and ■ neuron states per data set [6.14]. These statistics are not satisfied between the current data sets due to their common overlap of facial features.

	$\mathbf{s}^{(1)}$	$\mathbf{s}^{(2)}$	$\mathbf{s}^{(3)}$
$\mathbf{s}^{(1)}$	1.000	0.611	0.729
$\mathbf{s}^{(2)}$	0.611	1.000	0.701
$\mathbf{s}^{(3)}$	0.729	0.701	1.000

Table 6.I The mutual orthogonalities between the three bipolar binary object vectors, $\mathbf{s}^{(1)}$, $\mathbf{s}^{(2)}$ and $\mathbf{s}^{(3)}$.

Using the three bipolar binary object vectors, Fig. 6.3, and the sharp step thresholding function, Fig. 6.1, Hopfields model, Eqs. (6.1) and (6.2), was computer simulated using different partial/distorted input vectors, $\hat{\mathbf{s}}^{(m_o)}$. The input object vectors employed, $\hat{\mathbf{s}}^{(m_o)}$, were distorted versions of any one of the three stored vectors, $\mathbf{s}^{(1)}$, $\mathbf{s}^{(2)}$ or $\mathbf{s}^{(3)}$. A successful autoassociative recall is illustrated in Fig. 6.4 using a distorted version of $\mathbf{s}^{(2)}$, Fig. 6.3b). The accompanying statistics are given in Table 6.II

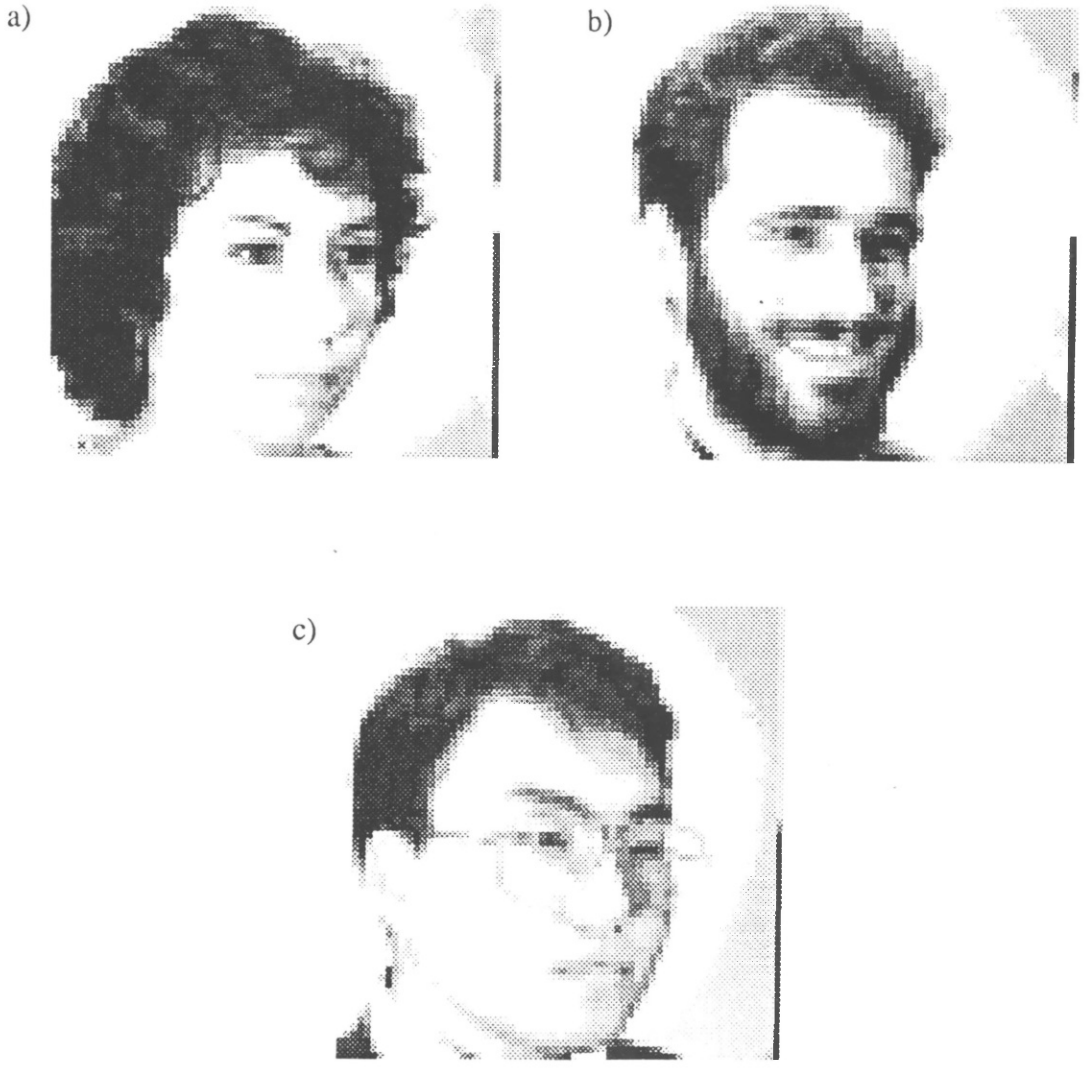


Figure 6.2 The three original 64×64 square array data sets with eight gray levels.

The initial input vector, iteration 0, Table 6.II, was most similar to the stored object vector $\mathbf{s}^{(2)}$. Immediately the output converged to $\mathbf{s}^{(2)}$ and was self–sustaining there after. Increasing the amount of distortion, the boundary of $\square$ $(+1)$ neuron states, reduced the correlations between the initial object vector and the three stored vectors and caused the output to, in general, either oscillate or stagnate at unrecognisable vector states. These results were dependent on both the stored information and the distortion method adopted and similar observations were made using the other two object vectors, $\mathbf{s}^{(1)}$ and $\mathbf{s}^{(3)}$.

The ability of the algorithm to perform autoassociative recall was found to be

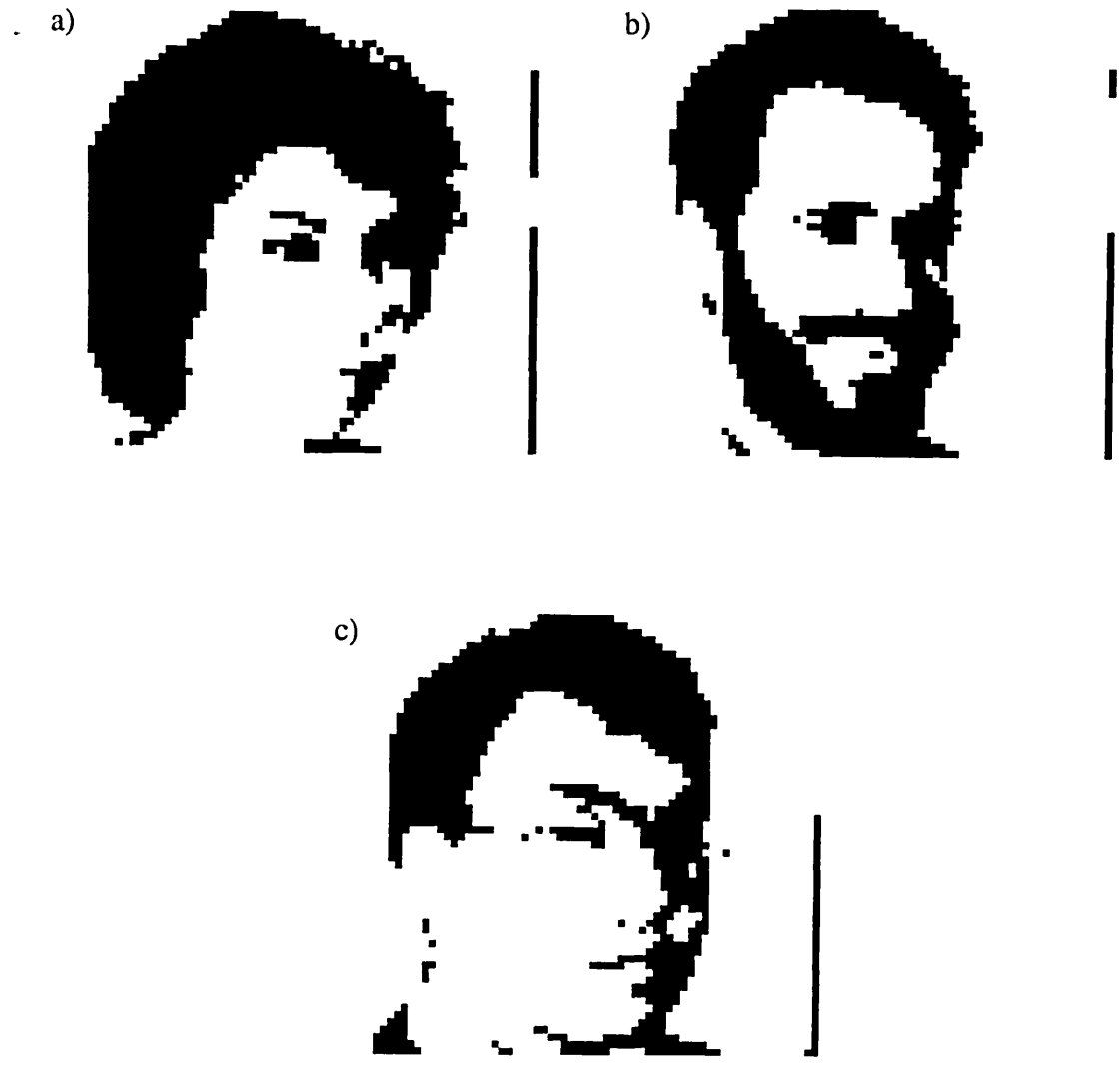


Figure 6.3 The three bipolar binary 64 × 64 object vectors; a) $\mathbf{s}^{(1)}$, b) $\mathbf{s}^{(2)}$ and c) $\mathbf{s}^{(3)}$.

dependent on both the number and mutual orthogonality of the stored data sets. When additional portraits were employed in the current computer simulation, the algorithm became increasingly inflexible as less distortion was allowed to be imposed on the input object vector, $\hat{\mathbf{s}}^{(m_o)}$, to permit successful association. The flexibility of the algorithm may be increased by pre-conditioning the stored data sets to create mutual orthogonalities of 0.500 and equal □ and ■ neuron states [6.14] and using a less rigorous thresholding function e. g. the sigmoid function.

The computer study highlighted the algorithms need to process the information

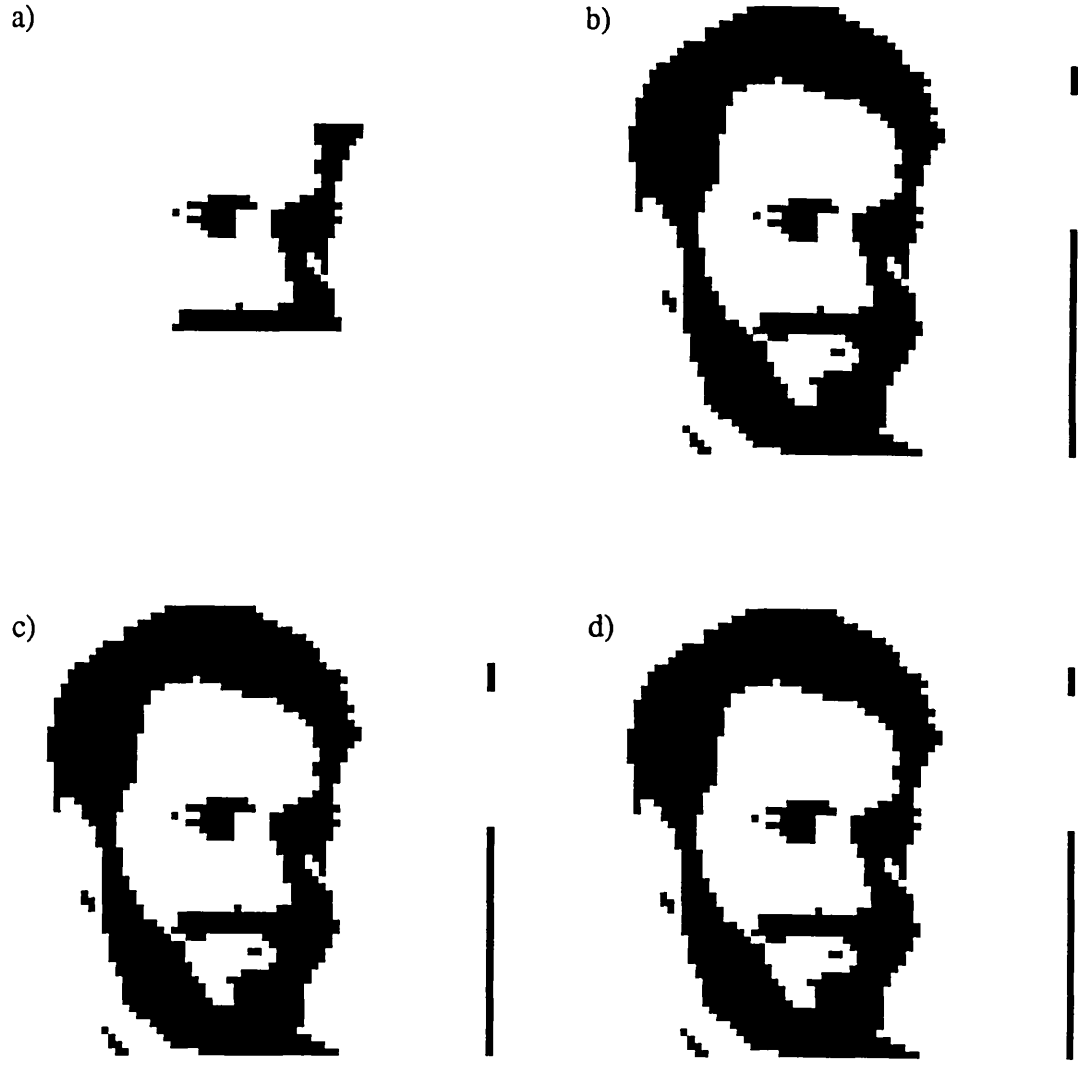


Figure 6.4 The initial and three subsequent bipolar binary 64 × 64 object vectors generated after three iterations.

in parallel and the demand for a large memory capacity. The serial computation was performed by a SUN-3/68020 processor and took approximately 1 hour per iteration and the 64 × 64 data set arrays, Fig. 6.3, required a 64 × 64 × 64 × 64 four dimensional association matrix, **T**, constituting a total of 1.68×10^7 matrix elements!

Iteration number	Correlation		
	s^1	s^2	s^3
0	0.540	0.737	0.684
1	0.611	1.000	0.701
2	0.611	1.000	0.701
3	0.611	1.000	0.701

Table 6.II The correlation between the three bipolar binary object vectors, $\mathbf{s}^{(1)}$, $\mathbf{s}^{(2)}$ and $\mathbf{s}^{(3)}$ and the current object vector of the Hopfield algorithm.

6.4 All optical autoassociative recall.

The parallel processing power of an image bearing light beam and the global interconnectivity with holographically stored information has stimulated much interest in employing optics for neural network applications [6.2→6.15]. Many optical systems have been proposed and demonstrated to perform autoassociative recall. Digital systems, in feed forward ring resonator configurations, which implement directly the digital neural network algorithms, such as Hopfield's, have been demonstrated [6.4,6.15]. Analogue systems, in both feed forward ring and feedback linear resonator configurations, have also recently been reported [6.5,6.6,6.8,6.12→6.15].

The linear resonator configuration, using phase conjugate mirrors to provide the necessary feedback, was first proposed and experimentally demonstrated by Soffer *et al* [6.5]. They initially employed a non-multiplexed Fresnel hologram as the global memory store and degenerate four wave mixing (DFWM) in a photorefractive (PR) crystal of barium titanate as the phase conjugate mirror (PCM). The phase conjugate (PC) feedback was both self-aligning and phase distortion correcting. The optical system presented here was a direct extension of the original research conducted by Soffer *et al* [6.5] and differed mainly by employing a multiplexed Fourier transform hologram as the global memory store.

The experimental investigation was conducted using an argon-ion laser operating on $\lambda = 514.5$nm, at $\sim$ 350mW power output and a coherence length of 5cm. A single domain PR crystal of barium titanate acted as the phase conjugate mirror via DFWM and dichromated gelatin was used to record the Fourier transform hologram. The optical system adopted consisted of an input plane, a Fourier transforming lens L_1, a hologram, a pinhole array situated in the correlation plane (the front focal plane of lens L_2) and a PCM to provide the necessary feedback to generate the recalled image at the output plane, Fig. 6.5.

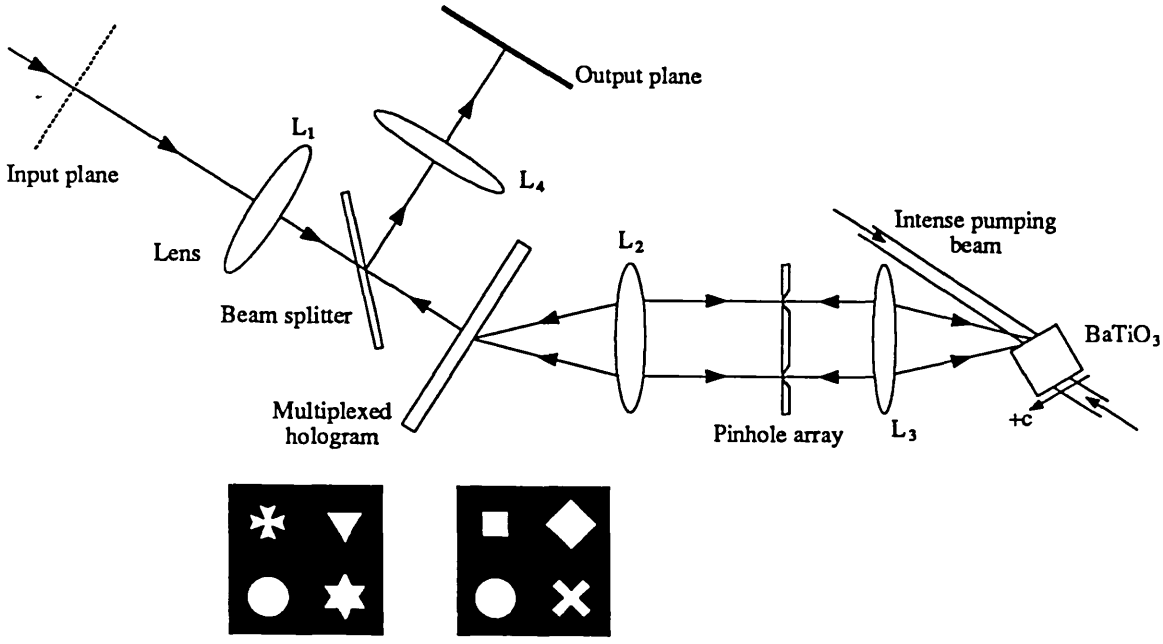


Figure 6.5 Schematic representation of the experimental apparatus.

The Fourier transform hologram was multiplexed by recording in succession the interference of the Fourier transform of each group of four geometric figures with their respective angularly offset plane reference beam. The two groups of four geometric figures, namely memory elements M_1 and M_2, are shown in Fig. 6.6a) and 6.6b) respectively and were similar only in having a circle in their lower left quadrants. The intensity levels of the plane reference beams were adjusted to maximise the interference fringe contrast for the high spatial frequencies of the Fourier transforms. This intensity weighting coupled with the dynamic range constraints of the recording medium meant the hologram exhibited a non-zero diffraction efficiency for only a limited spatial frequency range. Such band-pass filtering in the Fourier plane results in characteristic edge enhancement in the reconstuction plane, with a zero-crossing at the edges themselves. After exposing and processing, the hologram was placed back in its original position in the system.

A unique set of four geometric figures were devised as the input test transparency; namely a Maltese cross, hexagon, circle and diagonal cross, Fig. 6.6c). With the input test transparency, Fig. 6.6c), placed in the input plane (the back focal plane of lens L_1) all but the circle were masked out and the circle's Fourier transform was presented to the hologram at the front focal plane of lens L_1. The high spatial frequency response of the hologram insured that the resultant correlation (overlap

integral) was between the circle and the edges of each set of four geometric figures and hence gave good discrimination between the different shapes. Two strong auto–correlation peaks were observed in the correlation plane (front focal plane of lens L_2) due to the circle circle overlap with both M_1 and M_2. Two precision pinholes (50μm diameter) were centered on their respective peaks which served to spatially filter out the cross–correlation components but at the expense of losing the shift invariance of the system. The transmitted beams were brought together to overlap inside the PR crystal of barium titanate using lens L_3. The crystal of $BaTiO_3$ was externally pumped by a counterpropagating pair of plane laser beams. The phase conjugate wavefronts, generated by DFWM within the volume of the crystal, traced the return paths of the two correlation peaks, passing back through their pinholes and arriving at the hologram as plane wavefronts of uniform intensity and approximately 3mm in diameter. The plane wavefronts were exactly counterpropagating to the direction of the original plane reference beams used during the hologram recording stage. The reconstructions from the hologram were sampled by the beam splitter and imaged at the output plane using lens L_4.

The system could be addressed with any combination of the four geometric figures of the input test transparency, Fig. 6.6c), by the relatively simple task of adjusting a mask placed in the laser beam just prior to the input plane. As the transparency remained fixed the results observed were impartial to the system's loss of shift invariance.

Initially each geometric figure was presented individually. First for the Maltese cross, there was a good correlation with memory elememt M_1, which contained the same Maltese cross, while a very poor correlation with element M_2. Consequently the two correlation peak intensities differed markedly and the stronger, having passed through its pinhole, was more succesfully phase conjugated. The PC wavefront returned to the hologram as a plane beam which reconstructed the Maltese cross and its three associates, the triangle, star and circle, at the output plane. The optical system in operation is schematically illustrated in Fig. 6.7a) and the experimental result is shown in Fig. 6.8a). The edge enhancement of the reconstructed geometric figures, Fig. 6.8a), was characteristic of the spatial frequency band pass filtering of the multiplexed Fourier transform hologram. The mask was adjusted to present the diagonal cross at the input plane, Fig. 6.7b). The difference in correlations with the two memory elements was reversed due to the absence and presence of the diagonal cross in elements M_1 and M_2 respectively. The stronger correlation peak was succesfully phase conjugated and memory element M_2 was reconstructed at the output plane, Fig. 6.8b). These two observations illustrated

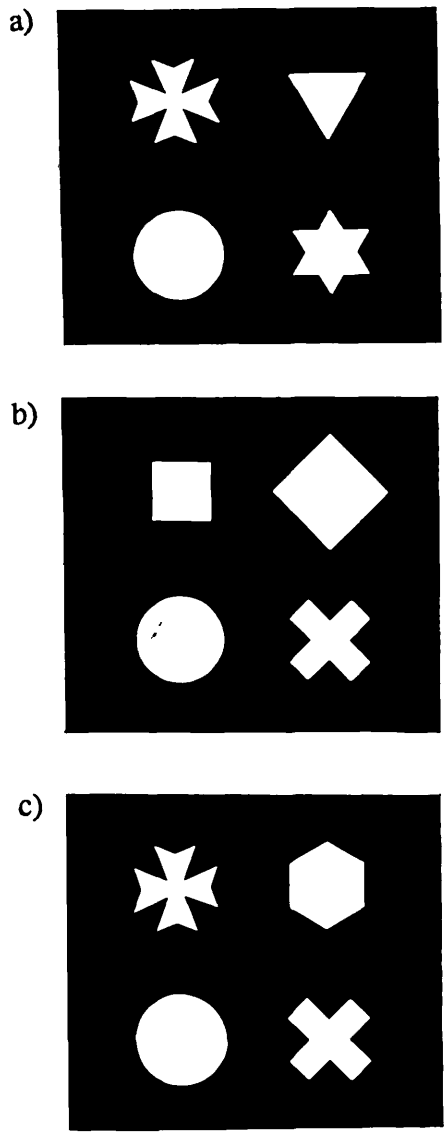


Figure 6.6 The two stored memory elements M_1 and M_2, a) and b) respectively and c) the input test transparency.

the ability of the optical system to retrieve the correct memory element with no visible cross talk when a partial component (25%) of each element was presented at the input.

Thirdly the circle was presented which was a feature common to both M_1 and M_2. The system was therefore unable to make any distinction between the two elements and consequently a superposition of M_1 and M_2 was both expected and observed at the output plane, Fig. 6.8c). Finally the fourth and last figure, the hexagon,

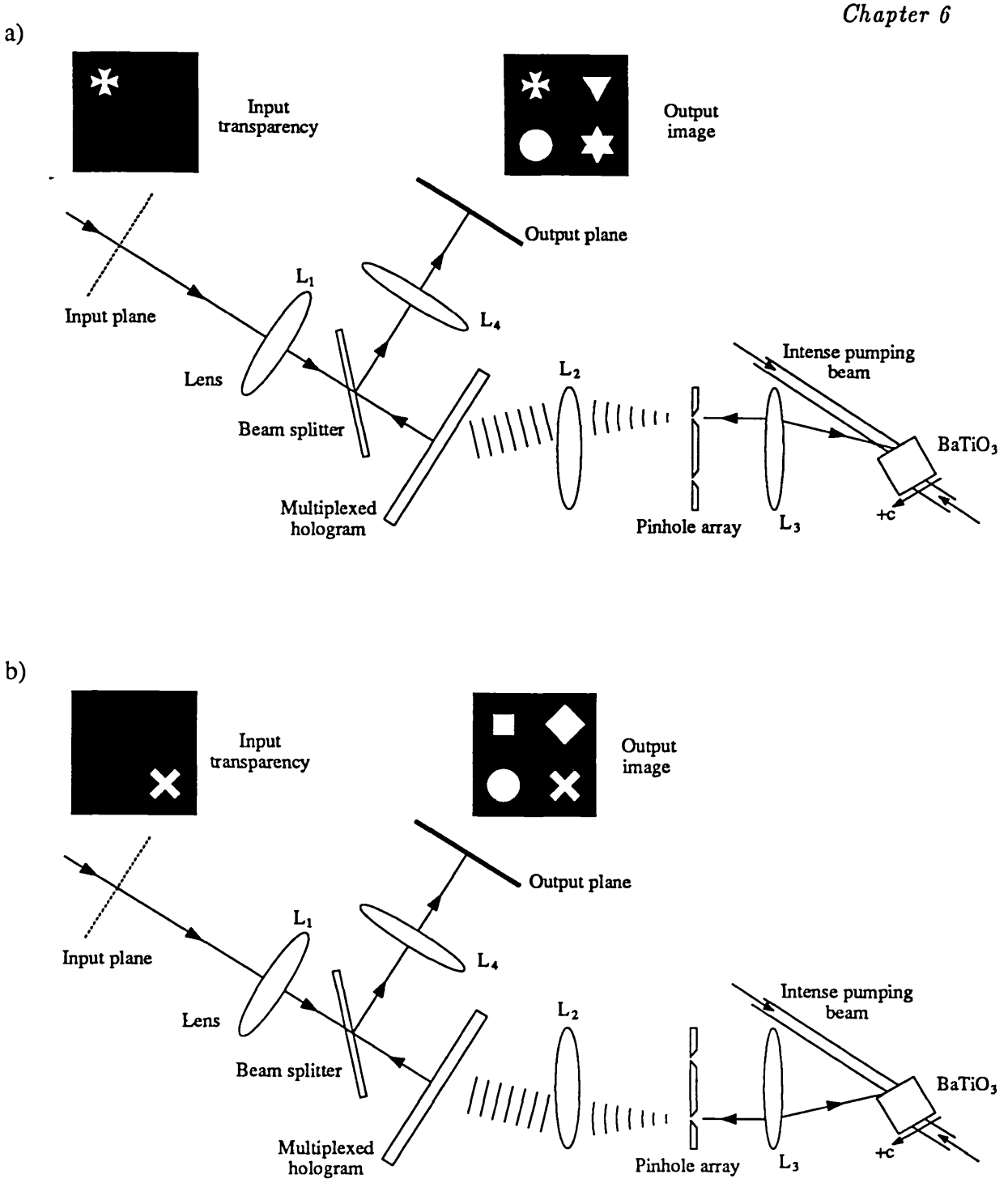


Figure 6.7 Schematic illustration of autoassociative recall of a) memory element M_1 and b) memory element M_2 using a Maltese and diagonal cross respectively.

was presented. The hexagon was a feature alien to both the memory elements. The system did not recognise either of M_1 or M_2 to be associates and consequently no reconstruction was observed at the output plane, Fig. 6.8d). In summary, the

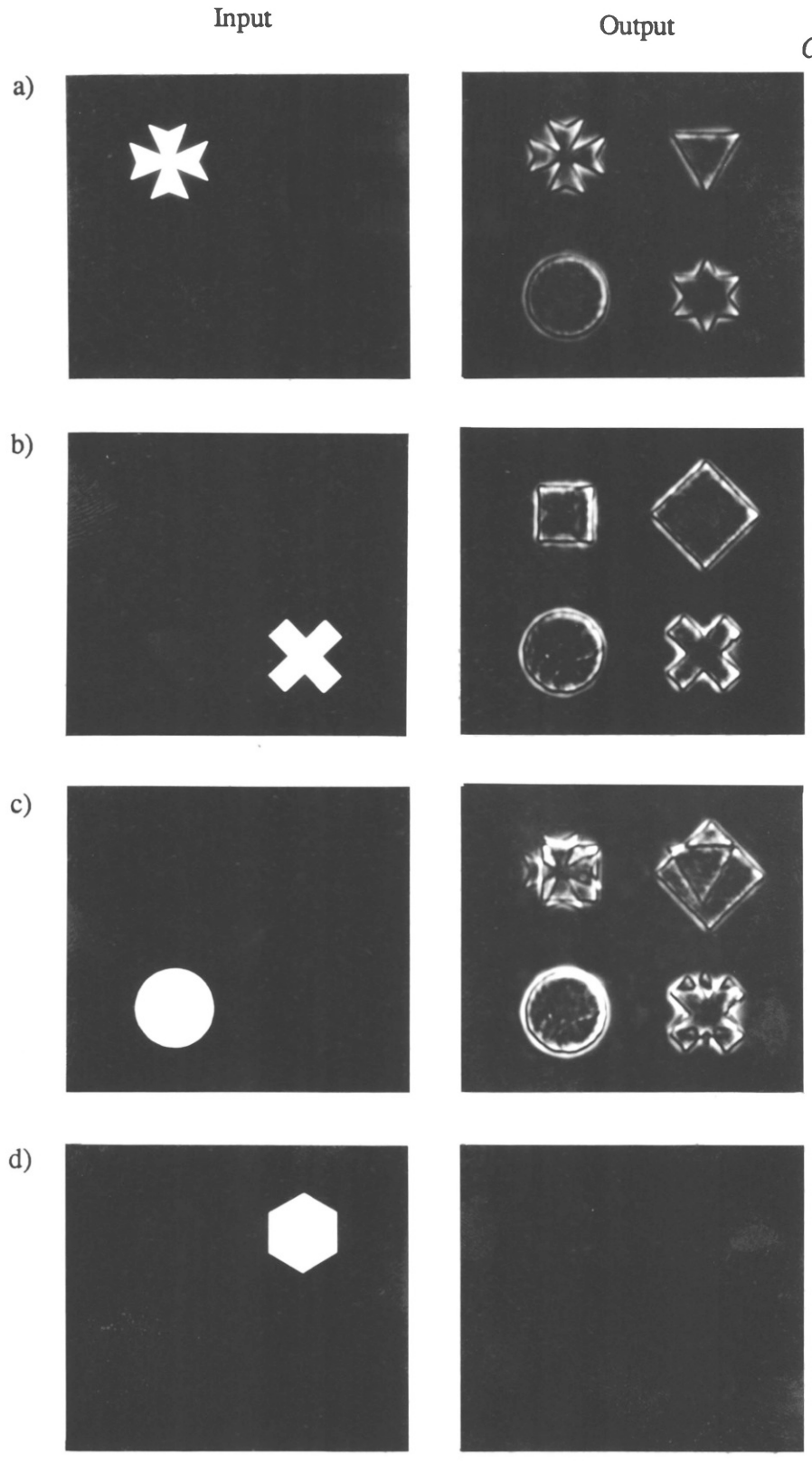


Figure 6.8 Autoassociative recall for differing partial inputs; a) Maltese cross, b) Diagonal cross, c) circle and d) hexagon.

four individual geometric figures presented at the input plane demonstrated the ability to associate correctly with the store information and produce the correct result at the output plane, Fig. 6.8.

Recall the result generated by the circle only, Fig. 6.8c). It was deduced and observed that the system was unable to recall a unique memory element at the output plane as insufficient information was avaliable to discriminate between M_1 and M_2. If truly associative, adding the Maltese cross to the circle should enable the system to converge to M_1 in preference to M_2. The experimental result, shown in Fig. 6.9a), indicated that a dominant M_1 was successfully retrieved but shadowed by a weak M_2. For the circle accompanied by the diagonal cross the converse result was observed, Fig. 6.9b). For the system to generate a single associate at the output, a property exhibited by many of the *neural network* architectures for associative memory, non–linear feedback is required. A phase conjugator which possesses an operating threshold for example, would selectively feedback the strongest correlation signal while quenching all others. Techniques for implementing thresholding using self pumping and grating competition in photorefractive materials such as $BaTiO_3$ and $Sr_{1-x}Ba_xNb_2O_6$ have been suggested [6.5,6.14]. Multiple iteration, another characteristic of *neural* information processing, can be implemented by placing a second PCM in the output plane. The input is then subject to multiple correlation, phase conjugation and thresholding operations allowing the system to selectively converge to a unique memory element after many iterations.

6.5 Conclusion.

In conclusion, an all optical associative memory, consisting of a Van der Lugt filter and phase conjugate feedback, was proposed and demonstrated. The system, in its simplicity, employed a multiplexed Fourier transform hologram as the global memory store and a single domain photorefractive crystal of barium titanate as the phase conjugate mirror. The system demonstrated the ability to recall at the output the correct associate of the partial information presented at the input plane. It was deduced that the system could be improved by incorporating both nonlinear feedback and multiple iterations which would allow the system to converge to a single, *unconfused*, memory element after many iterations.

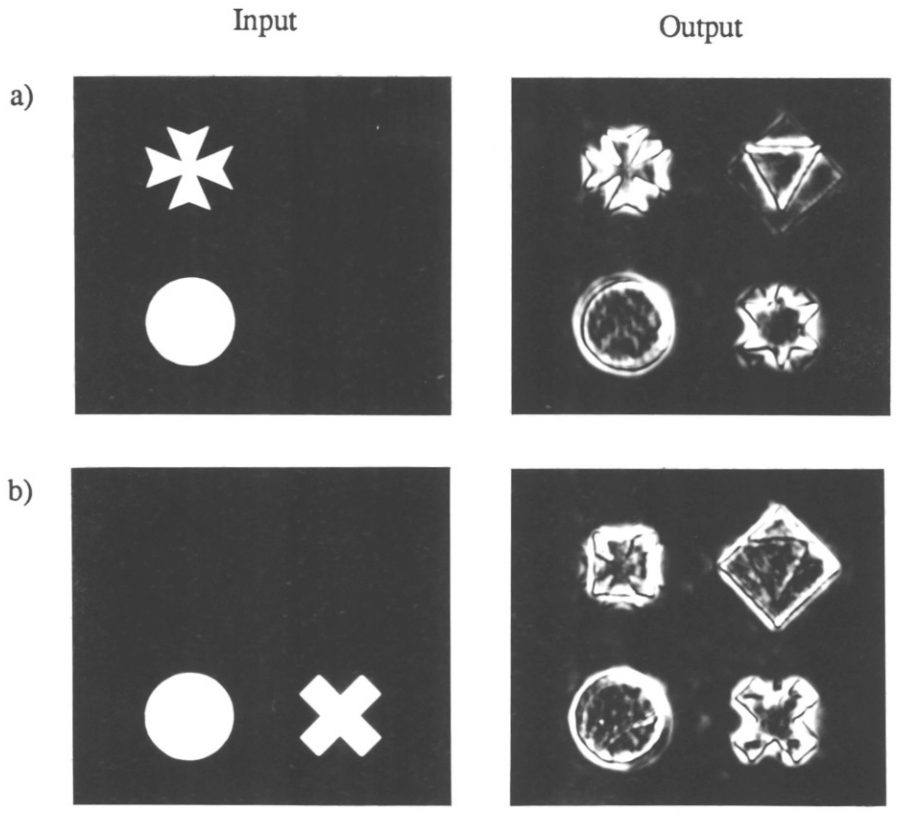


Figure 6.9 Autoassociative recall for selected pairs of geometric figures; a) the circle and Maltese cross and b) the circle and diagonal cross.

6.6 References.

[6.1] T. Kohonen,"Associative Memory, A System-Theoretical Approach,"(Springer-Verlag, Berlin, 1977).

[6.2] D. Gabor, "Associative holographic memories," IBM J.Res.Develop. **13**, 156–159 (1969).

[6.3] H.J. Caufield, "Associative Mappings by optical holography," Opt.Commun. **55**, 80–82 (1985).

[6.4] D. Psaltis and N. Farhat, "Optical information processing based on an associative–memory model of neural nets with thresholding and feedback," Opt.Lett. **10**, 98–100 (1985).

[6.5] B.H. Soffer, G.J. Dunning, Y. Owechko and E. Marom, "Associative holographic memory with feedback using phase–conjugate mirrors," Opt.Lett. **11**, 118–120 (1986).

[6.6] A. Yariv and Sze–Keung Kwong, "Associative memories based on message–bearing optical modes in phase–conjugate resonators," Opt.Lett. **11**, 186–188 (1986).

[6.7] J. Hong and D. Psaltis, "Storage capacity of holographic associative memories," Opt.Lett. **11**, 812–814 (1986).

[6.8] A. Yariv, Sze–Keung Kwong and K. Kyuma, "Demonstration of all–optical associative holographic memory," Appl.Phys.Lett. **48**, 1114–1116 (1986).

[6.9] J.A. Neff, "Major initiatives for optical computing," Opt.Eng. **26**, 2–9 (1987).

[6.10] D. Psaltis and J. Hong, "Shift–invariant optical associative memories," Opt.Eng. **26**, 10–15 (1987).

[6.11] Y.S. Abu–Mostafa and D. Psaltis, "Optical neural computers," Sci.Am. **256**, 66–73 (March 1987).

[6.12] E.G. Paek and D. Psaltis, "Optical associative memory using Fourier transform holograms," Opt.Eng. **26**, 428–433 (1987).

[6.13] G.J. Dunning, E. Marom, Y. Owechko and B.H. Soffer, "All–optical associative memory with shift invariance and multiple–image recall," Opt.Lett. **12**, 346–348 (1987).

[6.14] Y. Owechko, G.J. Dunning, E. Marom and B.H. Soffer, "Holographic associative memory with nonlinearities in the correlation domain," Appl.Opt. **26**, 1900–1910 (1987).

[6.15] H.J. White, N.B. Aldridge and I. Lindsay, "Digital and analogue holographic associative memories," Opt.Eng. **27**, 30–37 (1988).

[6.16] J.J. Hopfield, "Neural networks and physical systems with emergent collective computational abilities," Proc.Natl.Acad.Sci. USA **79**, 2554–2558 (1982).

[6.17] H.J. White and W.A. Wright, "Holographic implementation of a Hopfield model with discrete weightings," Appl.Opt. **27**, 331–338 (1988).

CHAPTER 7

THE ILLUMINATION OF PHOTOREFRACTIVE MATERIALS WITH A CIRCULARLY SYMMETRIC GAUSSIAN INTENSITY PROFILE.

7.1 Introduction.

The majority of theoretical investigations of the photorefractive (PR) effect have been confined to the simple one dimensional cosinusoidal illuminating intensity profile (e. g. Chapters 3 and 4 and Appendices C, D and G). The profile is analytically expressed as follows

$$I = I_o[1 + M\cos(\mathbf{k}.\mathbf{r})], \tag{7.1}$$

where I_o, M and $\mathbf{k}$ are the total intensity, fringe contrast and profile wavevector respectively. The one dimensionality and periodicity of the profile, Eq. (7.1), greatly simplifies the theoretical analysis of the effect as presented in Chapter 3 and Appendix C. The theoretical investigation presented in this chapter is concerned with intensity profiles which are both circularly symmetric and spatially confined. The profile of particular interest is the *Gaussian* which is analytically defined as follows

$$I(\rho) = I_o \exp(-\rho^2/\omega^2), \tag{7.2}$$

where ρ and ω are the radial distance from the origin and the characteristic beam width respectively. The intensity profile, Eq. (7.2), is illustrated in Fig. 7.1.

7.2 Theory.

Recall the generalised coupled band transport equations which describe the PR effect as initially derived by Kukhtarev *et al* [7.1], Chapter 3.

$$\frac{\partial n}{\partial t} = \frac{\partial N_D^+}{\partial t} + \nabla.(D\nabla n + \mu n\mathbf{E}), \tag{7.3}$$

$$\frac{\partial N_D^+}{\partial t} = (N_D - N_D^+)(sI + \beta) - \gamma_R n N_D^+, \tag{7.4}$$

$$\nabla.(\varepsilon\varepsilon_o\mathbf{E}) = q(N_D^+ - N_A - n) \tag{7.5}$$

and

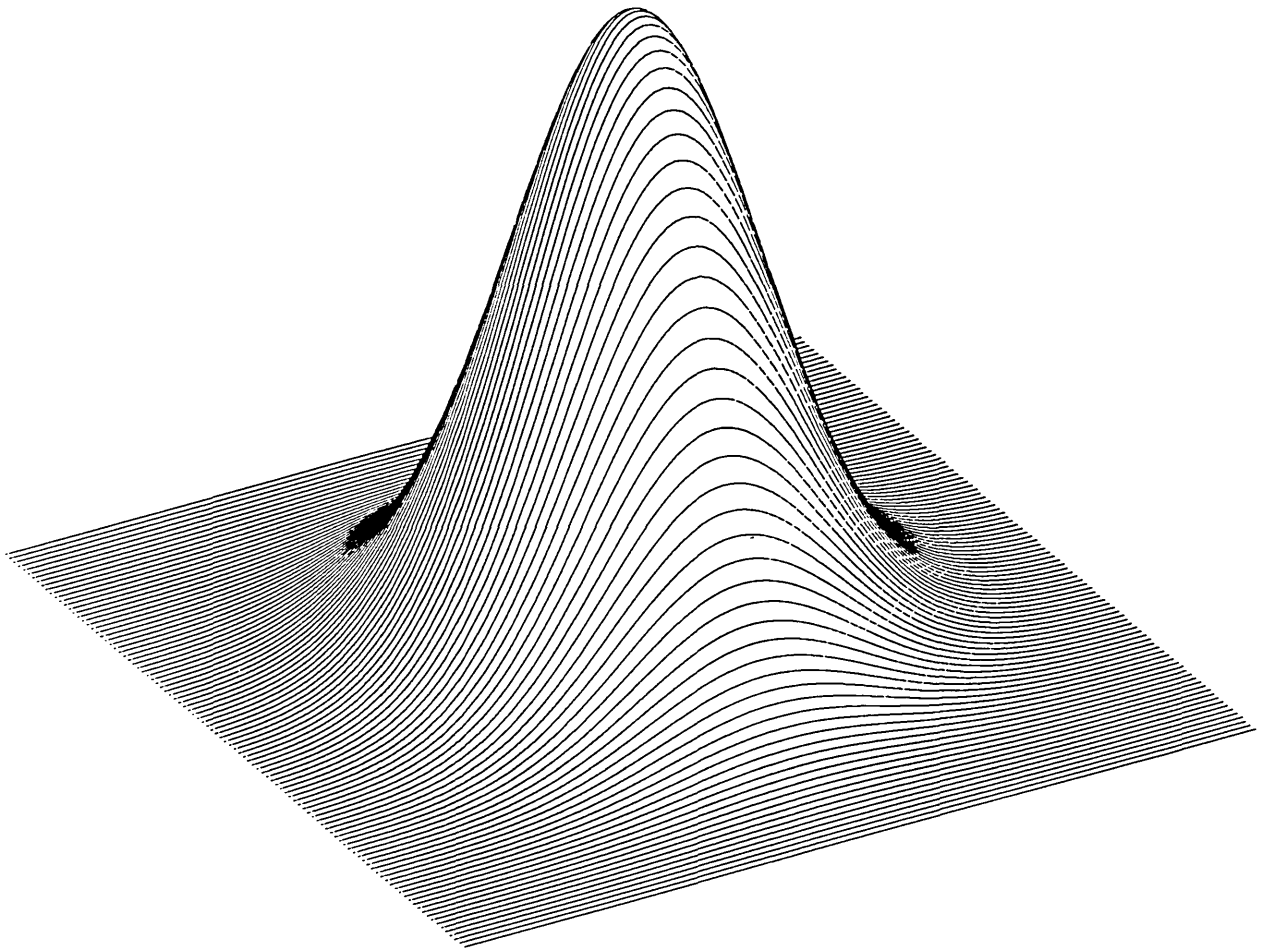


Figure 7.1 The circularly symmetric *Gaussian* intensity profile.

$$\nabla \times \mathbf{E} = 0. \tag{7.6}$$

Where, as previously defined, n, N_D^+, N_D and N_A are the number densities of free electrons, ionised donor sites, total donors and compensatory acceptors respectively. The material parameters D, μ, s, β, γ_R and ε are the coefficient of diffusion, electron mobility, photoionisation constant, thermal generation rate, recombination constant and relative permittivity (dielectric constant) respectively. Further, q, $\mathbf{E}$ and ε_o are the elementary unit of charge, induced static electric field and the permittivity of free space. The system of coupled equations, Eqs (7.3) $\rightarrow$ (7.6), serve to dictate both the transient behaviour and steady state profile of the induced static electric field for any illuminating intensity profile. However the complexity of their nonlinear coupling prevents analytic solutions being attained for all but

the simplest of intensity profiles e. g. the one dimensional cosinusoidal profile.

Circularly symmetric intensity profiles, like the *Gaussian*, in the absence of externally applied electric fields, will induce migration of the PR species in a radial direction away from the high intensity central axis out to the low intensity wings, Fig. 7.1. For a PR medium with an isotropic relative permittivity, $\varepsilon_x = \varepsilon_y = \varepsilon_z = \varepsilon$, and neglecting dynamic feedback, the induced static electric field will also be confined to a radial direction. Consequently the coupled band transport equations, Eqs. (7.3) $\rightarrow$ (7.6), are more convenient if re–expressed in the standard circularly cylindrical co–ordinate system, $(x, y, z) \rightarrow (\rho, \phi, z)$. Using the standard results [7.2]

$$\nabla f = \frac{\partial f}{\partial \rho}\mathbf{e}_\rho + \frac{1}{\rho}\frac{\partial f}{\partial \phi}\mathbf{e}_\phi + \frac{\partial f}{\partial z}\mathbf{e}_z, \tag{7.7a}$$

$$\nabla.\mathbf{A} = \frac{1}{\rho}\frac{\partial}{\partial \rho}(\rho A_\rho) + \frac{1}{\rho}\frac{\partial A_\phi}{\partial \phi} + \frac{\partial A_z}{\partial z}, \tag{7.7b}$$

and assuming spatial invariance w. r. t. ϕ and z the system of equations, Eqs. (7.3) $\rightarrow$ (7.5), become

$$\frac{\partial n}{\partial t} = \frac{\partial N_D^+}{\partial t} + \frac{1}{\rho}\frac{\partial}{\partial \rho}\left[\rho\left(D\frac{\partial n}{\partial \rho} + \mu n E_\rho\right)\right], \tag{7.8}$$

$$\frac{\partial N_D^+}{\partial t} = \left(N_D - N_D^+\right)(sI + \beta) - \gamma_R n N_D^+, \tag{7.9}$$

$$\frac{1}{\rho}\frac{\partial}{\partial \rho}[\rho E_\rho] = \frac{q}{\varepsilon \varepsilon_o}\left(N_D^+ - N_A - n\right), \tag{7.10}$$

where E_ρ is the amplitude of $\mathbf{E}$ which, by convention, is positive when pointing radially outwards. The system of coupled nonlinear equations, Eqs (7.8) $\rightarrow$ (7.10), are analysed in both the initial transient and fully developed steady state regimes.

7.2.1 Initial transient regime.

Assume the illuminating intensity profile is initially incident at t=0 and is held constant for $t > 0$. During the time interval $0 < t < \tau_R$, where $\tau_R = 1/\gamma_R N_A$ is the characteristic recombination time, the induced electric field is very small and the radial *diffusion* of the mobile photoexcited electrons, due to their spatially varying concentration, is unhindered by the opposing radial *drift*. The number density of ionised donors, N_D^+, is assumed to have changed little from its dark homogeneous value, N_A, and the system of coupled band transport equations, Eqs. (7.8) $\rightarrow$ (7.10), become

$$\frac{\partial n}{\partial t} = \frac{\partial N_D^+}{\partial t} + \frac{1}{\rho}\frac{\partial}{\partial \rho}\left[\rho D\frac{\partial n}{\partial \rho}\right], \tag{7.11}$$

$$\frac{\partial N_D^+}{\partial t} = (N_D - N_A)(sI + \beta) - n/\tau_R \tag{7.12}$$

and

$$\frac{1}{\rho}\frac{\partial}{\partial \rho}[\rho E_\rho] = \frac{q}{\varepsilon \varepsilon_o}\left(N_D^+ - N_A - n\right). \tag{7.13}$$

Differentiating Gauss's law, Eq. (7.13), w. r. t. time gives

$$\frac{\partial}{\partial t}\left[\frac{1}{\rho}\frac{\partial}{\partial \rho}[\rho E_\rho]\right] = \frac{q}{\varepsilon \varepsilon_o}\left(\frac{\partial N_D^+}{\partial t} - \frac{\partial n}{\partial t}\right), \tag{7.14}$$

substituting in Eq. (7.11) yields

$$= -\frac{q}{\varepsilon \varepsilon_o}\frac{1}{\rho}\frac{\partial}{\partial \rho}\left[\rho D \frac{\partial n}{\partial \rho}\right], \tag{7.15}$$

$$\frac{1}{\rho}\frac{\partial}{\partial \rho}\left[\rho \frac{\partial E_\rho}{\partial t}\right] = -\frac{q}{\varepsilon \varepsilon_o}\frac{1}{\rho}\frac{\partial}{\partial \rho}\left[\rho D \frac{\partial n}{\partial \rho}\right] \tag{7.16}$$

and hence

$$\frac{\partial E_\rho}{\partial t} = -\frac{q}{\varepsilon \varepsilon_o} D \frac{\partial n}{\partial \rho}. \tag{7.17}$$

Within the time interval specified, $0 < t < \tau_R$, *generation* is the dominant operational mechanism. Using Eqs. (7.11) and (7.12) and in the absence of thermal generation, the free electron number density is approximated by

$$n \simeq (N_D - N_A)\, sIt. \tag{7.18}$$

Substituting Eq. (7.18) into Eq. (7.17) yields

$$\frac{\partial E_\rho}{\partial t} \simeq -\frac{q}{\varepsilon \varepsilon_o}(N_D - N_A)\, sD \frac{dI}{d\rho} t, \tag{7.19}$$

$$E_\rho \approx -\frac{q}{\varepsilon \varepsilon_o}(N_D - N_A)\, sD \frac{dI}{d\rho} t^2, \tag{7.20}$$

$$\propto -\frac{dI}{d\rho} t^2. \tag{7.21}$$

Hence during the initial transient stages the induced electric field is expected to exhibit t^2 temporal and $-dI/d\rho$ spatial behaviours.

To confirm these results the system of band transport equations, Eqs (7.8) $\rightarrow$ (7.10), were solved numerically using conventional techniques. Initially, the coupled equations, Eqs. (7.8) $\rightarrow$ (7.10), were reduced to dimensionless forms as follows

$$\frac{\partial y_n}{\partial \zeta} = \frac{\partial y_{N_D^+}}{\partial \zeta} + \frac{1}{\eta}\frac{\partial}{\partial \eta}\left[\eta\left(\frac{\partial y_n}{\partial \eta} + y_n \xi\right)\right], \tag{7.22}$$

$$\frac{\partial y_{N_D^+}}{\partial \zeta} = \left(1 - y_{N_D^+}\right)\left[\frac{\omega^2}{D}(sI + \beta)\right] - y_n y_{N_D^+}\left[\frac{1}{\tau_R}\frac{N_D}{N_A}\frac{\omega^2}{D}\right], \tag{7.23}$$

$$\frac{1}{\eta}\frac{\partial}{\partial \eta}[\eta\xi] = \frac{q}{\varepsilon\varepsilon_o}\left(y_{N_D^+} - \frac{N_A}{N_D} - y_n\right)\left[\frac{\omega^2}{D}\mu N_D\right], \tag{7.24}$$

where $y_n = n/N_D$, $y_{N_D^+} = N_D^+/N_D$, $\xi = \mu\omega E_\rho/D$, $\eta = \rho/\omega$ and $\zeta = tD/\omega^2$. The quantities $\tau_D = \omega^2/D$ and $E_D = D/\mu\omega$ are the characteristic diffusion time and radial electric field of the PR material for a characteristic beam width of ω (c.f. the diffusion time for a one dimensional cosinusoidal intensity profile, Eq. (7.1), is given by $\tau_D = \Lambda^2/D$ where Λ is the fringe separation). The initial, boundary and global conditions associated with the Eqs. (7.22) → (7.24) are as follows. At t=0 ($\zeta = 0$) the illuminating intensity is turned on and the free electron number density, ionised donor number density and induced static electric field are still at their dark homogeneous and isotropic values of zero, N_A and zero respectively. The initial conditions become

$$y_n(\eta, 0) = 0, \tag{7.25a}$$

$$y_{N_D^+}(\eta, 0) = \frac{N_A}{N_D}, \tag{7.25b}$$

$$\xi(\eta, 0) = 0. \tag{7.25c}$$

The intensity profile considered, Eqs. (7.2), is spatially confined and hence at $\rho = \infty$ ($\eta = \infty$) the illuminating intensity is zero. The free electron and ionised donor number densities and the induced static electric field must all again equal their dark values. In addition, the induced static electric field must equal zero at the origin in order to satisfy the vector field symmetry requirments. The boundary conditions become

$$y_n(\infty, \zeta) = 0, \tag{7.26a}$$

$$y_{N_D^+}(\infty, \zeta) = \frac{N_A}{N_D}, \tag{7.26b}$$

$$\xi(\infty, \zeta) = 0, \tag{7.26c}$$

$$\xi(0, \zeta) = 0. \tag{7.26d}$$

Finally, overall charge neutrality must prevail through out the bulk of the material at all times. This global condition is expressed as follows

$$\int_0^\infty 2\pi\omega^2\left(y_{N_D^+} - \frac{N_A}{N_D} - y_n\right)\eta d\eta = 0 \tag{7.27a}$$

and employing Eq. (7.24) is re-expressed as

$$\underset{\eta \to \infty}{\text{Limit}} \quad \eta\xi(\eta, \zeta) \to 0. \tag{7.27b}$$

The intensity profile and material parameters employed in the numerical analysis were typical values encountered in the laboratory and for the PR material $BaTiO_3$ respectively. The absorption coefficient, α, was extracted from the spectrophotometric data, Appendix B Table B.II, and the free carrier mobility, μ, recombination time, τ_R, and relative permittivity, ε, were taken from Tables 2.II and 2.III for $\varepsilon = \varepsilon_x$, Chapter 2. Using the linear relation between the photoionisation constant, s, and the absorption coefficient, α, Chapter 2, and the Einstein relationship, Chapter 3, values for s, D, τ_D and E_D were deduced. The parameter values used are highlighted in Table 7.I.

Parameter	Value
I_o	$1 Wcm^{-2}$
λ	514.5nm
ω	1mm
T	293K
α	$2.81 cm^{-1}$
ε	3600
τ_R	1ns
μ	$1 cm^2 V^{-1} s^{-1}$
β	0
Φ	1
N_A	$3.0 \times 10^{16} cm^{-3}$
$N_A : N_D$	1:100
s	$2.4 \times 10^{-4} m^2 J^{-1}$
D	$2.5 \times 10^{-6} m^2 s^{-1}$
τ_D	0.4s
E_D	$2.5 kV cm^{-1}$

Table 7.I Parameter values used in transient numerical analysis.

The finite difference numerical method was employed [7.3]. The spatial and temporal dimensions were confined to 4ω and $1.0 \times 10^{-9}\tau_D$ ($0.4\tau_R$) respectively and the analysis was performed over 400 and 100 iterations respectively.

Using the *Gaussian* intensiy profile, Eq. (7.2) and Fig. 7.1, the peak induced electric field at $t = 1.0 \times 10^{-9}\tau_D$ was $E_\rho = 2.16 \times 10^{-10} E_D$, located at $\rho = 0.71\omega$. The temporal and spatial numerical data of the induced electric field, o, are presented in Fig. 7.2 and 7.3 respectively. The temporal data, corresponding to $\rho = 0.71\omega$, is accompanied by a t^2 curve fit, ——. It is observed that they are in good agreement, especially for $t <\sim 0.5 \times 10^{-9}\tau_D$. The normalised spatial numerical data, o Fig. 7.3, corresponding to $t = 1.0 \times 10^{-9}\tau_D$, is accompanied

by the normalised and inverted first derivative of the *Gaussian* w.r.t. ρ, ——, and they appear to match very closely. These two observations are in obvious agreement with Eq. (7.21) and charge neutrality was preserved, Eq. (7.27b).

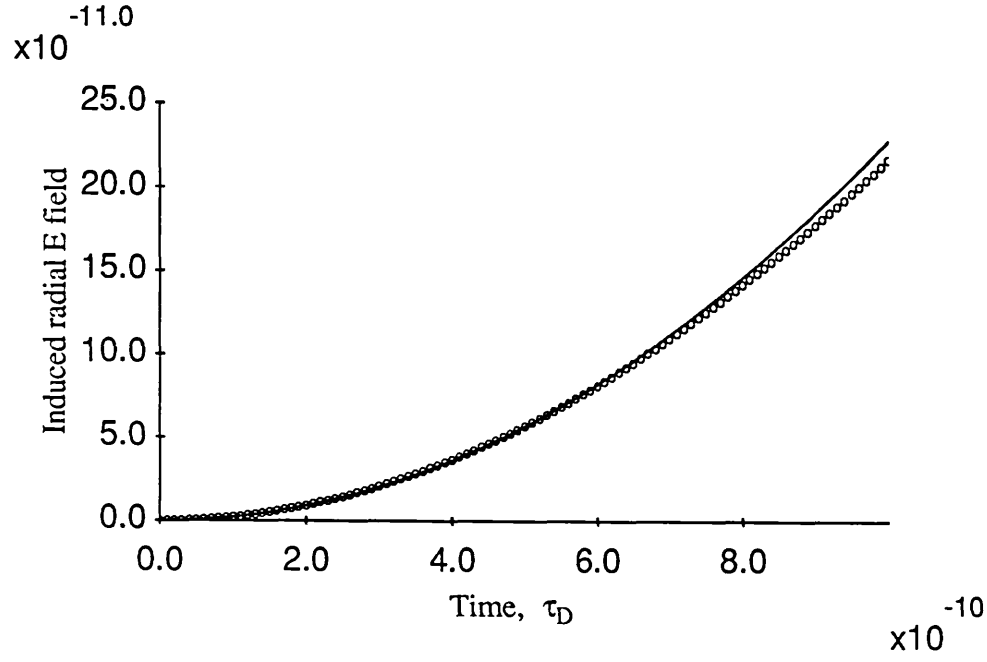


Figure 7.2 The temporal numerical data, o, of the induced electric field at $\rho = 0.71\omega$ for a *Gaussian* illuminating intensity profile. The solid curve, ——, corresponds to a t^2 data fit.

To further emphasis the spatial relationship between the induced electric field for $t < \tau_R$, two additional intensity profiles were considered. More spatially complicated, they were a *soft tophat* and a *difference of Gaussians* and are analytically expressed as

$$I(\rho) = \frac{I_o}{\exp\left[(\rho - \omega)/\tau\right] + 1} \tag{7.28a}$$

and

$$I(\rho) = I_o \left[\exp(v_a \rho^2/\omega^2) - \exp(v_b \rho^2/\omega^2)\right]. \tag{7.28b}$$

The *soft tophat* profile, Eq. (7.28a), is defined by the Fermi–Dirac distribution function, more commonly employed in quantum statistical thermodynamics. The edge definition of the profile is characterised by the quantity τ. Their two dimensional perspective projections are shown in Fig. 7.4 for $\tau = 0.15$ and Fig. 7.6 for

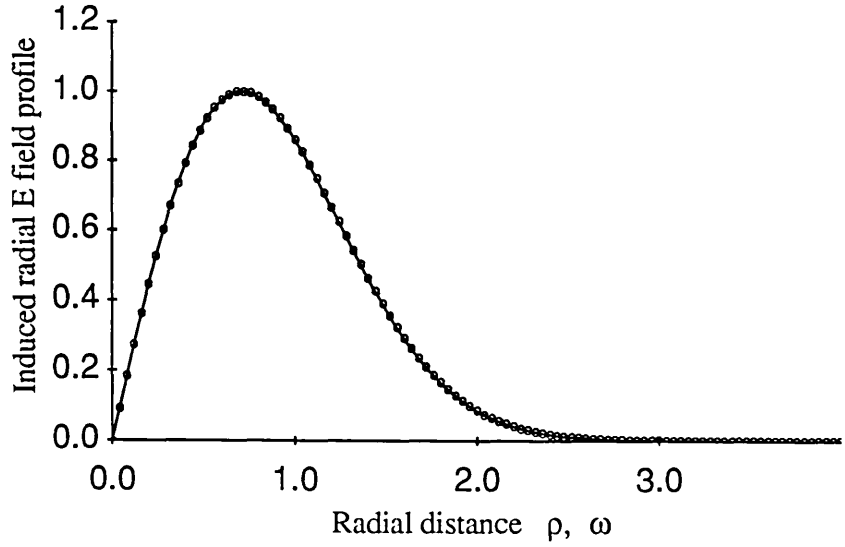


Figure 7.3 The spatial numerical data, o, of the normalised induced electric field at $t = 1.0 \times 10^{-9}\tau_D$ for a *Gaussian* illuminating intensity profile. The solid curve, ——, corresponds to the normalised and inverted first derivative of the *Gaussian* illuminating intensity.

$v_a = 2.6$ and $v_b = 3.2$ respectively. While the temporal evolutions of the induced electric fields were very similar to that of the *Gaussian*, Fig. 7.2, the spatial profiles at $t = 1.0 \times 10^{-9}\tau_D$, differed considerably. Accompanyed by the normalised and inverted first derivatives of their intensity profiles, ——, the normalised induced electric fields, o, @ $t = 1.0 \times 10^{-9}\tau_D$ are shown in Figs. 7.5 and 7.7 respectively. Once more the data sets are in excellent agreement.

7.2.2 Steady state regime.

Assuming the illuminating intensity profile is held constant for a sufficiently long period after t=0, the *generation*, *migration* and *recombination* mechanisms establish mutual equilbrium. The *generation* and *recombination* rates are equal and the *diffusion* and *drift* contributions to the *migration* rate are equal and opposite. The number densities of free electrons, n, and ionised donors, N_D^+, and the induced electric field, E_ρ, are all time independent and the coupled band transport equations, Eqs (7.8) → (7.10), become

$$0 = \frac{1}{\rho}\frac{d}{d\rho}\left[\rho\left(D\frac{dn}{d\rho} + \mu n E_\rho\right)\right], \tag{7.29}$$

$$0 = \left(N_D - N_D^+\right)(sI + \beta) - \gamma_R n N_D^+, \tag{7.30}$$

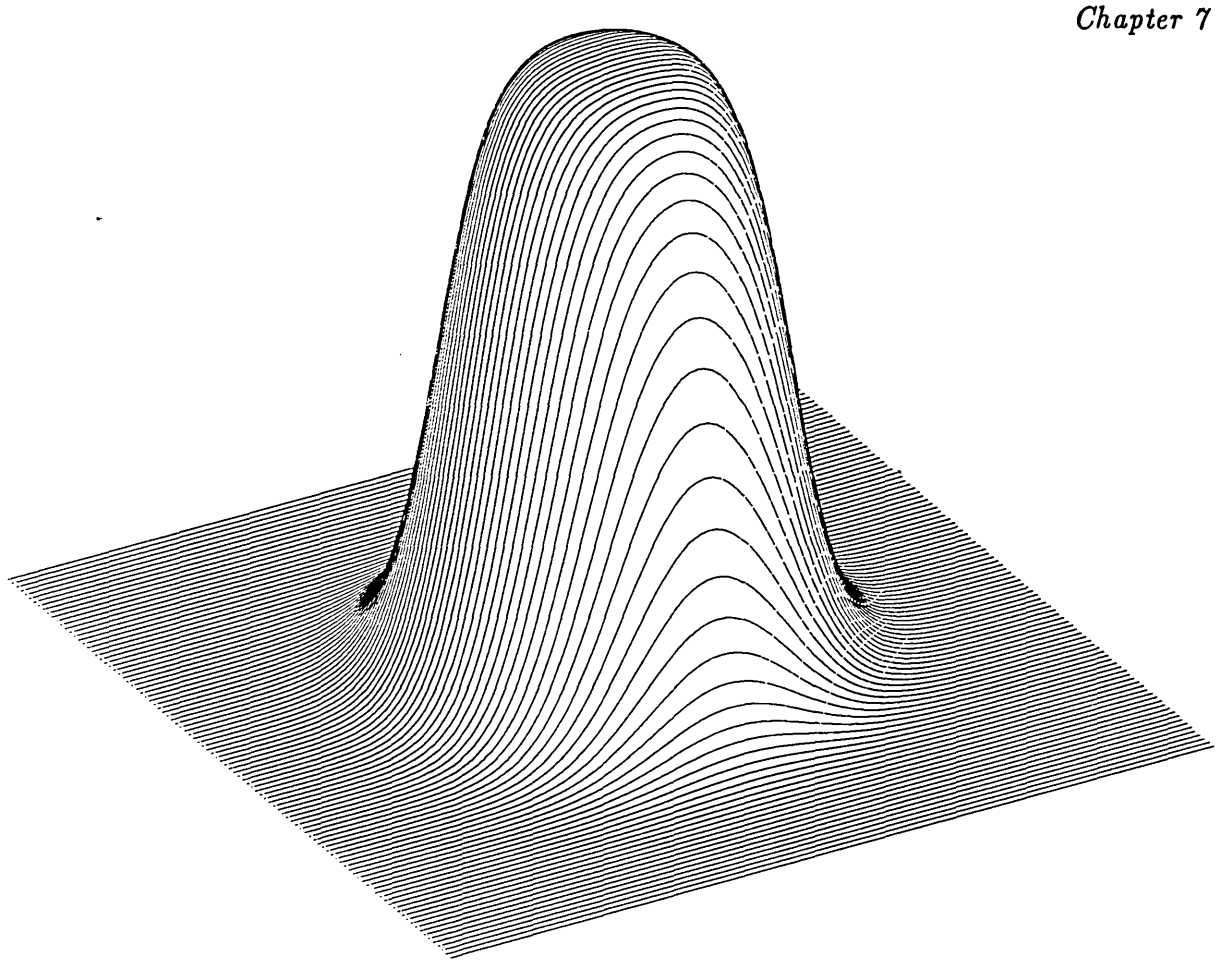


Figure 7.4 The two dimensional perspective projection of a *soft tophat* intensity profile.

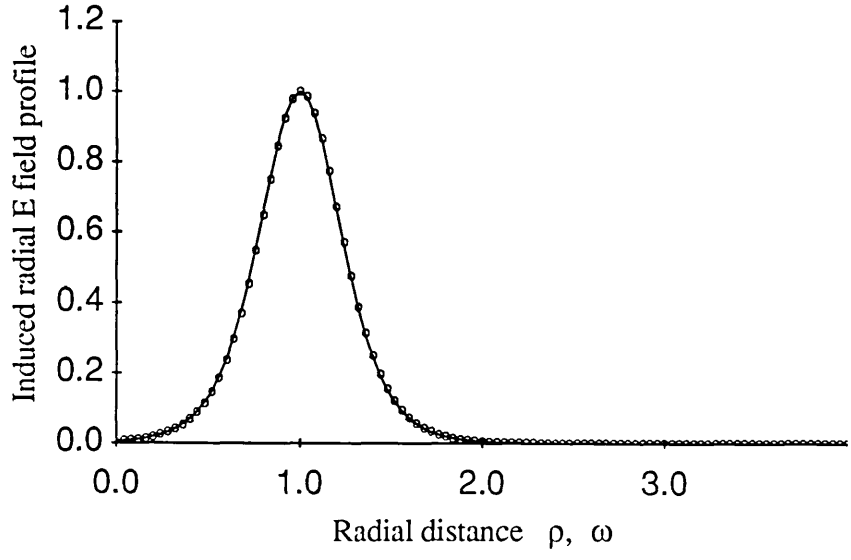


Figure 7.5 The spatial numerical data, o, of the normalised induced electric field at $t = 1.0 \times 10^{-9} \tau_D$ for a *soft tophat* intensity profile.

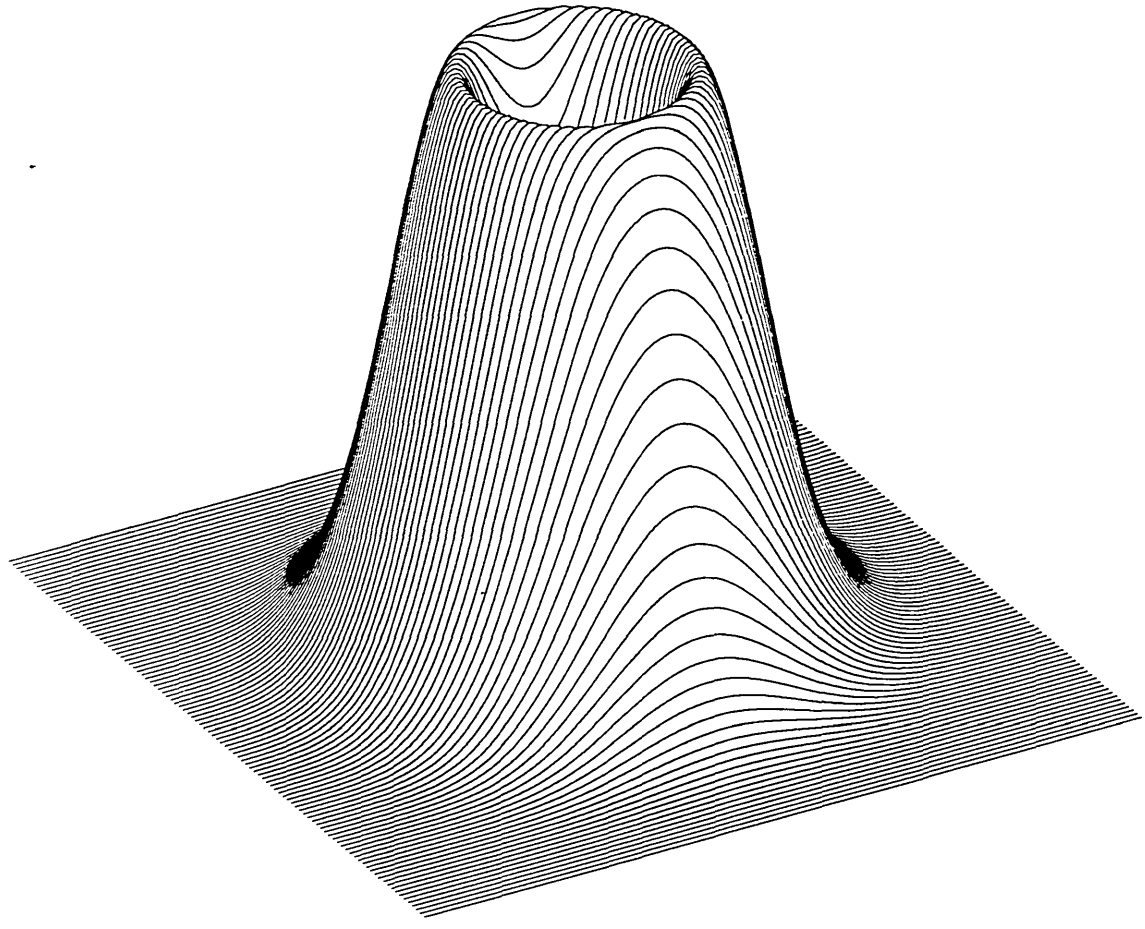


Figure 7.6 The two dimensional perspective projection of a *difference of Gaussians* intensity profile.

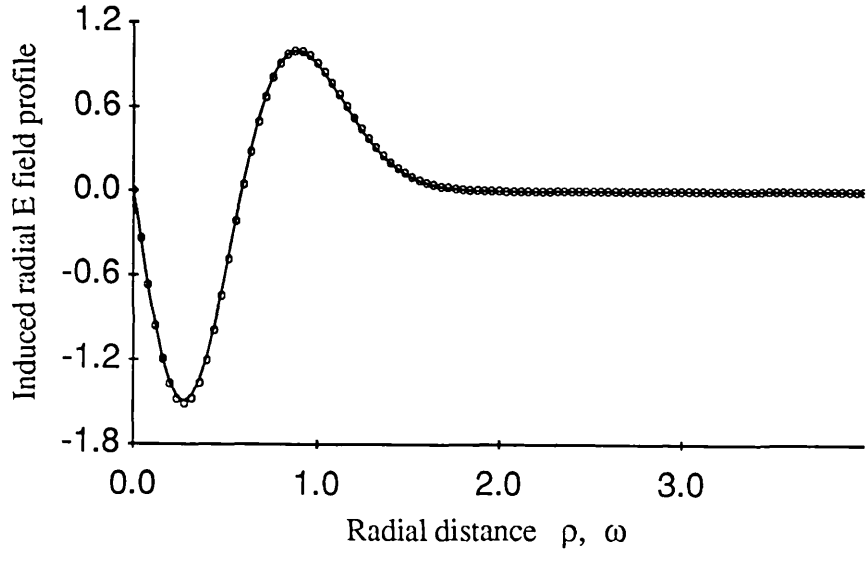


Figure 7.7 The spatial numerical data, o, of the normalised induced electric field at $t = 1.0 \times 10^{-9} \tau_D$ for a *difference of Gaussians* intensity profile.

$$\frac{1}{\rho}\frac{d}{d\rho}[\rho E_\rho] = \frac{q}{\varepsilon\varepsilon_o}\left(N_D^+ - N_A - n\right). \tag{7.31}$$

Consider the non-saturation regime to prevail, then $N_D^+ \simeq N_A$ and Eq. (7.30) becomes

$$0 = (N_D - N_A)(sI + \beta) - n/\tau_R, \tag{7.32}$$

which, when rearranged, reveals

$$n = \tau_R (N_D - N_A) sI, \tag{7.33a}$$

$$\propto I, \tag{7.33b}$$

in the absence of thermal generation. It is apparent from Eq. (7.29) that,

$$\rho\left(D\frac{dn}{d\rho} + \mu n E_\rho\right) = \textit{constant}. \tag{7.34}$$

The illuminating intensity profile, I, is spatially confined and using Eq. (7.33b) the free electron number density, n, and its first derivative w. r. t. ρ, $dn/d\rho$, must both reduce to zero as $\rho \rightarrow \infty$. Consequently, the *constant* of integration in Eq. (7.34) must equal zero. Equation (7.34) becomes

$$D\frac{dn}{d\rho} + \mu n E_\rho = 0, \tag{7.35}$$

which, when rearranged, yields

$$E_\rho = -\frac{D}{\mu}\frac{1}{n}\frac{dn}{d\rho}. \tag{7.36}$$

Employing Eq. (7.33a) gives

$$E_\rho = -\frac{D}{\mu}\frac{1}{I}\frac{dI}{d\rho}, \tag{7.37a}$$

$$\propto -\frac{1}{I}\frac{dI}{d\rho}. \tag{7.37b}$$

Returning to the intensity profile of particular interest, the *Gaussian*, Eq. (7.2) and Fig. 7.1. The corresponding induced electric field was calculated using Eq. (7.37a) to be

$$E_\rho = \frac{D}{\mu}\frac{2\rho}{\omega^2}, \tag{7.38}$$

and graphically represented in Fig. 7.8.

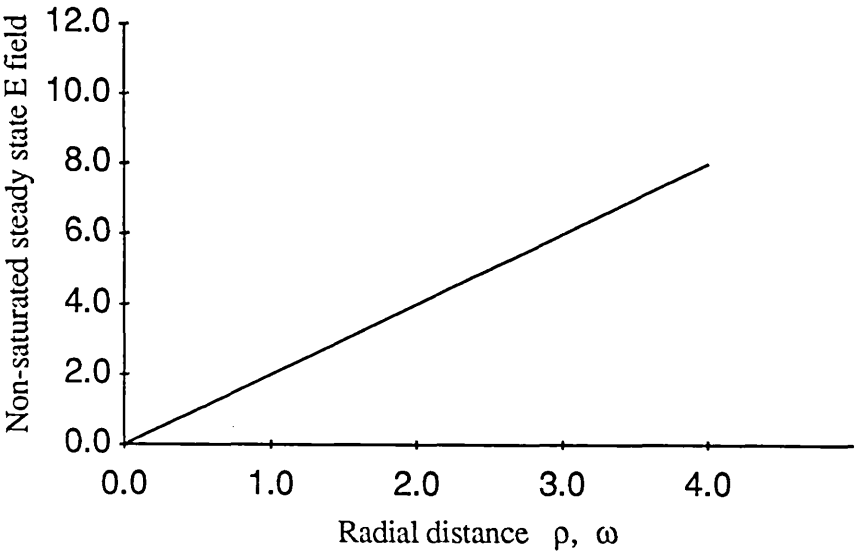


Figure 7.8 The normalised non-saturated steady state electric field profile induced by *Gaussian* illumination.

It is observed from Fig. 7.8 that the non-saturated steady state electric field tends linearly to ∞ as $\rho \rightarrow \infty$. This unique field profile is required to hold the otherwise free electrons, n, with a *Gaussian* profile, Eq. (7.33b), stationary in both time and space. The result, however, is physically absurd as the field would require the redistribution of an infinite number of PR species. Consequently it is concluded that, due to the unbound nature of the intensity profile, saturation of the PR species must be inevitable in order that the induced electric field be reduced to zero in the limit as $\rho \rightarrow \infty$ and that conservation of charge be maintained. The steady state coupled band transport equations, Eqs. (7.29) $\rightarrow$ (7.31), can not be solved analytically in the absence of the non-saturation condition. Hence the finite difference numerical method, as described earlier, was adopted. In the initial transient regime, Section 7.2.1, the numerical analysis was performed using material parameter values typical of PR barium titanate. The characteristic recombination and diffusion times, τ_R and τ_D, were 1ns and 0.4s respectively and 100 temporal iterations were performed to accurately reach $1.0 \times 10^{-9}\tau_D$. This implies that 10^{11} temporal iterations would be necessary to reach $1\tau_D$ and hence the near vicinity of the steady state regime! Such an iteration number is impractical and consequently new material parameter values were chosen to perform the analysis over a more convient computational time scale. The recombination time, τ_R, and the free carrier mobility, μ, were artificially exaggerated by three and four orders of magnitude respectively. Consequently the coefficient of diffusion, D, and the characteristic diffusion time, τ_D, were increased and decreased by four orders

of magnitude respectively while the magnitude of the characteristic radial electric field, E_D, remained unchanged. The parameter values employed are highlighted in Table 7.II.

Parameter	Value
I_o	$1 Wcm^{-2}$
λ	514.5nm
ω	1mm
T	293K
α	$2.81 cm^{-1}$
ε	3600
τ_R	$1\mu s$
μ	$10^4 cm^2 V^{-1} s^{-1}$
β	0
Φ	1
N_A	$3.0 \times 10^{16} cm^{-3}$
$N_A : N_D$	1:100
s	$2.4 \times 10^{-4} m^2 J^{-1}$
D	$2.5 \times 10^{-2} m^2 s^{-1}$
τ_D	$40\mu s$
E_D	$2.5 kVcm^{-1}$

Table 7.II Parameter values used in the steady state numerical analysis.

The spatial and temporal dimensions were confined to 5ω and $2\tau_D$ respectively and the analysis was performed over 1 000 and 200 000 iterations respectively. The *Gaussian* profile induced a peak electric field value of $5.09E_D$ at $t = 2\tau_D$ and $\rho = 2.56\omega$. The temporal behaviour, o, is illustrated in Fig. 7.9 and is accompanied by an exponential rise data fit, ——. The characteristic rise time was found to be $\tau_{rise} = 0.45\tau_D$ and the steady state regime was almost attained at $t = 2\tau_D$.

The spatial behaviour is illustrated in Fig. 7.10 and is accompanied by the non–saturation curve, Eq. (7.38), ——, for comparison. The numerical data sets correspond to 20%, +, 60%, $\star$, and 100%, o, of the total time period, $2\tau_D$. It is observed that the induced electric field conforms to the non–saturation curve, ——, for small radial distances. However at large ρ saturation prevails and the field rapidly decends and tails off to zero. Overall charge neutrality, Eq. (7.27b) was found to be maintained

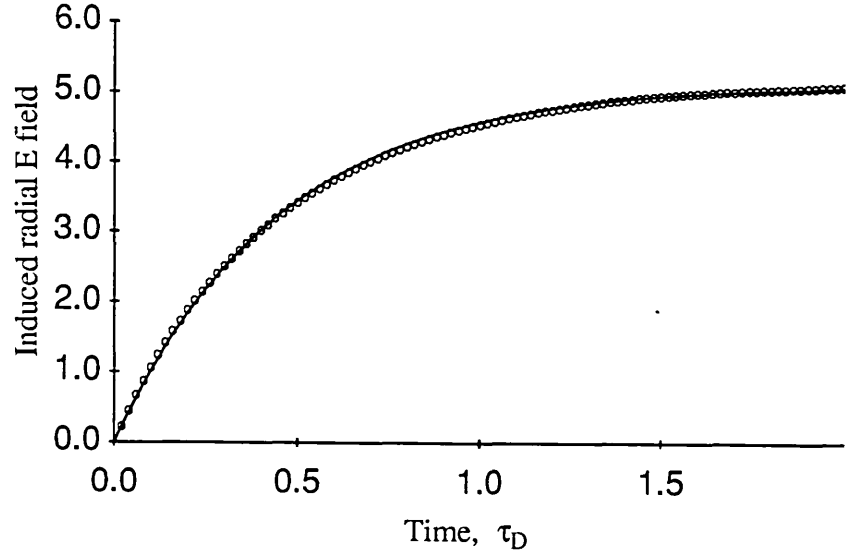


Figure 7.9 The temporal numerical data, o, of the induced electric field at $\rho = 2.55\omega$. The solid curve, ——, corresponds to a $E_\rho = E_{\rho o}[1 - \exp(-t/\tau_{rise})]$ data fit with $\tau_{rise} = 0.45\tau_D$.

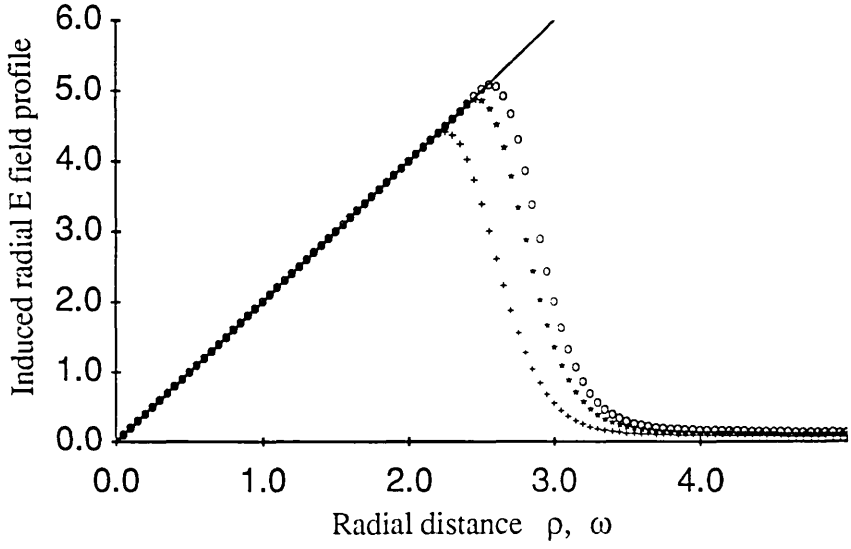


Figure 7.10 The spatial numerical data of the induced electric field for 20%, +, 60%, ⋆, and 100%, o, of the total time period. The solid curve, ——, is the non-saturated electric field profile, Eq. (7.38).

7.3 Resultant refractive index profiles.

The form and orientation of the induced electric field, a vector field, is dictated only by the form and orientation of the illuminating intensity profile, a scalar field. The resultant refractive index modulation is, however, dictated not only by the electric field profile but also its orientation w. r. t. the crystallographic axes of the PR material and the polarisation state of the incident light.

Reverting back to the cartesian co-ordinate system, (x, y, z), the general form of the optical indicatrix for both barium titanate and strontium barium niobate PR materials is

$$\begin{aligned}&\frac{x^2}{n_o^2}+\frac{y^2}{n_o^2}+\frac{z^2}{n_e^2}\\&+r_{13}x^2E_z+r_{23}y^2E_z+r_{33}z^2E_z\\&+2r_{42}yzE_y+2r_{51}xzE_x\\&=1,\end{aligned}\tag{7.39}$$

where E_x, E_y and E_z are the components of the electric field, **E**, along the x, y and z directions respectively. The principle optic, +c, and z cartesian co-ordinate axis are co-linear. Consider the incident light to travel in the α ray direction as defined in Fig. 7.11. The induced electric field, as discussed earlier, is confined to the α plane. The component values of the field are given by

$$E_x = -E_\rho \cos\varphi \sin\alpha, \tag{7.40a}$$

$$E_y = E_\rho \sin\varphi, \tag{7.40b}$$

$$E_z = E_\rho \cos\varphi \cos\alpha. \tag{7.40c}$$

The two polarisation states of particular interest are the *ordinary* and *extra-ordinary*, corresponding to the **E** wave of the incident light aligned perpendicular to and in the plane of the optic axis respectively. The most appropriate co-ordinate change is given by

$$x = x' \cos\alpha - z' \sin\alpha, \tag{7.41a}$$

$$y = y', \tag{7.41b}$$

$$z = x' \sin\alpha + z' \cos\alpha, \tag{7.41c}$$

where x', y' and z' are the new co-ordinate axis as shown in Fig. 7.11. Substituting into the optical indicatrix, Eq. (7.39), the refractive index enviroments for light

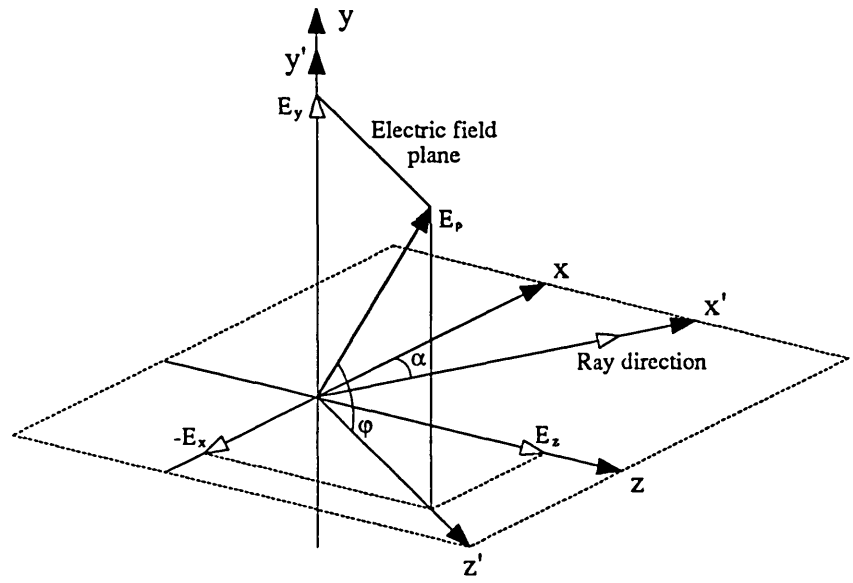


Figure 7.11 Cartesian co-ordinate system used to define the ray direction of the incident light and the induced electric field plane.

polarised along the y' and z' directions, *ordinary* and *extra-ordinary* polarisations respectively, are as follows

$$n_{y'} = \left[1/n_o^2 + r_{23}E_z\right]^{-1/2} \tag{7.42a}$$

$$\begin{aligned} n_{z'} = \Big[&\left(1/n_o^2 + r_{13}E_z\right)\sin^2\alpha \\ &+ \left(1/n_e^2 + r_{33}E_z\right)\cos^2\alpha \\ &- 2r_{51}E_x\cos\alpha\sin\alpha\Big]^{-1/2}. \end{aligned} \tag{7.42b}$$

Using the spatial numerical data of the induced electric field at $t = 2\tau_D$ in Fig. 7.10, o, and employing Eqs. (7.42a) and (7.42b), the modulated *ordinary* and *extra-ordinary* RI enviroments, $\Delta n_{y'}$, Eq. (7.43a), and $\Delta n_{z'}$, Eq. (7.43b), respectively, were calculated for barium titanate.

$$\begin{aligned} \Delta n_{y'} &= n_{y'}(E \neq 0) - n_{y'}(E = 0) \\ &= n_{y'}(E \neq 0) - n_o, \end{aligned} \tag{7.43a}$$

$$\begin{aligned} \Delta n_{z'} &= n_{z'}(E \neq 0) - n_{z'}(E = 0) \\ &= n_{z'}(E \neq 0) - n_e(\alpha). \end{aligned} \tag{7.43b}$$

The sign of the induced electric field was reversed to accomodate for the predominant p-type photoconductive nature of $BaTiO_3$ and the linear electro-optic coefficients from Table 2.III were used. It is important to appreciate that the numerical analysis represents only a crude approximation to the response of $BaTiO_3$

to a *Gaussian* illuminating intensity profile. The recombination time, τ_R, and the carrier mobility, μ, material parameters were artificially exaggerated while the characteristic electric field, E_D, was unchanged. The extensive anisotropic nature of the dielectric constant, $\varepsilon_x = \varepsilon_y = 3600$ and $\varepsilon_z = 135$, Table 2.III, was not accomodated and dynamic feedback was ignored.

The one dimensional *ordinary* and *extra–ordinary* RI modulations along the z′ axis, for $\alpha = -5°(\times)$, $0°(+)$, $10°(\star)$ and $25°(o)$, are shown in Figs. 7.12 and 7.13 respectively. The peak values of $\Delta n_{y'}$ and $\Delta n_{z'}$ for the chosen ray directions are presented in Table 7.III. The two dimensional perspective projection of the modulated *extra–ordinary* RI enviroment, for $\alpha = 0°$, is shown in Fig. 7.14.

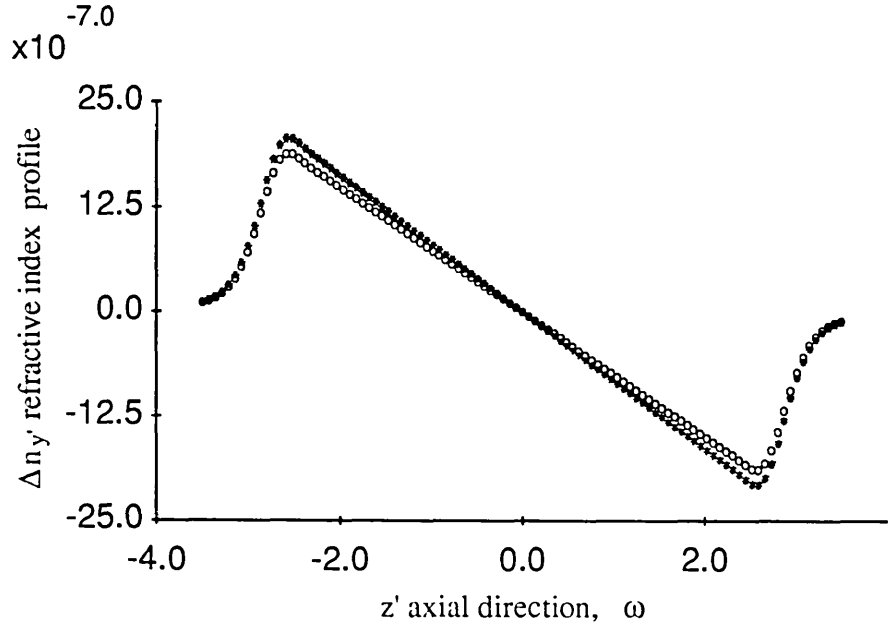


Figure 7.12 The one dimensional profile of $\Delta n_{y'}$ along the z′ axis for $\alpha = -5°(\times)$, $0°(+)$, $10°(\star)$ and $25°(o)$ for $BaTiO_3$.

The two polarisation states experience very different RI enviroments. The *ordinary* one dimensional RI profile along the z′ axis, Fig. 7.12, is weakly dependent on the ray direction, α, and displays a pronounced linear RI slope with a negative gradient. The maximum RI amplitude is $\Delta n_{y'} = 2.08 \times 10^{-6}$ corresponding to $\alpha = 0°$, Table 7.III. By contrast, the *extra–ordinary* RI profile, Fig. 7.13, exhibits a strong geometric dependence on α and the linear RI slope has a positive gradient. Further, the peak values of $\Delta n_{z'}$ are three orders of magnitude larger

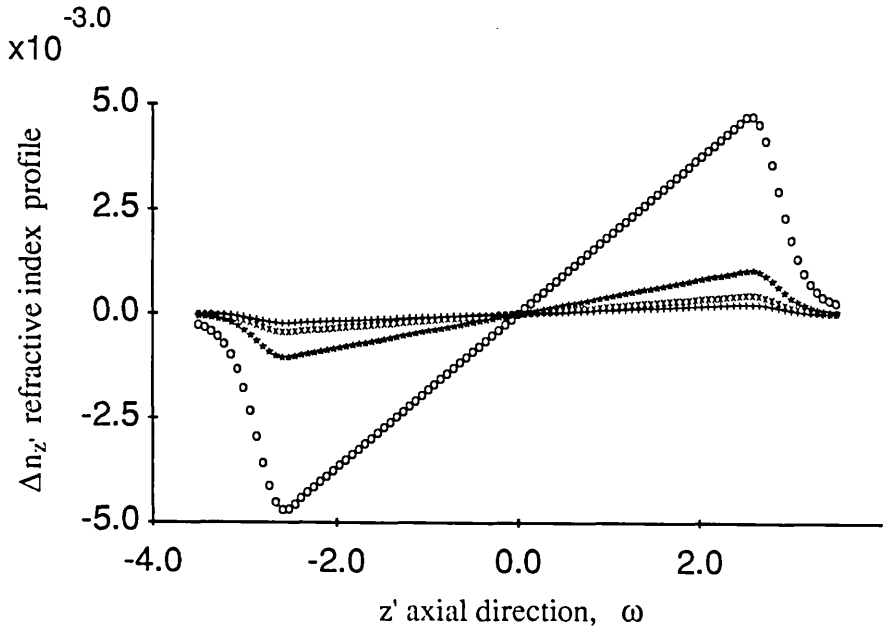


Figure 7.13 The one dimensional profile of $\Delta n_{z'}$ along the z′ axis for $\alpha = -5°(\times)$, $0°(+)$, $10°(\star)$ and $25°(o)$ for $BaTiO_3$.

than $\Delta n_{y'}(\alpha = 0)$, Table 7.III. The maximum amplitude of $\Delta n_{z'}$ is 1.14×10^{-2} corresponding to $\alpha = 56°$.

The two dimensional perspective projection of $\Delta n_{z'}$ at $\alpha = 0°$ is shown in Fig. 7.14. The y′ and z′ axis are along north westerly, ↖, and north easterly, ↗, directions respectively. The RI enviroment exhibits reflection symmetry about the x′z′ plane and 180° rotation (inversion) symmetry about the x′y′ plane. The RI modulation, $\Delta n_{z'}$, equals zero along the y′ axis. The dominant feature is the flat sloping RI disc with a positive gradient w. r. t. the z′ axis. The disc, when projected onto the y′z′ plane, has a characteristic radius of 2.56ω, as dictated by the induced electric field, Fig. 7.10, which confines 99.8% of the transmitted optical power of the illuminating *Gaussian* intensity profile, Fig. 7.1. The magnitude and symmetry of $\Delta n_{z'}$ is expected to distort the incident wavefront in a particular manner. That portion of the transmitted beam in the $z' > 0$ half space experiences a larger RI and hence slower velocity than that portion in the $z' < 0$ half space. As a result light will be refracted predominately into the $z' > 0$ half space. The displaced or scattered light will be coherently amplified by wave mixing with the undeflected light [7.4,7.5,7.6] and complex dynamic feedback will ensue.

The *ordinary* polarisation state is also expected to cause asymmetric fanning but

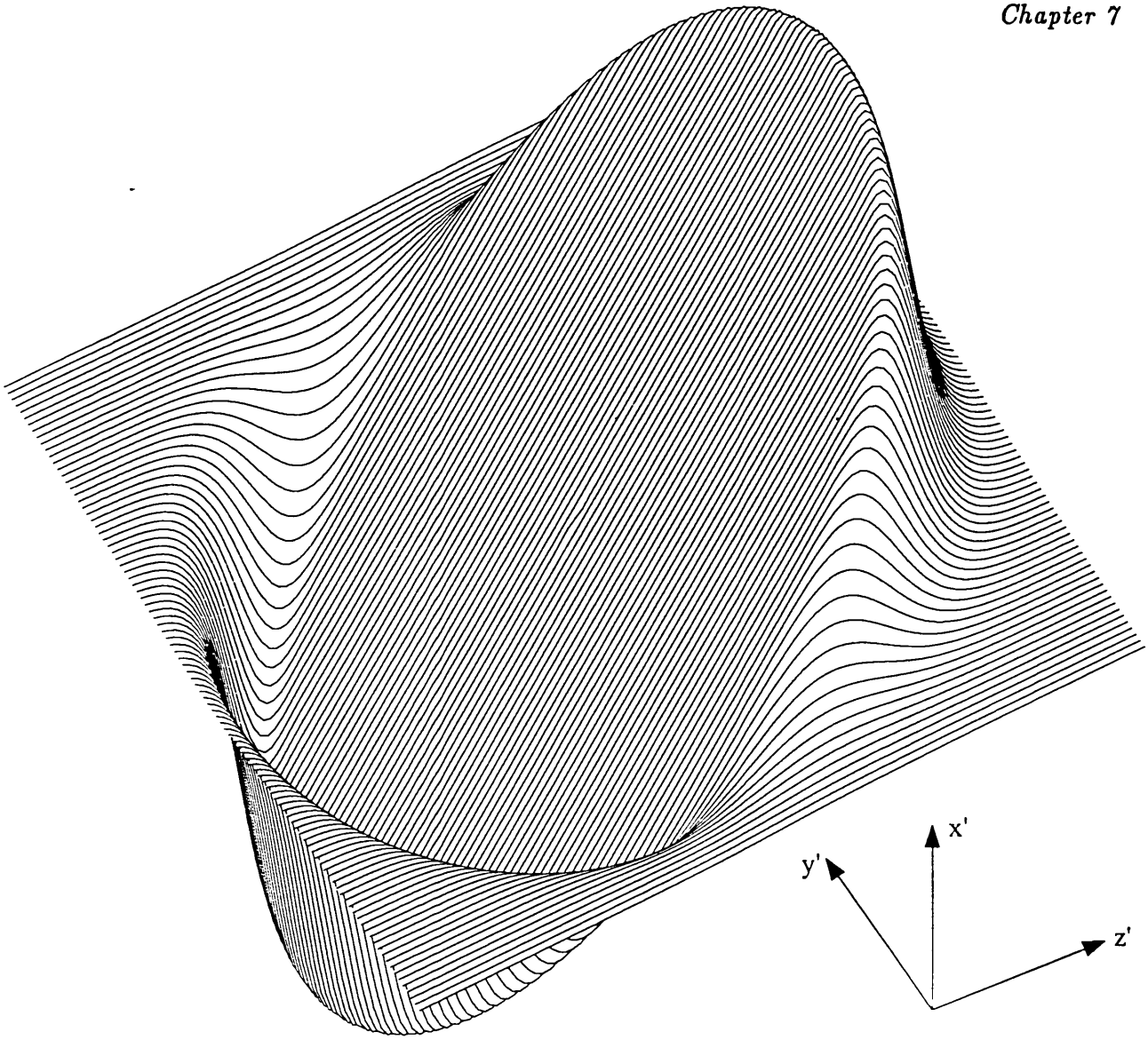


Figure 7.14 The two dimensional perspective projection of $\Delta n_{z'}$ at $\alpha = 0°$ for $BaTiO_3$.

α Degrees	$\Delta n_{y'}$	$\Delta n_{z'}$
-5	2.07×10^{-6}	4.41×10^{-4}
0	2.08×10^{-6}	2.35×10^{-4}
10	2.05×10^{-6}	1.05×10^{-3}
25	1.89×10^{-6}	4.72×10^{-3}

Table 7.III Peak values of $\Delta n_{y'}$ and $\Delta n_{z'}$ for chosen ray directions in $BaTiO_3$.

the scatter direction will be reversed. The scattering will be much weaker in extent as the amplitudes of $\Delta n_{y'}$ are much smaller than $\Delta n_{z'}$, Table 7.III and dynamic

feedback will serve to quench the fanned light.

7.4 Experimental procedure and results.

Asymmetric fanning or self–defocusing of a *Gaussian* intensity profile was easily demonstrated in the laboratory using the barium titanate sample $^{\#2}$ and the argon ion laser operating on $\lambda = 514.5$nm. The intensity cross section of the laser beam, taken direct from the source, was scanned and found to resemble very closely the expected *Gaussian* form. The experimental data, o, accompanied by a *Gaussian* data fit, ——, are shown in Fig. 7.15. The laser beam was found to have a characteristic width of $\omega = 0.39$mm. The incident intensity, I, and angle of incidence, θ Fig. 7.16, were $\sim 2\text{Wcm}^{-2}$ and 20° respectively, corresponding to $\alpha = 7.9°$ and 8.1° for *ordinary* and *extra–ordinary* polarisation states respectively.

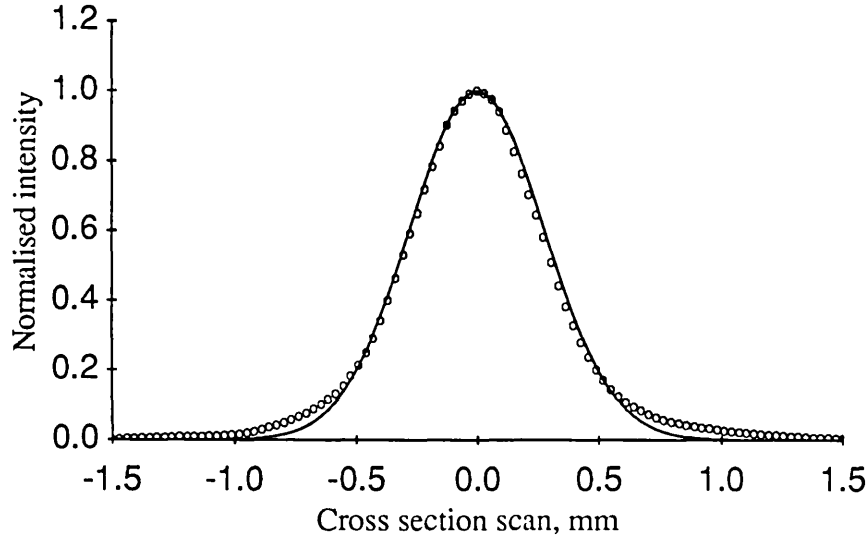


Figure 7.15 The intensity cross section of the argon ion laser beam ($\lambda = 514.5$nm), o, accompanied by the *Gaussian* profile data fit, ——.

The transmitted intensity profiles were recorded and are presented in Fig. 7.17a) and b) for *ordinary* and *extra–ordinary* polarisations respectively. The incident light was initially *ordinary* polarised and, as predicted, the transmitted beam suffered minimal distortion, Fig. 7.17a). However, changing the polarisation state to *extra–ordinary* a pronounced asymmetric fan of light was observed to develope during a transient stage, reaching the steady state profile shown in Fig. 7.17b).

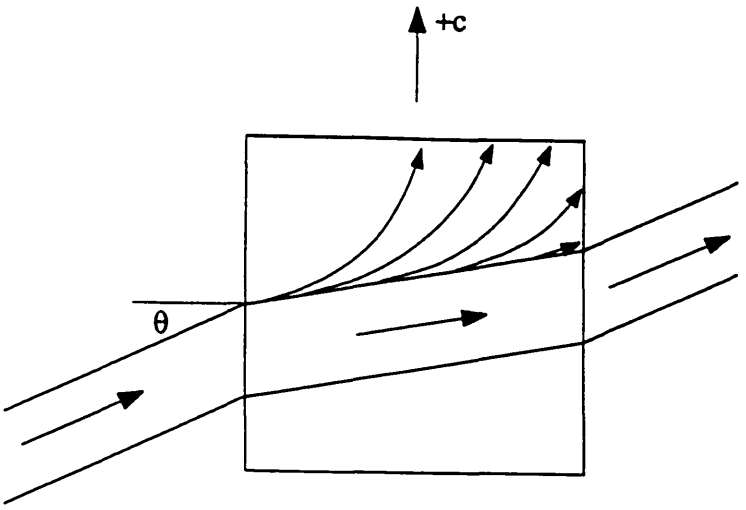


Figure 7.16 Schematic diagram of asymmetric beam fanning in $BaTiO_3$.

The fan direction was along the +c axis and was found to be more pronounced at larger angles of incidence, θ.

Similar experimental observations have been reported by Feinberg [7.4], Temple *et al* [7.7], Ewbank *et al* [7.8] and Chen *et al* [7.9]. The instantaneously scattered ring of light reported in references [7.8] and [7.9] was observed but is not apparent from Fig. 7.17b).

7.5 Conclusions.

The electric field induced in a photorefractive (PR) material by a circulary symmetric *Gaussian* intensity profile was both analytically investigated and numerically analysised. During the initial transient stage the induced electric field was found to evolve with t^2 and $-dI/d\rho$ temporal and spatial dependences respectively. These general analytic results were confirmed numerically using the *Gaussian*, *soft tophat* and *difference of Gaussian* illuminating intensity profiles. The steady state numerical analysis illustrated that saturation of the PR species was inevitable for a spatially confined intensity profile. The induced electric field conformed to the non–saturation profile at small radial distances, ρ, but was quenched to zero at large ρ due to the finite number density of active PR species.

The resultant refractive index (RI) profile was calculated using the linear electro–optic coefficients of the PR material barium titanate. Significant polarisation

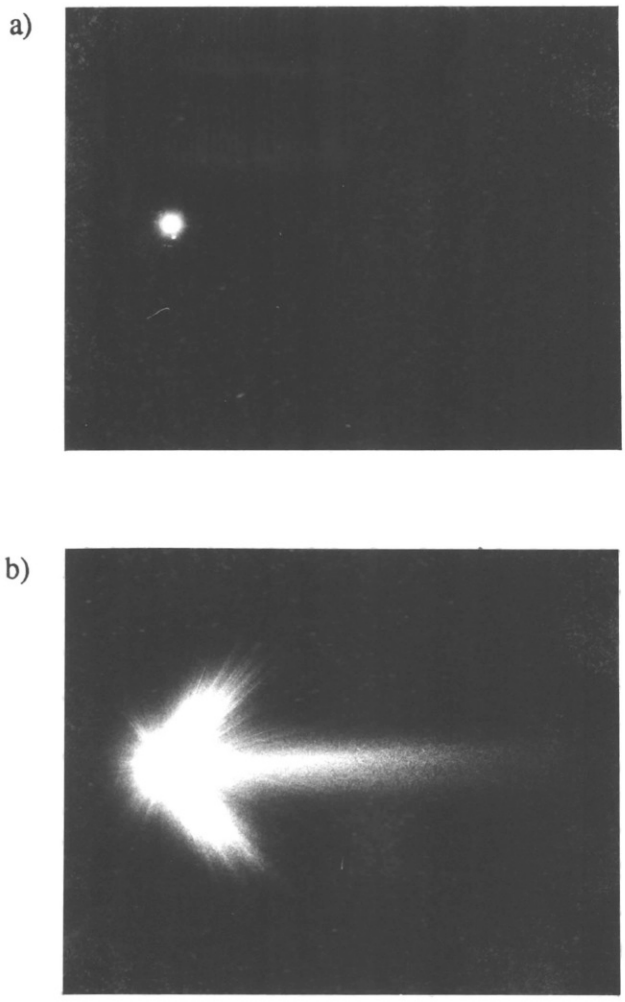


Figure 7.17 Asymmetric beam fanning observed for a a)*ordinary* and b)*extra–ordinary* polarised *Gaussian* laser beam transmitted through $BaTiO_3^{\#2}$.

state and geometric dependences were highlighted. The *extra–ordinary* polarisation state was found to experience very large RI modulations with a strong geometric dependence and, without raytracing, extensive asymmetric fanning of *Gaussian* laser beam was qualitatively predicted and observed experimentally. The *ordinary* polarisation state was found to experience a greatly reduced RI modulated enviroment and minimal optical disturbance was both qualtitatively predicted and observed experimentally.

7.6 References.

[7.1] N.V. Kukhtarev, V.B. Markov, S.G. Odulov, M.S. Soskin and V.L. Vinetskii, "Holographic storage in electrooptic crystals. I Steady state," Ferroelectrics **22**, 949–960 (1979).

[7.2] Lorrain P. and Corson D.,"Electromagnetic Fields and Waves," 2nd Ed. (Freeman, New York ,1970).

[7.3] Atkinson K.E., "An Introduction to Numerical Analysis," (Wiley, New York, 1978).

[7.4] J. Feinberg, "Asymmetric self-defocusing of an optical beam from the photorefractive effect," J.Opt.Soc.Am. **72**, 46–51 (1982).

[7.5] J. Marotz, K.H. Ringhofer, R.A. Rupp and S. Treichel, "Light-induced scattering in photorefractive crystals," IEEE J.Quant.Electron. **QE–22**, 1376–1383 (1986).

[7.6] J. Marotz, K.H. Ringhofer and R.A. Rupp, "Holographic light scattering in photorefractive materials," Topical meeting on Photorefractive materials, effects and devices, Technical digest series **17**, 106–109 (1987).

[7.7] D.A. Temple and C. Warde, "Anistropic scattering in photorefractive crystals," J.Opt.Soc.Am.B. **3**, 337–341 (1986).

[7.8] M.D. Ewbank, P. Yeh and J. Feinberg, "Photorefractive conical diffraction in $BaTiO_3$," Opt.Commun. **59**, 423–428 (1986).

[7.9] W.–H. Chen, C.–M. Peng and P. Yeh, "Anisotropic conical diffractions in a $BaTiO_3$ crystal," Topical meeting on Photorefractive materials, effects and devices, Technical digest series **17**, 118–121 (1987).

CHAPTER 8

SUMMARY AND CONCLUSIONS

The main thrust of this thesis was the theoretical interpretation of the photorefractive effect, an appreciation of the selection of photorefractive materials currently available and an investigation into potential applications for real time adaptive image processing.

The band transport model of the photorefractive effect was rigorously derived and easily amended to accommodate for electron/hole competition and deep donor/-shallow traps. The photorefractive response to spatially varying illumination is interpreted by a three stage mechanism. The preferential *generation* of free charged carriers at regions of high irradiance, the *migration* by diffusion to regions of low irradiance and/or by drift under the influence of an externally applied electric field and finally the *recombination* with an empty trap spatially separated from the original parent of the carrier. The steady state regime is attained when the drift and diffusion transport mechanisms are equal and opposite and consequently the *migration* rate is reduced zero. The *generation* and *recombination* rates are equal and the induced static electric field modulates the refractive index of the medium by the electro-optic effect. The illuminating spatially varying intensity profile consequently induces a phase volume hologram through the bulk of the medium.

Two wave mixing and coherent light amplification were analysed in detail. The photorefractive response to a one dimensional cosinusoidal intensity profile was investigated in both the linear in generation/recombination and saturation regimes. The induced electric field amplitude was found to be linearly dependent on the grating wavenumber and reduced modulation, for the fringe contast much less than unity, in the linear regime while inversely proportional to the grating wavenumber in the saturation regime. The grating is, in general, shifted in phase with respect to the illuminating intensity profile and the unshifted and $\pi/2$ shifted components are responsible for the exchange of phase and energy between the two *mixing* waves, resulting in both curved and contrast varying interference fringes through the depth of the photorefractive medium. Two wave mixing in the photorefractive ferroelectric oxide materials barium titanate, $BaTiO_3$, and cerium doped strontium barium niobate, SBN:60, exhibited such grating wavenumber dependence and available number densities of photorefractive species and peak induced electric field amplitudes of $3.4 \times 10^{16}\text{cm}^{-3}$, 3.37kVcm^{-1} and $1.9 \times 10^{16}\text{cm}^{-3}$, 0.88kVcm^{-1}

were deduced respectively. Coherent light amplification of an image bearing signal beam was demonstrated using a crystal of $BaTiO_3$ and a reference:signal beam intensity ratio of 100:1. The transmitted image was recorded and found to have experienced an intensity gain of 11.7. Two wave mixing transient measurements were performed and characteristic grating rise, decay and dark storage times were investigated. The sample of barium titanate studied was found to have a characteristic rise time of 1.52 seconds for an incident intensity ratio of unity and a total intensity of $1 Wcm^{-2}$. The dark storage time of the same sample of $BaTiO_3$ was found to be $\sim$ 5.75 seconds at an ambient room temperature of 20°C. This value is inconsistent with previously reported times of many hours and has remained a mystery. By comparison the dark storage time of the sample of SBN:60 was estimated to be $\sim$ 19 hours!

Phase conjugation by degenerate four wave mixing in photorefractive materials was studied and the interacting wave coupling investigated. The phase distortion correcting, lensless imaging and self–aligning characteristics of phase conjugate optics were experimentally demonstrated using an externally pumped sample of $BaTiO_3$. Phase distortion correction and image subtraction (EXOR digital logic) experimental results are presented to provide qualitative evidence of the fidelity of phase conjugate generated in $BaTiO_3$. The quality of the results are of a high standard which emphasizes both the capabilities of $BaTiO_3$ as a photorefractive material and the unique imaging properties of phase conjugate optics. Barium titanate was also observed to readily self–pump via the internal reflection of asymmertically fanned light. Three different temporal modes were recorded and are presented, namely steady state *cw*, regular oscillatory and randomly chaotic. The *cw* phase conjugate reflectivity was measured up to 30.5% and self–oscillation with a nearby specularly reflecting object and the mutual self–oscillation between two self–pumping crystals of $BaTiO_3$ were observed.

The inter–cavity complex amplitudes of a phase conjugate Fabry–Perot interferometer, constructed from a phase conjugate and conventional mirror, and their coupling with the external fields were extensively analysed. Specular reflection cancellation and enhancement was predicted with complete extinction with a perfect phase conjugate mirror, unit phase conjugate reflectivity, independent of the reflectivity of the lossless conventional plane mirror. The theoretical predictions were verified experimentally using a lossless plane dielectric beam splitter and an externally pumped sample of $BaTiO_3$ as the conventional and phase conjugate mirrors respectively. Both extensive specular reflection cancellation and enhancement were observed. The maximum extinction recorded was a drop to 5% of

the original intensity for a phase conjugate reflectivity of unity and in conclusion, the experimental results were supportive of the general scattering theory of phase distortion correction by phase conjugation.

Holographic associative memories were studied and one all–optical configuration with phase conjugate feedback was proposed and experimentally demonstrated. The Hopfield neural network model was discussed and its computer simulation, using a SUN–3/68020 processor, highlighted the models strong dependence on the number and orthogonality of the stored data, the distortion imposed on the initial input data, the demand for a large memory capacity and the need to process the information in parallel. The experimental demonstration consisted of a reference beam multiplexed Fourier transform hologram as the global memory store and a phase conjugate mirror to provide self–aligned phase distortion corrected feedback. The stored information consisted of two groups of four binary geometric figures. The system demonstrated the ability to recover any one complete image at the output plane when a discriminating partial piece of information was presented at the input. Improvements to the system to increase its flexibility would have been to incorporate thresholding, amplification, multiple iterations and a memory store capable of *learning*.

The photorefractive response to spatially confined circularly symmetric intensity profiles in general and the Gaussian profile in particular were theoretically investigated. The coupled band transport equations, expressed in the circular cylindrical co–ordinate system, were solved in both the initial transient and linear steady state regimes in the absence of dynamic feedback. In the initial transient regime, $0 < t < \tau_R$, the induced radial electric field evolved with a t^2 temporal characteristic and a spatial profile proportional to the inverted first derivative of the illuminating intensity profile with respect to the radial co–ordinate. These two results were confirmed using numerical techniques and the Gaussian, soft tophat and difference–of–Gaussians intensity profiles. The coupled band transport equations were solved analytically in the linear in generation/recombination steady state regime. The spatial profile of the induced electric field was found to be proportional to the inverted first derivative of the illuminating intensity profile divided by the intensity itself. For the Gaussian profile a linear dependence on radial distance is predicted with ultimately an infinite electric field at an infinite radius! This non–physical result served to indicate that saturation of the photorefractive species must be inevitable in the steady state to yield a spatially confined electric field as well as illuminating intensity profile. The numerical analysis was extended to the steady state and for the Gaussian profile the induced electric field followed

the linear dependence for small radial distances but ultimately saturated, rolled over and fell to zero at large distances. The peak electric field was 12.7kVcm^{-1} for a number density of 3.0×10^{16}cm^{-3} available photorefractive species and located at a radial distance of 2.56mm for a characteristic beam width of 1mm. The numerically derived steady state electric field for Gaussian illumination was employed to investigate the resultant refractive index modulation induced in barium titanate. Accommodating for both light polarisation and geometric considerations the peak refractive index modulations for normal incidence, perperdicular to the crystallographic c axis, were 2.08×10^{-6} and 2.35×10^{-4} for *ordinary* and *extra–ordinary* polarisations respectively. The symmetry and form of the two dimensional refractive index enviroments suggested the asymmetric fanning of light along the +c axis direction for p–type photoconduction and *extra–ordinary* polarisation while minimal optical disturbance for *ordinary* polarisation. These suggestions were confirmed by experimental observation.

Currently around the world there are many varied and exciting branches of research into the photorefractive effect, the materials and their potential applications. Materials are being grown with different stoichiometric configurations, dopants and reduction/oxidation treatments. Proposed applications range from photolithography to real time interferometery, the novelty filter to the ultra–fast optical switch and incoherent–to–coherent light conversion to image colour conversion. The future development of the science will be dependent on many factors including the development of new photorefractive materials and the location of commercially viable applications. These two factors are inherently intertwined with the progress of new potential applications possibly hindered by the limited selection of photorefractive materials available; the science would benefit from a broader range of materials extending further across the spectral region and with more varied combinations of photoconducting and electro–optic characteristics.

The ultra–fast photorefractive effect and its application to high speed switching and digital logic has recently stimulated much interest and activity in the field, and may be particularly fruitful in the future. Ultra–fast photorefractive response characteristics have been demonstrated by members from all three famillies of photorefractive materials using pico and nanosecond optical pulse durations and $\sim$ 1mJ energies per pulse. The experimental observations made have investigated temporal and fluence dependences, and the results are encouraging. Future research needs to examine the possible repetition rates, spatial beam qualities and potential applications of ultra–fast real time adaptive optics.

Finally and independent of the future developments made, the photorefractive effect will always remain an intriguing physical phenomenon which will continue to challenge the imagination of research scientists.

APPENDIX A

THE ELECTRO–OPTIC NATURE OF BARIUM TITANATE AND STRONTIUM BARIUM NIOBATE.

The most general form of the optical indicatrix for both barium titanate and strontium barium niobate is [A.1]

$$\begin{aligned}&\frac{x^2}{n_o^2}+\frac{y^2}{n_o^2}+\frac{z^2}{n_e^2}\\&+r_{13}x^2E_z+r_{23}y^2E_z+r_{33}z^2E_z\\&+2r_{42}yzE_y+2r_{51}xzE_x\\&=1,\end{aligned}\tag{A.1}$$

where the principle optic axis of the crystal, +c, is coincident with the z co-ordinate axis. Considering an induced electric field confined to the xz plane, the electric field components become $E_x \neq 0$, $E_y = 0$ and $E_z \neq 0$ and the optical indicatrix is reduced to

$$\begin{aligned}&x^2\left(1/n_o^2+r_{13}E_z\right)\\&+y^2\left(1/n_o^2+r_{23}E_z\right)\\&+z^2\left(1/n_e^2+r_{33}E_z\right)\\&+2r_{51}xzE_x\\&=1.\end{aligned}\tag{A.2}$$

On inspection of Eq. (A.2) it is seen that only x and z participate in the mixed term. To eliminate that term and hence locate the principle dielectric axis an axis rotation about y is suggested. Consider the following cartesian co-ordinate change illustrated in Fig. A.1 and analytically expressed by

$$x = x'\cos\theta - z'\sin\theta \tag{A.3a}$$

$$y = y' \tag{A.3b}$$

$$z = x'\sin\theta + z'\cos\theta. \tag{A.3c}$$

Hence

$$x^2 = x'^2\cos^2\theta + z'^2\sin^2\theta - 2x'z'\sin\theta\cos\theta \tag{A.4a}$$

$$y^2 = y'^2 \tag{A.4b}$$

$$z^2 = x'^2\sin^2\theta + z'^2\cos^2\theta + 2x'z'\sin\theta\cos\theta \tag{A.4c}$$

and

$$xz = x'^2 \sin\theta\cos\theta + x'z'\cos^2\theta - x'z'\sin^2\theta - z'^2\sin\theta\cos\theta. \qquad (A.4d)$$

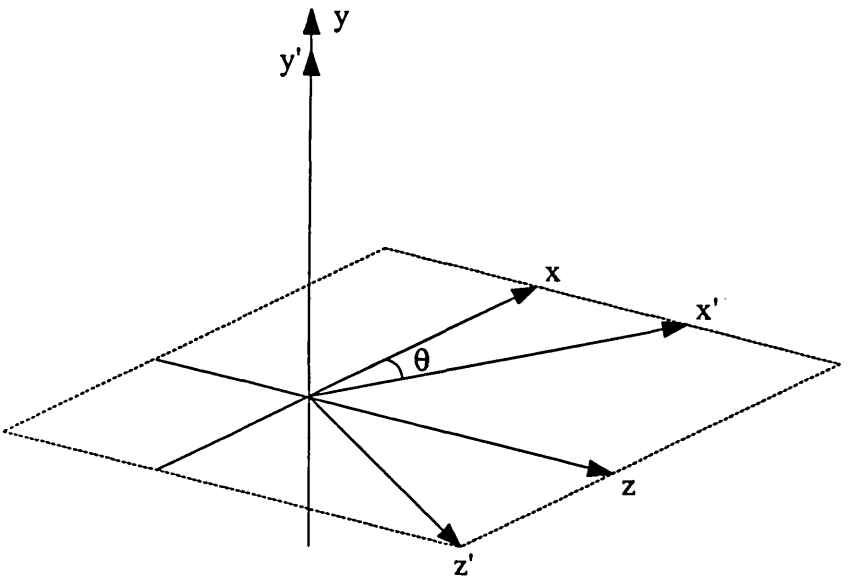


Figure A.1 Cartesian co-ordinate change to locate principle dielectric axis in $BaTiO_3$ and SBN.

Substituting Eqs. (A.4a), (A.4b), (A.4c) and (A.4d) back into the expression for the optical indicatrix, Eq. (A.2), yields

$$\begin{aligned}
&x'^2\left[(1/n_o^2 + r_{13}E_z)\cos^2\theta + (1/n_e^2 + r_{33}E_z)\sin^2\theta + 2r_{51}E_x\sin\theta\cos\theta\right] \\
&+ y'^2\left[(1/n_o^2 + r_{23}E_z)\right] \\
&+ z'^2\left[(1/n_o^2 + r_{13}E_z)\sin^2\theta + (1/n_e^2 + r_{33}E_z)\cos^2\theta - 2r_{51}E_x\sin\theta\cos\theta\right] \\
&+ x'z'\left[(1/n_o^2 + r_{13}E_z)(-2\sin\theta\cos\theta)\right. \\
&\qquad + (1/n_e^2 + r_{33}E_z)2\sin\theta\cos\theta \\
&\qquad \left. + 2r_{51}E_x(\cos^2\theta - \sin^2\theta)\right] \\
&= 1. \qquad (A.5)
\end{aligned}$$

The angle θ is chosen to eliminate the cross terms in the above equation, Eq. (A.5). Thus

$$(1/n_o^2 + r_{13}E_z)(-\sin 2\theta) + (1/n_e^2 + r_{33}E_z)\sin 2\theta + 2r_{51}E_x\cos 2\theta = 0,$$

and hence θ is defined by

$$\tan 2\theta = \frac{2r_{51}E_x}{(1/n_o^2 + r_{13}E_z) - (1/n_e^2 + r_{33}E_z)}. \qquad (A.6)$$

The optical indicatrix becomes

$$\begin{aligned} & x'^2 \left[(1/n_o^2 + r_{13}E_z)\cos^2\theta + (1/n_e^2 + r_{33}E_z)\sin^2\theta + 2r_{51}E_x \sin\theta\cos\theta\right] \\ & + y'^2 \left[(1/n_o^2 + r_{23}E_z)\right] \\ & + z'^2 \left[(1/n_o^2 + r_{13}E_z)\sin^2\theta + (1/n_e^2 + r_{33}E_z)\cos^2\theta - 2r_{51}E_x \sin\theta\cos\theta\right] \\ & = 1. \end{aligned} \tag{A.7}$$

The expression may be simplified further as follows. Consider the principle RI for x', $n_{x'}$

$$1/n_{x'}^2 = \left[(1/n_o^2 + r_{13}E_z)\cos^2\theta + (1/n_e^2 + r_{33}E_z)\sin^2\theta + 2r_{51}E_x \sin\theta\cos\theta\right]$$

and using $\cos^2\theta = \frac{1}{2}(1 + \cos 2\theta)$ and $\sin^2\theta = \frac{1}{2}(1 - \cos 2\theta)$ becomes

$$\begin{aligned} &= (1/n_o^2 + r_{13}E_z) - \frac{1}{2}\left[(1/n_o^2 + r_{13}E_z) - (1/n_e^2 + r_{33}E_z)\right] \\ &\quad + \frac{1}{2}\left[(1/n_o^2 + r_{13}E_z) - (1/n_e^2 + r_{33}E_z)\right]\cos 2\theta \\ &\quad + r_{51}E_x \sin 2\theta, \\ &= (1/n_o^2 + r_{13}E_z) - \frac{1}{2}\left[(1/n_o^2 + r_{13}E_z) - (1/n_e^2 + r_{33}E_z)\right](1 - \cos 2\theta) \\ &\quad + r_{51}E_x \sin 2\theta. \end{aligned}$$

Using the definition of θ, Eq. (A.6)

$$\begin{aligned} &= (1/n_o^2 + r_{13}E_z) - r_{51}E_x \frac{\cos 2\theta(1 - \cos 2\theta)}{\sin 2\theta}, \\ &\quad + r_{51}E_x \sin 2\theta \\ &= (1/n_o^2 + r_{13}E_z) + r_{51}E_x \left[\frac{\sin^2 2\theta + \cos^2 2\theta - \cos 2\theta}{\sin 2\theta}\right], \\ &= (1/n_o^2 + r_{13}E_z) + r_{51}E_x \left[\frac{1 - \cos 2\theta}{\sin 2\theta}\right], \\ 1/n_{x'}^2 &= (1/n_o^2 + r_{13}E_z) + r_{51}E_x \tan\theta. \end{aligned} \tag{A.8a}$$

Similarly for $n_{z'}$

$$1/n_{z'}^2 = (1/n_e^2 + r_{33}E_z) - r_{51}E_x \tan\theta. \tag{A.8b}$$

Finally the optical indicatrix may be expressed in terms of the new principle dielectric axis as

$$\frac{x'^2}{n_{x'}^2} + \frac{y'^2}{n_{y'}^2} + \frac{z'^2}{n_{z'}^2} = 1 \tag{A.9}$$

and accompanyed by the principle refractive indices

$$n_{x'} = \left[1/n_o^2 + r_{13}E_z + r_{51}E_x \tan\theta\right]^{-1/2}, \tag{A.10a}$$

$$n_{y'} = \left[1/n_o^2 + r_{23}E_z\right]^{-1/2} \tag{A.10b}$$

and

$$n_{z'} = \left[1/n_e^2 + r_{33}E_z - r_{51}E_x \tan\theta\right]^{-1/2} . \qquad (A.10c)$$

References.

[A.1] Yariv A. and Yeh P., "Optical Waves in Crystals," (Wiley series in pure and applied optics, New York, 1984).

APPENDIX B

SPECTROPHOTOMETRIC DATA.

Wavelength nm	Absorption coefficients cm^{-1} BSO#1, ■
800	0.723
790	0.723
780	0.737
770	0.737
760	0.746
750	0.760
740	0.774
730	0.783
720	0.797
710	0.797
700	0.806
690	0.806
680	0.820
670	0.829
660	0.829
650	0.843
640	0.843
630	0.852
620	0.875
610	0.884
600	0.898
590	0.935
580	0.967
570	1.022
560	1.082
550	1.220
540	1.391
530	1.704
520	2.210
510	2.993
500	4.099

Table B.I Bismuth silicon oxide spectrophotometric data

Wavelength nm	Absorption coefficients cm^{-1}		
	$BaTiO_3^{\#1}$, ■	$BaTiO_3^{\#2}$, △	$BaTiO_3^{\#3}$, ×
800	1.151	0.950	0.480
790	1.174	0.996	0.487
780	1.197	1.025	0.487
770	1.220	1.065	0.499
760	1.257	1.123	0.499
750	1.289	1.180	0.507
740	1.312	1.238	0.518
730	1.359	1.307	0.530
720	1.405	1.382	0.537
710	1.451	1.451	0.549
700	1.483	1.514	0.568
690	1.534	1.583	0.576
680	1.566	1.652	0.587
670	1.612	1.727	0.603
660	1.658	1.888	0.622
650	1.704	1.842	0.645
640	1.727	1.871	0.664
630	1.796	1.974	0.683
620	1.833	2.044	0.702
610	1.865	2.101	0.729
600	1.920	2.170	0.760
590	1.957	2.199	0.779
580	2.003	2.331	0.806
570	2.049	2.418	0.825
560	2.072	2.475	0.844
550	2.109	2.544	0.871
540	2.141	2.636	0.894
530	2.164	2.694	0.921
520	2.187	2.763	0.952
510	2.197	2.821	0.967
500	2.210	2.832	0.998
490	2.220	2.878	1.028
480	2.257	2.907	1.067
470	2.326	2.936	1.101
460	2.418	2.936	1.159
450	2.533	3.005	1.247
440	2.731	3.166	1.389
430	3.062	3.442	1.631
420	3.615	4.030	2.034
410	4.882		3.128
400			

Table B.II Barium titanate spectrophotometric data

Wavelength nm	Absorption coefficients cm^{-1}	
	SBN : $60^{\#1}$, ■	SBN : $60^{\#2}$, △
800	0.495	1.091
790	0.495	1.091
780	0.495	1.102
770	0.495	1.114
760	0.495	1.148
750	0.507	1.159
740	0.507	1.170
730	0.507	1.182
720	0.507	1.193
710	0.518	1.204
700	0.518	1.227
690	0.530	1.261
680	0.530	1.284
670	0.541	1.318
660	0.564	1.341
650	0.587	1.352
640	0.599	1.364
630	0.622	1.375
620	0.656	1.386
610	0.691	1.420
600	0.737	1.454
590	0.794	1.477
580	0.852	1.511
570	0.921	1.546
560	0.990	1.591
550	1.128	1.625
540	1.186	1.670
530	1.278	1.704
520	1.393	1.750
510	1.485	1.784
500	1.566	1.818
490	1.646	1.864
480	1.704	1.898
470	1.761	1.909
460	1.808	1.909
450	1.865	1.909
440	1.934	1.920
430	2.026	1.954
420	2.153	2.023
410	2.372	2.159
400	2.798	2.409

Table B.III Cerium doped strontium barium niobate spectrophotometric data

Wavelength μm	Absorption coefficients cm^{-1}	
	GaAs, ■	InP, △
1.848	0.107	
1.808	0.117	
1.768	0.156	
1.727	0.195	
1.687	0.264	
1.647	0.352	
1.606	0.469	
1.566	0.605	
1.526	0.840	
1.485	1.074	
1.445	1.406	0.107
1.405	1.797	0.098
1.365	2.227	0.098
1.324	2.656	0.107
1.284	3.086	0.127
1.244	3.516	0.156
1.203	3.926	0.205
1.163	4.316	0.283
1.123	4.648	0.391
1.082	4.883	0.547
1.042	4.961	0.840
1.002	5.098	1.406
0.969	5.332	4.688
0.929	5.938	

Table B.IV Gallium arsenide and indium phosphide spectrophotometric data

APPENDIX C

ANALYTIC SOLUTION OF THE BAND TRANSPORT EQUATIONS FOR A ONE DIMENSIONAL COSINUSOIDAL INTENSITY PROFILE.

In the steady state and linear in generation/recombination regimes the coupled band transport equations, for the simple intensity profile

$$I(z) = I_o\,[1 + M\cos kz]\,, \tag{C.1}$$

are reduced to [C.1]

$$0 = 0 + \frac{d}{dz}\left[D\frac{dn}{dz} + \mu n E_z\right], \tag{C.2}$$

$$0 = (N_D - N_A)\,(sI_o\,[1 + M\cos kz] + \beta) - n/\tau_R, \tag{C.3}$$

$$\frac{dE_z}{dz} = \frac{q}{\varepsilon\varepsilon_o}N^+_{D_{Migration}}. \tag{C.4}$$

We wish to solve this system of coupled equations, Eqs. (C.2)→(C.4), for the induced electric field E_z. Re-arranging Eq. (C.3) yields

$$0 = (N_D - N_A)(sI_o + \beta) + (N_D - N_A)sI_oM\cos kz - n/\tau_R, \tag{C.5}$$

$$= (N_D - N_A)(sI_o + \beta) + (N_D - N_A)(sI_o + \beta)\frac{sI_oM}{(sI_o + \beta)}\cos kz - n/\tau_R, \tag{C.6}$$

$$= G(I_o)\,[1 + m\cos kz] - n/\tau_R, \tag{C.7}$$

where $G(I_o) = (N_D - N_A)(sI_o + \beta)$. The reduced modulation m accomodates for the competition between thermal and photogeneration mechanisms to smooth and create respectively the spatial variations in free electron number density and is given by

$$m = \frac{M}{(1 + \beta/sI_o)}. \tag{C.8}$$

From Eq. (C.7) the free electron number density is given by

$$n = n_o\,[1 + m\cos kz]\,, \tag{C.9}$$

where $n_o = G(I_o)\tau_R$ i.e. within the constraints of the initial assumptions, the free electron number density is linearly proportional to the illuminating intensity profile.

Re–arranging Eq. (C.2) yields

$$\frac{d}{dz}\left[D\frac{dn}{dz} + \mu n E_z\right] = 0, \qquad (C.10)$$

$$D\frac{dn}{dz} + \mu n E_z = j/q, \qquad (C.11)$$

$$E_z = \left(j - qD\frac{dn}{dz}\right)/q\mu n, \qquad (C.12)$$

where j, the constant of integration, is a photoelectron current density induced by an externally applied d. c. electric field. Substituting Eq. (C.9) into (C.12) yields

$$E_z = \frac{j}{q\mu n_o}\frac{1}{(1 + m\cos kz)} - \frac{Dk}{\mu}\frac{m\sin kz}{(1 + m\cos kz)}. \qquad (C.13)$$

To eliminate the unknown parameter j, consider an external d. c. electric field E_A applied across a material length l. The accompanying boundary condition must be

$$\frac{1}{l}\int_{-l/2}^{l/2} E_z dz = E_A. \qquad (C.14)$$

Applying to Eq. (C.13) gives

$$E_A = \frac{1}{l}\frac{j}{q\mu n_o}\int_{-l/2}^{l/2}\frac{dz}{(1 + m\cos kz)} - \frac{1}{l}\frac{Dk}{\mu}\int_{-l/2}^{l/2}\frac{m\sin kz}{(1 + m\cos kz)}dz. \qquad (C.15)$$

Employing the standard integral 2.553(3) from reference [C.2]

$$\int \frac{dz}{(a + b\cos z)} = \frac{2}{\sqrt{a^2 - b^2}}\text{arctg}\frac{\sqrt{a^2 - b^2}\,tg(z/2)}{a + b} \quad \text{for } a^2 > b^2 \qquad (C.16)$$

and using conventional integration techniques, the two integrals within Eq. (C.15) become

$$\frac{1}{l}\int_{-l/2}^{l/2}\frac{dz}{(1 + m\cos kz)} = \frac{1}{\sqrt{1 - m^2}}, \qquad (C.17a)$$

$$\frac{1}{l}\int_{-l/2}^{l/2}\frac{m\sin kz}{(1 + m\cos kz)}dz = 0. \qquad (C.17b)$$

Substituting back into Eq. (C.15) yields

$$E_A = \frac{j}{\sigma_o}\frac{1}{\sqrt{1-m^2}} \qquad (C.18)$$

and hence

$$j = \sigma_o\sqrt{1-m^2}E_A, \qquad (C.19)$$

where $\sigma_o = q\mu n_o$ is the characteristic material conductivity under uniform illumination. It is seen from Eqs. (C.17a) and (C.17b) that the only contribution to the photoelectron current density is from the *drift* transport mechanism, Eq. (C.17a), and none from *diffusion*, (C.17b). Under cosinusoidal illumination the conductivity is reduced by the factor $\sqrt{1-m^2}$ relative to the conductivity for uniform illumination, σ_o. The darker regions within the material are more insulating and hence serve to restrict the transverse flow or *drift* of the free electrons.

The final expression for the induced electric field in the steady state and linear in generation/recombination regimes is

$$E_z = E_A\frac{\sqrt{1-m^2}}{(1+m\cos kz)} - E_D\frac{m\sin kz}{(1+m\cos kz)}. \qquad (C.20)$$

The characteristic electric field E_D is given by

$$E_D = \frac{Dk}{\mu} = \left[\frac{k_BT}{q}\right]k, \qquad (C.21)$$

where the Einstein relationship, Eq. (2.11), has been employed.

The induced electric field, Eq. (C.20), is clearly not perfectly sinusoidal in form, especially for large values of m. The fundamental Fourier components of Eq. (C.20) are calculated and used as a first order approximation to the field.

The Fourier series representation of a general periodic function f(z) of period 2π is given by [C.3]

$$f(z) = a_o + \sum_{n=1}^{\infty}(a_n\cos nz + b_n\sin nz)\,. \qquad (C.22)$$

Accompanyed by the Fourier coefficients

$$a_o = \frac{1}{2\pi}\int_{-\pi}^{\pi} f(z)dz, \qquad (C.23a)$$

$$a_n = \frac{1}{\pi}\int_{-\pi}^{\pi} f(z)\cos(nz)dz \qquad (C.23b)$$

and

$$b_n = \frac{1}{\pi}\int_{-\pi}^{\pi} f(z)\sin(nz)dz. \qquad (C.23c)$$

The d. c. and fundamental coefficients of the E_z are calculated as follows. Firstly,

$$a_o = \frac{1}{2\pi}\int_{-\pi}^{\pi} E_A \frac{\sqrt{1-m^2}}{(1+m\cos kz)}d(kz). \qquad (C.24)$$

Employing the standard integral Eq. (C.16) reveals

$$a_o = E_A. \qquad (C.25)$$

Further, the even fundamental coefficient, a_1, is calculated

$$a_1 = \frac{1}{\pi}\int_{-\pi}^{\pi} E_A \frac{\sqrt{1-m^2}\cos kz}{(1+m\cos kz)}d(kz). \qquad (C.26)$$

Employing the standard integrals 2.554(2) [C.2]

$$\int \frac{A+B\cos z}{(a+b\cos z)}dz = \frac{B}{b}z + \frac{Ab-aB}{b}\int \frac{dz}{(a+b\cos z)} \qquad (C.27)$$

and 2.553(3) [C.2], Eq. (C.16) reveals

$$a_1 = -\frac{2E_A}{m}[1-\sqrt{1-m^2}]. \qquad (C.28)$$

Finally, the odd fundamental coefficient,

$$b_1 = -\frac{1}{\pi}\int_{-\pi}^{\pi} E_D \frac{m\sin^2 kz}{(1+m\cos kz)}d(kz), \qquad (C.29)$$

is calculated using the method of integration by parts and the above two standard integrals, Eqs. (C.16) and (C.27). The final result is

$$b_1 = -\frac{2E_D}{m}[1-\sqrt{1-m^2}]. \qquad (C.30)$$

The first order approximation of the induced electric field, E_z, is thus given by

$$E_z \simeq E_A - \frac{2}{m}[1-\sqrt{1-m^2}]\,(E_A\cos kz + E_D\sin kz)\,, \qquad (C.31)$$

$$\simeq E_A - \frac{2}{m}[1-\sqrt{1-m^2}]\sqrt{E_A^2+E_D^2}\cos(kz+\phi). \qquad (C.32)$$

Where the phase shift, ϕ, between the induced electric field and illuminating intensity profile is given by

$$\tan\phi = E_D/E_A. \qquad (C.33)$$

For $m \ll 1$ the term $2[1-\sqrt{1-m^2}]/m \simeq m$ and are graphically compared, ▪ and —— respectively, in Fig. C.1. The electric field is thus further approximated to

$$E_z \approx E_A - m\sqrt{E_A^2+E_D^2}\cos(kz+\phi). \qquad (C.34)$$

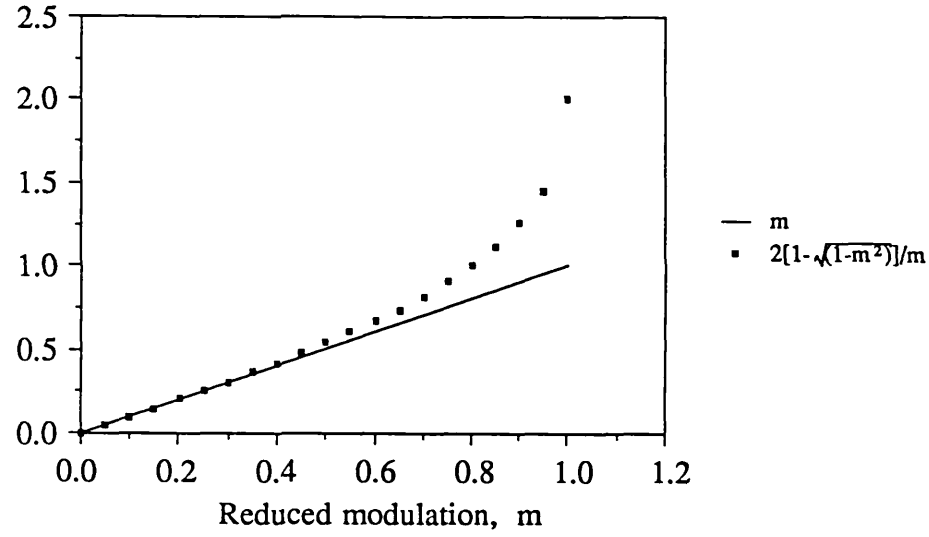


Figure C.1 The linear in modulation approximation.

References.

[C.1] T.J. Hall, R. Jaura, L.M. Conners and P.D. Foote, "The photorefractive effect–A review," Prog.Quant.Electr. **10**, 77–146 (1985).

[C.2] Gradshteyn I.S. and Ryzhik I.M., "Table of Integrals, Series and Products – Corrected and enlarged edition," (Academic Press, Inc., London, 1980).

[C.3] Kreyszig E.,"Advanced Engineering Mathematics – 4th Ed.," (John Wiley & Sons, Inc., New York, 1979).

APPENDIX D

THE COUPLED WAVE THEORY FOR A DYNAMIC MEDIUM.

Consider an electric field, **E**, to be composed of a reference and signal field

$$\mathbf{E} = \Big[\mathrm{R(x)}\exp[i(\omega t - \varrho.\mathbf{r} + \phi_{\mathrm{R}}(\mathrm{x}))] + \mathrm{S(x)}\exp[i(\omega t - \varrho.\mathbf{s} + \phi_{\mathrm{S}}(\mathrm{x}))]\Big]\hat{\mathbf{e}} \qquad (D.1)$$

where $\hat{\mathbf{e}}$ is the polarisation unit vector. We wish to solve the wave equation for a dynamic medium [D.1]

$$\nabla^2\mathbf{E} - \frac{1}{\mathrm{c}^2}\frac{\partial^2(\mathrm{n}^2\mathbf{E})}{\partial t^2} - \mu\mu_{\mathrm{o}}\sigma_{\mathrm{e}}\frac{\partial \mathbf{E}}{\partial t} = 0. \qquad (D.2)$$

Consider the amplitude and phase terms to be time independent, R(x), S(x), $\phi_{\mathrm{R}}(\mathrm{x})$ and $\phi_{\mathrm{S}}(\mathrm{x})$ and the RI profile within the dynamic medium approximated by

$$\mathrm{n} = \mathrm{n_o} + \mathrm{n_{dc}(x)} + \mathrm{n_c(x)}\cos\mathbf{k}.\mathbf{r} + \mathrm{n_s(x)}\sin\mathbf{k}.\mathbf{r}, \qquad (D.3)$$

also considered to be time independent. Only the fundamental Fourier components have been considered and are re-arranged to give

$$\mathrm{n} = \mathrm{n_o}(1+\delta) + \Delta\mathrm{n(x)}\cos(\mathbf{k}.\mathbf{r} + \phi(\mathrm{x})) \qquad (D.4)$$

where $\delta = \mathrm{n_{dc}}/\mathrm{n_o}$, $\Delta\mathrm{n} = \sqrt{\mathrm{n_c^2} + \mathrm{n_s^2}}$ and $\tan\phi = -\mathrm{n_s}/\mathrm{n_c}$. An approximate expression for n^2 can be derived as follows;

$$\mathrm{n}^2 = \mathrm{n_o^2}(1+\delta)^2 + 2\mathrm{n_o}(1+\delta)\Delta\mathrm{n(x)}\cos(\mathbf{k}.\mathbf{r} + \phi(\mathrm{x})) + \Delta\mathrm{n}^2\cos(\mathbf{k}.\mathbf{r} + \phi(\mathrm{x})), \qquad (D.5)$$

$$\approx \mathrm{n_o^2}(1+2\delta) + 2\mathrm{n_o}\Delta\mathrm{n}\cos(\mathbf{k}.\mathbf{r} + \phi(\mathrm{x})) \qquad (D.6)$$

as $1 \gg \delta$ and $\mathrm{n} \gg \Delta\mathrm{n}$.

The first and second derivatives of **E** with respect to time are given by

$$\frac{\partial \mathbf{E}}{\partial t} = i\omega\mathbf{E} \qquad (D.7a)$$

$$\frac{\partial^2(\mathrm{n}^2\mathbf{E})}{\partial t^2} = \mathrm{n}^2\frac{\partial^2\mathbf{E}}{\partial t^2} = -\omega^2\mathrm{n}^2\mathbf{E}. \qquad (D.7b)$$

Continuing

$$\nabla^2\mathbf{E} = \frac{\partial^2\mathbf{E}}{\partial x^2} + \frac{\partial^2\mathbf{E}}{\partial y^2} + \frac{\partial^2\mathbf{E}}{\partial z^2} \tag{D.8}$$

$$\begin{aligned} &= \frac{\partial}{\partial x}\left\{\left[\frac{\partial R}{\partial x} + iR\left(-\rho_x + \frac{\partial\phi_R}{\partial x}\right)\right]\exp\left[i(\omega t - \varrho.\mathbf{r} + \phi_R)\right]\right\} \\ &\quad - (\rho_y^2 + \rho_z^2)R\exp\left[i(\omega t - \varrho.\mathbf{r} + \phi_R)\right] \\ &\quad + F(s), \end{aligned} \tag{D.9}$$

$$\begin{aligned} &= \left\{\frac{\partial^2 R}{\partial x^2} + i\frac{\partial R}{\partial x}\left(-\rho_x + \frac{\partial\phi_R}{\partial x}\right)\right. \\ &\quad - i\rho_x\left[\frac{\partial R}{\partial x} + iR\left(-\rho_x + \frac{\partial\phi_R}{\partial x}\right)\right] \\ &\quad \left. + i\left[\left(\frac{\partial R}{\partial x}\frac{\partial\phi_R}{\partial x} + R\frac{\partial^2\phi_R}{\partial x^2}\right) + iR\frac{\partial\phi_R}{\partial x}\left(-\rho_x + \frac{\partial\phi_R}{\partial x}\right)\right]\right\} \\ &\quad .\exp\left[i(\omega t - \varrho.\mathbf{r} + \phi_R)\right] \\ &\quad - (\rho_y^2 + \rho_z^2)R\exp\left[i(\omega t - \varrho.\mathbf{r} + \phi_R)\right] \\ &\quad + F(s), \end{aligned} \tag{D.10}$$

$$\begin{aligned} &= \left\{\frac{\partial^2 R}{\partial x^2} - i2\rho_x\frac{\partial R}{\partial x} - \rho_x^2 R - \rho_y^2 R - \rho_z^2 R\right. \\ &\quad \left. + i2\frac{\partial R}{\partial x}\frac{\partial\phi_R}{\partial x} + 2\rho_x R\frac{\partial\phi_R}{\partial x} + iR\frac{\partial^2\phi_R}{\partial x^2} + iR\left(\frac{\partial\phi_R}{\partial x}\right)^2\right\} \\ &\quad .\exp\left[i(\omega t - \varrho.\mathbf{r} + \phi_R)\right] \\ &\quad + F(s). \end{aligned} \tag{D.11}$$

In the limit of the slowly varying amplitude approximation and phase we can approximates as follows

$$\frac{\partial^2 R}{\partial x^2} \sim 0, \quad \frac{\partial^2\phi_R}{\partial x^2} \sim 0, \quad \left(\frac{\partial\phi_R}{\partial x}\right)^2 \sim 0 \quad \text{and} \quad \frac{\partial R}{\partial x}\frac{\partial\phi_R}{\partial x} \sim 0,$$

and thus able to simplify as follows

$$\begin{aligned} \nabla^2\mathbf{E} = &\left\{-i2\rho_x\frac{\partial R}{\partial x} - |\rho|^2 R + 2\rho_x R\frac{\partial\phi_R}{\partial x}\right\}\exp\left[i(\omega t - \varrho.\mathbf{r} + \phi_R)\right] \\ &+ \left\{-i2\sigma_z\frac{\partial S}{\partial x} - |\sigma|^2 S + 2\sigma_x S\frac{\partial\phi_S}{\partial x}\right\}\exp\left[i(\omega t - \varrho.\mathbf{r} + \phi_S)\right]. \end{aligned} \tag{D.12}$$

The wave equation becomes

$$\begin{aligned}
&\left\{-i2\rho_x\frac{\partial R}{\partial x}-|\rho|^2R+2\rho_xR\frac{\partial\phi_R}{\partial x}\right\}\exp\left[i(\omega t-\varrho.\mathbf{r}+\phi_R)\right]\\
&+\left\{-i2\sigma_x\frac{\partial S}{\partial x}-|\sigma|^2S+2\sigma_xR\frac{\partial\phi_S}{\partial x}\right\}\exp\left[i(\omega t-\varsigma.\mathbf{r}+\phi_S)\right]\\
&+\left\{\frac{\omega^2}{c^2}n_o^2(1+2\delta)-i\mu\mu_o\sigma_e\omega\right\}\\
&\quad.\left(R\exp\left[i(\omega t-\varrho.\mathbf{r}+\phi_R)\right]+S\exp\left[i(\omega t-\varsigma.\mathbf{r}+\phi_S)\right]\right)\\
&+\frac{\omega^2}{c^2}n_o^2(1+\delta)\Delta n\\
&\quad.\left(\exp\left[i((\varrho-\varsigma).\mathbf{r}+\phi)\right]+\exp\left[-i((\varrho-\varsigma).\mathbf{r}+\phi)\right]\right)\\
&\quad.\left(R\exp\left[i(\omega t-\varrho.\mathbf{r}+\phi_R)\right]+S\exp\left[i(\omega t-\varsigma.\mathbf{r}+\phi_S)\right]\right)\\
&=0,
\end{aligned}\tag{D.13}$$

$$\begin{aligned}
&\left\{-i2\rho_x\frac{\partial R}{\partial x}-|\rho|^2R+2\rho_xR\frac{\partial\phi_R}{\partial x}\right\}\exp\left[i(-\varrho.\mathbf{r}+\phi_R)\right]\\
&+\left\{-i2\sigma_x\frac{\partial S}{\partial x}-|\sigma|^2S+2\sigma_xR\frac{\partial\phi_S}{\partial x}\right\}\exp\left[i(-\varsigma.\mathbf{r}+\phi_S)\right]\\
&+(\beta_o^2+\beta_o^2 2\delta-i\alpha\beta_o)\\
&\quad.\left(R\exp\left[i(-\varrho.\mathbf{r}+\phi_R)\right]+S\exp\left[i(-\varsigma.\mathbf{r}+\phi_S)\right]\right)\\
&+\beta_o\frac{2\pi}{\lambda}(1+\delta)\Delta n\\
&\quad.\left(R\exp\left[i(-\varsigma.\mathbf{r}+\phi+\phi_R)\right]S\exp\left[i(-\varrho.\mathbf{r}-\phi+\phi_S)\right]\right)\\
&=0,
\end{aligned}\tag{D.14}$$

where terms $\exp\left[-i((2\varrho-\varsigma).\mathbf{r})\right]$ and $\exp\left[i((\varrho-2\varsigma).\mathbf{r})\right]$, which violate the Bragg condition, have been neglected.

Equating coefficients of $\exp\left[i(-\varrho.\mathbf{r})\right]$ and $\exp\left[i(-\varsigma.\mathbf{r})\right]$ yields

$$\begin{aligned}
&\left\{-i2\rho_x\frac{\partial R}{\partial x}-|\rho|^2R+2\rho_xR\frac{\partial\phi_R}{\partial x}\right\}\exp(i\phi_R)\\
&+(\beta_o^2+\beta_o^2 2\delta-i\alpha\beta_o)\,R\exp(i\phi_R)\\
&+\beta_o\frac{2\pi}{\lambda}(1+\delta)\Delta nS\exp[i(\phi_S-\phi)]\\
&=0
\end{aligned}\tag{D.15}$$

and

$$\left\{-i2\sigma_x\frac{\partial S}{\partial x} - |\sigma|^2 R + 2\sigma_x S\frac{\partial\phi_S}{\partial x}\right\}\exp[i\phi_S]$$
$$+ \left(\beta_o^2 + \beta_o^2 2\delta - i\alpha\beta_o\right) S\exp[i\phi_S]$$
$$+ \beta_o\frac{2\pi}{\lambda}(1+\delta)\Delta n R\exp[i(\phi_R+\phi)]$$
$$= 0. \qquad (D.16)$$

Rearranging Eq. (D.15) gives

$$-i2\rho_x\frac{\partial R}{\partial x} + 2\rho_x R\frac{\partial\phi_R}{\partial x}$$
$$+ \left(\beta_o^2 2\delta - i\alpha\beta_o\right) R$$
$$+ \beta_o\frac{2\pi}{\lambda}(1+\delta)\Delta n S\exp[i(\phi_S-\phi-\phi_R)]$$
$$= 0, \qquad (D.17)$$

$$-i\cos\theta\frac{\partial R}{\partial x} + \cos\theta R\frac{\partial\phi_R}{\partial x} + \left(\beta_o\delta - i\frac{\alpha}{2}\right) R$$
$$+ \frac{\pi}{\lambda}\Delta n S\exp[-i(\phi_R-\phi_S+\phi)]$$
$$= 0, \qquad (D.18)$$

$$\cos\theta\frac{\partial R}{\partial x} + iR\cos\theta R\frac{\partial\phi_R}{\partial x} + \left(\frac{\alpha}{2} + i\beta_o\delta\right) R$$
$$+ \frac{\pi}{\lambda}\Delta n S\exp[-i(\phi_R-\phi_S+\phi)]$$
$$= 0, \qquad (D.19)$$

$$\frac{\partial R}{\partial x} + iR\frac{\partial\phi_R}{\partial x} + \left(\frac{\alpha}{2\cos\theta} + i\frac{\beta_o\delta}{\cos\theta}\right) R$$
$$+ i\frac{\pi}{\lambda\cos\theta}\Delta n S\exp[-i(\phi_R-\phi_S+\phi)]$$
$$= 0, \qquad (D.20)$$

and similarly for S

$$\frac{\partial S}{\partial x} + iS\frac{\partial\phi_S}{\partial x} + \left(\frac{\alpha}{2\cos\theta} + i\frac{\beta_o\delta}{\cos\theta}\right) S$$
$$+ i\frac{\pi}{\lambda\cos\theta}\Delta n R\exp[+i(\phi_R-\phi_S+\phi)]$$
$$= 0. \qquad (D.21)$$

In the present context the amplitudes R and S are not complex as the intrinsic phase terms ϕ_R and ϕ_S have been expessed explicitly. Thus we have coupled wave equations containing both real and imaginary terms.

Equating these real and imaginary terms yields

Real;

$$\frac{\partial R}{\partial x} + \frac{\alpha}{2\cos\theta}R + \frac{\pi}{\lambda\cos\theta}\Delta n S \sin\Phi = 0, \qquad (D.22)$$

$$\frac{\partial S}{\partial x} + \frac{\alpha}{2\cos\theta}S + \frac{\pi}{\lambda\cos\theta}\Delta n R \sin\Phi = 0. \qquad (D.23)$$

Imaginary;

$$R\frac{\partial\phi_R}{\partial x} + \frac{\beta_o\delta}{\cos\theta}R + \frac{\pi}{\lambda\cos\theta}\Delta n S \cos\Phi = 0, \qquad (D.24)$$

$$S\frac{\partial\phi_S}{\partial x} + \frac{\beta_o\delta}{\cos\theta}S + \frac{\pi}{\lambda\cos\theta}\Delta n R \cos\Phi = 0. \qquad (D.25)$$

where $\Phi = \phi_R - \phi_S + \phi$.

To re-express in terms of intensities recall the following

$$I_R = R^2 \Rightarrow \frac{dI_R}{dx} = 2R\frac{dR}{dx}$$

and hence

$$2R\frac{dR}{dx} + \frac{\alpha}{\cos\theta}R^2 = -\frac{2\pi}{\lambda\cos\theta}\Delta n RS \sin\Phi,$$

$$2S\frac{dS}{dx} + \frac{\alpha}{\cos\theta}S^2 = \frac{2\pi}{\lambda\cos\theta}\Delta n RS \sin\Phi.$$

Using

$$I = I_o[1 + M\cos(\mathbf{k}.\mathbf{r} - \phi]$$

the RS product becomes

$$RS = \frac{1}{2}MI_o$$

For the real terms;

$$\frac{dI_R}{dx} + \frac{\alpha}{\cos\theta}I_R = -\frac{2\pi}{\lambda\cos\theta}\left(-\frac{1}{2}n_o^3 r_{eff}E'_{sc}\right)2\frac{I_R I_S}{MI_o}\sin\Phi,$$
$$= -\frac{\Gamma}{\cos\theta}\frac{I_R I_S}{I_o}, \qquad (D.26)$$

where Γ is given by

$$\Gamma = 2\delta\frac{E'_{sc}}{M}\sin\Phi \qquad \text{and} \qquad \delta = -\frac{\pi}{\lambda}n_o^3 r_{eff}.$$

Similarly for S

$$\frac{dI_S}{dx} + \frac{\alpha}{\cos\theta}I_S = \frac{\Gamma}{\cos\theta}\frac{I_R I_S}{I_o}. \qquad (D.27)$$

For the imaginary terms;

$$R\frac{\partial\phi_R}{\partial x}+\frac{\beta_o\delta}{\cos\theta}R+\frac{\pi}{\lambda\cos\theta}\Delta nS\cos\Phi=0, \qquad (D.24)$$

$$S\frac{\partial\phi_S}{\partial x}+\frac{\beta_o\delta}{\cos\theta}S+\frac{\pi}{\lambda\cos\theta}\Delta nR\cos\Phi=0, \qquad (D.25)$$

and

$$\Phi=\phi_R-\phi_S+\phi \quad\Rightarrow\quad \frac{\partial\Phi}{\partial x}=\frac{\partial\phi_R}{\partial x}-\frac{\partial\phi_S}{\partial x}. \qquad (D.28)$$

Expression D.28 is simplifyed by letting $\delta\sim 0$

$$\frac{\partial\phi_R}{\partial x}+\frac{\pi\Delta n}{\lambda\cos\theta}\frac{S}{R}=0, \qquad (D.29)$$

$$\frac{\partial\phi_S}{\partial x}+\frac{\pi\Delta n}{\lambda\cos\theta}\frac{R}{S}=0, \qquad (D.30)$$

$$\frac{\partial\phi_R}{\partial x}-\frac{\partial\phi_S}{\partial x}=\frac{\phi\Delta n}{\lambda\cos\theta}\left(\frac{R}{S}-\frac{S}{R}\right)\cos\Phi, \qquad (D.31)$$

$$\frac{d\Phi}{dx}=\frac{\pi}{\lambda\cos\theta}\left(-\frac{1}{2}n_o^3r_{eff}E'_{sc}\right)\frac{R^2-S^2}{SR}\cos\Phi \qquad (D.32)$$

$$=\frac{\pi}{\lambda\cos\theta}\left(-n_o^3r_{eff}E'_{sc}\right)\frac{I_R-I_S}{MI_o}\cos\Phi, \qquad (D.33)$$

$$=\frac{\gamma}{\cos\theta}\frac{I_R-I_S}{I_o}, \qquad (D.34)$$

where

$$\gamma=\delta\frac{E'_{sc}}{M}\cos\Phi$$

Summary:

$$\frac{dI_R}{dx}+\frac{\alpha}{\cos\theta}I_R=-\frac{\Gamma}{\cos\theta}\frac{I_RI_S}{I_o} \qquad (D.26)$$

$$\frac{dI_S}{dx}+\frac{\alpha}{\cos\theta}I_S=\frac{\Gamma}{\cos\theta}\frac{I_RI_S}{I_o} \qquad (D.27)$$

$$\frac{d\Phi}{dx}=\frac{\gamma}{\cos\theta}\frac{I_R-I_S}{I_o} \qquad (D.34)$$

These coupled first order differential equations, Eqs. (D.26), (D.27) and (D.34), can be solved as follows,

$$\frac{dI_R}{dx}=-\frac{dI_S}{dx}, \quad \text{in the absence of absorption}$$

$$\Rightarrow \quad I_R=I_S+\textit{constant}$$

$$I_R+I_S=I_o \quad \text{Conservation of energy}$$

For I_R;

$$\frac{dI_R}{dx} = -\frac{\Gamma}{I_o} I_R I_S,$$
$$= -\frac{\Gamma}{I_o} I_R (I_o - I_R),$$
$$= \frac{\Gamma}{I_o} I_R (I_R - I_o),$$
$$\frac{I_o}{I_R(I_R - I_o)} dI_R = \Gamma dx,$$
$$\int \left[\frac{1}{(I_R - I_o)} - \frac{1}{I_R} \right] dI_R = \int \Gamma dx,$$
$$\ln(I_R - I_o) - \ln I_R + \ln C = \Gamma x,$$
$$\ln \frac{(I_R - I_o)C}{I_R} = \Gamma x.$$

Apply the boundary condition $I_{So}/I_{Ro} = \beta_o$

$$\ln(-\beta_o C) = 0 \quad \Rightarrow \quad C = -\frac{1}{\beta_o},$$
$$\ln \left[-\frac{(I_R - I_o)}{I_R} \frac{1}{\beta_o} \right] = \Gamma x$$
$$\frac{(I_o - I_R)}{I_R} = \beta_o \exp(\Gamma x),$$
$$I_o = I_R [1 + \beta_o \exp(\Gamma x)]$$

and

$$I_R = \frac{I_o}{[1 + \beta_o \exp(\Gamma x)]}. \qquad (D.35)$$

Similarly for I_S;

$$I_S = \frac{I_o \beta_o \exp(\Gamma x)}{[1 + \beta_o \exp(\Gamma x)]}. \qquad (D.36)$$

For the phase term we have;

$$\frac{d\Phi}{dx} = \gamma \frac{I_R - I_S}{I_o}, \qquad (D.34)$$

using the Eqs. (D.35) and (D.36)

$$\frac{d\Phi}{dx} = \gamma \frac{1 - \beta_o \exp(\Gamma x)}{1 + \beta_o \exp(\Gamma x)},$$
$$d\Phi = \gamma \frac{1 - \beta_o \exp(\Gamma x)}{1 + \beta_o \exp(\Gamma x)} dx,$$
$$\int d\Phi = \gamma \int 1 - \frac{2\beta_o \exp(\Gamma x)}{1 + \beta_o \exp(\Gamma x)} dx,$$

$$\Phi + constant = \gamma x - 2\beta_o\gamma \int \frac{\exp(\Gamma x)}{1+\beta_o \exp(\Gamma x)} dx$$

$$\text{let} \qquad u = 1 + \beta_o \exp(\Gamma x),$$

$$du = \beta_o \Gamma \exp(\Gamma x) dx,$$

$$\Phi + constant = \gamma x - 2\frac{\gamma}{\Gamma} \int \frac{du}{u},$$

$$= \gamma x - 2\frac{\gamma}{\Gamma} \ln u,$$

$$= \gamma x - 2\frac{\gamma}{\Gamma} \ln[1 + \beta_o \exp(\Gamma x)].$$

Apply the boundary condition $\Phi_o = \Phi_{x=0}$

$$\Phi_o + constant = -2\frac{\gamma}{\Gamma} \ln(1+\beta_o),$$

$$-constant = \Phi_o + 2\frac{\gamma}{\Gamma} \ln(1+\beta_o),$$

$$\Rightarrow \qquad \Phi(x) = \Phi_o + 2\frac{\gamma}{\Gamma} \ln(1+\beta_o) + \gamma x - 2\frac{\gamma}{\Gamma} \ln(1+\beta_o \exp(\Gamma x),$$

$$= \Phi_o + \gamma x + 2\frac{\gamma}{\Gamma} \ln \frac{1+\beta_o}{1+\beta_o \exp(\Gamma x)},$$

$$= \Phi_o + \frac{\gamma}{\Gamma} \ln[\exp(\Gamma x)] + \frac{\gamma}{\Gamma} \ln \frac{[1+\beta_o]^2}{[1+\beta_o \exp(\Gamma x)]^2},$$

$$= \Phi_o + \frac{\gamma}{\Gamma} \ln \frac{[1+\beta_o]^2 \exp(\Gamma x)}{[1+\beta_o \exp(\Gamma x)]^2}. \qquad (D.37)$$

Summary:

$$I_R = \frac{I_o}{[1+\beta_o \exp(\Gamma x)]}, \qquad (D.35)$$

$$I_S = \frac{I_o \beta_o \exp(\Gamma x)}{[1+\beta_o \exp(\Gamma x)]}, \qquad (D.36)$$

$$\Phi(x) = \Phi_o + \frac{\gamma}{\Gamma} \ln \frac{[1+\beta_o]^2 \exp(\Gamma x)}{[1+\beta_o \exp(\Gamma x)]^2}. \qquad (D.37)$$

References.

[D.1] P. Günter, "Holography, coherent light amplification and optical phase conjugation with photorefractive materials," Physics Reports **93**, 199–299 (1982).

APPENDIX E

TABULATED TWO WAVE MIXING DATA FOR BARIUM TITANATE AND CERIUM DOPED STRONTIUM BARIUM NIOBATE.

$BaTiO_3^{\#2}$, Δ	
Normalised grating wavenumber $k/(n\omega/c)$	Beam coupling $\Delta I/I$
0.039	0.124
0.070	0.206
0.139	0.411
0.195	0.449
0.238	0.503
0.281	0.577
0.336	0.605
0.371	0.619
0.405	0.602
0.447	0.641
0.478	0.628
0.503	0.616

$BaTiO_3^{\#3}$, $\times$	
Normalised grating wavenumber $k/(n\omega/c)$	Beam coupling $\Delta I/I$
0.053	0.010
0.091	0.006
0.136	0.036
0.191	0.083
0.238	0.111
0.282	0.094
0.333	0.108
0.374	0.127
0.405	0.125
0.444	0.137
0.475	0.132
0.527	0.099

Table E.I Two beam coupling of $BaTiO_3^{\#2}$ and $^{\#3}$ versus the normalised grating wavenumber.

SBN : $60^{\#1}$, ■	
Normalised grating wavenumber $k/(n\omega/c)$	Beam coupling $\Delta I/I$
0.040	0.317
0.054	0.418
0.066	0.498
0.099	0.597
0.117	0.612
0.149	0.593
0.160	0.584
0.181	0.535
0.200	0.495
0.238	0.456
0.277	0.402
0.324	0.347
0.419	0.245

Table E.II Two beam coupling of cerium doped SBN:$60^{\#1}$ versus the normalised grating wavenumber.

$BaTiO_3^{\#1}$		
$\log[\beta_o]$, Δ	$\log[\beta_{exit}]$, ■	Diffraction efficiency
-1.770	-1.420	0.008
-1.921	-1.721	0.001
-1.796	-1.569	0.004
-1.523	-1.149	0.020
-1.260	-0.818	0.038
-1.032	-0.526	0.059
-0.854	-0.361	0.074
-0.688	-0.180	0.091
-0.542	-0.027	0.102
-0.387	0.100	0.108
-0.262	0.228	0.115
-0.156	0.360	0.113
-0.021	0.463	0.111
0.100	0.567	0.104
0.224	0.691	0.095
0.359	0.794	0.084
0.493	0.919	0.072
0.632	1.057	0.059
0.789	1.187	0.048
0.974	1.373	0.033
1.204	1.569	0.022
1.480	1.777	0.012
1.909	2.132	0.005
1.455	2.408	0.001

Table E.III Diffraction efficiency, η versus the incident, β_o, and exit, β_{exit}, writing beam ratios for $BaTiO_3^{\#1}$.

SBN : $60^{\#1}$		
$\log[\beta_o]$, Δ	$\log[\beta_{exit}]$, ■	Diffraction efficiency
-1.770	-1.638	0.004
-1.921	-1.854	0.000
-1.796	-1.658	0.000
-1.523	-1.276	0.014
-1.260	-0.971	0.028
-1.032	-0.752	0.044
-0.854	-0.553	0.059
-0.688	-0.384	0.072
-0.542	-0.264	0.082
-0.387	-0.099	0.088
-0.262	0.012	0.090
-0.156	0.122	0.090
-0.021	0.270	0.084
0.100	0.354	0.079
0.224	0.483	0.070
0.359	0.595	0.061
0.493	0.713	0.050
0.632	0.889	0.039
0.789	1.069	0.029
0.974	1.225	0.021
1.204	1.456	0.013
1.480	1.718	0.007
1.909	2.027	0.003
1.455	2.414	0.001

Table E.IV Diffraction efficiency, η, versus the incident, β_o, and exit, β_{exit}, writing beam ratios for SBN : $60^{\#1}$.

$BaTiO_3^{\#1}$, ■	
$\log(I_o)$ $\log(Wcm^{-2})$	τ_{rise} seconds
-0.824	2.697
-0.521	2.298
-0.220	1.782
0.081	1.358
0.381	0.920
0.683	0.665

Table E.V Characteristic grating rise time, τ_{rise}, versus the total incident writing intensity, I_o, for $BaTiO_3^{\#1}$.

$BaTiO_3^{\#1}$, ■	
$\log(I_{probe})$ $\log(Wcm^{-2})$	τ_{decay} seconds
-3.308	5.479
-2.242	5.304
-1.222	4.380
0.050	2.087

Table E.VI Characteristic grating decay time, τ_{decay}, versus the probe beam intensity, I_{probe}, for $BaTiO_3^{\#1}$.

SBN:$60^{\#1}$, ■	
$\log(I_{probe})$ $\log(Wcm^{-2})$	τ_{decay} seconds
-3.426	834
-2.369	365
-1.351	96
-0.727	12.2
-0.497	8.6
-0.267	5.1
-0.075	4.1

Table E.VII Characteristic grating decay time, τ_{decay}, versus the probe beam intensity, I_{probe}, for SBN:$60^{\#1}$.

APPENDIX F

PHASE CONJUGATION BY DEGENERATE FOUR WAVE MIXING.

Phase conjugation by degenerate four wave mixing can be analysed quantitatively using the characteristic third-order nonlinear susceptibility, χ_{ijkl}, of the nonlinear medium [F.1]. The *mixing* of the waves consists of a counterpropagating pair of intense pump beams, $\mathbf{E}_1$ and $\mathbf{E}_2$, and a counterpropagating pair of weak signal beams, $\mathbf{E}_3$ and $\mathbf{E}_4$. All the waves are of the same temporal angular frequency, ω, and the DFWM geometry is schematically illustrated in Fig. F.1.

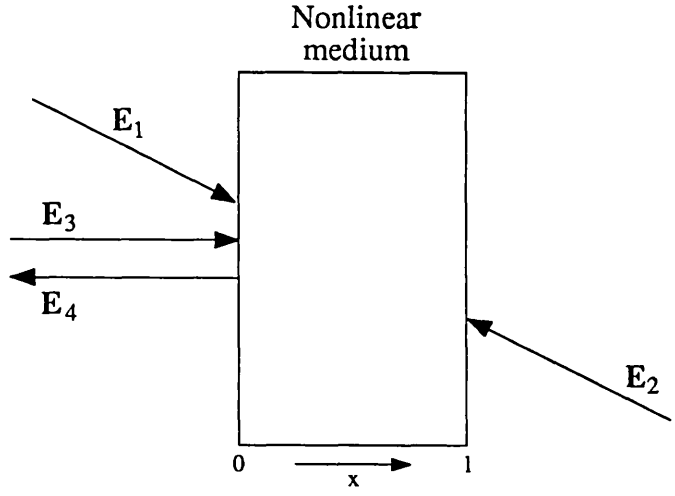


Figure F.1 Degenerate four wave mixing geometry.

The fields are taken to be plane wave as follows

$$\mathbf{E}_j = A_j(r)\exp[i(\omega t - \mathbf{k}_j.\mathbf{r})]\hat{e} \qquad (F.1)$$

where j=1,2 and

$$\mathbf{E}_3 = A_3(x)\exp[i(\omega t - kx)]\hat{e} \qquad (F.2)$$

where $\hat{e}$ is the unit polarisation vector of the electric field. The four waves are coupled via the induced nonlinear polarisation in accordance with Eq. (4.2). Considering only the third-order nonlinear susceptibility and an induced polarisation at frequency ω, the nonlinear polarisation, $\mathbf{P}_{NL}$, is given by

$$\begin{aligned}\mathbf{P}_{NL} &= \frac{1}{2}\chi^{(3)}A_1A_2A_3^*\exp[i((\omega+\omega-\omega)t - (\mathbf{k}_1+\mathbf{k}_2).\mathbf{r} + kx)]\hat{e} \\ &= \frac{1}{2}\chi^{(3)}A_1A_2A_3^*\exp[i(\omega t + kx)]\hat{e}, \qquad (F.3)\end{aligned}$$

since $\mathbf{k}_1 = -\mathbf{k}_2$ as the pumping beams are counterpropagating. The $\chi^{(3)}$ term is the effective third-order nonlinear susceptibility for the given geometric configuration. Equation (F.3) corresponds to a polarisation wave with frequency ω and wavevector -k, which will excite a fourth field $\mathbf{E}_4$ of the form

$$\mathbf{E}_4 = \mathrm{A}_4(\mathrm{x}) \exp[i(\omega \mathrm{t} + \mathrm{kx})]\hat{\mathbf{e}}. \qquad (F.4)$$

The solution of $\mathrm{A}_4(\mathrm{x})$ is found by solving the wave equation for the third-order nonlinearity in the induced polarisation.

The electric displacement, $\mathbf{D}$, and the induced electric polarisation, $\mathbf{P}$, are related by the simple expression

$$\mathbf{D} = \varepsilon_\mathrm{o}\mathbf{E} + \mathbf{P} \qquad (F.5a)$$

which in the presence of polarisation nonlinearities becomes

$$\begin{aligned} &= \varepsilon_\mathrm{o}\mathbf{E} + \mathbf{P}_\mathrm{L} + \mathbf{P}_\mathrm{NL}, \\ &= \varepsilon\varepsilon_\mathrm{o}\mathbf{E} + \mathbf{P}_\mathrm{NL}. \end{aligned} \qquad (F.5b)$$

Consequently Maxwell's wave equation for a lossless medium becomes

$$\nabla^2\mathbf{E} - \mu_\mathrm{o}\varepsilon\varepsilon_\mathrm{o}\frac{\partial^2\mathbf{E}}{\partial \mathrm{t}^2} - \mu_\mathrm{o}\frac{\partial^2\mathbf{P}_\mathrm{NL}}{\partial \mathrm{t}^2} = 0. \qquad (F.6)$$

Solving Maxwell's equation for $\mathbf{E}_4$ in the non-pump depletion regime, A_1 and A_2 both constant, we obtain

$$\begin{aligned} \nabla^2\mathbf{E} &= \frac{\partial^2\mathbf{E}_4(\mathrm{x},\mathrm{t})}{\partial \mathrm{x}^2}, \\ &= \frac{1}{2}\frac{\partial}{\partial \mathrm{x}}\left[\frac{\mathrm{dA}_4}{\mathrm{dx}}\exp[i(\omega \mathrm{t} + \mathrm{kx})] + i\mathrm{kA}_4\exp[i(\omega \mathrm{t} + \mathrm{kx})] + \mathrm{c.c.}\right], \\ &= \frac{1}{2}\left[\frac{\mathrm{d}^2\mathrm{A}_4}{\mathrm{dx}^2}\exp[i(\omega \mathrm{t} + \mathrm{kx})] + 2i\mathrm{k}\frac{\mathrm{dA}_4}{\mathrm{dx}}\exp[i(\omega \mathrm{t} + \mathrm{kx})]\right. \\ &\qquad \left. - \mathrm{k}^2\mathrm{A}_4\exp[i(\omega \mathrm{t} + \mathrm{kx})] + \mathrm{c.c.}\right]. \end{aligned} \qquad (F.7)$$

In the limit of the slowly varying envelope approximation the amplitude of $\mathbf{E}_4$, A_4, is considered to change only very slowly w. r. t. x. The following approximations can be made

$$\frac{\mathrm{d}^2\mathrm{A}_4}{\mathrm{dx}^2} \ll \mathrm{k}\frac{\mathrm{dA}_4}{\mathrm{dx}} \ll \mathrm{k}^2\mathrm{A}_4. \qquad (F.8)$$

Consequently neglecting the second order derivative of A_4 in x, Eq. (F.7) becomes

$$\nabla^2\mathbf{E} = \frac{1}{2}\left[2i\mathrm{k}\frac{\mathrm{dA}_4}{\mathrm{dx}}\exp[i(\omega \mathrm{t} + \mathrm{kx})] - \mathrm{k}^2\mathrm{A}_4\exp[i(\omega \mathrm{t} + \mathrm{kx})] + \mathrm{c.c.}\right]. \qquad (F.9)$$

The time derivatives of $\mathbf{E}$ and $\mathbf{P}_{\mathrm{NL}}$ are simply

$$\frac{\partial^2 \mathbf{E}}{\partial t^2} = \frac{1}{2}\left[-\omega^2 A_4 \exp[i(\omega t + kx)] + \text{c.c.}\right] \qquad (F.10)$$

and using Eq. (F.3)

$$\frac{\partial^2 \mathbf{P}_{\mathrm{NL}}}{\partial x^2} = \frac{1}{2}\left[-\omega^2 \chi^{(3)} A_1 A_2 A_3^* \exp[i(\omega t + kx)] + \text{c.c.}\right]. \qquad (F.11)$$

Combining Eqs. (F.9), (F.10) and (F.11) the nonlinear wave equation, Eq. (F.6), becomes

$$\frac{1}{2}\left[2ik\frac{dA_4}{dx} - k^2 A_4 + \mu_o \varepsilon \varepsilon_o \omega^2 A_4\right] \exp[i(\omega t + kx)]$$
$$= -\frac{1}{2}\omega^2 \mu_o \chi^{(3)} A_1 A_2 A_3^* \exp[i(\omega t + kx)], \qquad (F.12)$$

where the complex conjugate, c.c., terms have been neglected. Using $k^2 = \mu_o \varepsilon \varepsilon_o \omega^2$ and $\omega/k = 1/\sqrt{\mu_o \varepsilon}$ the expression, Eq. (F.12), is reduced to

$$\frac{dA_4}{dx} = i\frac{\omega}{2}\sqrt{\frac{\mu_o}{\varepsilon}}\chi^{(3)} A_1 A_2 A_3^* \qquad (F.13a)$$

and similarly

$$\frac{dA_3^*}{dx} = i\frac{\omega}{2}\sqrt{\frac{\mu_o}{\varepsilon}}\chi^{(3)} A_1^* A_2^* A_4. \qquad (F.13b)$$

The above system of coupled first order differential equations, Eqs. (F.13a) and (F.13b), can be rewritten as follows

$$\frac{dA_4}{dx} = i\kappa^* A_3^*, \qquad (F.14a)$$

$$\frac{dA_3^*}{dx} = i\kappa A_4, \qquad (F.14b)$$

where κ is defined as

$$\kappa = \frac{\omega}{2}\sqrt{\frac{\mu_o}{\varepsilon}}\chi^{(3)} A_1 A_2. \qquad (F.15)$$

Equations (F.14a) and (F.14b) are soluble using the following general boundary conditions, $A_4(l) = 0$ and $A_3^*(0) = \textit{constant}$. They are decoupled using their second derivatives as follows

$$\frac{d^2 A_4}{dx^2} = i\kappa^* \frac{dA_3^*}{dx} = -\kappa\kappa^* A_4, \qquad (F.16a)$$

$$\frac{d^2 A_3^*}{dx^2} = i\kappa \frac{dA_4}{dx} = -\kappa^*\kappa A_3^*. \qquad (F.16b)$$

General solutions can be expressed as follows

$$A_4(x) = a\cos|\kappa|x + ib\sin|\kappa|x \qquad (F.17a)$$

$$A_3^*(x) = c\cos|\kappa|x + id\sin|\kappa|x, \qquad (F.17b)$$

and applying the boundary conditions

$$0 = a\cos|\kappa|l + ib\sin|\kappa|l, \tag{F.18a}$$

$$A_3^*(0) = c. \tag{F.18b}$$

Back substituting the general solutions, Eqs. (F.17a) and (F.17b), into the original coupled differential equations, Eqs. (F.14a) and (F.14b), gives

$$-a|\kappa|\sin|\kappa|x + ib|\kappa|\cos|\kappa|x = i\kappa^*(c\cos|\kappa|x + id\sin|\kappa|x), \tag{F.19a}$$

$$-c|\kappa|\sin|\kappa|x + id|\kappa|\cos|\kappa|x = i\kappa(a\cos|\kappa|x + ib\sin|\kappa|x) \tag{F.19b}$$

and equating the real and imaginary terms yields

$$a|\kappa| = d\kappa^*, \tag{F.20a}$$

$$b|\kappa| = c\kappa^*. \tag{F.20b}$$

Employing the boundary condition equations, Eqs. (F.18a) and (F.18b), the unknown coefficient a, b, c and d can be expressed as follows

$$c = A_3^*(0), \tag{F.21a}$$

$$b = \frac{\kappa^*}{|\kappa|}c = \frac{\kappa^*}{|\kappa|}A_3^*(0) \tag{F.21b}$$

$$\begin{aligned} 0 &= a\cos|\kappa|l + ib\sin|\kappa|l, \\ &= a\cos|\kappa|l + i\frac{\kappa^*}{|\kappa|}A_3^*(0)\sin|\kappa|l, \\ a &= -i\frac{\kappa^*}{|\kappa|}A_3^*(0)\tan|\kappa|l, \end{aligned} \tag{F.21c}$$

and

$$\begin{aligned} d &= \frac{|\kappa|}{\kappa^*}a, \\ &= -iA_3^*(0)\tan|\kappa|l. \end{aligned} \tag{F.21d}$$

Substituting the coefficients back into the analytic expressions for $A_4(x)$ and $A_3^*(x)$, Eqs. (F.17a) and (F.17b), yields

$$\begin{aligned} A_4(x) &= -i\frac{\kappa^*}{|\kappa|}A_3^*(0)\tan|\kappa|l\cos|\kappa|x + i\frac{\kappa^*}{|\kappa|}A_3^*(0)\sin|\kappa|x, \\ &= i\frac{\kappa^*}{|\kappa|}A_3^*(0)\frac{\sin|\kappa|x\cos|\kappa|l - \cos|\kappa|x\sin|\kappa|l}{\cos|\kappa|l}, \\ &= i\frac{\kappa^*}{|\kappa|}A_3^*(0)\frac{\sin[|\kappa|(x-l)]}{\cos|\kappa|l} \end{aligned} \tag{F.22a}$$

and

$$\begin{aligned} A_3^*(x) &= A_3^*(0)\cos|\kappa|x + i\,(-iA_3^*(0)\tan|\kappa|l)\sin|\kappa|x, \\ &= A_3^*(0)\frac{\cos|\kappa|x\cos|\kappa|l + \sin|\kappa|x\sin|\kappa|l}{\cos|\kappa|l}, \\ &= A_3^*(0)\frac{\cos[|\kappa|(x-l)]}{\cos|\kappa|l}. \end{aligned} \qquad (F.22b)$$

The complex amplitude of the fourth wave leaving the nonlinear medium at x=0, $A_4(0)$, is observed from Eq. (F.22a) to be linearly proportional to the complex conjugate of the complex amplitude of the incident signal wave, $A_3^*(0)$. Further, in the limit as $|\kappa|l \to 0$ the complex amplitudes of all the *mixing* waves are related as follows

$$A_4(0) \propto \chi^{(3)} A_1 A_2 A_3^*(0),$$

and using Eqs. (F.1), (F.2) and (F.4) becomes

$$\mathbf{E}_4(0) \propto \chi^{(3)} \mathbf{E}_1 \mathbf{E}_2 \mathbf{E}_3^*(0). \qquad (F.23)$$

The intensity of the fourth wave at x=0 can be deduced from Eq. (F.22a) and Eq. (F.4) as follows

$$\begin{aligned} I_4(x) &= A_4(x)A_4^*(x), \\ &= I_3(0)\frac{\kappa^*\kappa}{|\kappa|^2}\frac{\sin^2[|\kappa|(x-l)]}{\cos^2|\kappa|l}, \\ &= I_3(0)\frac{\sin^2[|\kappa|(x-l)]}{\cos^2|\kappa|l}, \end{aligned}$$

$$I_4(0) = I_3(0)\tan^2|\kappa|l \qquad (F.24)$$

and the PC reflectivity, R_{PC}, at x=0 is given by

$$R_{PC} = \tan^2|\kappa|l. \qquad (F.25)$$

For $\pi/4 < |\kappa|l < 3\pi/4$ the PC reflectivity is observed to exceed unity and hence the optical system acts as a PCM with gain. The above analysis can be extended to show that the signal field $\mathbf{E}_3$ need not be a plane wave but the wavefront may be of any arbitrary form and the same general result for $\mathbf{E}_4$ will be obtained. Further, the plane wave condition on the pumping beams, $\mathbf{E}_1$ and $\mathbf{E}_2$, can also be relaxed and the more general condition of the pumping beams being any PC pair inforced.

References.

[F.1] Yariv A. and Yeh P., "Optical Waves in Crystals," (Wiley series in pure and applied optics, New York, 1984).

APPENDIX G

PHOTOREFRACTIVE DEGENERATE FOUR WAVE MIXING COUPLED WAVE THEORY.

The basic wave interaction geometry for degenerate four wave mixing (DFWM) in a photorefractive (PR) material is illustrated in Fig. G.1.

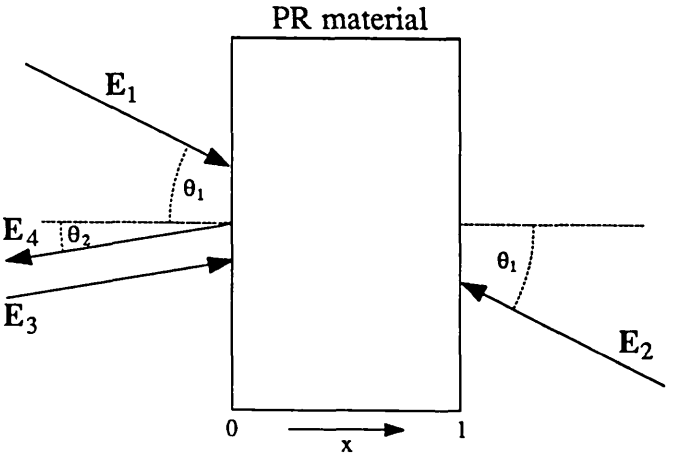


Figure G.1 Phase conjugation by DFWM in a PR material.

The four waves, of equal frequency ω and polarisation state, are all considered to be mutually coherent. The fields are considered to be plane wave as follows [G.1]

$$\mathbf{E}_j = A_j(r)\exp[i(\omega t - \mathbf{k}_j.\mathbf{r})]\hat{e}, \qquad (G.1)$$

where j=1, 2, 3 and 4, and the complex amplitudes, $A_j(r)$, are considered to be time independent. The wavevectors, $\mathbf{k}_j$, are all equal in magnitude and from Fig. G.1 are related by $\mathbf{k}_1 = -\mathbf{k}_2$ and $\mathbf{k}_3 = -\mathbf{k}_4$. Each wave generates an interference pattern with each of the other three waves and collectively the four waves generate six. However, particular to the DFWM geometry illustrated in Fig. G.1, the four waves form two counterpropagating pairs and the interference pattern due to fields $\mathbf{E}_1$ and $\mathbf{E}_3$ coincides with that of $\mathbf{E}_2$ and $\mathbf{E}_4$, differing only in phase and amplitude. Similarly the interference pattern due to $\mathbf{E}_1$ and $\mathbf{E}_4$ coincides with that of $\mathbf{E}_2$ and $\mathbf{E}_3$. Hence the six are reduced to four distinguishable interference patterns.

Assuming a linear response from the PR material, the induced phase volume hologram will consist of four multiplexed phase gratings and the resultant spatial profile of refractive index (RI) can be expressed as follows

$$\begin{aligned} n = n_o &+ \frac{1}{2} n_I \frac{A_1 A_3^* + A_2^* A_4}{I_o} \exp(i\phi_I) \exp(i\mathbf{k}_I.\mathbf{r}) + \text{c.c.} \\ &+ \frac{1}{2} n_{II} \frac{A_1 A_4^* + A_2^* A_3}{I_o} \exp(i\phi_{II}) \exp(i\mathbf{k}_{II}.\mathbf{r}) + \text{c.c.} \\ &+ \frac{1}{2} n_{III} \frac{A_1 A_2^*}{I_o} \exp(i\phi_{III}) \exp(i\mathbf{k}_{III}.\mathbf{r}) + \text{c.c.} \\ &+ \frac{1}{2} n_{IV} \frac{A_3 A_4^*}{I_o} \exp(i\phi_{IV}) \exp(i\mathbf{k}_{IV}.\mathbf{r}) + \text{c.c.}, \end{aligned} \tag{G.2}$$

where n_j and ϕ_j, $j = I \rightarrow IV$, are the grating amplitudes and phases respectively. I_o is the total incident intensity and the wavevectors are given by

$$\mathbf{k}_I = \mathbf{k}_1 - \mathbf{k}_3, \tag{G.3a}$$

$$\mathbf{k}_{II} = \mathbf{k}_1 - \mathbf{k}_4, \tag{G.3b}$$

$$\mathbf{k}_{III} = 2\mathbf{k}_1, \tag{G.3c}$$

$$\mathbf{k}_{IV} = 2\mathbf{k}_3. \tag{G.3d}$$

To reveal the coupled nature of the four interacting fields we solve Maxwell's paraxial wave equation for a lossless medium in the slowly varying envelope approximation for the RI enviroment specified by Eq. (G.2). The wave equation is given as follows

$$\begin{aligned} \nabla^2 \mathbf{E} - \mu_o \varepsilon \varepsilon_o \frac{\partial^2 \mathbf{E}}{\partial t^2} &= 0, \\ \nabla^2 \mathbf{E} + k^2 \mathbf{E} &= 0, \end{aligned} \tag{G.4}$$

where $k = n\omega/c$. The electric field $\mathbf{E}$ is the superposition of all four fields

$$\mathbf{E} = \sum_{j=1}^{4} A_j(r) \exp[i(\omega t - \mathbf{k}_j.\mathbf{r})]\hat{e} \tag{G.5}$$

and the wave equation becomes

$$\begin{aligned} \frac{\partial^2 \mathbf{E}}{\partial x^2} = \frac{\partial}{\partial x} \Bigg\{ &\left[\frac{\partial A_1(r)}{\partial x} - i k_{1_x} A_1(r) \right] \exp[i(\omega t - \mathbf{k}_1.\mathbf{r})] \\ &+ \left[\frac{\partial A_2(r)}{\partial x} - i k_{2_x} A_2(r) \right] \exp[i(\omega t - \mathbf{k}_2.\mathbf{r})] \\ &+ \left[\frac{\partial A_3(r)}{\partial x} - i k_{3_x} A_3(r) \right] \exp[i(\omega t - \mathbf{k}_3.\mathbf{r})] \end{aligned}$$

$$+\left[\frac{\partial A_4(r)}{\partial x} - ik_{4_x}A_4(r)\right]\exp[i(\omega t - \mathbf{k}_4.\mathbf{r})]\Bigg\},$$

$$= \left\{\left[\frac{\partial^2 A_1(r)}{\partial x^2} - 2ik_{1_x}\frac{\partial A_1(r)}{\partial x} - k_{1_x}^2 A_1(r)\right]\right.$$

$$\left.\cdot\exp[i(\omega t - \mathbf{k}_1.\mathbf{r})] + \ldots\right\} \qquad (G.6)$$

Employing the slowly varying envelope approximation we can assume

$$\frac{\partial^2 A_1(r)}{\partial x^2} \ll k_{1_x}\frac{\partial A_1(r)}{\partial x} \ll k_{1_x}^2 A_1(r) \qquad (G.7)$$

and Eq. (G.6) becomes

$$\frac{\partial^2 \mathbf{E}}{\partial x^2} = \left\{-\left[2ik_{1_x}\frac{\partial A_1(r)}{\partial x} + k_{1_x}^2 A_1(r)\right]\exp[i(\omega t - \mathbf{k}_1.\mathbf{r})] + \ldots\right\} \qquad (G.8a)$$

and similarly for y and z

$$\frac{\partial^2 \mathbf{E}}{\partial y^2} = \left\{-\left[2ik_{1_y}\frac{\partial A_1(r)}{\partial y} + k_{1_y}^2 A_1(r)\right]\exp[i(\omega t - \mathbf{k}_1.\mathbf{r})] + \ldots\right\}, \qquad (G.8b)$$

$$\frac{\partial^2 \mathbf{E}}{\partial z^2} = \left\{-\left[2ik_{1_z}\frac{\partial A_1(r)}{\partial z} + k_{1_z}^2 A_1(r)\right]\exp[i(\omega t - \mathbf{k}_1.\mathbf{r})] + \ldots\right\}. \qquad (G.8c)$$

Substituting Eqs. (G.2), (G.5) and (G.8a), (G.8b) and (G.8c) into the wave equation, Eq.(G.4), and equating the coefficients of the exponential term $\exp[i(\omega t - \mathbf{k}_1.\mathbf{r})]$ yields,

$$-\left[2i\left(k_{1_x}\frac{\partial A_1(r)}{\partial x} + k_{1_y}\frac{\partial A_1(r)}{\partial y} + k_{1_z}\frac{\partial A_1(r)}{\partial z}\right) + \left(k_{1_x}^2 + k_{1_y}^2 + k_{1_z}^2\right)A_1(r)\right]$$

$$+\frac{\omega^2}{c^2}\left\{n_o^2 A_1 + 2n_o\frac{1}{2}n_I\frac{A_1A_3^* + A_2^*A_4}{I_o}A_3\exp(i\phi_I)\right.$$

$$+ 2n_o\frac{1}{2}n_{II}\frac{A_1A_4^* + A_2^*A_3}{I_o}A_4\exp(i\phi_{II})$$

$$\left.+ 2n_o\frac{1}{2}n_{III}\frac{A_1A_2^*}{I_o}A_2\exp(i\phi_{III})\right\} = 0. \qquad (G.9)$$

Consider the variation in the amplitudes, $A_j(r)$, to be confined predominately along the x direction. The amplitude changes in y and z directions can consequently be neglected and the following approximations may be made

$$\frac{\partial A_j(r)}{\partial y} \simeq \frac{\partial A_j(r)}{\partial z} \simeq 0 \qquad (G.10a)$$

and

$$\frac{\partial A_j(r)}{\partial x} \simeq \frac{dA_j(r)}{dx} \not\simeq 0. \qquad (G.10b)$$

Substituting Eqs. (G.10a) and (G.10b), for j=1, into Eq. (G.9) yields

$$-2ik_{1_x}\frac{dA_1}{dx} - |k_1|^2 A_1 + \frac{n_o^2\omega^2}{c^2}A_1$$
$$\frac{\omega^2}{c^2}\Bigg\{ n_o n_I \frac{A_1A_3^* + A_2^*A_4}{I_o}A_3 \exp(i\phi_I)$$
$$+ n_o n_{II}\frac{A_1A_4^* + A_2^*A_3}{I_o}A_4\exp(i\phi_{II})$$
$$+ n_o n_{III}\frac{A_1A_2^*}{I_o}A_2\exp(i\phi_{III})\Bigg\} = 0$$

which simplifies to

$$2\frac{c}{\omega}\cos\theta_1\frac{dA_1}{dx} = -i\frac{n_I\exp(i\phi_I)}{I_o}(A_1A_3^* + A_2^*A_4)A_3$$
$$-i\frac{n_{II}\exp(i\phi_{II})}{I_o}(A_1A_4^* + A_2^*A_3)A_4$$
$$-i\frac{n_{III}\exp(i\phi_{III})}{I_o}A_1A_2^*A_2. \qquad (G.11a)$$

Similarly for A_2, A_3 and A_4 as follows

$$2\frac{c}{\omega}\cos\theta_1\frac{dA_2}{dx} = i\frac{n_I\exp(-i\phi_I)}{I_o}(A_1^*A_3 + A_2A_4^*)A_4$$
$$+i\frac{n_{II}\exp(-i\phi_{II})}{I_o}(A_1^*A_4 + A_2A_3^*)A_3$$
$$+i\frac{n_{III}\exp(-i\phi_{III})}{I_o}A_1^*A_2A_1, \qquad (G.11b)$$

$$2\frac{c}{\omega}\cos\theta_2\frac{dA_3}{dx} = -i\frac{n_I\exp(-i\phi_I)}{I_o}(A_1^*A_3 + A_2A_4^*)A_1$$
$$-i\frac{n_{II}\exp(i\phi_{II})}{I_o}(A_1A_4^* + A_2^*A_3)A_2$$
$$-i\frac{n_{IV}\exp(i\phi_{IV})}{I_o}A_3A_4^*A_4 \qquad (G.11c)$$

and

$$2\frac{c}{\omega}\cos\theta_2\frac{dA_4}{dx} = i\frac{n_I\exp(i\phi_I)}{I_o}(A_1A_3^* + A_2^*A_4)A_2$$
$$+i\frac{n_{II}\exp(-i\phi_{II})}{I_o}(A_1^*A_4 + A_2A_3^*)A_1$$
$$+i\frac{n_{IV}\exp(-i\phi_{IV})}{I_o}A_3^*A_4A_3. \qquad (G.11d)$$

Equations (G.11a), (G.11b), (G.11c) and (G.11d) are the general coupled nonlinear first order differential equations for the optical system depicted in Fig. G.1. In

practise one of the four destinct phase gratings will in general dominate as governed by the choice of geometry, polarisation and relative coherence between the four waves.

Consider the transmission grating to dominate, hence we can assume

$$n_I \gg n_{II}, n_{III}, n_{IV}$$

and the coupled equations, Eqs. (G.11a)→(G.11d), become

$$\frac{dA_1}{dx} = -\frac{\gamma}{I_o}(A_1 A_3^* + A_2^* A_4)A_3, \qquad (G.12a)$$

$$\frac{dA_2^*}{dx} = -\frac{\gamma}{I_o}(A_1 A_3^* + A_2^* A_4)A_4^*, \qquad (G.12b)$$

$$\frac{dA_3^*}{dx} = \frac{\gamma}{I_o}(A_1 A_3^* + A_2^* A_4)A_1^*, \qquad (G.12c)$$

$$\frac{dA_4}{dx} = \frac{\gamma}{I_o}(A_1 A_3^* + A_2^* A_4)A_2, \qquad (G.12d)$$

where the amplitude coupling constant γ has been defined as

$$\gamma = \frac{i\omega n_I \exp(i\phi_I)}{2c\cos\theta_1}, \qquad (G.13)$$

for the symmetric optical configuration, $\theta_1 = \theta_2$.

Re-expressing the coupled equations in terms of intensities

$$\begin{aligned}
\frac{dI_1}{dx} &= \frac{dA_1 A_1^*}{dx}, \\
&= A_1 \frac{dA_1^*}{dx} + A_1^* \frac{dA_1}{dx}, \\
&= -A_1 \frac{\gamma^*}{I_o}(A_1^* A_3 + A_2 A_4^*)A_3^* - A_1^* \frac{\gamma}{I_o}(A_1 A_3^* + A_2^* A_4)A_3, \\
&= -2\Re\left[\frac{\gamma}{I_o}(A_1 A_1^* A_3 A_3^* + A_1^* A_2^* A_3 A_4)\right], \\
&= \frac{\Gamma}{I_o}\left[I_1 I_3 + \sqrt{I_1 I_2 I_3 I_4}\cos(\varphi)\right], \qquad (G.14a)
\end{aligned}$$

and similarly for I_2, I_3 and I_4

$$\frac{dI_2}{dx} = \frac{\Gamma}{I_o}\left[I_2 I_4 + \sqrt{I_1 I_2 I_3 I_4}\cos(\varphi)\right], \qquad (G.14b)$$

$$\frac{dI_3}{dx} = -\frac{\Gamma}{I_o}\left[I_1 I_3 + \sqrt{I_1 I_2 I_3 I_4}\cos(\varphi)\right], \qquad (G.14c)$$

$$\frac{dI_4}{dx} = -\frac{\Gamma}{I_o}\left[I_2 I_4 + \sqrt{I_1 I_2 I_3 I_4}\cos(\varphi)\right], \qquad (G.14d)$$

where the intensity coupling constant, Γ, and the relative phase of the interfering waves, φ, are defined as follows

$$\Gamma = \frac{\omega n_I \sin\phi_I}{c\cos\theta_1}, \tag{G.15a}$$

$$\varphi = \varphi_3 + \varphi_4 - \varphi_1 - \varphi_2. \tag{G.15b}$$

Assuming the nondepleted pump approximation for $I_1, I_2 \gg I_3, I_4$ the system of coupled equations Eqs. (G.12a)→(G.12d) become

$$\frac{dA_1}{dx} = 0, \tag{G.16a}$$

$$\frac{dA_2^*}{dx} = 0, \tag{G.16b}$$

$$\frac{dA_3^*}{dx} = \frac{\gamma}{I_o}[|A_1|^2 A_3^* + (A_1^* A_2^*)A_4], \tag{G.16c}$$

$$\frac{dA_4}{dx} = \frac{\gamma}{I_o}[(A_1 A_2)A_3^* + |A_2|^2 A_4]. \tag{G.16d}$$

The coupled differential equations Eqs. (G.16c) and (G.16d) are decoupled using their second derivatives as follows

$$\begin{aligned}
\frac{d^2A_3^*}{dx^2} &= \frac{\gamma}{I_o}\left\{|A_1|^2\frac{dA_3^*}{dx} + (A_1^*A_2^*)\frac{dA_4}{dx}\right\}, \\
&= \frac{\gamma}{I_o}\left\{|A_1|^2\frac{dA_3^*}{dx}\right. \\
&\qquad \left. + (A_1^*A_2^*)\frac{\gamma}{I_o}\left[(A_1A_2)A_3^* + |A_2|^2A_4\right]\right\}, \\
&= \frac{\gamma}{I_o}\left\{|A_1|^2\frac{dA_3^*}{dx}\right. \\
&\qquad \left. + (A_1^*A_2^*)\frac{\gamma}{I_o}\left[(A_1A_2)A_3^* + \frac{|A_2|^2}{(A_1^*A_2^*)}\left(\frac{I_o}{\gamma}\frac{dA_3^*}{dx} - |A_1|^2A_3^*\right)\right]\right\}, \\
&= \frac{\gamma}{I_o}\left[|A_1|^2 + |A_2|^2\right]\frac{dA_3^*}{dx}
\end{aligned}$$

and hence

$$\frac{d^2A_3^*}{dx^2} - \gamma\frac{I_1 + I_2}{I_o}\frac{dA_3^*}{dx} = 0, \tag{G.17a}$$

similarly for A_4

$$\frac{d^2A_4}{dx^2} - \gamma\frac{I_1 + I_2}{I_o}\frac{dA_4}{dx} = 0. \tag{G.17b}$$

The corresponding general solutions can be assumed to be

$$A_3^* = a\exp[\gamma(I_1 + I_2)x/I_o] + b, \qquad (G.18a)$$

$$A_4 = c\exp[\gamma(I_1 + I_2)x/I_o] + d, \qquad (G.18b)$$

which are accompanyed by the boundary conditions $A_3^*(0)$ and $A_4(l) = 0$,

$$A_3^*(0) = a + b, \qquad (G.19a)$$

$$0 = c\exp[\gamma(I_1 + I_2)l/I_o] + d. \qquad (G.19b)$$

Substituting Eqs. (G.18a) and (G.18b) with their first derivatives back into the original coupled differential equations, Eqs. (G.16c) and (G.16d), yields

$$c\gamma\frac{I_1 + I_2}{I_o}\exp[\gamma(I_1 + I_2)x/I_o] = \frac{\gamma}{I_o}\Big\{(A_1A_2)\,[a\exp[\gamma(I_1 + I_2)x/I_o] + b] + I_2\,[c\exp[\gamma(I_1 + I_2)x/I_o] + d]\Big\}. \qquad (G.20)$$

Consider x=0, Eq. (G.20) becomes

$$c\gamma\frac{I_1 + I_2}{I_o} = \frac{\gamma}{I_o}\Big\{A_1A_2A_3^*(0) + I_2(c + d)\Big\}$$

and solving for c becomes

$$c\gamma\frac{I_1 + I_2}{I_o} = \frac{\gamma}{I_o}\Big\{A_1A_2A_3^*(0) + cI_2 - c\exp(\gamma l)I_2\Big\},$$

$$cI_1 = A_1A_2A_3^*(0) - c\exp(\gamma l)I_2,$$

$$c = A_3^*(0)\frac{A_1}{A_2^*}\frac{\exp(-\gamma l)}{[\exp(-\gamma l)/\beta + 1]}, \qquad (G.21a)$$

where $\beta = I_2/I_1$. Returning to Eq. (G.20) and solving for d at x=0 yields

$$d = -A_3^*(0)\frac{A_1}{A_2^*}\frac{1}{[\exp(-\gamma l)/\beta + 1]}. \qquad (G.21b)$$

Similarly Eq. (G.20) can be solved for a and b at x=l to give

$$a = A_3^*(0)\frac{\exp(-\gamma l)/\beta}{[\exp(-\gamma l)/\beta + 1]}, \qquad (G.21c)$$

$$b = A_3^*(0)\frac{1}{[\exp(-\gamma l)/\beta + 1]}. \qquad (G.21d)$$

Substituting the solutions for a, b, c and d back into Eqs. (G.18a) and (G.18b) yields

$$A_3^*(x) = A_3^*(0)\frac{1}{[\exp(-\gamma l)/\beta + 1]}\,[\exp[\gamma(x - l)]/\beta + 1], \qquad (G.22a)$$

$$A_4(x) = A_3^*(0)\frac{A_1/A_2^*}{[\exp(-\gamma l)/\beta + 1]}\,[\exp[\gamma(x - l)] - 1]. \qquad (G.22b)$$

Further, the phase conjugate reflectivity, R_{PC}, is defined as

$$R_{PC} = \left| \frac{A_4(0)}{A_3^*(0)} \right|^2 \qquad (G.23)$$

and from Eq. (G.22b) we immediately deduce

$$\begin{aligned} \frac{A_4(0)}{A_3^*(0)} &= \frac{A_1}{A_2^*} \frac{[\exp(-\gamma l) - 1]}{[\exp(-\gamma l)/\beta + 1]}, \\ &= -\frac{A_1}{A_2^*} \frac{\exp(-\gamma l/2)}{\exp[-(\gamma l + \ln\beta)/2]} \frac{[\exp(\gamma l/2) - \exp(-\gamma l/2)]}{[\exp[(\gamma l + \ln\beta)/2] + \exp[-(\gamma l + \ln\beta)/2]]}, \\ &= -\frac{A_1}{A_2^*} \sqrt{\beta} \frac{\sinh(\gamma l/2)}{\cosh[(\gamma l + \ln\beta)/2]}, \\ &= \sqrt{\frac{A_1 A_2}{A_1^* A_2^*}} \frac{\sinh(\gamma l/2)}{\cosh[(\gamma l + \ln\beta)/2]} \end{aligned} \qquad (G.24)$$

and finally R_{PC} is given by

$$R_{PC} = \left| \frac{\sinh(\gamma l/2)}{\cosh[(\gamma l + \ln\beta)/2]} \right|^2. \qquad (G.25)$$

References.

[G.1] B. Fischer, M. Cronin–Golomb, J.O. White and A. Yariv, "Amplified reflection, transmission, and self–oscillation in real–time holography," Opt.Lett. **6**, 519–521 (1981).

APPENDIX H

STOKES'S RELATIONS FOR TIME REVERSED WAVES AT A LOSSLESS BEAM SPLITTER.

Consider a linearly polarised plane wave, $\mathbf{E}_1$, defined by

$$\mathbf{E}_1 = A_1 \exp[i(\omega t - \mathbf{k}_1.\mathbf{r})]\hat{\mathbf{e}}, \qquad (H.1)$$

with a complex amplitude A_1 and unit polarisation vector $\hat{\mathbf{e}}$, incident from a vacum onto a lossless plane beam splitter as illustrated in Fig. H.1. [H.1,H.2]

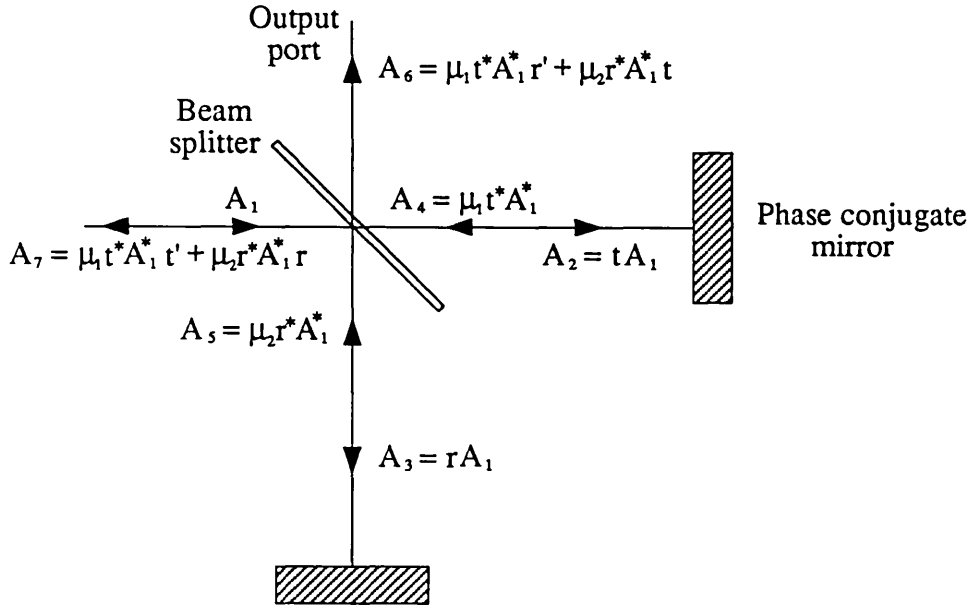


Figure H.1 Complex amplitudes at various locations and both directions in a PC Michelson interferometer.

The transmitted and reflected waves, $\mathbf{E}_2$ and $\mathbf{E}_3$ respectively, will also be plane wave and will have complex amplitudes, A_2 and A_3, given by

$$A_2 = tA_1, \qquad (H.2a)$$

$$A_3 = rA_1, \qquad (H.2b)$$

where t and r are the complex amplitude coefficients of transmittance and reflectance respectively for the lossless beam splitter, illuminated from the left hand side. The two waves $\mathbf{E}_2$ and $\mathbf{E}_3$ are phase conjugated at their respective PCMs,

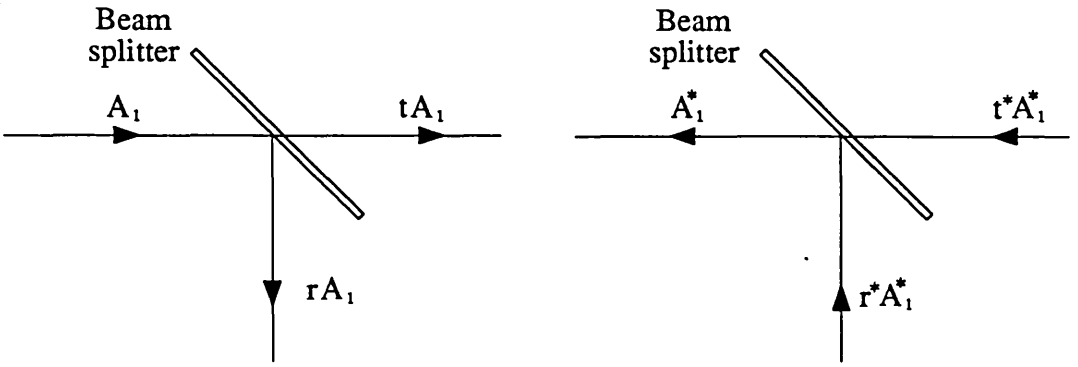


Figure H.2 The principle of time reversal invariance of light.

generating two PC waves $\mathbf{E}_4$ and $\mathbf{E}_5$ respectively with associated complex amplitudes as follows

$$A_4 = \mu_1 t^* A_1^*, \qquad (H.3a)$$

$$A_5 = \mu_2 r^* A_1^*, \qquad (H.3b)$$

where μ_1 and μ_2 are the complex amplitude coefficients of reflectance for the two PCMs. The waves $\mathbf{E}_4$ and $\mathbf{E}_5$ return back to the beam splitter where they combine to generate a wave travelling out the fourth port, $\mathbf{E}_6$, and a wave travelling counterdirectional to the incident wave $\mathbf{E}_1$, $\mathbf{E}_7$. Their corresponding complex amplitudes are

$$A_6 = \mu_1 t^* A_1^* r' + \mu_2 r^* A_1^* t, \qquad (H.4a)$$

$$A_7 = \mu_1 t^* A_1^* t' + \mu_2 r^* A_1^* r, \qquad (H.4b)$$

where t' and r' are the complex amplitude coefficients of transmittance and reflectance for the lossless beam splitter illuminated from the right hand side.

Let us now consider the waves $\mathbf{E}_4$ and $\mathbf{E}_5$ to be the exact time reversed replicas of $\mathbf{E}_2$ and $\mathbf{E}_3$ respectively. This requirment is only satisfied if the PC reflections performed by both PCMs are perfect i.e. $\mu_1 = \mu_2 = 1$. The complex amplitudes of the waves $\mathbf{E}_4$ and $\mathbf{E}_5$ become

$$A_4 = t^* A_1^*, \qquad (H.5a)$$

$$A_5 = r^* A_1^*. \qquad (H.5b)$$

Applying the principle of time reversal invariance of light, schematically illustrated in Fig. H.2, we observe that the waves $\mathbf{E}_4$ and $\mathbf{E}_5$ combine at the beam splitter to generate the time reversed replica of the incident wave $\mathbf{E}_1$, $\mathbf{E}_1^*$, travelling counterdirectional to $\mathbf{E}_1$, and no wave is generated out the fourth port. Using Eqs. (H.4a) and (H.4b) with Eqs. (H.5a) and (H.5b), the complex amplitudes of waves $\mathbf{E}_6$ and $\mathbf{E}_7$ become

$$A_1^*(t^*r' + r^*t) = 0, \qquad (H.6a)$$

$$A_1^*(t^*t' + r^*r) = A_1^*, \qquad (H.6b)$$

from which the generalised Stokes's relations are deduced as follows

$$t^*r' + r^*t = 0, \qquad (H.7a)$$

and

$$t^*t' + r^*r = 1. \qquad (H.7b)$$

References.

[H.1] P.D. Drummond and A.T. Friberg, "Specular reflection cancellation in an interferometer with a phase–conjugate mirror," J.Appl.Phys. **54**, 5618–5625 (1983).

[H.2] Hecht E. and Zajac A., "Optics," (Addison–Wesley publishing company, Massachusetts, 5th Ed, 1980).

APPENDIX I

SPECULAR REFLECTION CANCELLATION AND ENHANCEMENT EXPERIMENTAL DATA.

Phase conjugate reflectivity R_{PC}	Relative intensity of specular reflection I_r o
0.044	0.346
0.051	0.340
0.062	0.337
0.076	0.329
0.098	0.319
0.113	0.307
0.124	0.306
0.153	0.292
0.156	0.292
0.164	0.290
0.185	0.275
0.193	0.276
0.236	0.253
0.287	0.229
0.298	0.227
0.375	0.194
0.404	0.179
0.415	0.181
0.422	0.162
0.436	0.176
0.440	0.168
0.487	0.148
0.542	0.125
0.593	0.105
0.625	0.089
0.658	0.068
0.731	0.055
0.742	0.066
0.796	0.037
0.822	0.044
0.865	0.033
0.891	0.030
0.975	0.018

contd...

contd...

1.025	0.022
1.109	0.027
1.149	0.028
1.153	0.033
1.167	0.027
1.175	0.031
1.233	0.046

Table I.I Phase conjugate reflectivity, R_{PC}, versus the relative intensity of the specularly reflected intensity, I_r, for R=0.37.

Phase conjugate reflectivity R_{PC}	Relative intensity of specular reflection	
	I_r(cancel) o	I_r(enhance) ⋆
0.682	0.118	0.823
0.744	0.131	0.762
0.829	0.099	0.858
0.868	0.099	0.845
0.891	0.093	0.893
0.930	0.093	0.919
0.977	0.090	1.011
1.054	0.067	1.021
1.101	0.067	1.056
1.178	0.064	1.136
1.233	0.054	1.143
1.287	0.058	1.293
1.333	0.061	1.424
1.349	0.058	1.194
1.519	0.067	1.565
1.566	0.051	1.331
1.767	0.045	1.447
2.000	0.064	1.632
2.155	0.080	1.668
2.411	0.083	1.792
2.581	0.109	1.796

Table I.II Phase conjugate reflectivity, R_{PC}, versus the relative intensity of the cancelled and enhanced specularly reflected intensities, I_r, for R=0.37.

REFERENCES

The alphabetical list of references cited in this thesis with their locations enclosed in square brackets e.g. [4.26].

Y.S. Abu-Mostafa and D. Psaltis, "Optical neural computers," Sci.Am. **256**, 66–73 (March 1987).
[6.11]

G.S. Agarwal and E. Wolf, "Theory of phase conjugation with weak scatters," J.Opt.Soc.Am. **72**, 321–326 (1982).
[5.16]

G.S. Agarwal, A.T. Friberg and E. Wolf, "Effect of backscattering in phase conjugation with weak scatterers," J.Opt.Soc.Am. **72**, 861–863 (1982).
[5.17]

G.S. Agarwal, A.T. Friberg and E. Wolf, "Scattering theory of distortion correction by phase conjugation," J.Opt.Soc.Am. **73**, 529–538 (1983).
[5.18]

J.J. Amodei, "Analysis of transport processes during holographic recording in insulators," RCA Review **32**, 185–198 (1971).
[1.4]

J.J. Amodei, "Electron diffusion effects during hologram recording in crystals," Appl.Phys.Lett. **18**, 22–24 (1971).
[1.5]

D.Z. Anderson, D.M. Lininger and J. Feinberg, "Optical tracking novelty filter," Opt.Lett. **12**, 123–125 (1987).
[1.21,5.5]

A. Ashkin, G.D. Boyd, J.M. Dziedzic, R.G. Smith, A.A. Ballman, J.J. Levinstein and K. Nassau, "Optically-induced refractive index homogenities in $LiNbO_3$ and $LiTaO_3$," Appl.Phys.Lett. **9**, 72–74 (1966).
[1.1]

Atkinson K.E., "An Introduction to Numerical Analysis," (Wiley, New York, 1978).
[7.3]

Bechmann R., Hearmon R.F.S. and Kurtz S.K., "Elastic, Piezoelectric, Piezooptic, Electrooptic Constants, and Nonlinear Dielectric Susceptibilities of Crystals," (Springer–Verlag, Heidelberg, 1969).
[2.26]

E.E. Bergmann, I.J. Bigio, B.J. Feldman and R.A. Fisher, "High–efficiency pulsed 10.6μm phase–conjugate reflection via degenerate four–wave mixing," Opt.Lett. **3**, 82 (1978).
[4.12]

A. Bledowski, W. Krolikowski and A. Kujawski, "Multistability in reflection grating real–time holography," IEEE J.Quant.Electron. **QE–22**, 1547–1550 (1986).
[4.22]

D.M. Bloom, P.F. Liao and M.P. Economoo, "Observation of amplified reflection by degenerate four wave mixing in a sodium vapour," Opt.Lett. **2**, 58 (1978).
[4.10,5.11]

H.J. Caufield, "Associative Mappings by optical holography," Opt.Commun. **55**, 80–82 (1985).
[6.3]

F.S. Chen, "Optically induced change in refractive indices in $LiNbO_3$ and $LiTaO_3$," J.Appl.Phys. **40**, 3389–3396 (1969).
[1.2]

W.–H. Chen, C.–M. Peng and P. Yeh, "Anisotropic conical diffractions in a $BaTiO_3$ crystal," Topical meeting on Photorefractive materials, effects and devices, Technical digest series **17**, 118–121 (1987).
[7.9]

A.E. Chiou and P. Yeh, "Parallel image subtraction using a phase conjugate Michelson interferometer," Opt.Lett. **11**, 306–308 (1986).
[1.20,4.27,5.4]

M.G. Clarke, F.J. DiSalvo, A.M. Glass and G.E. Peterson, "Electronic structure and optical index damage of iron doped lithium niobate," J.-Chem.Phys. **59**, 6209–6219 (1973).
[2.12]

M. Cronin–Golomb, J.O. White, B. Fischer and A. Yariv, "Exact solution of a nonlinear model of four–wave mixing and phase conjugation," Opt.Lett **7**, 313–315 (1982).
[4.21]

P.D. Drummond and A. T. Friberg, "Specular reflection cancellation in an interferometer with a phase–conjugate mirror," J.Appl.Phys. **54**, 5618–5625 (1983).
[5.22,H.1]

S. Ducharme and J. Feinberg, "Altering the photorefractive properties of $BaTiO_3$ by reduction and oxidation at 650 °C," J.Opt.Soc.Am. B **3**, 283–292 (1986).
[2.7]

G.J. Dunning, E. Marom, Y. Owechko and B.H. Soffer, "All–optical associative memory with shift invariance and multiple–image recall," Opt.Lett. **12**, 346–348 (1987).
[5.9,6.13]

R.W. Eason and A.M.C. Smout, "Bistability and noncommutative behaviour of multiple–beam self–pulsing and self–pumping in $BaTiO_3$," Opt.-Lett. **12**, 51–53 (1987).
[1.30,4.37]

M.D. Ewbank, P. Yeh, M. Khoshnevisan and J. Feinberg, "Time reversal by an interferometer with a coupled phase–conjugate reflectors," Opt.Lett. **10**, 282–284 (1985).
[1.28]

M.D. Ewbank, P. Yeh and J. Feinberg, "Photorefractive conical diffraction in $BaTiO_3$," Opt.Commun. **59**, 423–428 (1986).
[7.8]

M.B. Ewbank, "Mechanism for photorefractive phase conjugation using incoherent beams," Opt.Lett. **13**, 47–49 (1988).
[1.31]

J. Feinberg, D. Heiman, A.R. Tanguay Jr. and R.W. Hellwarth, "Photorefractive effects and light–induced charge migration in barium titanate," J.Appl.Phys. **51**, 1297–1305 (1980).
[1.12,2.6,3.4]

J. Feinberg, "Real-time edge enhancement using the photorefractive effect," Opt.Lett. **5**, 330–332 (1980).
[1.18]

J. Feinberg and R.W. Hellwarth, "Phase conjugating mirror with continuous wave gain," Opt.Lett. **5**, 519–521 (1980).
[4.14,5.12]

J. Feinberg, "Self-pumped, continuous-wave phase conjugator using internal reflection," Opt.Lett. **7**, 486–488 (1982).
[1.26,4.31]

J. Feinberg, "Asymmetric self-defocusing of an optical beam from the photorefractive effect," J.Opt.Soc.Am. **72**, 46–51 (1982).
[4.29,7.4]

J. Feinberg, "Continuous-wave self-pumped phase conjugator with wide field of view," Opt.Lett. **8**, 480–482 (1983).
[4.38,5.25]

J. Feinberg, "Interferometer with a self-pumped phase-conjugating mirror," Opt.Lett **8**, 569–571 (1983).
[4.25]

B. Fischer, M. Cronin-Golomb, J.O. White and A. Yariv, "Amplified reflection, transmission and self oscillation in real time holography," Opt.Lett. **6**, 519–521 (1981).
[4.20,G.1]

Fisher R.A., "Optical Phase Conjugation," (Academic Press, New York, 1983).
[1.27,3.4,5.3]

A. T. Friberg and P.D. Drummond, "Reflection of a linearly polarized plane wave from a lossless stratified mirror in the presence of a phase-conjugate mirror," J.Opt.Soc.Am. **73**, 1216–1219 (1983).
[5.21]

D. Gabor, "Associative holographic memories," IBM J.Res.Develop. **13**, 156–159 (1969).
[6.2]

C.R. Giuliano, "Applications of optical phase conjugation," Phys.Today **34**, 27–35 (April 1981).
[5.7]

A.M. Glass, D. von der Linde and T.J. Negran, "High–voltage bulk photovoltaic effect and the photorefractive process in $LiNbO_3$," Appl.Phys.Lett. **25**, 233–235 (1974).
[1.6]

A.M. Glass, A.M. Johnson, D.H. Olson, W. Simpson and A.A. Ballman, "Fourwave mixing in semi–insulating InP and GaAs using photorefractive effect," Appl.Phys.Lett. **44**, 948–950 (1979).
[2.23]

J. Goltz, F. Laeri and T. Tschudi, "Nearly degenerate four–wave mixing in photorefractive crystals, an analytical treatment," Opt.Commun. **64**, 63–66 (1987).
[4.24]

M.C. Gower, "Phase conjugate mirrors," Phys.Bull. **38**, 220–222 (1987).
[1.22,5.8]

Gradshteyn I.S. and Ryzhik I.M., "Table of Integrals, Series and Products – Corrected and enlarged edition," (Academic Press, Inc., London, 1980).
[C.2]

P. Günter, U. Flückiger, J.P. Huignard and F. Micheron, "Optically induced refractive index changes in $KNbO_3$: Fe," Ferroelectrics **13**, 297–299 (1976).
[1.14]

P. Günter and F. Micheron, "Photorefractive effects and photocurrents in $KNbO_3$: Fe," Ferroelectrics **18**, 27–38 (1978).
[3.2]

P. Günter, "Holography, coherent light amplification and optical phase conjugation with photorefractive materials," Physics Reports **93**, 199–299 (1982).
[3.6,D.1]

P. Günter, E. Voit, M.Z. Zha and J. Albers, "Self–pulsation and optical chaos in self–pumped photorefractive $BaTiO_3$," Opt.Commun. **55**, 210–214 (1985).
[4.34,5.26]

T.J. Hall, R. Jaura, L.M. Connors and P.D. Foote, "The photorefractive effect–a review," Prog.Quant.Electr. **10**, 77–146 (1985).
[3.3,C.1]

Hecht E. and Zajac A., "Optics," (Addison–Wesley publishing company, Massachusetts 5th Ed, 1980).
[2.11,4.28,H.2]

J. Hong and D. Psaltis, "Storage capacity of holographic associative memories," Opt.Lett. **11**, 812–814 (1986).
[6.7]

J.J. Hopfield, "Neural networks and physical systems with emergent collective computational abilities," Proc.Natl.Acad.Sci. USA **79**, 2554–2558 (1982).
[6.16]

S.L. Hou, R.B. Lauer and R.E. Aldrich, "Transport processes of photoinduced carriers in $Bi_{12}SiO_{20}$," J.Appl.Phys. **44**, 2652–2658 (1973).
[2.20]

J.P. Huignard, J.P. Herriau, P. Aubourg and E. Spitz, "Phase conjugate wavefront generation via real time holography in $Bi_{12}SiO_{20}$ crystals," Opt.-Lett. **4**, 21–23 (1979).
[1.17,4.13]

S.M. Jenson and R.W. Hellwarth, "Observation of the time reversed replica of a monochromatic optical wave," Appl.Phys.Lett. **32**, 166 (1978).
[4.11]

J.M.C. Jonathan, G. Roosen and Ph. Roussignol, "Time resolved build-up of the photorefractive effect produced in $Bi_{12}SiO_{20}$ by picosecond light pulses," OSA Top.Meet. Technical Digest **17**, 97–100 (1987).
[1.36]

D.M. Kim, R.R. Shah, T.A. Rabson and F.K. Tittel, "Nonlinear dynamic theory for photorefractive phase hologram formation," Appl.Phys.Lett. **28**, 338–340 (1974).
[1.7]

M.B. Klein and G.C. Valley, "Beam coupling in $BaTiO_3$ at 442nm," J.-Appl.Phys. **57**, 4901–4905 (1985).
[2.8]

M.B. Klein and R.N. Schwartz, "Photorefractive effect in $BaTiO_3$: microscoptic origins," J.Opt.Soc.Am. B **3**, 293–305 (1986).
[2.15]

M.B. Klein, G.J. Dunning, G.C. Valley, R.C. Lind and T.R. O'Meara, "Imaging threshold detector using a phase conjugate resonator in $BaTiO_3$," Opt.Lett. **11**, 575–577 (1986).
[5.6]

T. Kohonen,"Associative Memory, A System-Theoretical Approach,"(Springer-Verlag, Berlin, 1977).
[6.1]

H. Kogelnik, "Coupled Wave Theory for Thick Hologram Gratings," Bell.-Syst.Tech.J. **48**, 2909–2947 (1969).
[3.5]

E. Krätzig, "Photorefractive effect and photoconductivity in $LiNbO_3$: Fe," Ferroelectrics **21**, 635–636 (1978).
[2.14]

Kreyszig E.,"Advanced Engineering Mathematics - 4th Ed.," (John Wiley & Sons, Inc., New York, 1979).
[C.3]

W. Krolikowski, "Multi–grating phase conjugation in photorefractive media," Opt.Commun. **60**, 319–322 (1986).
[4.23]

A.D. Kudryavtseva, A.I. Sokolovskaya, J. Gazengel, N.P. Xuan and G. Rivoire, "Reconstruction of the laser wavefront by stimulated scattering in the picosecond range," Opt.Commun **26**, 446 (1978).
[4.6]

N.V. Kukhtarev, V.B. Markov, S.G. Odulov, M.S. Soskin and V.L. Vinetskii, "Holographic storage in electro–optic crystals. I Steady state," Ferroelectrics **22**, 949–960 (1979).
[1.8,2.1,3.1,7.1]

N.V. Kukhtarev, V.B. Markov, S.G. Odulov, M.S. Soskin and V.L. Vinetskii, "Holographic storage in electro–optic crystals. II Beam coupling – light amplification," Ferroelectrics **22**, 961–964 (1979).
[1.9,2.2]

N. Kukhtarev and S. Odoulov, "Degenerate four–wave mixing in $LiNbO_3$ and $LiTaO_3$," Opt.Commun. **32**, 183–186 (1980).
[4.19]

Sze–Keung Kwong and A. Yariv, "Bistable oscillations with a self–pumped phase–conjugate mirror," Opt.Lett. **11**, 377–379 (1986).
[4.35]

Sze–Keung Kwong, G.A. Rakuljic and A. Yariv, "Real time image subtraction and "exclusive or" operation using a self–pumped phase conjugate mirror," Appl.Phys.Lett **48**, 201–203 (1986).
[4.26]

G. Le Saux and A. Brun, "Photorefractive material response to short pulse illuminations," IEEE J.Quantum Electron **QE–23**, 1680–1688 (1979).
[1.11,2.5]

G. Le Saux, G. Roosen and A. Brun, "Nanosecond light energy transfer in $Bi_{12}SiO_{20}$ at 532nm," Opt.Commun. **58**, 238–240 (1986).
[1.35]

L.H. Lin, "Holographic measurements of optically induced refractive index inhomogeneties in bismuith titanate," Proc. IEEE **57**, 252–253 (1969).
[1.15]

I. Lindsay and J.C. Dainty, "Partial cancellation of specular reflection in the presence of a phase–conjugate mirror," Opt.Commun. **59**, 405–410 (1986).
[5.19]

I. Lindsay, "Specular reflection cancellation/enhancement in the presence of a phase–conjugate mirror," J.Opt.Soc.Am. B **4**, 1810–1815 (1987).
[5.20]

D.C. Look, "Model for Fe^{2+} intracenter–induced photoconductivity in InP:Fe," Phys.Rev. B **20**, 4160–4166 (1979).
[2.24]

Lorrain P. and Corson D.,"Electromagnetic Fields and Waves," 2nd Ed. (Freeman, New York ,1970).
[7.2]

D. Mahgerefteh and J. Feinberg, "Nanosecond reponse and "coasting" in photorefractive barium titanate," OSA Topical meeting on *Photorefractive materials, effects and devices* (Los Angeles, C.A.), Technical Digest **17**, 92 (August 1987).
[2.9]

J. Marotz, K.H. Ringhofer, R.A. Rupp and S. Treichel, "Light–induced scattering in photorefractive crystals," IEEE J.Quant.Electron. **QE–22**, 1376–1383 (1986).
[7.5]

J. Marotz, K.H. Ringhofer and R.A. Rupp, "Holographic light scattering in photorefractive materials," Topical meeting on Photorefractive materials, effects and devices, Technical digest series **17**, 106–109 (1987).
[7.6]

K. Megumi, H. Kozuka, M. Kobayashi and Y. Furuhata, "High–sensitive holographic storage in Ce–doped SBN," Appl.Phys.Lett. **30**, 631–633 (1977).
[2.16]

M.J. Miller, E.J. Sharp, G.L. Wood, W.W. Clark III, G. J. Salamo and R.R. Neurgaonkar, "Time response of a cerium–doped $Sr_{0.75}Ba_{0.25}Nb_2O_6$ self–pumped phase–conjugate mirror," Opt.Lett. **12**, 340–342 (1987).
[4.32]

S.R. Montgomery, J. Yarrison–Rice, D.O. Pederson, M.J. Miller, W.W. Clark III, G.L. Wood, E.J. Sharp and R.R. Neurgaonkar, "Self–pumped phase conjugation in the red in photorefractive $Ba_{2-x}Sr_xK_{1-y}Na_yNb_5O_{15}$ and $Sr_xBa_{1-x}Nb_2O_6$ with cerium 9–fold coordinated sites," OSA Topical Meeting on *Photorefactive Materials, Effects and Devices* Technical Digest Series **17**, 171–174 (1987).
[4.33]

M. Nazarathy, "A Fabry–Perot etalon with one phase–conjugate mirror," Opt.Commun. **45**, 5618–5625 (1983).
[5.23]

J.A. Neff, "Major initiatives for optical computing," Opt.Eng. **26**, 2–9 (1987).
[6.9]

R.R. Neurgaonkar, W.K. Cory, J.R. Oliver, M.D. Ewbank, W.F. Hall, "Development and modification of photorefractive properties in the tungsten bronze family crystals," Opt.Eng. **26**, 392–405 (1987).
[2.18]

M.G. Nicholson, I.R. Cooper, G.G. Gibbons and C.R. Petts, "Optimization of an updatable optical image correlator," Opt.Eng. **26**, 445–452 (1987).
[1.19]

M. Nieto-Vesperinas, "Fields generated by a Fabry-Perot interferometer with a phase-conjugate mirror," J.Opt.Soc.Am. A **2**, 427-436 (1985).
[5.24]

O.Yu. Nosach, V.I. Popovichev, V.V. Ragul'skii and F.S. Faizullov, "Cancellation of phase distortion in an amplifying medium with a "Brillouin Mirror"," Sov.Phys. JETP **16**, 435-438 (1972).
[4.2]

Y. Owechko, G.J. Dunning, E. Marom and B.H. Soffer, "Holographic associative memory with nonlinearities in the correlation domain," Appl.Opt. **26**, 1900-1910 (1987).
[1.25,6.14]

E.G. Paek and D. Psaltis, "Optical associative memory using Fourier transform holograms," Opt.Eng. **26**, 428-433 (1987).
[6.12]

G. Pauliat, J.P. Herrriau, A. Delboulbé, G. Roosen and J.P. Huignard, "Dynamic beam deflection using photorefractive gratings in $Bi_{12}SiO_{20}$ crystals," J.Opt.Soc.Am.B **3**, 306-314 (1986).
[1.23]

M. Peltier and F. Micheron, "Volume hologram recording and charge transfer process in $Bi_{12}SiO_{20}$ and $Bi_{12}GeO_{20}$," J.Appl.Phys. **48**, 3683-3690 (1977).
[1.16]

D.M. Pepper, "Non-linear optical phase-conjugation," Opt.Eng. **21**, 156-183 (1983).
[5.2]

D. Psaltis and N. Farhat, "Optical information processing based on an associative-memory model of neural nets with thresholding and feedback," Opt.Lett. **10**, 98-100 (1985).
[6.4]

D. Psaltis and J. Hong, "Shift-invariant optical associative memories," Opt.Eng. **26**, 10-15 (1987).
[6.10]

G.A. Rakuljic, A. Yariv and R.R. Neurgaonkar, "Photorefractive properties of undoped, cerium doped and iron doped single crystal $Sr_{0.6}Ba_{0.4}Nb_2O_6$," Opt.Eng. **25**, 1212-1216 (1986).
[2.17]

D. Rutz, M.B. Klein, B.A. Wechsler, R.N. Schwartz and K.W. Kirby, "Growth and Characterization of photorefractive $Bi_{12}TiO_{20}$ (BTO)," OSA Topical meeting on *Photorefractive materials, effects and devices* (los Angeles, C.A.), Technical Digest **17**, 41–43 (August 1987).
[2.22]

G. Salamo, M.J. Miller, W.W. Clark III, G.L. Wood and E.J. Sharp, "Strontium barium niobate as a self–pumped phase conjugator," Opt.Commun. **59**, 417–422 (1986).
[4.30]

Sanders Associates, Inc., "Guiddines for the preparation of single domain $BaTiO_3$ crystals," Sanders Associates, Inc., Defense Systems Division, 15 Canal St, Nashua, New Hampshire, U.S.A.
[2.25]

Y. Shi, D. Psaltis, A. Marrakchi and A.R. Tanguay, Jr., "Photorefactive incoherent–to–coherent optical converter," Appl.Opt **22**, 3665–3667 (1983).
[1.24]

E.I. Shtyrkov and V.V. Samartsev, "Imaging properties of dynamic echo holograms in resonant media," Opt.Spectrosc. **40**, 224 (1976).
[4.7]

A.L. Smirl, G.C. Valley, R.A. Mullen, K. Bohnert, C.D. Mire and T.F. Boggess, "Picosecond photorefractive effect in $BaTiO_3$," Opt.Lett. **12**, 501–503 (1987).
[1.33]

A.M.C. Smout, R.W. Eason and M.C. Gower, "Regular oscillations and self–pulsating in self–pumped $BaTiO_3$," Opt.Commun. **59**, 77–82 (1986).
[4.36]

B.H. Soffer, G.J. Dunning, Y. Owechko and E. Marom, "Associative holographic memory with feedback using phase–conjugate mirrors," Opt.Lett. **11**, 118–120 (1986).
[6.5]

A.I. Sokolovskaya, G.L. Brekhovskikh and A.D. Kudryavtseva, "Restoration of wavefront of light beams during stimulated Raman scattering," Sov.Phys.Dokl. **22**, 156 (1977).
[4.5]

R.A. Sprague, "Effect of bulk carriers on PROM sensitivity," J.Appl.Phys. **46**, 1673–1678 (1975).
[2.19]

D.L. Staebler and W. Philips, "Fe–doped $LiNbO_3$ for read–write applications," Appl.Opt. **13**, 788–794 (1974).
[2.13]

S.I. Stepanov and M.P. Petrov, "Efficient unstationary holographic recording in photorefractive crystals under an external alternating electric field," Optics Comm. **53**, 292–295 (1985).
[2.28]

S. Sternklar and B. Fischer, "Double–colour–pumped photorefractive oscillator and image colour conversion," Opt.Lett. **12**, 711–713 (1987).
[1.32]

F.P Strohkendl, J.M.C. Jonathan and R.W. Hellwarth, "Hole–electron competition in photorefractive gratings," Optics Lett **11**, 312–314 (1986).
[1.10,2.3]

F.P. Strohkendl, P. Tayebati and R.W. Hellwarth, "A comparative study of the photorefractive effect in $Bi_{12}SiO_{20}$ crystals," OSA Topical meeting on *Photorefractive materials, effects and devices* (los Angeles, C.A.), Technical Digest **17**, 32–34 (August 1987).
[2.21]

D.A. Temple and C. Warde, "Anistropic scattering in photorefractive crystals," J.Opt.Soc.Am.B. **3**, 337–341 (1986).
[7.7]

J.B. Thaxter, "Electrical control of holographic storage in strontium barium niobate," Appl.Phys.Lett. **15**, 210–212 (1969).
[1.3]

R.L. Townsend and J.T. La Macchia, "Optically induced refractive index changes in $BaTiO_3$," J.Appl.Phys. **41**, 5188–5192 (1970).
[1.13]

G.C. Valley, A.L. Smirl, M.B. Klein, K. Bohnert and T.F. Boggess, "Picosecond photorefractive beam coupling in GaAs," Opt.Lett. **11**, 647–649 (1986).
[1.34]

G.C. Valley, "Simultaneous electron/hole transport in photorefractive materials," J.Appl.Phys **59**, 3363–3366 (1986).
[2.4]

S. Weiss, S. Sternklar and B. Fischer, "Double phase conjugate mirror: analysis, demonstration and applications," Opt.Lett. **12**, 114–116 (1987).
[1.29]

S.H. Wemple, M. DiDomenico Jr. and I. Camlibel, "Dielectric and optical properties of melt–grown $BaTiO_3$," J.Phys.Chem.Solids **29**, 1797–1803 (1968).
[2.27]

H.J. White, N.B. Aldridge and I. Lindsay, "Digital and analogue holographic associative memories," Opt.Eng. **27**, 30–37 (1988).
[5.10,6.15]

H.J. White and W.A. Wright, "Holographic implementation of a Hopfield model with discrete weightings," Appl.Opt. **27**, 331–338 (1988).
[6.17]

A. Yariv, "On transmission and recovery of three–dimensional image information in optical waveguides," J.Opt.Soc.Am. **66**, 301 (1976).
[4.8]

A. Yariv, "Compensation for atmospheric degradation of optical beam transmission by nonlinear optical mixing," Opt.Commun. **21**, 49 (1977).
[4.9,5.14]

A. Yariv and D.M. Pepper, "Amplified reflection, phase conjugation and oscillation in degenerate four wave mixing," Opt.Lett **1**, 16–18 (1977).
[4.16,5.13]

A. Yariv, "Phase conjugate optics and real–time holography," IEEE J.-Quant.Electron. **QE–14**, 650–660 (1978).
[4.17,5.1]

A. Yariv, "Four wave nonlinear optical mixing as real time holography," Opt.Commun **25**, 23–25 (1978).
[4.18]

Yariv A. and Yeh P., "Optical Waves in Crystals," (Wiley series in pure and applied optics, New York, 1984).
[2.10,4.15,A.1,F.1]

A. Yariv and Sze–Keung Kwong, "Associative memories based on message–bearing optical modes in phase–conjugate resonators," Opt.Lett. **11**, 186–188 (1986).
[6.6]

A. Yariv, Sze–Keung Kwong and K. Kyuma, "Demonstration of all–optical associative holographic memory," Appl.Phys.Lett. **48**, 1114–1116 (1986).
[6.8]

B.Ya. Zel'dovich, V.I. Popovichev, V.V. Ragul'skii and F.S. Faizullov, "Connection between the wave fronts of the reflected and exciting light in stimulated Mandel'shtam–Brillouin scattering," Sov.Phys. JETP **15**, 109–113 (1972).
[4.1,5.15]

B.Ya. Zel'dovich and V.V. Shkunov, "Wavefront reproduction in stimulated Raman scattering," Sov.J.Quantum.Electron. **7**, 610 (1977).
[4.4]

PUBLICATIONS

I. Lindsay and J.C. Dainty, "Partial cancellation of specular reflection in the presence of a phase–conjugate mirror," Opt.Commun. **59**, 405–410 (1986).
[5.19]

I. Lindsay, "Specular reflection cancellation/enhancement in the presence of a phase–conjugate mirror," J.Opt.Soc.Am. B **4**, 1810–1815 (1987).
[5.20]

H.J. White, N.B. Aldridge and I. Lindsay, "Digital and analogue holographic associative memories," Opt.Eng. **27**, 30–37 (1988).
[5.10,6.15]